



Universiteit Antwerpen

FACULTEIT WETENSCHAPPEN  
DEPARTEMENT FYSICA

Accurate and precise perfusion parameter estimation in  
pseudo-continuous arterial spin labeling MRI

---

Accuraat en precies schatten van perfusieparameters in  
pseudo-continuous arterial spin labeling MRI

Proefschrift voorgelegd tot het behalen van de graad van  
**Doctor in de Wetenschappen: Fysica**  
aan de Universiteit Antwerpen te verdedigen door  
**Piet BLADT**

*Promotoren:*  
Prof. Dr. Jan SIJBERS  
Dr. Ir. Arnold J. DEN DEKKER  
Prof. Dr. Eric ACHTEN

Antwerpen,  
2020

## **Doctoral committee**

### **Chairman**

Prof. Dr. Sandra Van Aert - University of Antwerp, Belgium

### **Members**

Prof. Dr. Jan Sijbers - University of Antwerp, Belgium

Dr. Ir. Arnold J. den Dekker - University of Antwerp, Belgium

Prof. Dr. Marleen Verhoye - University of Antwerp, Belgium

Prof. Dr. Eric Achten - Ghent University, Belgium

### **External members**

Prof. Dr. Patrícia Figueiredo - University of Lisbon, Portugal

Prof. Dr. Matthias J.P. van Osch - Leiden University, The Netherlands

## **Contact information**

Piet Bladt

imec - Vision Lab, Department of Physics, University of Antwerp

Universiteitsplein 1, 2610 Antwerp

Belgium

piet.bladt@uantwerpen.be



This research was financially supported by FWO, the Research Foundation - Flanders.





# Acknowledgements - Dankwoord

Apart from publicly defending my thesis, writing these acknowledgements is the final action in my PhD journey that started in 2015. This part is important to me, because this work is in many ways the result of a great deal of support. I chose to write this part in English as well, because it is the language I associate with this chapter of my life.

I want to start by thanking Jan and Arjan, my two main promotors. We have shared this journey starting from my Masters research back in 2013 up to this point. Before that, I also did a Bachelor project with Jan as promotor on the topic of Magnetic Particle Imaging. I still remember an email I sent Jan back then stating: "Dear Professor, my code won't run and I don't see the problem, could you have a look?". I hope we can agree that I made some steps since then. You both gave me the opportunity to start this research project in arterial spin labeling, an imaging modality that back in 2015 had not been studied before in the Vision Lab. While the project originated from a specific idea, I was given the freedom to approach this research field with an open mind and to pursue some of my own ideas regarding potential research opportunities. I am very grateful to both of you for trusting me with that responsibility and supporting me at each step along the way. Nonetheless, I think you would agree that it has not been easy to earn our place in the arterial spin labeling research community. In the end, however, I believe we have succeeded. Thank you for your continued support throughout these years.

I also want to thank Rik, my third promotor. While we have not worked together that often, I always enjoyed and learned from our discussions, even the ones in a sleep-deprived state in a shared taxi towards a conference center or in the terminal of some airport. You also made me feel part of your research group, for example by inviting me when you organized a dinner with your team during a conference. As I sometimes felt a bit lost in the first years at conferences trying to build up a network in the ASL community on my own, those gestures meant a lot to me.

Around the halfway mark of my PhD, I properly introduced myself to Professor

Matthias van Osch, a pivotal point in my trajectory. It led to a collaboration that resonates in two contributions of this work. It took a while before he could convince me to stop greeting him with ‘professor’, but after a while I got the hang of it. Thijs, it was a privilege to work with you, thank you.

I want to thank my colleague and good friend Patricia Clement for all her help in the past years. She helped me acquire MRI data many times in Ghent and was always available for advice. She also made short work of my insecurities about reaching out to big names in our research field by introducing me to a few of them at conferences out of the blue. Expanding your network with a free adrenalin rush on top. In those early days, it was the small push I needed. Thank you for everything, Patricia.

I am grateful for having had the chance to work with so many talented and interesting colleagues at the Vision Lab, too many to all name here. A few of them stand out to me. Gabriel, Dr. Ramos-Llordén, we have shared an office for most of the years I worked at the Vision Lab. I learned a lot from you, especially in the early days when you co-supervised my Masters thesis. More importantly, I have always enjoyed our talks and laughs, in the office, at a conference, or with a beer in a bar. Gabriel, you are not just a colleague to me, but a close friend. When Gabriel left, Shabab took his place across from me in the office. He is truly one of a kind; extremely talented, outgoing and extravert to the power of two, and overall too nice for this world. I want to thank you, Shabab, for making this last, often stressful, year so much more enjoyable. You mean a great deal to me.

When I made the switch from studying Medicine to Physics ten years ago, I met Sibylle, Niels and Jan. They were kind enough to give the old guy in class a chance. From there on out, there have been so many highlights. The semi-drunk group hug after a night out during a trip to CERN might be my favourite. After our Physics studies, all four of us took on PhD studies, creating a unique connection. Yet, in the end, I believe our friendship has little to do with our shared professional trajectory. Now that I have finished my PhD, I will stop complaining about it in our WhatsApp group and compensate it by doubling my outrage about politics in that cosy leftist echo chamber of ours. Thank you for everything, Sibylle, Niels, and Jan.

I want to thank some of my best friends who I leaned on for advice and, more importantly, who I could count on to take my mind off work. Yannick, I have enjoyed our many talks throughout the years, even though most of them were virtual. I guess we were just ahead of our time. I admire your persistence and hard

work in the many adventures you take on. Steven, I enjoyed our long conversations about anything and everything across the bars in Antwerp. Outgoing, interesting, smart, caring, easy to talk to; people like you are rare. I hope many more nights out will follow. Sam and Vincent, my friends from back in high school, my two best friends, thank you for the countless fun evenings. Our long tradition of get togethers has always been really important to me. You are both extremely talented, and that is why I am sure that, some day, you guys will start figuring out that poker game and stop losing your money to me.

Lastly, I want to thank everyone in my family and the family of my partner Sofie for supporting me in many different ways. Some of them have played a huge role and they deserve a paragraph of their own.

My younger sisters, Eva and Lola. I always like to highlight, with great pride, that I am the least talented of the three of us. Eva, Master in Physics with greatest distinction, PhD in Physics and now post-doc; extremely strong scientifically combined with stellar social and communicative skills, a rare combination. Lola, Master Product Development with greatest distinction and since then the central pillar of a start-up company reinventing uroflowmetry; exceptionally talented and driven beyond comparison. And this is all just skills, only a small part of the great individuals you both are. Throughout my doctoral studies, I have been able to benefit from the expertise of you both. Thank you for always being there and for having my back.

My mother, Elsie. For those who do not know her, allow me to brag a little bit. My mom is a civil engineer who finished her studies top of her year with greatest distinction. After that, she managed to build up a full-time career, while raising three children. Truth be told, that professional career could have been far more prestigious considering her intelligence and talents. Yet, at every turn, she made decisions putting the interest of her children first. I want to thank you for teaching me to work hard, for always being there, and for supporting me in every decision I make. In the last years you have occasionally said that your contribution to my studies has diminished gradually going from high school, over university, to my doctoral studies. While that might be partially true from a content-perspective, it is far from the truth in every other way. There is no one who has contributed more. Dank u voor alles, mama.

My own little family, Sofie and Asa. In terms of support during these past 5 years, Sofie has been irreplaceable. Especially in the past months, which have not been the easiest and in which, regrettably, I have not been the most pleasant. Caring

and sweet beyond comparison, smart, thoughtful. A few of your many assets. I was and still am proud that those qualities were recognized and celebrated when you received the price for best teaching assistant in the Pharmacy department of our university, as chosen by the students. I cannot think of anyone who would deserve a recognition like that more. Sofie, you truly are one of a kind and you mean the world to me. You were there for all the ups and the downs during this PhD journey. Thank you for always being there. As of a little under two years ago, however, you have to share the number one spot. Our daughter, Asa, was born. Asa, your presence has helped me put certain things, like finishing this PhD, into perspective. My favourite moment of a work day is when I arrive at the daycare center to pick you up. Every time, you start jumping up and down with excitement when you spot me. The most pure and innocent type of connection. It would make me forget about any work issue, even if only for a moment. Moments like that are invaluable. Without being aware of it, you played a big role in supporting me during the second half of my PhD, in your own little way. Sofie and Asa, I feel lucky to have you both by my side. Jullie zijn mijn twee grootste schatten.





# Summary

Perfusion is the delivery of blood to the capillary bed of the vascular system, where exchange of molecules between the blood and tissue compartment can occur. In the brain, perfusion is usually referred to as the cerebral blood flow (CBF). It is defined as the volume of blood (mL) delivered to a unit volume of brain tissue (100g) within a certain amount of time (min). The CBF can be affected in multiple brain disorders, such as in stroke, neurodegenerative diseases, cancer and epilepsy. It is therefore a potential biomarker for the diagnosis of such disorders or treatment follow-up. Arterial spin labeling (ASL) is a magnetic resonance imaging (MRI) technique that allows for absolute quantification of the CBF. It stands out from other imaging techniques capable of visualizing capillary perfusion, such as dynamic susceptibility contrast MRI and  $^{15}\text{O}$  positron emission tomography, by its non-invasiveness, as no exogenous tracer is needed in ASL. In recent years, the position of ASL in the clinic has significantly matured with the help of the recommended clinical implementation put forth by the ASL research community.

Despite the potential for absolute quantification, its non-invasiveness and the ease of the recommended implementation of ASL, significant issues remain. The inherently low signal-to-noise ratio of ASL data is at the origin of most of these issues. When estimating parameters (such as the CBF) from ASL data acquired in a clinical setting with a limited amount of scan time, the low SNR limits the amount of parameters that can be estimated with an acceptable precision. Adhering to this limit requires the use of simplified models with a small amount of parameters to be estimated, which often comes at a cost of accuracy (i.e., causes a bias). **The balance between accuracy and precision of perfusion parameter estimation in ASL MRI is at the basis of each contribution of this work.** Both the signal generation and imaging part on the one hand, and the quantification part of ASL, on the other hand, impact this balance. **In this work, strategies are put forth to improve on the existing trade-off between accuracy and precision in ASL given certain acquisition settings.**

This thesis consists of two parts. Part I contains the introductory chapters (Chapter 1-4), which provide the background for the three contributions (Chapter 5-7)

collected in Part II.

Chapter 1 is a short chapter motivating the use of the accuracy-precision trade-off in the build-up of the introductory chapters describing ASL.

In Chapter 2, an overview of the basic concepts of MRI is given. Understanding the basic principles of MRI are a prerequisite to studying ASL MRI. Therefore, a short overview of signal generation and detection in MRI is given, highlighting aspects that are of particular interest in ASL MRI. An attempt was made to go beyond the typical MRI introduction by highlighting some common misconceptions that often lead to an erroneous description of certain concepts in MRI.

Chapter 3 contains a description of the recommended clinical implementation of ASL from labeling of arterial blood water to quantification of CBF. Instead of attempting to merely rewrite the relevant parts of the recommendations, each aspect of signal generation and imaging is explicitly linked to potential effects on accuracy and/or precision in the quantification step.

In the recommended ASL experiment, the ASL signal is sampled repeatedly at one time point. In light of the accuracy-precision trade-off in quantitative ASL studied in this work, multi-delay ASL acquisition strategies have also been explored. These are introduced in Chapter 4. Sampling the ASL signal at multiple time points requires fitting a model to the data in order to estimate perfusion parameters. An overview of perfusion models, varying in complexity, describing the dynamic ASL signal is therefore given. Finally, parameter estimation techniques, using a certain perfusion model and given a certain multi-delay PCASL data set, are described.

Chapter 5 focusses on the impact of the amount of parameters to be estimated on the accuracy and precision of parameter estimation in multi-time-point ASL. We compared two estimators that used the same quantification model, yet with a different amount of parameters to be estimated. One estimator quantified the longitudinal relaxation time of tissue  $T_{1t}$  alongside the CBF and the arterial transit time (ATT), a parameter that describes the travel time from the labeling site to the local tissue voxel. The second estimator only quantified both perfusion parameters and kept  $T_{1t}$  fixed to a population average, as is conventional for quantification from multi-delay ASL data. As  $T_{1t}$  varies inter- and intrasubject, estimating it alongside the perfusion parameters is expected to reduce estimation bias compared to keeping it fixed to a population average. However, increasing the number of parameters to be estimated can reduce estimation precision. In order to maximally compensate for this expected loss in precision when adding a parameter to be estimated, the experiment design was optimized for this estimator using Cramér-Rao lower bound theory. The viability of both estimators in terms of accuracy and precision was examined in simulation and real data experiments.

While we showed that  $T_{1t}$  plays an important role in parameter estimation from ASL data, there are two other parameters that are prone to variability: the labeling efficiency  $\alpha$  and the longitudinal relaxation time of blood  $T_{1b}$ . Contrary to  $T_{1t}$ ,  $\alpha$  and  $T_{1b}$  also play a central role in the quantification model for single-time-point ASL, the recommended clinical implementation. They are also usually fixed to literature values. Just like fixing the value of  $T_{1t}$ , fixing the values of  $\alpha$  and  $T_{1b}$  could result in systematic errors (i.e., bias) in perfusion parameter estimation, as  $\alpha$  can vary over repetitions of the experiment and  $T_{1b}$  varies throughout the general population. However, both parameters are not independently identifiable from the CBF; they can not be estimated alongside the CBF and can therefore only be determined from supporting (MRI) experiments. Measuring  $\alpha$  and  $T_{1b}$  and using those measured values instead of fixing both parameters to literature averages is expected to increase the accuracy of CBF estimation on a population level. However, if we assume a fixed total scan time, performing extra experiments would diminish the scan time for acquiring the core ASL data. This is expected to reduce the precision of CBF estimation. Is it worth to sacrifice ASL scan time to perform these supporting measurements in terms of the accuracy-precision trade-off? That is the central topic of Chapter 6.

In Chapter 7, the effects of the acquisition strategy on perfusion parameter estimation are further explored. When using a conventional multi-slice readout strategy for ASL, the SNR of the ASL signal reduces in subsequently acquired slices due to increasing post-label delay times and fading background suppression. This limits the amount of slices that can be acquired with an SNR sufficient for a reproducible measurement of the ASL signal. It makes whole-brain coverage using a conventional sequential multi-slice readout strategy, without multiband, infeasible when isotropic high-resolution ASL data (i.e.,  $3 \times 3 \times 3 \text{ mm}^3$ ) is required. We explored the feasibility of combining super-resolution reconstruction (SRR) methods with single-time-point ASL and its potential when whole-brain coverage and 2D multi-slice readout are both required. The goal of SRR is to restore a high-resolution (HR) image from a set of differently acquired 2D multi-slice images with a low through-plane resolution. In structural MRI, relaxometry and diffusion MRI, it has been shown that super-resolution reconstructed HR images or HR parameter maps can break the trade-off between SNR, spatial resolution and scan time to which images directly acquired at a high resolution or parameter maps estimated from images directly acquired at a high resolution, respectively, are bound. In this work, we demonstrated that SRR is compatible with single-time-point ASL in simulations and real data. Furthermore, its potential to improve on the balance between SNR, resolution and scan time was shown in a first validation experiment

by comparing it to a conventional single-time-point ASL experiment with multi-slice readout.

# Samenvatting

Perfusie wordt gedefinieerd als de doorbloeding van de capillaire microvasculatuur van een orgaan, waar uitwisseling van verschillende moleculen gebeurt tussen het bloed en het weefsel. In de hersenen wordt perfusie beschreven aan de hand van de cerebrale bloeddorstrooming, ook wel cerebral blood flow (CBF) genoemd. De CBF is het volume bloed (mL) dat geleverd wordt aan een eenheid hersenweefsel (100g) binnen een bepaald tijdsinterval (min). De bloeddorstrooming is afwijkend bij verschillende hersenaandoeningen, waaronder beroertes, neurodegeneratieve ziekten, tumoren en epilepsie. In zulke gevallen kan de CBF een biomarker zijn voor het stellen van een diagnose en voor de opvolging van therapie.

De CBF kan gekwantificeerd worden met arterial spin labeling (ASL), een magnetische resonantie beeldvormingstechniek. ASL maakt gebruik van arterieel bloed als lichaamseigen tracer om de perfusie te visualiseren. Dat arterieel bloed wordt namelijk magnetisch gelabeld vlak voor het de hersenen instroomt. Na een wachttijd, waarin het gelabelde bloed langs de cerebrale vasculatuur tot in het capillaire bed van het hersenweefsel stroomt, wordt een beeld van de hersenen opgenomen. Hierna wordt er een beeld uitgelezen zonder voorafgaand labelen van het arteriële bloed. Het verschil tussen die twee beelden levert een perfusie-gewogen beeld op. Met een gepast wiskundig model kan tot slot een CBF map geschat worden vanuit dat perfusie-gewogen beeld.

ASL onderscheidt zich door die niet-invasiviteit van andere perfusie-beeldvormingstechnieken, zoals dynamische susceptibiliteit-contrast magnetische resonantie beeldvorming (DSC-MRI) en  $^{15}O$  positron emissie tomografie. In de laatste jaren vindt ASL ook zijn weg naar de kliniek, mede dankzij de aanbevelingen rond de klinische implementatie die in 2015 naar voor werden gebracht door de ASL onderzoeksgemeenschap.

Ondanks de mogelijkheid tot absolute kwantificatie van de CBF, de niet-invasiviteit en de duidelijke aanbevelingen rond klinisch gebruik, resteren er significante problemen die het wijdverspreid gebruik van ASL in de weg staan. Het ASL signaal is erg klein ten opzichte van het achtergrondsignaal van het hersenweefsel. Wanneer het verschil wordt genomen tussen het gelabeld en het niet-gelabeld beeld, is het signaal amper te onderscheiden van de ruis. Deze lage signaal-ruis

verhouding, vaak signal-to-noise ratio (SNR) genoemd, ligt aan de basis van de meeste van die significante problemen in ASL. Wanneer parameters (zoals de CBF) geschat worden uit ASL data opgenomen in een klinische setting met een beperkte beschikbare scantijd, beperkt de lage SNR de hoeveelheid parameters die geschat kunnen worden met een acceptabele precisie. Om aan die limiet te voldoen wordt er meestal een vereenvoudigd model met een klein aantal te schatten parameters gebruikt. Het gebruik van een vereenvoudigd model brengt echter de accuraatheid van het parameterschatten in het gedrang. **De balans tussen de accuraatheid en de precisie van het schatten van perfusieparameters in ASL ligt aan de basis van elke bijdrage in deze scriptie.** Zowel het genereren van het signaal en de beeldvorming enerzijds, als het parameterschatten anderzijds, beïnvloeden die balans. **In dit werk worden strategieën aangebracht om de huidige compromis tussen accuraatheid en precisie in ASL te doorbreken.**

Dit proefschrift bestaat uit twee delen. Deel I bevat de inleidende hoofdstukken (Hoofdstuk 1-4), die als relevante achtergrond dienen voor de drie hoofdbijdragen (Hoofdstuk 5-7) in Deel II.

Hoofdstuk 1 is een kort hoofdstuk waarin het gebruik van de accuraatheid-precisie balans in de opbouw van de inleidende hoofdstukken gemotiveerd wordt.

In Hoofdstuk 2 wordt een overzicht gegeven van de basisconcepten van magnetische resonantie beeldvorming, ook wel magnetic resonance imaging (MRI) genoemd. De beginselen van MRI begrijpen is een voorwaarde om ASL MRI te bestuderen. Daarom worden signaalopwekking en -detectie in MRI kort beschreven, met een nadruk op de aspecten die een belangrijke rol spelen in ASL. Er werd ook een poging gedaan om verder te gaan dan de typische MRI introductie door enkele veel voorkomende misvattingen te beschrijven die vaak leiden tot een foute beschrijving van bepaalde concepten in MRI.

Hoofdstuk 3 bevat een beschrijving van de aanbevolen klinische implementatie van ASL, gaande van het labelen van arterieel bloed tot en met de kwantificatie van CBF. In plaats van de relevante delen van de aanbevelingen gewoon te herschrijven, wordt elk aspect van signaalopwekking en beeldvorming expliciet gekoppeld aan mogelijke effecten op accuraatheid en precisie in de uiteindelijke parameterschatting.

In het aanbevolen ASL experiment wordt het ASL signaal herhaaldelijk uitgelezen op één tijdstip om de SNR van het uiteindelijke perfusie-gewogen beeld te verhogen. Dit wordt single-delay ASL genoemd. Een alternatief is het variëren van de wachttijd tussen labelen en beeldopname waardoor het ASL signaal op meerdere tijdstippen in zijn evolutie bemonsterd wordt. Zulke multi-delay ASL acquisitiestrategieën worden ingeleid in Hoofdstuk 4, opnieuw met het evenwicht

tussen accuraatheid en precisie als referentiepunt. Wanneer ASL data op meerdere tijdstippen verkregen is, kan de CBF geschat worden door een model te fitten aan de data. Hoofdstuk 4 bevat bijgevolg een overzicht van geschikte perfusiemodellen, met verschillende niveaus van complexiteit. Tot slot wordt de techniek gebruikt voor het parameterschatten, gebruik makend van een bepaald model en gegeven bepaalde ASL data, uitvoerig beschreven.

In de eerste bijdrage in hoofdstuk 5 wordt de impact van het aantal te schatten parameters op de accuraatheid en precisie van parameterschatten in multi-delay ASL bestudeerd. Er werden twee schatters vergeleken die hetzelfde onderliggende kwantificatiemodel hanteerden, weliswaar met een verschillend aantal te schatten parameters. Één schatter kwantificeert de longitudinale relaxatietijd van het weefsel  $T_{1t}$  samen met de twee lokale perfusieparameters, zijnde de CBF en de arteriële transitietijd (ATT), een parameter die beschrijft hoe lang het duurt voor het label om zicht van de plaats van labelen naar de lokale weefsel-voxel te verplaatsen. De tweede schatter kwantificeert enkel de perfusieparameters en houdt  $T_{1t}$  vast op een populatiegemiddelde, de conventionele aanpak in multi-delay ASL. Aangezien  $T_{1t}$  varieert in de hersenen en tussen individuen, wordt verwacht dat het schatten van  $T_{1t}$  samen met de perfusieparameters de accuraatheid van de schatter verhoogt. Echter, het aantal te schatten parameters verhogen kan ten koste gaan van precisie. Om het verlies van precisie maximaal te compenseren, werd het ontwerp van het experiment geoptimaliseerd door gebruik te maken van ‘Cramér-Rao lower bound’ theorie. Beide schatters werden met elkaar vergeleken wat accuraatheid en precisie betreft in simulatie-experimenten en experimenten met vrijwilligers.

Naast  $T_{1t}$  zijn er nog twee belangrijke parameters in ASL kwantificatie modellen: de labeling efficiëntie  $\alpha$  en de longitudinale relaxatie tijd van bloed  $T_{1b}$ . In tegenstelling tot  $T_{1t}$ , spelen zowel  $\alpha$  als  $T_{1b}$  een centrale rol in het kwantificatie model voor single-delay ASL. Voor beide parameters wordt meestal een vaste literatuurwaarde gekozen. Net zoals voor  $T_{1t}$ , kan dit leiden tot een inaccurate schatting van de CBF, aangezien  $\alpha$  kan variëren over verschillende herhalingen van een ASL experiment en  $T_{1b}$  varieert per individu. Beide parameters kunnen echter niet samen met de CBF geschat worden, aangezien ze niet onafhankelijk identificeerbaar zijn in het kwantificatie model. Ze kunnen echter wel bepaald worden vanuit ondersteunende experimenten. Het meten van  $\alpha$  en  $T_{1b}$  en die waarden gebruiken in plaats van de globale literatuurwaarden zou de accuraatheid van de CBF schatting moeten verbeteren in de algemene populatie. Echter, uitgaande van een vaste totale scantijd, zullen die ondersteunende experimenten ten koste gaan van scantijd voor de acquisitie van de ASL data. Dit veroorzaakt op zijn beurt een verminderde precisie van de CBF schatting. Loont het om ASL scantijd op te offeren voor deze ondersteunende experimenten wat de accuraatheid-precisie

balans betreft in de algemene populatie? Dat is het centrale thema van Hoofdstuk 6.

In Hoofdstuk 7 wordt het effect van de data acquisitiestrategie op het schatten van perfusieparameters verder onderzocht. Wanneer een conventionele multi-slice acquisitiestrategie wordt gebruikt voor het uitlezen van ASL data, zal de SNR van het ASL signaal verminderen in opeenvolgende uitgelezen snedes. Dit beperkt het aantal snedes dat kan uitgelezen worden met een SNR die voldoende hoog is voor een reproduceerbare meting van het ASL signaal. Het maakt de opname van ASL data van de volledige hersenen onhaalbaar wanneer een multi-slice uitleesstrategie gebruikt wordt en een isotrope hoge resolutie, zijnde  $3 \times 3 \times 3 \text{ mm}^3$  in ASL, vereist is. Het gebruik van super-resolutie reconstructie (SRR) methoden biedt een mogelijke oplossing. Het doel van SRR is om een hoog-resolutie beeld te reconstrueren op basis van een set verschillend opgenomen multi-slice beelden met een lage resolutie in de snede-selecterende richting. In structurele MRI, relaxometrie en diffusie MRI is het aangetoond dat het gunstiger is, wat de balans tussen SNR, spatiale resolutie en scantijd betreft, om hoog-resolutie beelden te reconstrueren met super-resolutie in plaats van ze rechtstreeks op te nemen aan die hoge resolutie. In dit werk hebben we aangetoond dat SRR compatibel is met single-delay ASL in simulatie-experimenten en in experimenten met echte data. Verder bleek ook dat, in vergelijking met een conventioneel multi-slice single-delay ASL experiment, de balans tussen SNR, resolutie en scantijd eveneens verbeterde wanneer super-resolutie reconstructie gebruikt werd.





# Contents

<b>Acknowledgements - Dankwoord</b>	<b>i</b>
<b>Summary</b>	<b>iv</b>
<b>Samenvatting</b>	<b>ix</b>
<b>I Arterial spin labeling MRI: from labeling to quantification</b>	<b>1</b>
<b>1 Introduction</b>	<b>3</b>
1.1 Arterial spin labeling: what is it and why do it? . . . . .	3
1.2 Accuracy and precision: the common thread in this work . . . . .	4
1.3 Motivation behind build-up of the introductory chapters . . . . .	5
<b>2 Magnetic resonance imaging: the basics</b>	<b>7</b>
2.1 Signal generation and detection . . . . .	7
2.1.1 Spin and magnetic moment . . . . .	7
2.1.2 Macroscopic effect of the static magnetic field . . . . .	8
2.1.3 Excitation away from equilibrium . . . . .	9
2.1.4 Classical description of the magnetization vector . . . . .	10
2.1.5 Relaxation back to equilibrium . . . . .	12
2.2 Image formation and readout strategies . . . . .	13
2.2.1 2D readout . . . . .	13
2.2.2 3D readout . . . . .	17
<b>3 Arterial spin labeling: recommended implementation</b>	<b>19</b>
3.1 Signal generation and imaging . . . . .	19
3.1.1 Labeling . . . . .	20
3.1.2 Delay after labeling . . . . .	23
3.1.3 Background suppression . . . . .	24
3.1.4 Readout . . . . .	25
3.2 Perfusion parameter estimation . . . . .	26

3.2.1	Quantification equation . . . . .	27
3.2.2	Accuracy and precision of the recommended quantification . . . . .	27
<b>4</b>	<b>Multi-delay arterial spin labeling</b>	<b>29</b>
4.1	Signal generation and imaging . . . . .	29
4.1.1	Conventional multi-delay implementation . . . . .	29
4.1.2	Time-encoded arterial spin labeling . . . . .	32
4.1.3	Pros and cons of multi-delay and time-encoded ASL . . . . .	34
4.2	Perfusion models . . . . .	36
4.2.1	Single-compartment model . . . . .	36
4.2.2	Multi-compartment models . . . . .	43
4.2.3	Dispersion effects . . . . .	48
4.3	Perfusion parameter estimation . . . . .	52
4.3.1	Model selection . . . . .	53
4.3.2	Maximum likelihood estimator . . . . .	54
4.4	Performance analysis of the estimator . . . . .	56
4.4.1	Accuracy analysis of the estimator . . . . .	57
4.4.2	Precision analysis of the estimator . . . . .	58
<b>II</b>	<b>Contributions</b>	<b>63</b>
<b>5</b>	<b>Estimating the <math>T_1</math> of tissue alongside the perfusion parameters in multi-delay ASL</b>	<b>65</b>
5.1	Introduction . . . . .	65
5.2	Theory . . . . .	67
5.2.1	Single-compartment quantification model . . . . .	67
5.2.2	Maximum likelihood estimation . . . . .	68
5.2.3	Optimization of multi-PLD PCASL acquisition settings for NLE3 . . . . .	69
5.3	Methods . . . . .	72
5.3.1	Parameter identifiability analysis . . . . .	72
5.3.2	Experiment design optimization . . . . .	73
5.3.3	Simulation experiments . . . . .	75
5.3.4	Real data experiments . . . . .	78
5.4	Results . . . . .	80
5.4.1	Parameter identifiability analysis . . . . .	80
5.4.2	Experiment design optimization . . . . .	80
5.4.3	Simulation experiments . . . . .	85

5.4.4	Real data experiments . . . . .	87
5.5	Discussion and conclusions . . . . .	91
<b>6</b>	<b>The benefit of supporting measurements in ASL</b>	<b>97</b>
6.1	Introduction . . . . .	98
6.2	Methods . . . . .	99
6.2.1	Simulation experiment . . . . .	99
6.2.2	Real data validation experiment . . . . .	106
6.3	Results . . . . .	108
6.3.1	Simulation experiment . . . . .	108
6.3.2	Real data validation experiment . . . . .	113
6.4	Discussion and Conclusions . . . . .	115
<b>7</b>	<b>Super-resolution reconstruction strategies for ASL</b>	<b>121</b>
7.1	Introduction . . . . .	121
7.2	Theory . . . . .	123
7.2.1	Super-resolution reconstruction in MRI: concept . . . . .	123
7.2.2	Super-resolution reconstruction in MRI: acquisition . . . . .	124
7.2.3	Super-resolution reconstruction in MRI: reconstruction . . . . .	125
7.3	Methods . . . . .	130
7.3.1	Data simulation and acquisition . . . . .	130
7.3.2	Reconstruction and quantification . . . . .	135
7.3.3	Performance analysis . . . . .	139
7.4	Results . . . . .	139
7.4.1	Simulation experiment . . . . .	139
7.4.2	Real data experiment . . . . .	143
7.5	Discussion and conclusions . . . . .	146
<b>8</b>	<b>Conclusions</b>	<b>149</b>
	<b>Epilogue</b>	<b>151</b>
	<b>Bibliography</b>	<b>152</b>
	<b>List of Abbreviations</b>	<b>169</b>
	<b>List of Symbols</b>	<b>171</b>
	<b>Academic overview</b>	<b>173</b>



## Part I

# Arterial spin labeling MRI: from labeling to quantification



## Chapter 1

# Introduction

### 1.1 Arterial spin labeling: what is it and why do it?

Arterial spin labeling (ASL) is a versatile non-invasive MRI technique which allows for a functional assessment of blood flow throughout the vascular system of an organ. ASL uses arterial blood as an endogenous tracer by inverting its magnetization using radiofrequency (RF) pulses. After a certain delay, in which labeled blood water travels through the arterial vascular tree towards the brain tissue, a so-called label image is acquired. Additionally, a control image is acquired without prior labeling. The difference between a label and a control image isolates the ASL signal. Depending on the delay between labeling and readout, the labeled arterial water will either still be in the arterial macrovasculature or will have reached the capillary bed where it can exchange with the tissue. The former case allows for an angiographic measurement of the supplying arteries, while the latter provides data suited for quantification of perfusion, the delivery of blood to the capillary bed of a tissue. Throughout this work, we will focus on using ASL for quantifying perfusion, applied to the organ most studied with ASL: the brain.

Perfusion in the brain is often referred to as the cerebral blood flow (CBF), defined as the volume of blood delivered to a certain tissue volume within a certain amount of time. It is a physiological parameter of high interest in a number of brain disorders, such as stroke, neurodegenerative diseases, epilepsy and cancer [1]. In recent years, the ability of ASL to detect these pathological changes in perfusion in a clinical setting has been demonstrated [2–4]. This emergence of ASL in a clinical setting is still ongoing, mainly due to it being a young technique relative to most other MRI modalities.

The inception of ASL dates back to the early 1990s, with the work of John Detre and others [5] generally considered as the earliest ASL publication [1]. An insightful overview of these early stages can be found in a recent review article by Jezzard et al. [4], showing that the general concept of ASL in fact dates back to

1959 [6]. In the past 25 years, the quality of the ASL method developed towards readiness for clinical application. However, clinical adoption of ASL was hindered by the large amount of implementation options, both in terms of signal generation and perfusion quantification. In 2015, this changed with the consensus statement on a recommended clinical implementation of ASL perfusion MRI by the ISMRM Perfusion Study Group and the European Consortium for ASL in Dementia [1]. It has propelled ASL to a mature competitor in the clinical perfusion MRI space.

There are many other techniques capable of visualizing capillary perfusion, yet all with distinct disadvantages. Cerebral perfusion can be measured with  $^{15}\text{O}$  positron emission tomography [7,8] (PET), xenon-computed tomography (CT) [9] and CT perfusion, but they all involve ionizing radiation. Dynamic susceptibility contrast (DSC) MRI is widely used in the clinic for perfusion measurements. It visualizes perfusion by injecting a bolus of gadolinium chelate contrast agent and subsequently imaging it as it passes through the cerebral capillary bed [10,11]. The gadolinium causes small local magnetic field inhomogeneities during its passage, ultimately resulting in a faster signal decay. The major drawbacks of DSC MRI are the invasiveness of the contrast injection and the difficulty to attain absolute quantification of perfusion [12]. Intravoxel incoherent motion (IVIM) is a method that postulates the measurement of tissue perfusion by modeling it as a pseudo-diffusion process [13]. In the brain, IVIM had no success, mainly due to low cerebral blood volume fractions and modeling issues [4]. Finally,  $^{17}\text{O}$ -water MRI is capable of absolute quantification of perfusion [14], but the high cost of the label limits its use on a large scale.

## 1.2 Accuracy and precision: the common thread in this work

Compared to the perfusion imaging techniques listed in the previous section, ASL stands out with its non-invasiveness and potential for absolute quantification of cerebral perfusion. However, despite these advantages and the ease of clinical applicability brought forth by the consensus statement, there are, obviously, a number of remaining issues and drawbacks. One of those issues revolves around a vital aspect of perfusion parameter quantification in ASL: accuracy versus precision. As the balance between accuracy and precision of perfusion parameter estimation is the main point of focus in all contributions of this work and will be referred to often in the introductory chapters following this first chapter, a formal definition of the accuracy and precision of an estimator (and by extension of perfusion quantification) is required.

### 1.3. Motivation behind build-up of the introductory chapters

---

Imagine an estimator  $\hat{\boldsymbol{\theta}}$  of an underlying true parameter vector  $\boldsymbol{\theta}_0$ . The accuracy of the estimator  $\hat{\theta}_k$  of a certain parameter  $\theta_{0,k}$  from  $\boldsymbol{\theta}_0$  is maximal if

$$E[\hat{\theta}_k] = \theta_{0,k}, \quad (1.1)$$

with  $E[\hat{\theta}_k]$  the expectation value of the estimator  $\hat{\theta}_k$ . The difference  $E[\hat{\theta}_k] - \theta_{0,k}$  is often referred to as the bias of the estimator. If Eq.(1.1) is fulfilled, the estimator is called unbiased. In all other cases the estimator is biased; the larger the absolute value of  $E[\hat{\theta}_k] - \theta_{0,k}$ , the larger the bias, the lower the accuracy of the estimator. Sources of bias are typically referred to as systematic errors and can be caused by fluctuations in the observations (i.e., the data), a mismatch between the estimation model and the underlying true process, and an insufficient number of observations [15].

The precision is related to the covariance of the estimator:

$$\text{cov}(\hat{\boldsymbol{\theta}}) = E \left[ (\hat{\boldsymbol{\theta}} - E[\hat{\boldsymbol{\theta}}])(\hat{\boldsymbol{\theta}} - E[\hat{\boldsymbol{\theta}}])^T \right]. \quad (1.2)$$

The diagonal elements of the covariance matrix represent the variance of the estimator for individual parameters  $\theta_k$  of  $\boldsymbol{\theta}$ , which is a measure of the precision of the estimator for each of those parameters. The precision of the estimator for a certain parameter is inversely related to the variance of the estimator for that same parameter; the higher the variance, the lower the precision. Variance is related to nonsystematic errors, which are caused by unpredictable fluctuations in the observations (i.e., noise in the data) [15]. Therefore, the precision of an estimator is directly related to the amount of measurements and the noise in the data. The essence of accuracy and precision is summarized in Figure 1.1.

### 1.3 Motivation behind build-up of the introductory chapters

ASL data notoriously suffers from a low signal-to-noise ratio (SNR). When fitting a model to ASL data acquired in a clinical setting with a limited amount of scan time, this low SNR puts a limit on the amount of parameters that can be estimated with an acceptable precision. Respecting this limit entails using simplified models with a small amount of parameters to be estimated, which often comes at a cost of accuracy. **The balance between accuracy and precision of perfusion parameter estimation in ASL perfusion MRI forms the crux of this work.** Both the signal generation and imaging part on the one hand, and the

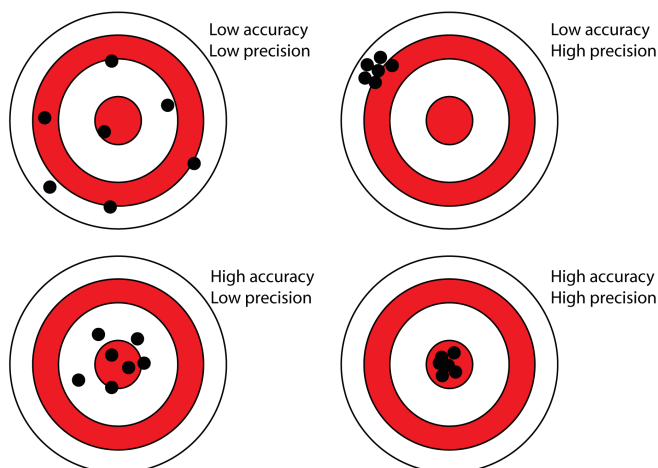


FIGURE 1.1: Visual representation of the accuracy and precision of an estimator. The underlying ground truth parameters are assumed to coincide with the bullseye. Precision is associated with random errors, accuracy is associated with systematic errors.

quantification part of ASL, on the other hand, impact this balance. The recommended clinical implementation of signal generation, imaging and quantification is introduced in Chapter 3. Sampling the dynamic ASL signal at multiple time points, an important alternative to the recommended implementation, is described in Chapter 4. These introductory chapters are written with the aforementioned balance in mind and contain the necessary background for the contributions in Part II.





## Chapter 2

# Magnetic resonance imaging: the basics

Understanding the basic principles of MRI is a prerequisite to studying ASL MRI. Therefore, in this chapter, a short overview of signal generation and detection in MRI is given, highlighting aspects that are of particular interest in ASL MRI. A more thorough description of the principles of MRI can be found in the work of Liang and Lauterbur [16].

In MRI, the application of a permanent strong magnetic field in combination with specifically timed electromagnetic radio frequency (RF) pulses and magnetic gradient pulses to an object or subject are used to generate spatially encoded signals that can be read out to generate images of internal structures. Specific combinations of these pulses give rise to a plethora of MRI sequences, which allow for a structural and/or functional assessment of a (part of a) subject. In this overview, first, the general concept behind generating and detecting an MRI signal is introduced. Then, image formation is briefly explained, focussing on two readout strategies typically used in ASL MRI.

In a relatively recent paper of Hanson [17], persistent misconceptions about basic concepts in MRI were highlighted. They often lead to misleading explanations of MRI, made by authors as well as educators. In the work of Hanson, alternatively, more accurate explanations are provided. These insights were incorporated in this chapter.

## 2.1 Signal generation and detection

### 2.1.1 Spin and magnetic moment

If an atomic nucleus has an odd number of protons or neutrons, it has an intrinsic angular momentum  $\mathbf{J} = \hbar\mathbf{I}$ , with  $\mathbf{I}$  the intrinsic spin, a dimensionless vector, and

$\hbar$  the reduced constant of Planck. Since a nucleus is charged, the intrinsic angular momentum  $\mathbf{J}$  is coupled with a magnetic dipole moment  $\boldsymbol{\mu}$ :

$$\boldsymbol{\mu} = \gamma\hbar\mathbf{I}, \quad (2.1)$$

with  $\gamma$  the gyromagnetic ratio of the nucleus. In quantum mechanics, the spin angular momentum operator  $\hat{\mathbf{J}} = \hbar\hat{\mathbf{I}}$  has eigenvalues  $\hbar\sqrt{I(I+1)}$  with  $I$  the spin quantum number. This spin quantum number is an intrinsic property of the nucleus, which is an integer or a half integer. In this study, and in the vast majority of clinical MRI exams, the considered nucleus is the hydrogen proton ( ${}^1\text{H}$ ). This proton has a high natural abundance in the human body in the form of water molecules. The spin quantum number of  ${}^1\text{H}$  is  $I = \frac{1}{2}$ . When there is an external magnetic field  $\mathbf{B}_0$  along the  $z$ -axis, the component of  $\hat{\mathbf{I}}$  parallel with the magnetic field,  $\hat{I}_z$ , has eigenvalues  $I_z$  that can take  $2I + 1$  values:  $-I, -I + 1, \dots, I$ . These eigenvalues  $I_z$  are the possible outcomes of a measurement of the angular momentum along the  $z$ -axis. In the case of  ${}^1\text{H}$ , there are two possible values: spin up,  $I_z = +1/2$ , or spin down,  $I_z = -1/2$ . Considering the linear relation between the intrinsic angular momentum  $\mathbf{I}$  and the magnetic moment  $\boldsymbol{\mu}$ , the proton magnetic moment has only two possible states:  $+\frac{1}{2}\gamma\hbar$  or  $-\frac{1}{2}\gamma\hbar$ . Those two discrete magnetic moments of the proton possess opposite potential energy in an external magnetic field  $\mathbf{B}_0$ :

$$E = -\boldsymbol{\mu} \cdot \mathbf{B}_0 = -\mu_z B_0 = \begin{cases} +\frac{1}{2}\gamma\hbar B_0 & \text{spin down } (I_z = -\frac{1}{2}) \\ -\frac{1}{2}\gamma\hbar B_0 & \text{spin up } (I_z = +\frac{1}{2}), \end{cases} \quad (2.2)$$

with ‘ $\cdot$ ’ the scalar product. This discrete difference between both energy levels is referred to as Zeeman-splitting. The lower energy level, spin up, corresponds to the  $z$ -component of the magnetic moment oriented parallel with  $\mathbf{B}_0$ , while the higher energy level, spin down, is compatible with the magnetic moment oriented anti-parallel with  $\mathbf{B}_0$ . Jumping from one energy level to another is possible by absorption or emission of a photon with energy  $\Delta E = \gamma\hbar B_0$ . Such photons have an angular frequency  $\omega_L = \gamma B_0$ , commonly referred to as the Larmor frequency.

### 2.1.2 Macroscopic effect of the static magnetic field

Up to this point, a single nucleus was considered. In matter, a large number of nuclei are present in close proximity of one another. While spin of a single nucleus is a quantum effect, an ensemble of nuclei allows to study magnetic resonance as a classical phenomenon [17]. This is justified by the correspondence principle, which

## 2.1. Signal generation and detection

---

states that the behaviour of systems described by quantum mechanics follows classical physics in the limit of large quantum numbers [18].

Without an external magnetic field, a proton spin can point in any direction. Such a random state can be described by a weighted sum of the energy eigenstates spin-up and spin-down as they form a basis for all possible states. A common misconception is that when an external magnetic field  $\mathbf{B}_0$  is switched on, all spins jump to either a spin-up or spin-down state [17]. The only thing that changes is that all spins will precess around the direction of the magnetic field with the Larmor frequency. Because of this precession, radio waves (with the Larmor frequency  $\omega_L$ ) are exchanged within the sample, which cause magnetic interactions between neighbouring nuclei. These interactions result in reorientation of the magnetic moments. Ultimately, such reorientations are responsible for a redistribution of the spins slightly skewed toward the direction of the external field [17]. As a result, the vectorial sum of all magnetic moments results in a netto magnetization  $\mathbf{M}$  along the direction of the external field  $\mathbf{B}_0$ . This magnetization  $\mathbf{M}$  is in equilibrium as long as  $\mathbf{B}_0$  remains on, even though the spins are precessing. Indeed, emitted radio waves due to precession are absorbed by neighbouring spins as stated above; there is no net emission of radio waves [17]. The difference between the distribution of spins in a sample without and with an external magnetic field applied is schematically shown in Figure 2.1.

### 2.1.3 Excitation away from equilibrium

In order to detect magnetization, an electrically conducting coil is placed around the subject. Rotating transverse magnetization ( $M_{x,y}$ ) will induce a voltage in the coil proportional to the magnitude of the transverse magnetization. However, as we argued in the previous section, in equilibrium, the magnetization vector  $\mathbf{M}$  is directed along the static magnetic field  $\mathbf{B}_0$ , i.e.  $M_x = M_y = 0$ . Therefore, in order to detect  $\mathbf{M}$ , it needs to be tilted away from equilibrium. Consider  $\mathbf{B}_1$  as a time varying magnetic field, perpendicular to  $\mathbf{B}_0$ , and oscillating at  $\omega_L$ , also referred to as a radio frequency (RF) pulse. Such an RF field rotates the spin distribution as a whole; it is again a classical phenomenon. For the formal proof, we refer to ‘proposition 3’ in the appendix of [17]. In Figure 2.2, the motion of the magnetization  $\mathbf{M}$  is shown when a resonant RF field  $\mathbf{B}_1$  is applied, both in the reference laboratory frame (left) and in a reference frame rotating at  $\omega_L$  along with  $\mathbf{M}$  and  $\mathbf{B}_1$  (right). In the laboratory frame, the magnetization spirals down towards the  $xy$ -plane on the surface of a sphere with radius  $|\mathbf{M}|$ . Indeed,  $|\mathbf{M}|$  remains constant as the RF field rotates the spin distribution as a whole (see above). In the rotating frame, the magnetization rotates perpendicular to  $\mathbf{B}_1$  at

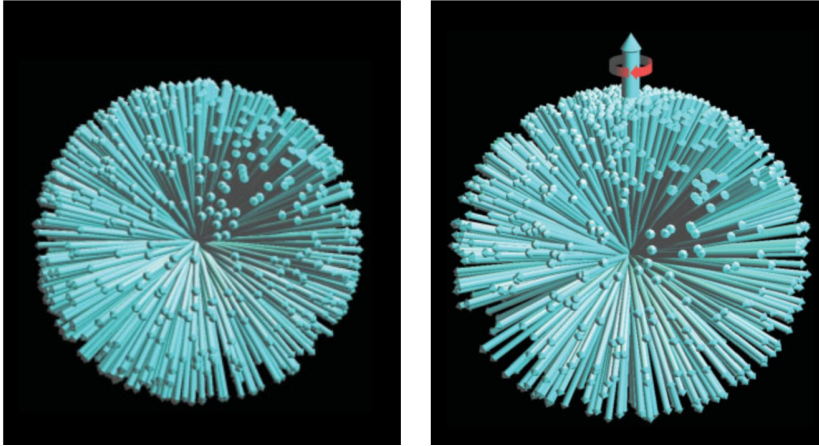


FIGURE 2.1: On the left, the spin orientation distribution is shown when no magnetic field is applied. Each spin has a random direction, resulting in a spherical angular distribution with no net magnetization. On the right, the situation is shown when an external magnetic field  $\mathbf{B}_0$  is switched on. The red arrow indicates that all spins are precessing around the magnetic field. The spin distribution in this case is slightly skewed toward the direction of the magnetic field, resulting in a net equilibrium magnetization  $\mathbf{M}$ , indicated by the large blue arrow. These images were taken from [17].

angular frequency  $\omega_1$ . Applying the RF pulse during a time interval  $\Delta t$ , flips the magnetization over an angle  $\alpha = \gamma B_1 \Delta t$ , the flip angle. In most sequences, flip angles are  $90^\circ$  or  $180^\circ$ .

#### 2.1.4 Classical description of the magnetization vector

Let us consider the magnetization vector  $\mathbf{M}$  from the moment the RF field  $\mathbf{B}_1$  is switched off, after it has been rotated over a certain arbitrary angle  $\alpha$ . Additionally, as a temporary assumption, let there be no interactions other than with the external static magnetic field  $\mathbf{B}_0$  directed along the  $z$ -axis. The macroscopic magnetization  $\mathbf{M}$  will experience a torque:

$$\frac{d\mathbf{M}}{dt} = \gamma(\mathbf{M} \times \mathbf{B}_0). \quad (2.3)$$

## 2.1. Signal generation and detection

---

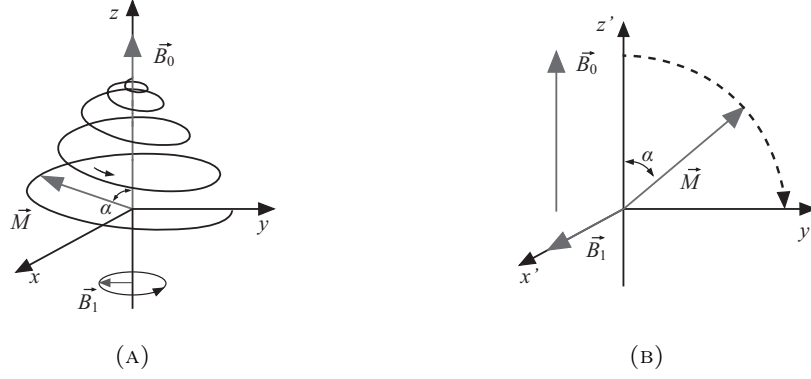


FIGURE 2.2: Evolution of magnetization  $\vec{M}$  experiencing a static longitudinal magnetic field  $\vec{B}_0$  and a transversal time varying magnetic field  $\vec{B}_1$  in the laboratory reference frame (left) and the rotating reference frame (right).

The components along the  $x$ ,  $y$  and  $z$ -direction are given by:

$$\frac{dM_x}{dt} = \gamma M_y B_0 \quad \frac{dM_y}{dt} = -\gamma M_x B_0 \quad \frac{dM_z}{dt} = 0. \quad (2.4)$$

Solving these differential equations results in an expression for the evolution of the different components of the magnetization in time:

$$M_x(t) = M_x(0) \cos(\omega_L t) + M_y(0) \sin(\omega_L t) \quad (2.5)$$

$$M_y(t) = M_y(0) \cos(\omega_L t) - M_x(0) \sin(\omega_L t) \quad (2.6)$$

$$M_z(t) = M_z(0). \quad (2.7)$$

Eq.(2.5-2.7) denote that the macroscopic magnetization vector precesses around the direction of the external magnetic field, as shown in Figure 2.3, with angular frequency  $\omega_L = \gamma B_0$ , the Larmor frequency.

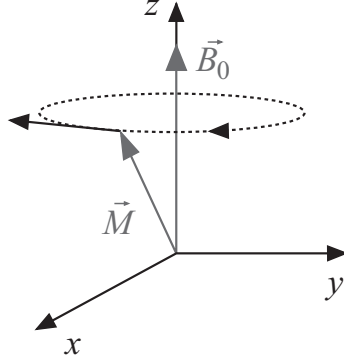


FIGURE 2.3: Schematic presentation of the torque on the macroscopic magnetization vector  $\mathbf{M}$  caused by the external magnetic field  $\mathbf{B}_0$

### 2.1.5 Relaxation back to equilibrium

In reality, the temporary assumption made in the previous section does not hold: the magnetization  $\mathbf{M}$  will return back to its equilibrium parallel to the static magnetic field  $\mathbf{B}_0$  due to interactions of the spins with their surroundings. This is referred to as relaxation and it can be added phenomenologically to Eq.(2.3). There are two distinct relaxation processes. On the one hand, the component of  $\mathbf{M}$  parallel to  $\mathbf{B}_0$ ,  $M_z$ , restores to its equilibrium value  $M_0$ , governed by spin-lattice relaxation, with time constant  $T_1$ . On the other hand, the components perpendicular to  $\mathbf{B}_0$ ,  $M_x$  and  $M_y$  return to zero, mediated by spin-spin relaxation, field inhomogeneities, and local differences in magnetic susceptibility, with time constant  $T_2^*$ :

$$\frac{dM_z}{dt} = \frac{M_0 - M_z}{T_1} \quad (2.8)$$

$$\frac{dM_{x,y}}{dt} = \gamma(\mathbf{M} \times \mathbf{B}_0)_{x,y} - \frac{M_{x,y}}{T_2^*}. \quad (2.9)$$

Eq. (2.3), (2.8) and (2.9) are known as the Bloch equations [19].

The relaxation of the components perpendicular to the static magnetic field,  $M_{x,y}$  is caused by a dephasing of spins. This dephasing is caused by local magnetic field inhomogeneities which are two-fold. Firstly, moving electrons and nuclei cause rapidly fluctuating magnetic field inhomogeneities leading to irreversible transverse

## 2.2. Image formation and readout strategies

---

relaxation called  $T_2$ -decay. Secondly, the static magnetic field  $\mathbf{B}_0$  is also spatially inhomogeneous, inherently and also due to differences in magnetic susceptibilities in different tissue types. These inhomogeneities also lead to transverse relaxation, yet reversible with sequence adjustments, as it is a constant process in time. If both effects are considered, it is called  $T_2^*$  relaxation.

Spin-lattice relaxation or  $T_1$  relaxation of the longitudinal component of the magnetization vector is caused by a combination of physical processes [20]. In order for the longitudinal component of the magnetization to change, energy needs to be exchanged with the surroundings (i.e., the lattice). The energy that is released is transferred to the lattice as molecular vibrations (phonons). This interaction with the lattice results in reorientations of magnetic moments, causing a redistribution of the spins (similarly as the process described in section 2.1.2 when a static magnetic field is suddenly switched on).

Relaxation times  $T_1$  and  $T_2$  vary among different tissue types and in certain pathophysiological states. Furthermore, it is important to note that both  $T_1$  and  $T_2$  relaxation times depend on the magnetic field strength; they are not inherent biomarkers of a certain tissue type [21].

## 2.2 Image formation and readout strategies

Generating rotating transverse magnetization using an RF pulse, as described above in section 2.1.3, allows for MR signal detection. However, such a signal is not yet linked to a certain spatial location. Spatial encoding is essential to perform MR imaging. It can be achieved by means of time dependent magnetic field gradients, that vary linearly in space, in the three spatial directions: slice encoding, frequency encoding and phase encoding, e.g. in the  $z$ -,  $x$ - and  $y$ -direction, respectively. Depending on the exact implementation of the slice encoding, two types of image acquisition strategies can be distinguished: 2D and 3D readout.

### 2.2.1 2D readout

When a slice encoding magnetic gradient  $G_z$  is applied along the  $z$ -axis, the strength of the total magnetic field in a plane at location  $z$  is equal to  $B_0 + G_z z$ . It implies that the angular frequency of precessing spins becomes dependent on the location  $z$ . When such a slice encoding gradient is applied simultaneously with an RF pulse rotating at the Larmor frequency, that RF pulse will be off-resonant for all spins at locations  $z \neq 0$ . In other words, only spins at  $z = 0$ , precessing at the Larmor frequency, would be excited. In reality, an RF pulse has a finite bandwidth  $\Delta\omega = \gamma G_z \Delta z$ . Therefore, spins with frequencies  $\omega_L \pm \Delta\omega/2$  will be

excited in a slice with a thickness equal to  $\Delta z$ . The slice position can be changed by using RF pulses with a frequency  $\omega_1 = \omega_L + \delta\omega$ , with  $\delta\omega$  a certain frequency offset.

After slice encoding, application of specifically timed phase encoding gradients  $G_y$  and frequency encoding gradients  $G_x$  along the  $y$ - and  $x$ -axis allows to spatially encode the MR signals within the excited slice [16, 22]:

$$S(k_x, k_y) = \int_{-\infty}^{+\infty} \int_{-\infty}^{+\infty} S(x, y) \exp(-i2\pi(k_x x + k_y y)) dx dy, \quad (2.10)$$

with  $S(x, y)$  the magnitude of the magnetization vector at a spatial location defined by coordinates  $x$  and  $y$ . The wave numbers  $k_x$  and  $k_y$  are equal to the temporal integral of the magnetic gradient applied for spatial encoding:

$$k_x = \frac{\gamma}{2\pi} \int_0^T G_x(t) dt \quad (2.11)$$

$$k_y = \frac{\gamma}{2\pi} \int_0^T G_y(t) dt, \quad (2.12)$$

where  $T$  equals the duration that covers the total time to acquire  $S(k_x, k_y)$ , inherently assuming that  $G_x(t)$  and  $G_y(t)$  are only nonzero at specific times where the respective gradients are switched on.

The MR signals  $S(k_x, k_y)$  are acquired in so-called  $k$ -space. It can be sampled at multiple frequencies  $(k_x, k_y)$  in order to obtain a 2D data set in  $k$ -space. As Eq.(2.10) shows that the MR signal  $S(k_x, k_y)$  is the Fourier transform of the spin density  $S(x, y)$ , an image of the spin densities in the spatial domain can be obtained by performing a 2D inverse Fourier transformation on the 2D data set in  $k$ -space [23]. An example is shown in Figure 2.4.

### Gradient and spin echo

Gradient echo and spin echo are two basic pulse sequences that lie at the basis of more advanced pulse sequences commonly used in ASL. In Figure 2.5a, a pulse sequence diagram is shown for gradient echo. A  $90^\circ$  pulse moves the magnetization, in a certain slice, into the  $xy$ -plane for signal detection. After phase encoding, using a certain gradient  $G_y$ , a gradient reversal on the frequency encoding axis forms an echo of the free-induction decay signal [24], which is read out. The time

## 2.2. Image formation and readout strategies

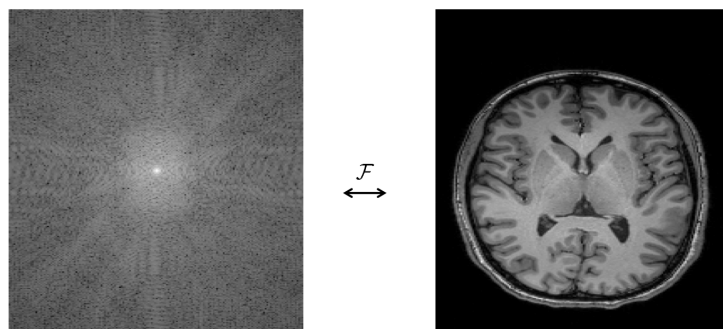


FIGURE 2.4: An example of the acquired MR signals in  $k$ -space on the left and its inverse Fourier transform, the MR image in the spatial domain, on the right. Note that both the  $k$ -space and real space image are originally complex valued, yet their respective magnitudes are shown here.

between the excitation pulse and the time of readout is called the echo time (TE). In this process, data is acquired for multiple wave numbers  $k_x$  along a line in cartesian space, linked to one  $k_y$  wave number. By choosing different gradients  $G_y$  (see the dotted lobes in Figure 2.5a), multiple lines in  $k$ -space can be sampled (see Figure 2.5b).

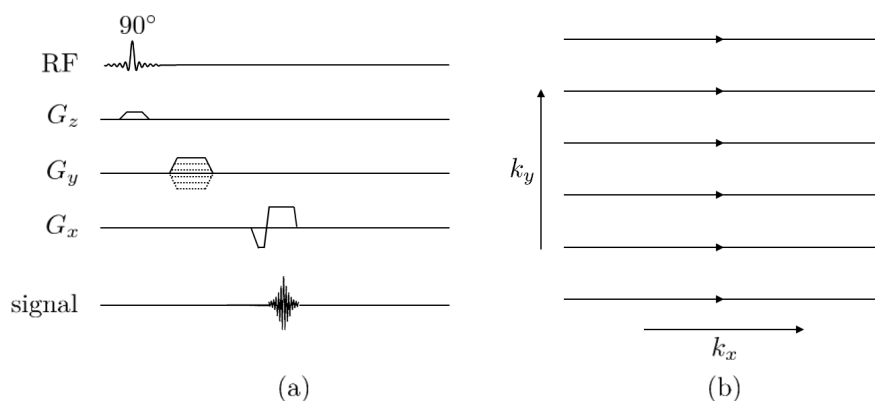


FIGURE 2.5: (a) Pulse sequence diagram for gradient echo readout (b) Schematic display of the way  $k$ -space is traversed using the gradient echo readout scheme depicted in (a).

A spin echo sequence contains a  $90^\circ$  excitation pulse and a  $180^\circ$  refocusing pulse. The refocusing pulse reverses reversible relaxation effects of the transverse magnetization, caused by spatial magnetic field inhomogeneities and differences in magnetic susceptibilities between tissues, at the time of the echo. Therefore, gradient echoes are weighted by the factor  $\exp(-TE/T_2^*)$ , while spin echoes are purely weighted by the irreversible spin-spin relaxation effects (i.e.,  $\exp(-TE/T_2)$ ). A diagram of the spin echo sequence is shown in Figure 2.6. More details concerning gradient and spin echo sequences can be found in the work of Bernstein et al. [24].

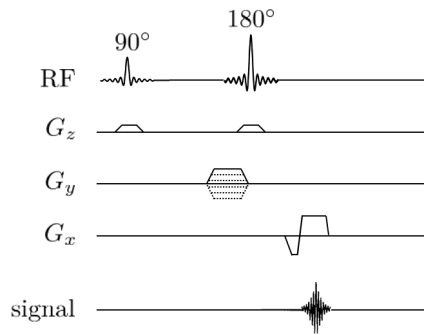


FIGURE 2.6: Pulse sequence diagram for spin echo readout.

### Single-shot EPI 2D readout

When 2D readout is used in ASL, single-shot echo-planar imaging (EPI) is recommended [1]. After excitation (i.e., slice selection), the entire 2D  $k$ -space is covered by an efficient use of time-varying gradients  $G_x$  and  $G_y$ . The EPI readout strategy is shown in Figure 2.7. After shortly switching on  $G_y$ , a line in the Cartesian coordinate system is sampled during the application of  $G_x$  (i.e., different frequencies  $k_x$  for a fixed frequency  $k_y$ ). Subsequent lines for different  $k_y$  are sampled by applying the phase encoding gradient for a very short time in between the positive and negative lobes of the frequency encoding gradient.

If data from multiple slices is required, the entire readout procedure can be repeated, with slice excitation at different locations along the  $z$ -axis. Therefore, 2D readout methods are often referred to as multi-slice imaging techniques.

While EPI has the benefit of being extremely fast, it is prone to a range of artifacts. The most prominent ones are ghosting and potential severe distortions, both along the phase-encoding direction [24].

## 2.2. Image formation and readout strategies

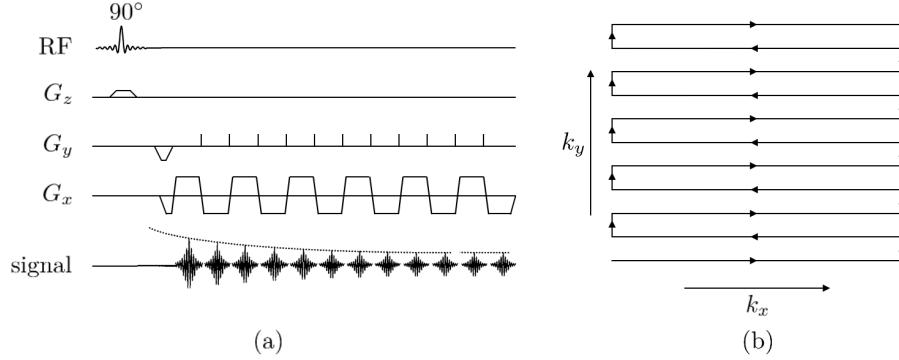


FIGURE 2.7: (a) Schematic display of single-shot EPI readout (b) Schematic display of the way  $k$ -space is traversed using the EPI readout scheme depicted in (a).

### 2.2.2 3D readout

The excitation of a slice, as described for 2D readout above, can be performed for a thicker slab. Indeed, the thickness of the excited volume  $\Delta z = \Delta\omega/(\gamma G_z)$  can be increased by increasing the bandwidth of the RF pulse or by reducing the gradient  $G_z$  applied during excitation. Once such a thicker slab is prepared, encoding is performed in three orthogonal directions: phase encoding along the  $z$ -axis and  $y$ -axis and frequency-encoding along the  $x$ -axis [24, 25]. In that way, MR signals are encoded in the three spatial directions within the excited slab:

$$S(k_x, k_y, k_z) = \int_{-\infty}^{+\infty} \int_{-\infty}^{+\infty} \int_{-\infty}^{+\infty} S(x, y, z) \exp(-i2\pi(k_x x + k_y y + k_z z)) dx dy dz, \quad (2.13)$$

with  $k_z$  the wave number corresponding to the temporal integral of the magnetic gradient used for encoding along the  $z$ -axis. In this case, a 3D image of the spin densities is obtained by performing a 3D inverse Fourier transformation on the acquired 3D  $k$ -space data set.

Compared to 2D readout, 3D readout is more SNR-efficient because a much larger volume is excited within a single excitation. When performing the discrete 3D inverse Fourier transformation instead of the 2D version, more  $k$ -space data points contribute to the generation of each data point in the spatial domain. For a formal comparison of the SNR efficiency between 2D and 3D readout, we refer to section 11.6.1 in [24].

### 3D GRASE readout

Segmented 3D readout, where a segment corresponds to a single excited slab as described above, is the recommended imaging method for ASL. A very fast variant is 3D gradient and spin echo (GRASE) [26], in which 3D  $k$ -space data is acquired within a single shot. It is important to stress that the single shot refers to the acquisition of data within the excited slab or segment. While a slab covers a larger part of the object to be imaged compared to 2D readout, often, two or more segments are still required to cover the entire object.

The single-shot 3D GRASE sequence is shown in Figure 2.8. After excitation, a series of  $180^\circ$  refocusing pulses are timed together with a phase modulation of all the spins in the slab, by switching on a gradient  $G_z$  for a short time. This process corresponds to sampling at a certain wave number  $k_z$ . Between each set of refocusing pulses, an EPI readout strategy is performed.

As is the case for EPI, GRASE readout also often results in ghosting artifacts [24]. Additionally, different levels of  $T_2$ -weighting at different times during readout cause changes in the signal amplitude, which ultimately results in through-plane blurring [1].

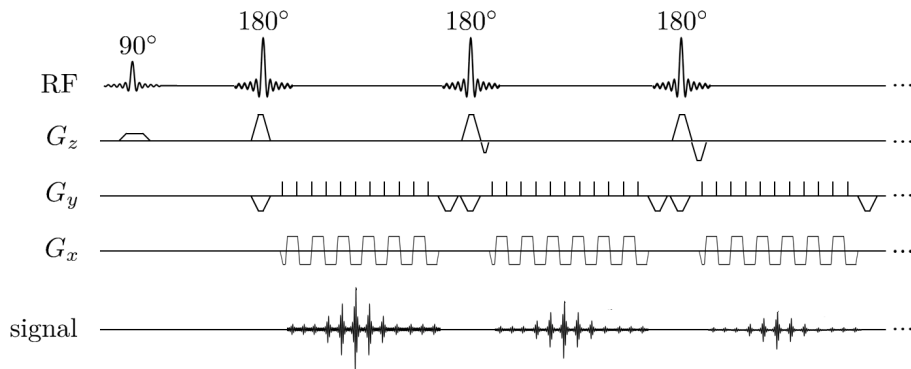


FIGURE 2.8: Schematic display of single-shot 3D GRASE readout





## Chapter 3

# Arterial spin labeling: recommended implementation

In this chapter, the entire process from labeling of arterial blood water to quantification of CBF is introduced as recommended for clinical implementation of ASL [1]. All relevant aspects of ASL signal generation and imaging are covered in section 3.1. Perfusion quantification according to recommendations is described in 3.2.

### 3.1 Signal generation and imaging

The consensus statement [1] on a recommended clinical implementation of ASL perfusion MRI put forth by the ISMRM Perfusion Study Group and the European Consortium for ASL in Dementia succeeded in distilling a go-to ASL experiment from approximately 25 years of research. It forms a suitable basis for the introduction of the ASL technique. Instead of attempting to merely rewrite the relevant parts of this publication, in the current chapter, each aspect of signal generation and imaging is explicitly linked to potential effects on accuracy and/or precision in the quantification step.

Before diving into the different facets of ASL signal generation and imaging, the core concept of ASL needs to be defined. In ASL, acquisition of a so-called label image consists of three subsequent parts: magnetic labeling of arterial blood proximal to the brain, a delay time to allow the labeled blood to flow to the brain tissue, and finally acquiring an image of the brain. Besides label images, control images without prior labeling are acquired. The signal difference between control and label images originates from the labeled spins delivered to the brain tissue by perfusion, thus resulting in a perfusion-weighted image. A schematic overview is shown in Figure 3.1.

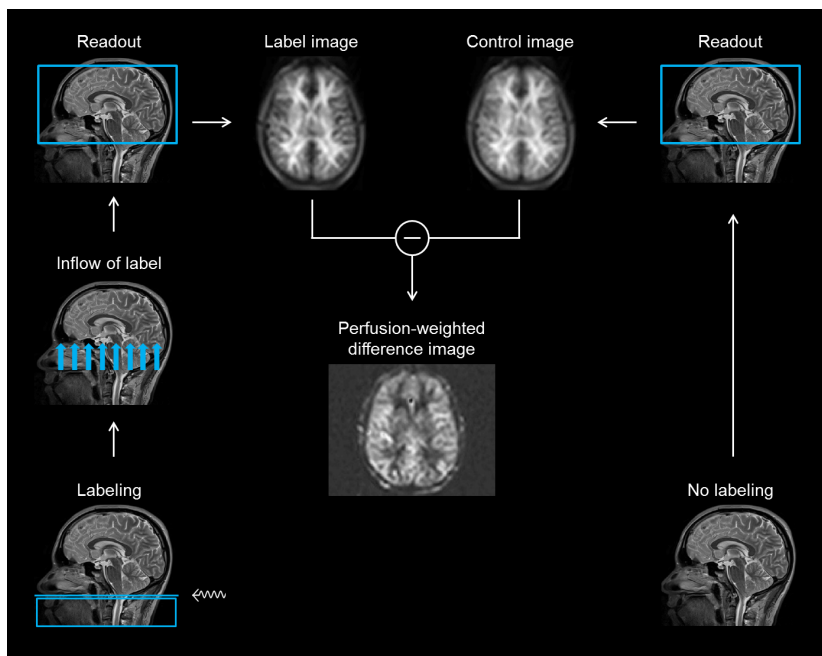


FIGURE 3.1: Schematic overview of the core concept on which ASL is built.

### 3.1.1 Labeling

In arterial spin labeling, as the name of the technique suggests, arterial blood is used as an endogenous tracer. The hydrogen nuclei of arterial blood water are magnetically labeled using RF pulses. There are multiple methods to perform this labeling, which are generally grouped in three classes: continuous labeling, pulsed labeling and velocity or acceleration selective labeling. Continuous labeling methods can be further subdivided in true continuous labeling and **pseudo-continuous labeling**. The latter has been put forth as the recommended labeling technique [1].

#### Overview of labeling techniques

Both in pulsed and continuous labeling, arterial blood is labeled proximal to the imaging volume. In pulsed ASL (PASL), one or a limited number of RF pulses invert the magnetization within a whole slab of tissue below the brain, which includes the supplying large arteries [27–29]. In continuous labeling methods, labeling is performed for a longer period (in the order of seconds) by applying continuous RF

### 3.1. Signal generation and imaging

---

energy to a labeling plane which inverts the magnetization of arterial blood as it flows through that plane, a process known as flow-driven adiabatic inversion. The difference between continuous ASL (CASL) and pseudo-continuous ASL (PCASL) lies in the way continuous RF energy is established. In CASL, adiabatic inversion is established by means of a constant gradient and a constant RF pulse [5,30]. In PCASL, the same effect as in CASL is created by a long train of slice-selective RF and gradient pulses [31]. A schematic overview of both PASL and (P)CASL is shown in Figure 3.2, which was taken from the consensus statement [1]. Note that all labeling pulses are off-resonance with respect to the imaging volume.

Velocity and acceleration selective labeling use motion-sensitizing gradients to generate label within the imaging volume [32,33]. These labeling techniques are fundamentally different from PASL and (P)CASL, They fall outside the scope of the contributions in this work and are therefore not discussed further.

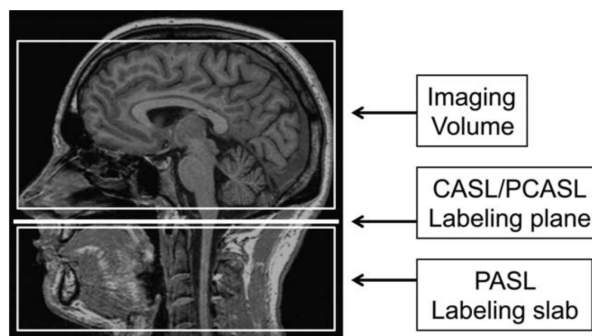


FIGURE 3.2: A schematic overview of the spatial aspects of PASL and (P)CASL. This figure was directly obtained from the ASL consensus paper [1].

#### The advantages of PCASL

In comparison with PASL and CASL, PCASL combines the best of both worlds. There are two distinct disadvantages to CASL. First, the long RF pulse leads to magnetization transfer effects in the background tissue of the brain. As these effects would not be present in the control image, this leads to significant errors when subtracting the label image from the control image. Efforts to change the pulse sequence to reduce magnetization transfer come at a cost of reduced labeling efficiency. Second, the required continuous RF power can not be provided by RF amplifiers in most MR scanners. PCASL achieves an equivalent labeling as CASL

with limited magnetization transfer effects. Furthermore, it is compatible with standard MR scanners.

PASL has the same advantages as PCASL compared to CASL. However, the SNR of PASL is lower than that of PCASL for two reasons. First, the spatial coverage of the RF coil limits the thickness of the labeling slab to 10-20 cm. With typical mean arterial blood velocities of approximately 20cm/s in supplying arteries, this limits the temporal duration of the labeled bolus to approximately 1 second. The temporal duration of a PASL bolus is equivalent to the labeling duration chosen in PCASL. In PCASL, it is possible to create larger boli with labeling durations longer than 1 second. As the ASL signal increases with the label duration, this results in higher SNRs for PCASL compared to PASL. Second, the labeling plane of PCASL is typically located near the distal end of the PASL labeling slab. In PCASL, for the entire bolus, blood magnetization is inverted as it flows through the labeling plane, while the entire bolus is inverted at one point in time in PASL. The back end of the PASL bolus has to travel for a longer time to the target tissue compared to the front end, causing the back end to have a more decayed ASL signal due to  $T_1$  relaxation. In PCASL, each part of the bolus will have traveled an equal distance when reaching the target tissue, equivalent to the distance traveled by the front end of the PASL bolus. Therefore, the PCASL bolus undergoes less  $T_1$  decay, resulting in a higher SNR.

In the remainder of this work, if not mentioned explicitly, PCASL labeling is implicitly assumed.

### **The importance of the labeling duration**

The choice of the duration of labeling in PCASL has a complex impact on the eventual precision of estimation of perfusion parameters. On the one hand, the ASL signal increases as the labeling duration increases. Note however that the gain in signal increases diminishes for labeling durations larger than the  $T_1$  of blood, which has a population average of 1.65 s at 3.0 T [34], and plateaus around 4s [1]. On the other hand, the repetition time (TR) increases as the labeling duration increases, which reduces the amount of label-control pairs that can be acquired per unit of time. Both of these effects have inverse implications: longer labeling durations increase the SNR, which has a positive effect on estimation precision, yet they reduce the amount of label-control pairs per unit of time, which has a negative effect on estimation precision.

In the consensus statement, a rather pragmatic choice of a **labeling duration of 1.8 s** was made. It is clear however that the labeling duration is an acquisition

parameter that can be optimized as a function of estimation precision. This option was explored as part of a research contribution presented in Chapter 5.

#### 3.1.2 Delay after labeling

In PCASL, the time between the end of labeling and the start of imaging is referred to as the post-labeling delay (PLD). In the recommendations, it is advised to use **a single PLD of 1800 ms**. That choice is based on the time it takes for the bolus to travel from the labeling plane through the arterial vascular tree towards a certain piece of tissue in a certain part of the brain, often referred to as the arterial transit time (ATT). Like the CBF, the ATT is a biophysical parameter that varies between different regions in the brain, between individuals and between healthy and pathological tissue [35, 36]. Typical values for ATT in gray matter are between 500 and 1500 ms, while they are on average slightly higher in white matter [1, 35, 37, 38]. Thus, the recommended PLD is longer than most ATTs in the population. This serves two main purposes. First, it allows the labeled bolus to reach the capillaries in the tissue, largely avoiding remaining ASL signal in large supplying arteries which would show up in the perfusion images as bright spots, mimicking hyperperfusion. Second, it (theoretically) guarantees the arrival of the entire bolus in the microcirculation of the target tissue throughout the brain, reducing the dependence of perfusion quantification on the underlying local ATT [39]. This point is more elaborately discussed in section 3.2.1, in which the recommended quantification model is discussed.

In deep white matter and pathological tissue, the ATT can be longer than 1800 ms [1]. In that case, CBF estimates can become less reliable as the PLD would be shorter than the ATT. In theory, one could choose the PLD even longer to meet the conditions described in the previous paragraph. However, longer PLDs will come at a further cost of reduced ASL signal due to  $T_1$  decay. A PLD of 2000 ms was recommended as a compromise between meeting the  $\text{PLD} > \text{ATT}$  requirement in most cases and maintaining a sufficient SNR. Even so, the average ASL signal will be higher for shorter PLDs. It can be debated whether meeting the  $\text{PLD} > \text{ATT}$  criterion, which ensures ATT-independent quantification, weighs up against the loss of ASL signal, which will reduce precision of perfusion quantification. This dilemma is revisited in the discussion of the contribution in Chapter 6.

The choice of using PCASL with a single PLD, in what follows referred to as single-PLD PCASL, is perhaps the most important aspect of the consensus statement. It implies that the entire scan time is used to repeat the acquisition of label-control pairs with fixed acquisition settings, often referred to as averaging.

Indeed, it allows for pairwise subtraction of label and control images and subsequent averaging of the perfusion-weighted difference images. This averaging is of vital importance, as the ASL signal in gray matter is typically of the order of 1% of the background signal [1]. Therefore, when subtracting a single label from a single control image pair, the ASL signal will be hardly distinguishable from the noise. Averaging of multiple pairwise subtracted label and control images boosts the SNR of the ASL signal.

### 3.1.3 Background suppression

As already briefly stated in the last paragraph of the previous section, ASL difference images generally suffer from a very low SNR. Background suppression is a method to significantly increase the overall SNR of the ASL signal. Before explaining the concept of background suppression, the different noise components in MR images need to be well understood.

#### Raw and physiological noise

When considering noise in MR, one generally considers thermal noise and scanner induced noise components, which can be described as raw noise characterized by a standard deviation  $\sigma_0$ . This noise is proportional to the static magnetic field strength  $B_0$  and independent of the MR-signal intensity [40]. However, as shown by Krüger and Glover [41], there are also noise components that are signal-dependent, denoted as physiological noise, described by a standard deviation  $\sigma_P = c \cdot S$ , with  $c$  a constant and  $S$  the MR-signal intensity. Such physiological noise is caused by multiple factors, such as local motion artifacts caused by cardiac and respiratory function and magnetic field modulations [41]. The total image noise can thus be described by the following standard deviation [41]:

$$\sigma = \sqrt{\sigma_0^2 + \sigma_P^2}. \quad (3.1)$$

For a certain signal intensity  $S$ , which is constant over time in the case of repeated acquisition of label-control image pairs when using a fixed PLD, the SNR can be formally defined as [41]:

$$\text{SNR} = \frac{S}{\sqrt{\sigma_0^2 + \sigma_P^2}} = \frac{\text{SNR}_0}{\sqrt{1 + c^2 \text{SNR}_0^2}}, \quad (3.2)$$

with  $\text{SNR}_0 = S/\sigma_0$  the signal-to-raw-noise ratio in the absence of physiological noise. The definition of SNR in Eq.(3.2), incorporating physiological noise, is often

### 3.1. Signal generation and imaging

---

used in BOLD and ASL to define so-called temporal SNR [42,43]. In that case, the underlying signal intensity as well as the standard deviation of the physiological noise are averaged over a certain time course.

#### The rational for and concept of background suppression

Knowing that physiological noise scales with the image signal intensity, it can be significantly reduced by suppressing the signal intensity. In the case of ASL, if the background signal  $S$  in the label and control images (which is theoretically equal in both images) can be suppressed without gravely affecting the ASL signal, it could significantly increase the SNR of the ASL signal in the eventual difference image. Indeed, if we assume the signal intensities in the unsubtracted images to be Gaussian distributed, the SNR of the ASL signal can be written as:

$$\text{SNR}_{\text{ASL}} = \frac{S_{\text{ASL}}}{\sqrt{2} \cdot \sqrt{\sigma_0^2 + \sigma_P^2}}. \quad (3.3)$$

Clearly, the  $\text{SNR}_{\text{ASL}}$  will increase as  $\sigma_P$ , which scales with the background signal  $S$ , reduces.

Such a background suppression can be achieved using a combination of a saturation pulse and a certain number of inversion pulses applied to the imaging volume [44,45]. By timing the inversion pulses correctly, the longitudinal magnetization of the background tissue will pass through zero at the time of readout. There is a trade-off in the amount of inversion pulses. Increasing this amount ensures suppression of the static tissue signal over an increasing range of  $T_1$  values. Unfortunately, due to inevitable imperfections in the inversion pulses, each extra inversion reduces the ASL signal with approximately 5%. In order to balance this trade-off, **background suppression with two inversion pulses** is recommended [1].

#### 3.1.4 Readout

##### Recommended readout sequence

**Segmented 3D sequences, such as 3D GRASE** [26,46], are the recommended readout method, followed by **single-shot 2D multi-slice readout as a back-up choice**. Both the 2D EPI multi-slice and the 3D GRASE readout are described in detail in sections 2.2.1 and 2.2.2, respectively. There are three main advantages of segmented 3D readout compared to single-shot 2D sequences. First, as the entire image is acquired in one excitation, background suppression can be maximal for the

entire volume by timing it correctly with the readout excitation. In 2D readout methods, there is an excitation for the acquisition of each slice. In that case, background suppression can only be optimal in the first slice and will become less effective in each subsequent slice. This can be considered the most important reason for choosing 3D over 2D readout in ASL. Second, 3D acquisition is less susceptible to magnetic field inhomogeneities. Finally, the total readout time for a volume is generally lower for 3D readout. However, this effect is limited, as the labeling duration and PLD take up most time of the TR. It is worth noting that a considerable downside of 3D readout is its sensitivity to subject motion during acquisition. Any movement that occurs during 3D readout, which takes 300-450 ms for whole-brain coverage using the recommended spatial resolution [43, 47], cannot be untangled afterwards in postprocessing. On the contrary, 2D multi-slice sequences are virtually insensitive to motion as the acquisition time of each slice is very short ( $\sim 50$  ms [47]).

### Recommended spatial resolution

The intrinsically low SNR of ASL difference images can be partially mediated by choosing a low spatial resolution for readout. Therefore, it has been recommended to use **a spatial resolution of 3-4mm in-plane and 4-8mm through-plane**. An obvious downside of a low spatial resolution is partial volume effects which visually result in losing a lot of fine anatomical details in the ASL perfusion-weighted images as well as in the quantified perfusion parameter maps. Correcting for these partial volume effects (PVEs) in ASL has been actively studied [48–51]. While PVE correction is not a central topic in this thesis, it is a potential benefit of combining ASL with super-resolution reconstruction, which has been explored in one of the three main contributions of this thesis, discussed in detail in Chapter 7.

## 3.2 Perfusion parameter estimation

In most applications of quantitative MRI, a certain signal that changes over time is sampled at multiple time points and quantitative parameters, which parameterize the signal change over time, are estimated by fitting a suitable model to the acquired data points. In that sense, the recommended single-PLD PCASL implementation is markedly different, as the dynamic PCASL signal is only sampled at one point in time. From such data, only one parameter, the CBF, can be quantified in a unique way. It also simplifies the estimation process drastically; data acquired at one time point allows for parameter quantification by means of a closed-form

expression between the data and the parameter to be quantified (section 3.2.1). This has major implications on the accuracy and precision of quantification of the CBF, which is discussed in section 3.2.2.

### 3.2.1 Quantification equation

When the assumption is made that the entire labeled bolus has arrived in the tissue microvasculature, no label flows out through the venous vasculature and the relaxation of the labeled spins is entirely described by the blood longitudinal relaxation time, the CBF in a certain voxel can be quantified in PCASL as [1, 52]:

$$\text{CBF} = 6000 \cdot \frac{\lambda \Delta S \exp\left(\frac{\text{PLD}}{T_{1b}}\right)}{2\alpha T_{1b} S_{\text{PD}} \left(1 - \exp\left(-\frac{\tau}{T_{1b}}\right)\right)}, \quad (3.4)$$

with  $\lambda$  the blood/brain partition coefficient in mL/g,  $\Delta S$  the averaged difference between the label and control signals,  $T_{1b}$  the blood longitudinal relaxation time,  $\alpha$  the labeling efficiency,  $S_{\text{PD}}$  the proton density signal (which is obtained from a separately acquired proton density image),  $\tau$  the labeling duration, and the factor of 6000 converting the units of the CBF from mL/g/s to mL/100g/min.

In essence, in (Eq.3.4), the relative single-PLD PCASL perfusion signal  $\Delta S$  is multiplied with a certain prefactor to obtain an absolute CBF estimate. This quantification formula was deduced from a more elaborate perfusion model described by Buxton et al. [52]. This deduction is described in detail in section 4.2.1 of Chapter 4, where different perfusion models are introduced.

Note that the recommended quantification model is independent of the ATT, another local perfusion parameter. This is directly due to two assumptions mentioned in the first paragraph of this section: the entire labeled bolus has arrived in the tissue microvasculature, i.e. the PLD is longer than the ATT (see section 3.1.2), and ASL signal relaxation is governed entirely by  $T_{1b}$ .

### 3.2.2 Accuracy and precision of the recommended quantification

In order to quantify CBF from observations acquired at a single time point, all parameters on the right side of Eq.(3.4) have to be either assumed as known or acquired from another experiment. The PLD and labeling duration  $\tau$  are acquisition parameters that are known. The proton density signal is acquired as a separate image. The remaining parameters are either fixed to population means, in the case of  $T_{1b}$  and  $\lambda$ , or to experiment repetition means, in the case of  $\alpha$ . Indeed, in the recommendations, the following assumptions are made:  $\lambda = 0,9$  mL/g,  $T_{1b} = 1.65$

s at 3.0 T,  $\alpha = 0.85$  [1]. As these parameters can vary significantly between individuals or between repetitions of the experiment, they are a potential source of bias. The effects of such a bias have been extensively studied in this work and are discussed in Chapter 6.

The recommended quantification formula on its own is also a source of inaccuracy, as it is based on assumptions that are approximations of reality. Of course, this comment will be true for any perfusion model to a certain degree, as it is unlikely any model exactly describes the physiological underlying PCASL perfusion process. Furthermore, especially in terms of the PLD, efforts have been made in the recommended implementation to minimize bias when quantifying the CBF with the equation above. Nonetheless, single-PLD PCASL is vulnerable to under- or overestimation of CBF, especially when the ATT varies over a large range in a subject or in the studied population [53, 54].

While single-PLD PCASL quantification clearly suffers from potential low accuracy, its strong suit is a high precision. Repeated measurements of label-control pairs at the same time point greatly increase the SNR of the ASL signal in the eventual averaged ASL difference image  $\Delta S$ . As all other parameters on the right hand side are known or assumed to be known, error propagation dictates that the precision of CBF quantification scales with the SNR of the averaged ASL difference image.

An alternative to single-PLD PCASL acquisition and quantification is the acquisition of ASL data at multiple time points. This allows a sampling of the dynamic evolution of the ASL signal. To such data, a perfusion model can be fit. In general, such models entail fewer assumptions compared to the recommended quantification formula above, thus leading to a more accurate estimation of CBF. However, it requires the estimation of other (perfusion) parameters alongside the CBF when fitting the model to the multi-time-point data. Increasing the amount of parameters to be estimated usually comes at a cost of precision. Note that the previous sentence is not a hard statement. Indeed, it is difficult to theoretically compare the precision of CBF estimation from single-delay ASL data to CBF estimation from multi-delay ASL data, as estimation would be performed on different data sets. This point is revisited in Chapter 6. Nonetheless, when considering single-delay or multi-delay ASL methods, the balance between accuracy and precision of CBF estimation takes center stage. In the next chapter, multi-delay PCASL methods are introduced.





## Chapter 4

# Multi-delay arterial spin labeling

In light of the accuracy-precision trade-off in quantitative ASL studied in this work, multi-delay ASL acquisition strategies have been explored. These are introduced in section 4.1. An overview of perfusion models, varying in complexity, describing the dynamic PCASL signal is given in section 4.2. Parameter estimation techniques, using a certain perfusion model and given a certain multi-delay PCASL data set, are described in section 4.3.

### 4.1 Signal generation and imaging

Acquiring ASL data using a single delay after labeling is arguably the most impactful recommendation in [1] with regard to the accuracy and precision of perfusion parameter quantification. An interesting alternative to single-PLD PCASL is a multi-delay version where, instead of averaging PCASL data acquired at a single time point, the ASL perfusion process is sampled dynamically at multiple time points. A recent discussion about a potential follow-up white paper at an ASL workshop at the University of Michigan<sup>1</sup> (March 2019) suggested that at least part of the ASL community entertains the idea of evolving in the direction of acquisition at multiple PLDs. There are two main ways of sampling the PCASL signal at multiple delays: multi-PLD PCASL and time-encoded PCASL. Both sampling methods play an important role in this work and are discussed below.

#### 4.1.1 Conventional multi-delay implementation

The conventional way of sampling the PCASL signal at multiple time points  $t_i$  is by changing the PLD for subsequent acquisitions of label-control pairs, usually referred to as multi-PLD PCASL [55, 56]. In order to also sample the PCASL signal as it flows through the macrovasculature and while only part of the bolus

---

<sup>1</sup>[http://fmri.research.umich.edu/events/ASL19\\_program.pdf](http://fmri.research.umich.edu/events/ASL19_program.pdf)

has reached the microvasculature, one can also shorten the labeling duration. By choosing smart combinations of the labeling durations and PLDs, the evolution of the PCASL signal can be visualized. An example is shown in Figure 4.1. In the top left image, the labeled bolus has not yet reached the structures in the transverse slice. The next four images display the potential of (PC)ASL to provide angiographic information as it mainly shows the labeled bolus travelling through the arterial macrovasculature. The last four images clearly visualize the (final part of the) perfusion phase; the entire labeled bolus has arrived in the tissue microvasculature where labeled arterial water eventually exchanges from the capillaries into the tissue compartment. In this phase, no more fresh labeled spins arrive, therefore, the PCASL signal decays due to  $T_1$  relaxation.

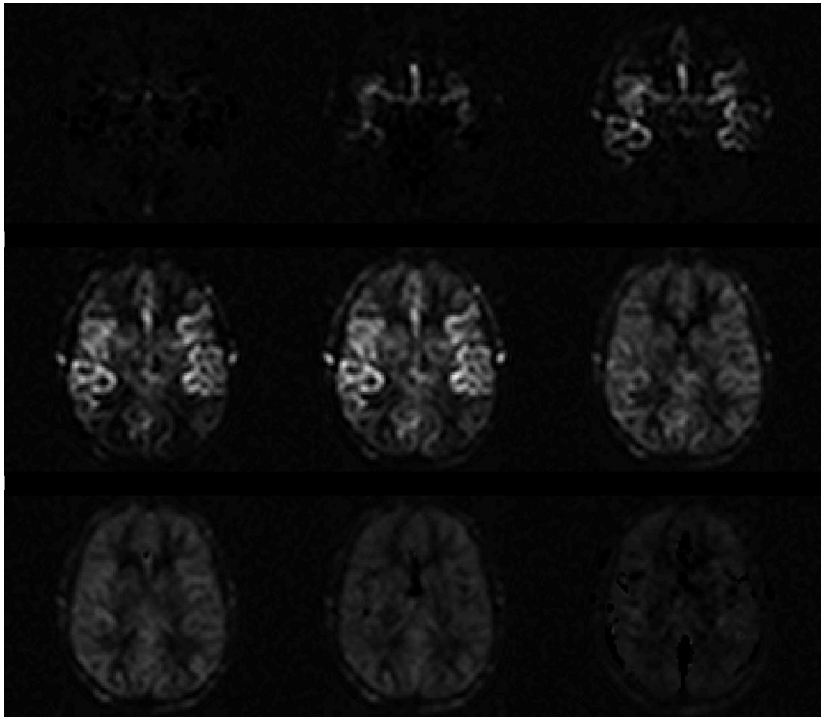


FIGURE 4.1: A transverse slice of ASL difference images, i.e. the result of the subtraction of a label and control image, acquired at 9 different time points,  $t = \{0.50, 0.94, 1.38, 1.82, 2.26, 2.70, 3.14, 3.58, 4.02\}$  s, during the evolution of the PCASL signal. The chronological evolution of the PCASL signal starts at the top left image and ends at the bottom right.

#### 4.1. Signal generation and imaging

---

As mentioned in the first chapter, we are interested in the ability of PCASL to visualize the perfusion process. A single voxel containing gray matter can be chosen from the transverse slice shown in Figure 4.1. In Figure 4.2, the PCASL signal in that particular voxel is shown for the 9 time points visualized in Figure 4.1 and for 10 additional time points. It shows the typical shape associated with the dynamic evolution of a PCASL signal. In a first phase, the signal increases in time as the labeled spins flow into the tissue microvasculature. In the second phase, when all labeled spins have arrived in the voxel, the signal decreases as  $T_1$  relaxation takes over. The temporal width of the first phase is approximately equal to the labeling duration  $\tau$ , which was equal to 1.8 s in this experiment. Note that for acquisition of data at time points  $t_i < 1.8$  s, the labeling duration was shortened and combined with a very short PLD. This method allows the sampling of the PCASL signal at any time point  $t_i$ . This point is more elaborately discussed in section 5.2.1.

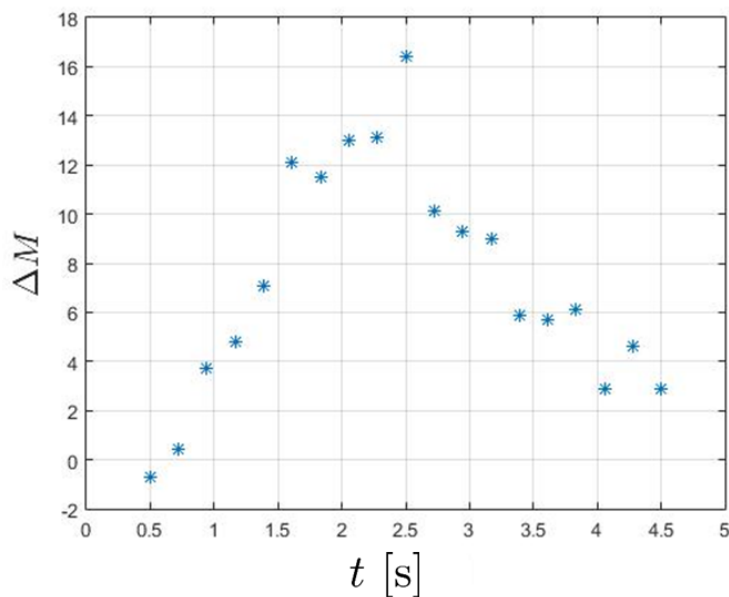


FIGURE 4.2: PCASL difference signal acquired at multiple time points in a voxel containing gray matter. It shows the evolution of the signal for a bolus with a labeling duration of  $\tau = 1.8$  s.

An important consequence of acquiring PCASL data at multiple time points is the fact that, for each time point, fewer (or no) averages can be acquired compared

to single-PLD PCASL, assuming a fixed total scan time. Therefore, the eventual (averaged) difference images at each time point in multi-PLD PCASL will be more noisy compared to the single-PLD PCASL difference image. In a clinical context, where ASL is often used without quantification, this is an important downside of multi-PLD PCASL.

### 4.1.2 Time-encoded arterial spin labeling

An alternative to sample the PCASL signal at multiple time points is time-encoded PCASL (te-PCASL), first introduced by Günther [57]. Where in single- or multi-PLD PCASL separate label and control images are acquired, this is no longer the case in te-PCASL. The time reserved for the labeling (or control) block and for the PLD is replaced by a series of ‘time blocks’ that are either used for labeling or for the control condition. In Figure 4.3, a multi-PLD acquisition scheme is contrasted with a time-encoded scheme. Selection of a label or control block is not random, as it may look like at first; it is Hadamard encoded. A Hadamard matrix is a  $n \times n$  square matrix with elements equal to either -1 or +1 and whose rows are mutually orthogonal [58]. The order of a Hadamard matrix can only be 1, 2 or a multiple of 4. In te-PCASL, a label block is chosen for each +1 entry and a control block for each -1 entry. Note that the first column of the Hadamard matrix is not used for te-PCASL encoding.

The  $n$  images acquired after applying a mixture of label and control blocks on their own are not interpretable. However, with certain linear combinations of the obtained images, the PCASL signal related to a block in a certain column can be filtered out. It is for this reason the label and control blocks are Hadamard encoded. Isolating the signal related to the label- and control-blocks in the first column of the te-PCASL encoding matrix is visualized in Figure 4.4. By choosing different linear combinations, this process can be repeated for each column. In that way,  $n - 1$  PCASL difference images are obtained. Such an image has a labeling duration equal to the temporal duration of the block in the respective column and an effective PLD equal to the duration between the end of the respective block and the beginning of readout. Furthermore, it can be seen as an ‘averaged’ difference image, as the labeling and control condition is repeated  $n/2$  times. In short, by acquiring  $n$  images using time-encoded PCASL, one ends up with  $n - 1$  PCASL difference images at  $n - 1$  different effective PLDs.

The time-encoded acquisition scheme shown in Figure 4.3b has a fixed block duration over all columns. The block duration can however be chosen differently in each column [59]. A very interesting option, shown in Figure 4.5, is the so-called ‘free-lunch’ encoding scheme [59]. It is an elegant extension of the conventional

#### 4.1. Signal generation and imaging

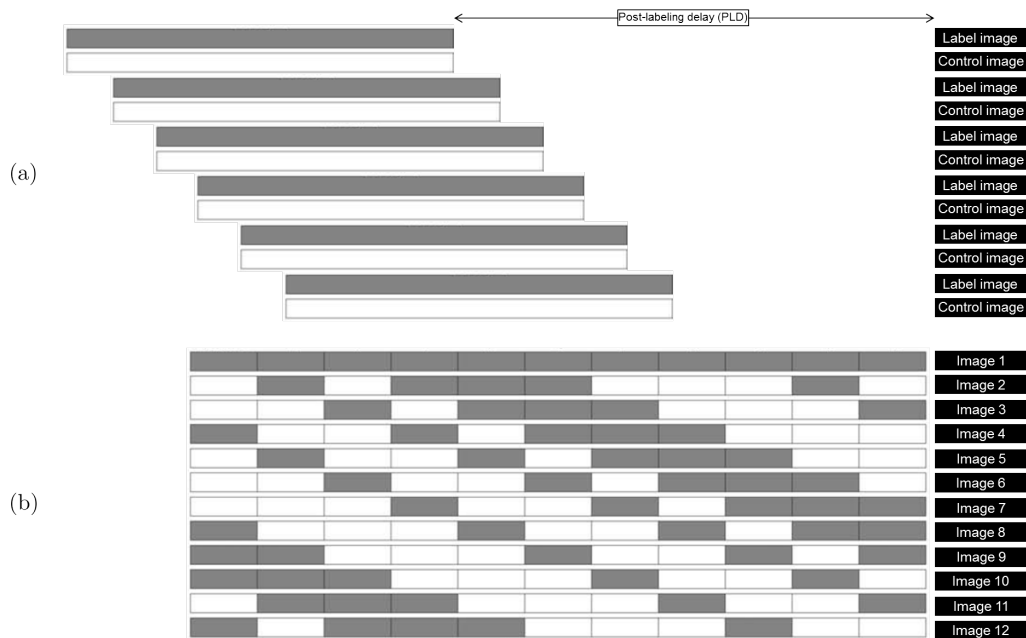


FIGURE 4.3: A multi-PLD PCASL protocol (a) contrasted with a time-encoded PCASL protocol (b). A pseudo-continuous labeling and control time block are presented by a gray and white block, respectively. This visualization is heavily based on the visualization made by Teeuwisse et al. in [59].

single-PLD PCASL protocol. Instead of simply waiting a certain time between labeling and readout, the PLD is filled up with a series of label-control blocks following a Hadamard matrix, as described above. By recombining the acquired images, one obtains an averaged difference image (from the first column in Figure 4.5) as one would obtain from conventional single-PLD PCASL data, with the same SNR [59]. Yet, on top of that, isolating the signals from the free-lunch columns will allow estimation of the ATT, which is an interesting parameter on its own and allows for a more accurate quantification of the CBF. The potential benefit of this ‘free’ extra information has also been studied in a population context in the contribution described in Chapter 6. In general, the durations of the blocks in each column can be seen as optimizable parameters with respect to the precision of estimation of perfusion parameters [60].

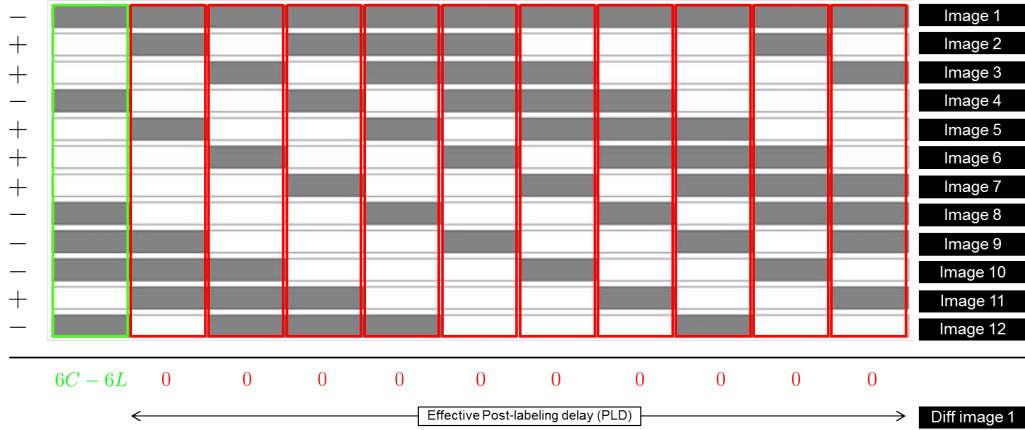


FIGURE 4.4: The difference signal related to the label and control time blocks in the first column can be isolated by choosing a certain linear combination of the 12 acquired images. In all columns but the first one, for each label (or control) block that is added, there is a label (or control) block subtracted, using the additions and subtractions shown on the left of the figure. The PCASL signals related to labeling blocks in these columns are cancelled out. In the first column, all control time blocks are added, while all label blocks are subtracted. Therefore, this linear combination results in a PCASL difference image equivalent to averaging 6 difference images from conventionally acquired label-control pairs with a labeling duration equal to the length of the time block in the first column and with an effective PLD as shown at the bottom of the figure. Using different linear combination of the acquired images, the difference signal related to each column, each with a different effective PLD, can be isolated.

### 4.1.3 Pros and cons of multi-delay and time-encoded ASL

As multi-PLD and time-encoded PCASL allow for sampling of the PCASL signal at multiple time points throughout its dynamic evolution in time, perfusion parameter can be quantified by fitting a model to the data in both cases. There are however some notable differences that will impact the SNR, the estimation accuracy and estimation precision.

An advantage of time-encoded PCASL that is often mentioned is the fact that fewer images are needed to sample the PCASL signal at a certain amount of PLDs compared to multi-PLD PCASL. Indeed, only  $n$  time-encoded PCASL images are needed to obtain PCASL signals at  $n - 1$  effective PLDs, while  $2 \times (n - 1)$

#### 4.1. Signal generation and imaging

---

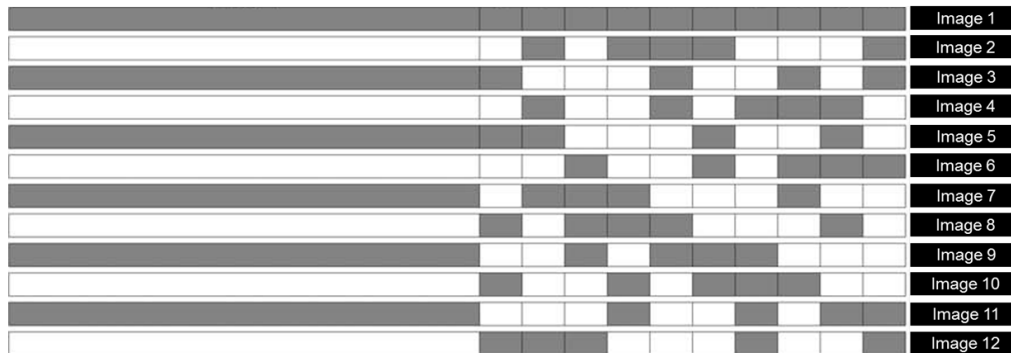


FIGURE 4.5: Free-lunch time-encoded PCASL protocol. A pseudo-continuous labeling and control time block are presented by a gray and white block, respectively. This visualization is heavily based on the visualization made by Teeuwisse et al. in [59].

images would need to be acquired with multi-PLD PCASL for data at  $n - 1$  PLDs. Furthermore, noise propagation is different between multi-PLD and time-encoded PCASL. Assuming that the noise in an acquired label, control or time-encoded image is white and normally distributed with zero mean and a standard deviation  $\sigma$ , the PCASL signal for a certain (effective) PLD is corrupted with normally distributed zero mean noise with a standard deviation of  $\sqrt{2}\sigma$  for multi-PLD PCASL, and  $(2/\sqrt{n})\sigma$  for time-encoded PCASL [61].

This gives the impression that time-encoded PCASL only has benefits compared to conventional sequential multi-PLD PCASL; fewer images need to be acquired for the same amount of covered PLDs and there is less noise per reconstructed image. However, these advantages would only play out one-to-one if the labeling durations and (effective) PLDs are chosen the same in both multi-PLD and time-encoded acquisition schemes. In reality, entirely different multi-PLD schemes can be chosen, for example the acquisition of fewer images with longer labeling durations. Longer labeling durations will, on average, result in larger PCASL signals. In general, the complete freedom in choosing a combination of a labeling duration and a PLD is a significant advantage of sequential multi-PLD PCASL acquisition. Time-encoded PCASL is much more rigid; once the time between the start of the first block and the start of readout is set, only the relative block durations can be changed.

The advantages and disadvantages mentioned in the previous paragraphs can be summarized by comparing the multi-PLD and time-encoded PCASL acquisition

scheme with the same total acquisition time in Figure 4.3. Even though the multi-PLD PCASL acquisition scheme in Figure 4.3a would result in fewer PCASL data points with higher noise compared to the time-encoded PCASL acquisition scheme in Figure 4.3b, the signal will on average be significantly larger in the multi-PLD PCASL scheme due to the much longer labeling durations.

In short, the interplay between effects of the length of the labeling duration, the amount of images, noise propagation in the images, the choice of PLDs in both sequential multi-PLD and time-encoded PCASL on one side and the effects on perfusion parameter estimation accuracy and precision on the other side is very complex. Comparing certain time-encoded and multi-PLD PCASL acquisition schemes in terms of perfusion parameter estimation accuracy and precision has already been performed [60, 62], but is still a subject of ongoing research and validation.

## 4.2 Perfusion models

After acquisition of PCASL data at multiple time points, perfusion parameters can be quantified by fitting a suitable model to the data. Perfusion parameter estimation consists of selecting both a suitable model and a suitable estimator. In this section, we will explore the former. Besides their use in quantification, perfusion models also play a central role in this work in terms of simulations. In certain simulation experiments, it is of interest to simulate PCASL data as realistic as possible, which requires models with higher complexity compared to typical quantification models. Throughout the past 25 years, a plethora of models have been introduced with varying levels of complexity. In this section, the models that were explored in light of the contributions of this work are introduced.

### 4.2.1 Single-compartment model

The most simple model describing the PCASL signal is the single-compartment model. The central assumption in this model is that, when the magnetically labeled water molecules reach the tissue voxel, there is unrestricted transfer of water molecules between the blood compartment and the tissue compartment. In other words, upon arrival in the tissue voxel, there is an immediate equal concentration of labeled water molecules in the blood compartment and the tissue compartment. Therefore, the tissue voxel can be seen as a single compartment. This concept is visualized in Figure 4.6.

The single-compartment dynamics can be described in two ways: using modified Bloch equations [5, 63] or by convolving a labeled spin bolus function with a

tissue response function [52]. Both options have been consistently used to create ASL models of different complexity throughout the years. Therefore, derivation of the single-compartment model using these two methods, described below, forms a solid basis to introduce more complex models in following sections.

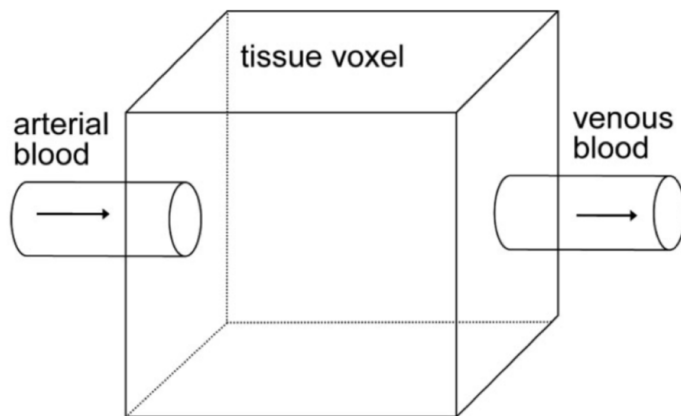


FIGURE 4.6: Schematic diagram of the single-compartment model. This figure is heavily based on a visualization made by Parkes and Tofts in [63].

### Derivation from modified Bloch equations

In section 2.1.5 of the general introduction to MRI, the Bloch equation (Eq.(2.8)) describing the change in longitudinal magnetization was introduced. Let us replicate this Bloch equation for a certain longitudinal magnetization  $M_z$  in a certain tissue voxel:

$$\frac{dM_z(t)}{dt} = \frac{M_0 - M_z(t)}{T_{1t}}, \quad (4.1)$$

with  $T_{1t}$  the tissue longitudinal relaxation time. In PCASL, labeled spins will enter and leave the tissue voxel with a perfusion rate  $f$ . Considering the assumption of a single, well-mixed compartment described above, Eq.(4.1) can be modified to incorporate the inflow and outflow of magnetization [5, 63]:

$$\frac{dM_z(t)}{dt} = \frac{M_0 - M_z(t)}{T_{1t}} + fm_a(t) - fm_v(t), \quad (4.2)$$

with  $m_a(t)$  the inflowing magnetization from the labeled bolus and  $m_v(t)$  the venous outflow of labeled spins. The unrestricted and instantaneous equilibration of the concentration of labeled spins between the vascular and tissue compartment upon entry of the labeled bolus in the tissue voxel implies that the outflowing blood has the same concentration of labeled spins as water in the tissue voxel [52]. The outflowing magnetization therefore scales with the tissue magnetization, weighted with the ratio of water contents between tissue and blood  $\lambda$  [52, 63]:

$$\frac{dM_z(t)}{dt} = \frac{M_0 - M_z(t)}{T_{1t}} + f m_a(t) - f \frac{M_z(t)}{\lambda}. \quad (4.3)$$

This ratio  $\lambda$  is usually referred to as the blood-brain partition coefficient of water. Knowing that in (conventional) ASL a label image is subtracted from a control image, Eq.(4.3) can be changed to [63]:

$$\Delta \frac{dM_z(t)}{dt} = \Delta \frac{M_0 - M_z(t)}{T_{1t}} + \Delta f m_a(t) - \Delta f \frac{M_z(t)}{\lambda}, \quad (4.4)$$

where  $\Delta$  represents the signal difference between the control and label image. Under the reasonable assumption that  $M_0$ ,  $T_{1t}$ ,  $\lambda$  and  $f$  do not change between the acquisition of both images, Eq.(4.4) can be rewritten as:

$$\frac{d\Delta M_z(t)}{dt} = -\frac{\Delta M_z(t)}{T_{1t}} + f \Delta m_a(t) - f \frac{\Delta M_z(t)}{\lambda} \quad (4.5)$$

$$= -\frac{\Delta M_z(t)}{T'_1} + f \Delta m_a(t), \quad (4.6)$$

with  $1/T'_1 = 1/T_{1t} + f/\lambda$ . This differential equation can be solved if  $\Delta m_a(t)$ , the difference in arterial magnetization flowing into the tissue voxel between the label and control image, is known. If uniform plug flow is assumed for the labeled bolus as it travels from the labeling plane to the tissue voxel, it can be described as [52]:

$$\Delta m_a(t) = \begin{cases} 0 & t < \Delta t \\ 2M_{0b}\alpha \exp\left(-\frac{\Delta t}{T_{1b}}\right) & \Delta t < t < \Delta t + \tau \\ 0 & t > \Delta t + \tau, \end{cases} \quad (4.7)$$

with  $\tau$  the pseudocontinuous labeling duration,  $\Delta t$  the arterial transit time between the labeling plane and the tissue voxel,  $M_{0b}$  the equilibrium magnetization of arterial blood in a unit voxel, and  $\alpha$  the inversion efficiency of the labeling. The

## 4.2. Perfusion models

---

factor  $\exp(-\Delta t/T_{1b})$  describes the magnetization loss due to longitudinal relaxation in the arterial blood compartment during the travel time from the labeling plane to the tissue voxel. Note that the factor 2 originates from the fact that Eq.(4.7) describes the difference in magnetization between the label and control image, which is equal to twice the equilibrium magnetization of blood at  $t = 0$  due to the  $180^\circ$  inversion of the arterial magnetization at the labeling plane. When Eq.(4.7) is used in Eq.(4.6), the following expression is found for the difference magnetization:

$$\Delta M(t) = \begin{cases} 0 & t < \Delta t \\ 2M_{0b}\alpha f T_1' \exp\left(-\frac{\Delta t}{T_{1b}}\right) \left(1 - \exp\left(-\frac{t-\Delta t}{T_1'}\right)\right) & \Delta t < t < \Delta t + \tau \\ 2M_{0b}\alpha f T_1' \exp\left(-\frac{\Delta t}{T_{1b}}\right) \exp\left(-\frac{t-\Delta t}{T_1'}\right) \left(\exp\left(-\frac{\tau}{T_1'}\right) - 1\right) & t > \Delta t + \tau, \end{cases} \quad (4.8)$$

which is commonly referred to as the single-compartment model (SCM). It consists of three distinct phases: no signal as long as the labeled bolus has not yet reached the tissue voxel ( $t < \Delta t$ ), a build-up of the PCASL signal as labeled spins flow into the tissue voxel ( $\Delta t < t < \Delta t + \tau$ ), followed by a phase where the entire labeled bolus has arrived in the tissue voxel and longitudinal relaxation exponentially decays the PCASL signal ( $t > \Delta t + \tau$ ). An example is shown in Figure 4.7.

Typical values for the different parameters in Eq.(4.8) in the general population are given in Table 4.1.

Parameter	Parameter distribution
cerebral blood flow $f$ [mL/100g/min]	$\mathcal{N}(53.9, 11.0)$ [64]
arterial transit time $\Delta t$ [s]	$\mathcal{N}(0.82, 0.15)$ [35, 38]
labeling efficiency $\alpha$ [ ]	$\mathcal{N}(0.80, 0.06)$ [65, 66]
longitudinal relaxation time of blood $T_{1b}$ [s]	$\mathcal{N}(1.65, 0.12)$ [67–69]
longitudinal relaxation time of tissue $T_{1t}$ [s]	$\mathcal{N}(1.45, 0.14)$ [70]

TABLE 4.1: Normal distributions of the SCM parameters representative for their distribution in the general population. The distributions for  $f$ ,  $\Delta t$  and  $T_{1t}$  are representative for the GM tissue type, specifically. A normal distribution is described as  $\mathcal{N}(\mu, \sigma)$  with  $\mu$  the mean and  $\sigma$  the standard deviation; a uniform distribution is described as  $\mathcal{U}(l, u)$  with  $l$  and  $u$  the lower and upper bound, respectively.

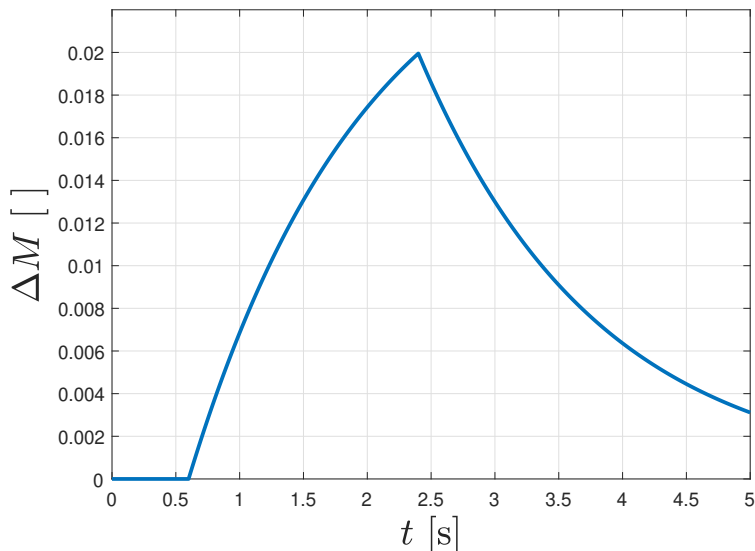


FIGURE 4.7: An example of the difference magnetization  $\Delta M$  as a function of time  $t$  according to the single-compartment model for a labeling duration  $\tau = 1.8$  s. Physiological parameters were chosen to represent a gray matter voxel:  $f = 50$  mL/100g/min,  $\Delta t = 0.6$  s,  $T_{1t} = 1.4$  s,  $T_{1b} = 1.65$  s,  $\lambda = 0.9$ . Values for  $T_{1t}$  and  $T_{1b}$  are given assuming a static magnetic field strength  $B_0 = 3.0$  T. Also,  $\alpha$  and  $M_{0b}$  were assumed equal to 0.85 and 1, respectively.

### Derivation from convolution approach

Another approach to describe the dynamics of the PCASL signal is by means of a convolution of a labeled spin bolus function, often also referred to as the delivery function or arterial input function (AIF), with a tissue impulse response (or residue) function (IRF). This method was first introduced for single-compartment kinetics by Buxton et al. [52]. The idea is summarized in the theoretical part of [52]: "*We can develop a general kinetic model for  $\Delta M(t)$  by considering this magnetization difference to be a quantity of magnetization that is carried into the voxel by arterial blood. Then, the amount of this magnetization in the tissue at time  $t$  will depend on the history of delivery of magnetization by arterial flow and clearance by venous flow and longitudinal relaxation. These various physical processes can be described by defining three functions of time: (a) the delivery function  $c(t)$  is the normalized arterial concentration of magnetization arriving at the voxel*

## 4.2. Perfusion models

---

at time  $t$ ; (b) the residue function  $r(t, t')$  is the fraction of tagged water molecules that arrived at time  $t'$  and are still in the voxel at time  $t$ ; and (c) the magnetization relaxation function  $m(t, t')$  is the fraction of the original longitudinal magnetization tag carried by the water molecules that arrived at time  $t'$  that remains at time  $t$ . With these definitions,  $\Delta M(t)$  can be constructed as a sum over the history of delivery of magnetization to the tissue weighted with the fraction of magnetization that remains in the voxel." This last sentence literally describes a convolution. The difference in magnetization between the label and control image at a time  $t$  can thus be described as [52]:

$$\Delta M(t) = 2M_{0b}\alpha f \int_0^t c(t')r(t-t')m(t-t')dt', \quad (4.9)$$

with  $2M_{0b}\alpha f c(t')$  the amount of arterial magnetization delivered to the tissue voxel between  $t'$  and  $t + dt'$ , and  $r(t-t')m(t-t')$  the amount of magnetization still present at time  $t$ . The integral in Eq.(4.9) describes a convolution:

$$\Delta M(t) = 2M_{0b}\alpha f [c(t) * [r(t)m(t)]]. \quad (4.10)$$

The exact same assumptions related to the single-compartment concept are made as in the method with modified Bloch equations. Firstly, the labeled bolus is delivered to the tissue voxel by means of uniform plug flow, resulting in the following delivery function:

$$c(t) = \begin{cases} 0 & t < \Delta t \\ \exp\left(-\frac{\Delta t}{T_{1b}}\right) & \Delta t < t < \Delta t + \tau \\ 0 & t > \Delta t + \tau. \end{cases} \quad (4.11)$$

Secondly, as the entire voxel is seen as one compartment, there is instantaneous and unrestricted exchange of water between blood and tissue. The concentration of labeled water molecules in tissue is therefore equal to the concentration in the venous outflow. Therefore, the fraction of labeled water molecules remaining in the tissue voxel is directly related to venous outflow of labeled water in single-compartment kinetics, weighted with the blood-brain partition coefficient:  $r(t) = \exp(-ft/\lambda)$ . Finally, it is assumed that all labeled water instantaneously resides in tissue upon arrival in the tissue voxel. Magnetization therefore decays with the tissue longitudinal relaxation time:  $m(t) = \exp(-t/T_{1t})$ . If these expressions for  $c(t)$ ,  $r(t)$  and  $m(t)$  are used in Eq.(4.10), the exact same single-compartment

model (SCM) is found as in Eq.(4.8), which was derived from the modified Bloch equation.

In Eq.(4.10),  $2M_{0b}\alpha fc(t)$  and  $r(t)m(t)$  are the aforementioned AIF and IRF, respectively, in case of single-compartment kinetics. **Both for the AIF and the IRF, more complex functions can be chosen that describe the underlying physical reality more accurately. Therefore, this convolutional approach is most suitable for gradually increasing the complexity of the signal model.** This is explored in the following sections.

### Recommended implementation

Before going into more complex models, it is interesting to shortly discuss the link between the single-compartment model and the recommended single-PLD PCASL quantification equation (Eq.(3.4)). Two major extra assumptions are made. Firstly, it is assumed that the entire labeled bolus has arrived in the tissue voxel, i.e. the PLD is longer than the arterial transit time  $\Delta t$ . Knowing that  $\text{PLD} = t - \tau$ ,  $\text{PLD} > \Delta t$  implies that the PCASL signal is described by the third regime of Eq.(4.8). Secondly, where for the single-compartment model the assumption is made that the labeled water molecules instantaneously cross the blood-brain barrier into the tissue upon arrival in the tissue voxel, the exact opposite is assumed in the recommended quantification model: the labeled spins remain in the blood compartment within the tissue voxel, assuming the blood vessels are impermeable. In that case, the difference magnetization decays with the blood longitudinal relaxation time  $T_{1b}$  instead of  $T_{1t}$ . With these two assumptions, Eq.(4.8) simplifies to

$$\Delta M(t) = 2M_{0b}\alpha f T_{1b} \exp\left(-\frac{\Delta t}{T_{1b}}\right) \exp\left(-\frac{t - \Delta t}{T_{1b}}\right) \left(\exp\left(-\frac{\tau}{T_{1b}}\right) - 1\right) \quad (4.12)$$

$$= 2M_{0b}\alpha f T_{1b} \exp\left(-\frac{t - \tau}{T_{1b}}\right) \left(1 - \exp\left(-\frac{\tau}{T_{1b}}\right)\right) \quad (4.13)$$

This is also referred to as the single blood-compartment model [63]. With  $\text{PLD} = t - \tau$  and  $M_{0b}$  approximated by the equilibrium magnetization in the tissue voxel divided by the blood-brain partition coefficient, i.e.  $M_{0b} = \text{SI}_{\text{PD}}/\lambda$ , rearranging Eq.(4.13) to the CBF  $f$  will result in the recommended quantification formula (Eq.(3.4) in the previous chapter).

### 4.2.2 Multi-compartment models

In single-compartment kinetics, it is assumed that the tissue voxel can be seen as one well-mixed compartment with unrestricted movement of labeled water molecules between the sub-compartments in the voxel. In reality, movement of labeled spins is restricted. Within the voxel, labeled water often has to flow through remaining impermeable arterial microvasculature before reaching the capillaries where exchange with the tissue can occur [37, 39, 71, 72]. Furthermore, diffusion of labeled water from blood to tissue in capillaries is not fully unrestricted; the permeability of capillaries for water is finite [63, 73, 74]. These effects can be accounted for in the convolutional approach by making changes to the IRF. Note that throughout this subsection, we assume the AIF to be unchanged as defined in the previous subsection:  $2M_{0b}\alpha f c(t)$  with  $c(t)$  given by Eq.(4.7).

#### Two-compartment model

To recap, the IRF in case of single-compartment kinetics where labeled molecules move freely between the blood and extravascular compartment of the tissue voxel is given by:

$$q(t) = \exp\left(-\frac{t}{T_{1t}} - \frac{f}{\lambda}\right). \quad (4.14)$$

Moving freely between the blood and tissue compartment is equal to an infinite permeability of the blood-brain barrier to water. In reality, this permeability is finite. Taking this into account requires a model that treats the blood and extravascular compartment as separate entities: a two-compartment model (Figure 4.8).

If we assume that water can diffuse to the extravascular compartment in all parts of the blood compartment in the tissue voxel and that the labeled water molecules do not flow back into the blood compartment before they have fully relaxed (single-pass approximation), the IRF can be written as follows [74, 75]:

$$q_{\text{TCM}}(t) = \beta \exp\left(-\frac{t}{T_{1t}}\right) + (1 - \beta) \exp\left(-t \left(\frac{1}{\tau_{\text{trans}}} + \frac{1}{T_{1b}}\right)\right), \quad (4.15)$$

with  $\beta = 1/(1 + \tau_{\text{trans}}(1/T_{1b} - 1/T_{1t}))$ , and  $\tau_{\text{trans}}$  the blood-to-tissue water transit time, reflecting the finite permeability of the blood-brain barrier to water. The blood-to-tissue water transit time is equal to the distribution volume of the labeled molecules in capillary space  $V_c$  divided by the product of the permeability  $P$  with the surface  $S$  of the capillaries [63, 74]  $\tau_{\text{trans}} = V_c/(PS)$ . It is often also referred

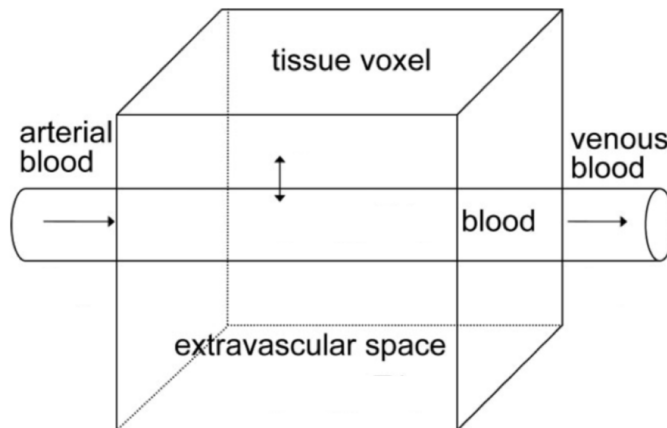


FIGURE 4.8: Schematic diagram of the two-compartment model. This figure is heavily based on a visualization made by Parkes and Tofts in [63].

to as a blood-to-tissue exchange rate of water, the inverse of  $\tau_{\text{trans}}$ , and denoted as  $k_c$  in [74] or  $k_w$  in [37].

Note that in Eq.(4.15), it is also implicitly assumed that the venous outflow of labeled spins out of the tissue voxel is negligible, which is supported by typical human blood flow rates [63, 74]. This becomes evident when we go back to single-compartment kinetics, implying infinite permeability and thus  $\tau_{\text{trans}}$  going to zero and  $\beta$  going to unity in Eq.(4.15). The only term that would remain in Eq.(4.15) is  $\exp(-t/T_{1t})$ . This is not equal to the single-compartment IRF, described by Eq.(4.14), as it contains the extra factor  $\exp(-f/\lambda)$ . However, this factor is directly related to the venous outflow. It is equal to unity if the same assumption of negligible venous outflow of labeled spins is made in the single-compartment theory.

The two-compartment model (TCM) for the difference magnetization can be formally written as:

$$\Delta M(t) = 2M_{0b}\alpha f[c(t) * q_{\text{TCM}}(t)], \quad (4.16)$$

with  $c(t)$  as defined in Eq.(4.7) and  $q_{\text{TCM}}(t)$  as defined in Eq.(4.15). The analytical expression for this convolution can be found in [37] as the five-parameter model with the arterial microvasculature transit time set to zero. The exact same model can also be obtained using modified Bloch equations. Parkes et al. [63] solved

## 4.2. Perfusion models

two-compartment Bloch equations by using their simplified solution neglecting backflow, which is equivalent to the single-pass assumption described above, and assuming no venous outflow.

In Figure 4.9, the TCM is contrasted with the SCM. For the same parameters, the TCM predicts a larger difference magnetization signal than the SCM. This is due to the fact that the labeled molecules stay longer in the blood compartment, where they relax slower towards equilibrium, as  $T_{1b}$  is typically longer than  $T_{1t}$ . It is also worth noting that, compared to the SCM, the TCM only has one extra parameter:  $\tau_{\text{trans}}$ , with typical values between 0.3 and 3.6 s [75–77].

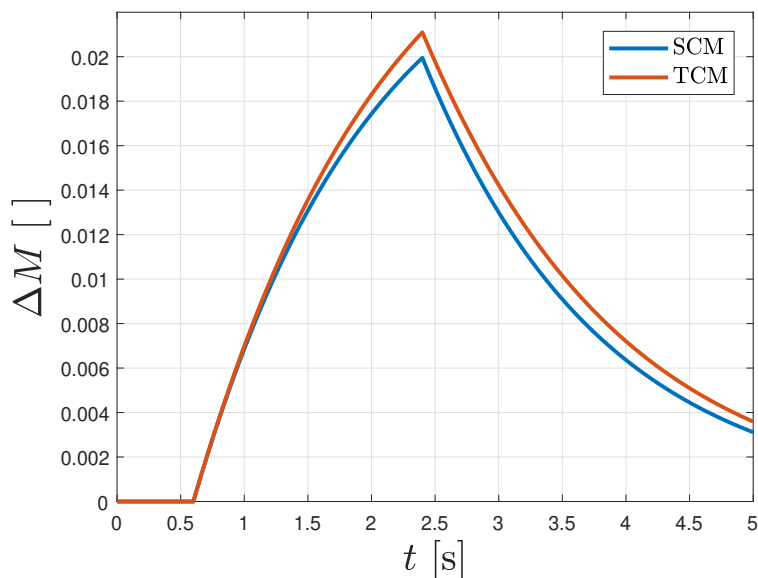


FIGURE 4.9: An example of the difference magnetization  $\Delta M$  as a function of time  $t$  according to the SCM and TCM for a labeling duration  $\tau = 1.8$  s. Physiological parameters were chosen to represent a gray matter voxel:  $f = 50$  mL/100g/min,  $\Delta t = 0.6$  s,  $\tau_{\text{trans}} = 1.5$  s,  $T_{1t} = 1.4$  s,  $T_{1b} = 1.65$  s,  $\lambda = 0.9$ . Values for  $T_{1t}$  and  $T_{1b}$  are given assuming a static magnetic field strength  $B_0 = 3.0$  T. Also,  $\alpha$  and  $M_{0b}$  were assumed equal to 0.85 and 1, respectively.

### Multiple blood compartments

Apart from accounting for a finite permeability in the capillaries, the blood compartment in a typical tissue voxel also contains an arterial and venous microvascular part before and after the capillaries, respectively. In these parts, the vessels are impermeable. The two-compartment IRF, given by Eq.(4.15), can be expanded to take the arterial and venous microvascular compartment into account. St. Lawrence et al. [74] derived such an IRF, again assuming the above described single-pass approximation, for the tissue-capillary-venous unit. If we also include the arterial microvascular compartment, the multi-compartment IRF is given by:

$$q_{\text{MCM}}(t) = \begin{cases} \exp\left(-\frac{t}{T_{1b}}\right) & t \leq \tau_a \\ \beta \exp\left(-\frac{t}{T_{1t}}\right) + (1 - \beta) \exp\left(-\left(\frac{1}{\tau_{\text{trans}}} + \frac{1}{T_{1b}}\right)t\right) & \tau_a < t \leq \tau_a + \tau_c \\ \beta E_R \exp\left(-\frac{t}{T_{1b}}\right) + (1 - E) \exp\left(-\frac{t}{T_{1t}}\right) & \tau_a + \tau_c < t \leq \tau_a + \tau_c + \tau_v \\ \beta E_R \exp\left(-\frac{t}{T_{1b}}\right) & \tau_a + \tau_c + \tau_v < t, \end{cases} \quad (4.17)$$

with  $\tau_a$ ,  $\tau_c$  and  $\tau_v$  the transit times through arterial, capillary and venous space, respectively,  $E_R = 1 - \exp(-PS/f - \delta R\tau_c)$ , with  $\delta R = 1/T_{1b} - 1/T_{1t}$ , and  $E = 1 - \exp(-PS/f)$ .

As with the single- and two-compartment IRF, the multi-compartment model (MCM) can be defined by convolving Eq.(4.17) with the AIF for uniform plug flow. The MCM contains three extra parameters with regard to the TCM: the transit times  $\tau_a$ ,  $\tau_c$  and  $\tau_v$ . Realistic values for  $\tau_c$  and  $\tau_v$  are often chosen by equating the transit time to the ratio of the blood compartment volume ( $V_c$  and  $V_v$ , respectively) and the local blood flow  $f$  [74]. Distributions of the extra parameters in the MCM in the general population are shown in Table 4.2. The MCM is again compared to the previous two models in Figure 4.10. It is clear that the difference in predicted magnetization between the MCM and the TCM is very limited.

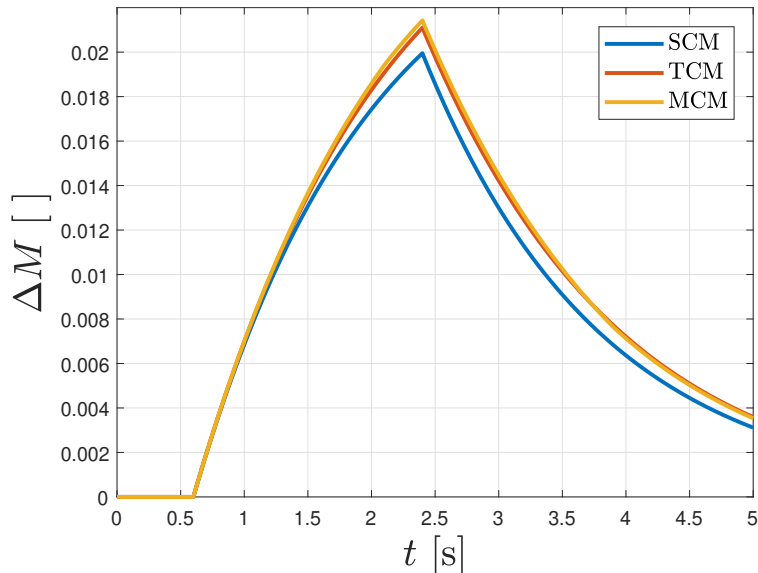


FIGURE 4.10: An example of the difference magnetization  $\Delta M$  as a function of time  $t$  according to the SCM, TCM and MCM for a labeling duration  $\tau = 1.8$  s. Physiological parameters were chosen to represent a gray matter voxel:  $f = 50$  mL/100g/min,  $\Delta t = 0.6$  s,  $\tau_{\text{trans}} = 1.5$  s,  $T_{1t} = 1.4$  s,  $T_{1b} = 1.65$  s,  $\lambda = 0.9$ ,  $\tau_a = 1.0$  s,  $V_c = 3$  mL/100g,  $V_v = 3$  mL/100g. Values for  $T_{1t}$  and  $T_{1b}$  are given assuming a static magnetic field strength  $B_0 = 3.0$  T. Also,  $\alpha$  and  $M_{0b}$  were assumed to be 0.85 and 1, respectively.

Parameter	Parameter distribution
arterial microvascular transit time $\tau_a$ [s]	$\mathcal{U}(0.30, 1.00)$ [78–80]
tracer capillary distribution volume $V_c$ [mL/100g]	$\mathcal{U}(2.0, 4.0)$ [63, 81]
tracer venous distribution volume $V_v$ [mL/100g]	$\mathcal{U}(1.0, 3.0)$ [82, 83]

TABLE 4.2: The prior distribution of the extra MCM parameters in GM in the general population. A normal distribution is described as  $\mathcal{N}(\mu, \sigma)$  with  $\mu$  the mean and  $\sigma$  the standard deviation; a uniform distribution is described as  $\mathcal{U}(l, u)$  with  $l$  and  $u$  the lower and upper bound, respectively.

### 4.2.3 Dispersion effects

The delivery of the labeled bolus to the destination voxel is described by the AIF. In all previously introduced models, uniform plug flow is assumed, resulting in a box-car shaped AIF in the case of pseudocontinuous labeling (as already discussed in section 4.2.1):

$$a(t) = \begin{cases} 0 & t < \Delta t \\ 2M_{0b}\alpha f \exp\left(-\frac{\Delta t}{T_{1b}}\right) & \Delta t < t < \Delta t + \tau \\ 0 & t > \Delta t + \tau. \end{cases} \quad (4.18)$$

In reality, flow in arteries is laminar, bifurcations of arteries disturb the blood flow and labeled water molecules undergo diffusion within the blood. All these effects, commonly referred to as dispersion effects, change the shape of the bolus as it passes through the arterial vasculature (Figure 4.11). Therefore, the shape of the bolus when it arrives in the tissue voxel will be different from the box-car shape it started with at the labeling plane. The AIF described in Eq.(4.18) does not take this into account. Modeling dispersion effects in the AIF has been the topic of multiple studies. The results can be divided in roughly two categories.

#### Dispersion mimicking functions

Some AIFs are based on ad hoc mathematical functions that mimic the effect of dispersion, such as the gamma-variate function [85, 86] or Gaussian dispersion kernels [87, 88]. The most recent work using this approach is by Chappell et al. [86]. They verified that the delivery of labeled water molecules to the tissue voxel can be accurately described by an AIF that is the result of a convolution of the box-car function, defined by Eq.(4.18), with a gamma kernel shape, which is given by [86]:

$$k(t) = \frac{s^{1+sp}}{\Gamma(1+sp)} t^{sp} \exp(-st), \quad (4.19)$$

where  $s$  determines how sharp the kernel is and  $p$  is the time-to-peak. With  $s \rightarrow \infty$  and  $p = 0$ , the kernel approaches a delta function, which would eliminate the dispersion effects again [86]. In a population with and without cerebrovascular pathologies, the distribution of estimated values for  $s$  and  $p$  can be described by  $\mathcal{N}(1.5, 0, 3)$  and  $\mathcal{N}(0.10, 0.03)$ , respectively [86].

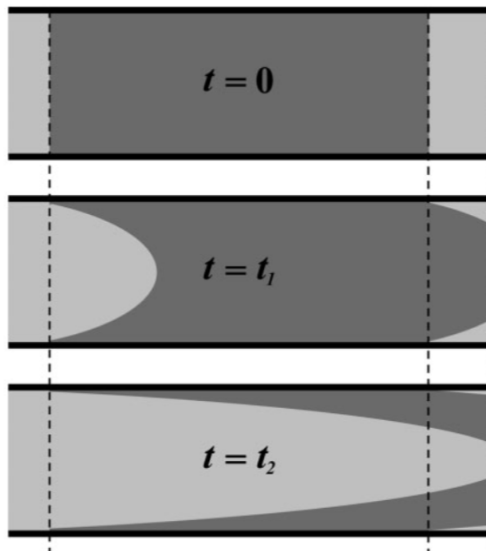


FIGURE 4.11: Part of a figure from the work of Gallichan et al. [84] showing the effect of laminar flow on the shape of the labeled bolus. In this figure,  $t = 0$  represents the bolus directly after inversion (assuming pulsed labeling). Times  $t = t_1$  and  $t = t_2$  show parts of the bolus arriving at the tissue voxel, taking the effect of laminar flow into account.

A dispersed version of any model discussed above describing the difference magnetization can thus be defined as:

$$\Delta M(t) = [a(t) * k(t)] * q(t) \quad (4.20)$$

$$= a_{\Gamma}(t) * q(t), \quad (4.21)$$

with  $a_{\Gamma}(t)$  the dispersed AIF using a gamma kernel shape,  $a(t)$  defined by Eq.(4.18),  $k(t)$  defined by Eq.(4.19) and  $q(t)$  the IRF defined by Eq.(4.14), Eq.(4.15), or Eq.(4.17) in case of the SCM, TCM or MCM. In Figure 4.12, the dispersed version of the SCM is compared to the SCM without dispersion.

Note that signal build up starts earlier when dispersion is incorporated. This is not an inherent aspect of the dispersion model. A slightly shorter value for the arterial transit time  $\Delta t$  was chosen for the dispersed SCM in Figure 4.12 to make the comparison with the SCM without dispersion more realistic. When the regular SCM would be fit to real data, which would be affected by dispersion, the sharp leading edge of the fit would not correspond to the leading edge of the labeled

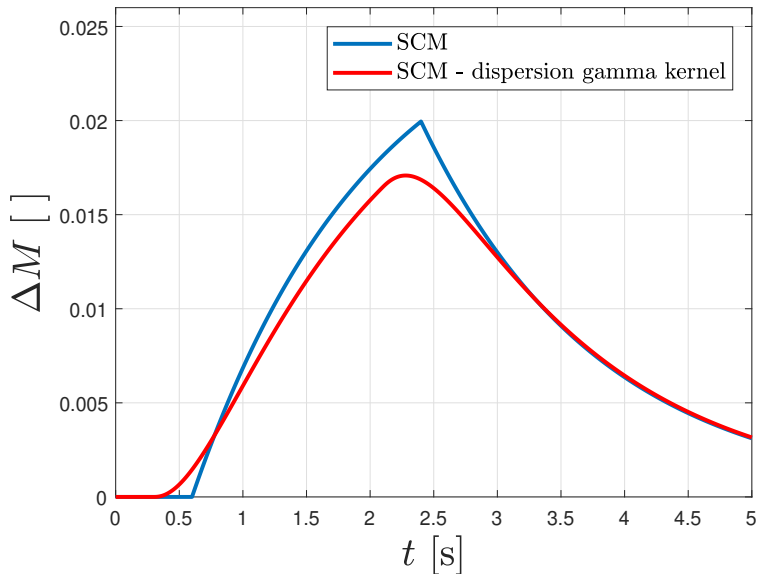


FIGURE 4.12: An example of the difference magnetization  $\Delta M$  as a function of time  $t$  according to the SCM without and with dispersion taken into account for a labeling duration  $\tau = 1.8$  s. Dispersion was introduced using a gamma kernel shape as defined in Eq.(4.19), with  $s = 1.5$  and  $p = 0.10$ . Physiological parameters were chosen to represent a gray matter voxel:  $f = 50$  mL/100g/min,  $\Delta t = 0.6$  s,  $\tau_{\text{trans}} = 1.5$  s,  $T_{1t} = 1.4$  s,  $T_{1b} = 1.65$  s,  $\lambda = 0.9$ . Values for  $T_{1t}$  and  $T_{1b}$  are given assuming a static magnetic field strength  $B_0 = 3.0$  T. Also,  $\alpha$  and  $M_{0b}$  were assumed to be 0.85 and 1, respectively.

bolus arriving in the tissue voxel. It would correspond to the time at which a certain amount of labeled molecules have arrived in the tissue voxel. This is a subtle, yet important difference. As in most studies,  $\Delta t$  is estimated with a model without dispersion, estimated values of  $\Delta t$  will on average be slightly longer than the exact time interval between the start of labeling and the arrival of the leading edge of the labeled bolus in the tissue voxel. Estimation of  $\Delta t$  with models that incorporate dispersion will result in shorter times compared to estimation with models without dispersion.

### Dispersion modeling using fluid dynamics

Another approach is to construct the AIF using principles of fluid dynamics [84, 89–91]. The methods proposed by Gall et al. [90] and Kellner et al. [91] stand out as the only ones taking into account laminar flow as well as bifurcations along the vascular tree. According to their theory, the AIF for PCASL can be modeled as a convolution of a transport function with a rectangular bolus, while taking  $T_1$  relaxation into account:

$$a_{\text{FD}}(t) = 2M_{0b}\alpha f[w(t, \tau) * (H(t) \exp(-t/T_{1b}))], \quad (4.22)$$

with  $w(t, \tau) = \Theta(\tau - t)$  the rectangular bolus, where  $\Theta(\cdot)$  is the step function that equals zero for negative and unity for positive arguments, and  $\tau$  is the labeling duration. The total transport function  $H(t)$  represents the distribution of travel times from the labeling site to the destination voxel:

$$H(t) = h_1(t) * h_2(t) * \dots * h_N(t), \quad (4.23)$$

where  $N$  is the number of arterial segments that the bolus passes and  $h_i(t)$  is the local transport function, which is the distribution of transport times within a certain arterial segment between two bifurcations. The local transport function can be assumed invariant of the vessel size and can be described as:

$$h(t) = (2t_0^2/t^3)\Theta(t - t_0), \quad (4.24)$$

with  $t_0$  the travel time in the center of the vessel [91]. This simplifies the total transport function to  $H(t) = [h(t)*]^N$ . Note that if  $\Delta t$  is defined as the travel time of the leading edge of the bolus from the labeling plane to the imaging site,  $\Delta t \approx Nt_0$ . The center-of-vessel travel time  $t_0$  in the general population can be approximated by  $\mathcal{N}(0.10, 0.01)$  s [90, 91]. As a consistency check, it can be verified that in the case of no dispersion (i.e.,  $H(t) = \delta(t - \Delta t)$ , where  $\delta(\cdot)$  is the delta function that equals unity if the argument is zero), the AIF defined in Eq.(4.22) equals the AIF without dispersion, defined in Eq.(4.18).

In Figure 4.13, the dispersed SCM using the dispersed AIF based on this fluid dynamics concept is compared to the SCM without dispersion and with dispersion mimicked with the gamma kernel shape. It should be emphasized that dispersed AIF can also be combined with the two- or multi-compartment IRFs, resulting in even more realistic representations of the underlying PCASL difference magnetization.

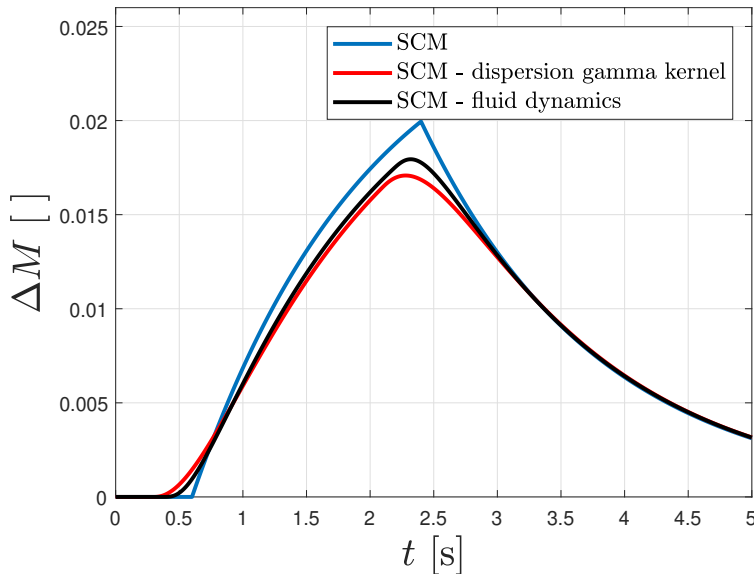


FIGURE 4.13: An example of the difference magnetization  $\Delta M$  as a function of time  $t$  according to the SCM without and with dispersion taken into account for a labeling duration  $\tau = 1.8$  s. The red curve shows the model function using dispersion mimicked with the gamma kernel shape as defined in Eq.(4.19), with  $s = 1.5$  and  $p = 0.10$ . The black curve represents the magnetization when dispersion is modeled using fluid dynamics, as given by Eq.(4.22), with  $t_0 = 0.10$  s. Physiological parameters were chosen to represent a gray matter voxel:  $f = 50$  mL/100g/min,  $\Delta t = 0.6$  s,  $\tau_{\text{trans}} = 1.5$  s,  $T_{1t} = 1.4$  s,  $T_{1b} = 1.65$  s,  $\lambda = 0.9$ . Values for  $T_{1t}$  and  $T_{1b}$  are given assuming a static magnetic field strength  $B_0 = 3.0$  T. Also,  $\alpha$  and  $M_{0b}$  were assumed to be 0.85 and 1, respectively.

### 4.3 Perfusion parameter estimation

With multi-delay PCASL data acquired and perfusion models describing the PCASL data available, the final step in the multi-delay PCASL experiment is selecting a suitable estimator to estimate perfusion parameters from the acquired data. The central parameter of interest is the cerebral blood flow  $f$ . In order to quantify this parameter from multi-delay PCASL data, there are three decisions that need to be made all impacting the eventual accuracy and precision with which  $f$  will be

estimated. The first two decisions to be made are closely related: which model will be used to fit to the PCASL data and which subset of parameters are estimated alongside the CBF  $f$ ? The impact and importance of this decision is introduced in section 4.3.1. The final decision to be made is which type of estimator is used. In section 4.3.2, the maximum likelihood estimator is introduced and arguments are presented supporting its use throughout all contributions of this work.

### 4.3.1 Model selection

In the previous section, an overview of the most common models was given. In what follows, a model is denoted as a function  $g_i(\boldsymbol{\theta})$ , with  $\boldsymbol{\theta}$  a parameter vector, describing the PCASL difference signal  $\Delta M$  acquired at an acquisition time point  $t_i$ . For example, the SCM would thus be represented as

$$g_i(\boldsymbol{\theta}) = \begin{cases} 0 & t_i < \Delta t \\ 2M_{0b}\alpha f T_1' \exp\left(-\frac{\Delta t}{T_{1b}}\right) \left(1 - \exp\left(-\frac{t_i - \Delta t}{T_1'}\right)\right) & \Delta t < t_i < \Delta t + \tau \\ 2M_{0b}\alpha f T_1' \exp\left(-\frac{\Delta t}{T_{1b}}\right) \exp\left(-\frac{t_i - \Delta t}{T_1'}\right) \left(\exp\left(-\frac{\tau}{T_1'}\right) - 1\right) & t_i > \Delta t + \tau, \end{cases} \quad (4.25)$$

with  $\boldsymbol{\theta}$  containing a certain subset of the unknown parameters, always including the CBF  $f$  and the arterial transit time  $\Delta t$ .

Choosing a model  $g_i(\boldsymbol{\theta})$  and the subset of parameters to be estimated  $\boldsymbol{\theta}$  has huge implications on the accuracy and precision of perfusion parameter estimation. In most studies with multi-delay ASL data, only  $f$  and  $\Delta t$  are estimated:  $\boldsymbol{\theta} = [f, \Delta t]$ . Other parameters in the chosen quantification model  $g_i(\boldsymbol{\theta})$  are then either fixed to population averages or estimated from other data. In this scenario, choosing a more accurate, more complex model introduces extra parameters that would also, most commonly, be fixed to an average value. Every parameter fixed to some global value potentially introduces a systematic error in the estimation, as they will vary between individuals and/or locally within an individual. Therefore, the potential gain in accuracy by choosing a more complex model would be lost when the extra parameters associated with the model are fixed instead of estimated. Of course, an alternative is to estimate other parameters alongside  $f$  and  $\Delta t$ . PCASL parameter estimation would be most accurate when a multi-compartment model including dispersion would be chosen and all parameters that potentially differ inter- and intra-subject would be added to  $\boldsymbol{\theta}$ . However, as more parameters are added to  $\boldsymbol{\theta}$ , assuming correlations between individual parameters in  $\boldsymbol{\theta}$ , the precision of estimation of  $f$  (and  $\Delta t$ ) might decrease [15]. Knowing that

PCASL data inherently suffers from a low SNR, it is to be expected that adding one or two extra parameters to  $\boldsymbol{\theta}$  would result in too low estimation precision, especially in a clinical setting. The balance between accuracy and precision when a parameter is either fixed to a population average or added to the parameter vector alongside  $f$  and  $\Delta t$  is the central topic of the contribution in Chapter 5. Another alternative to adding a parameter to  $\boldsymbol{\theta}$  or fixing it to population averages is quantifying it from other acquired (MRI) data. This would improve the accuracy of perfusion parameter estimation. However, assuming a fixed total time for imaging in a clinical setting, performing a supporting experiment for quantification of an extra parameter comes at a cost of scan time for the core PCASL data. This in turn negatively impacts the precision of perfusion parameter estimation. The potential benefits of certain supporting experiments in this context is extensively covered in the contribution described in Chapter 6.

In short, the impact of choices made with regards to the model and the parameters to be estimated on the accuracy-precision balance cannot be stressed enough. It is vital to keep this impact in mind in order to comprehensively judge absolute CBF maps quantified from ASL data.

### 4.3.2 Maximum likelihood estimator

When PCASL data is acquired and a parameter vector  $\boldsymbol{\theta}$  and a model  $g_i(\boldsymbol{\theta})$  have been chosen, the parameters can be estimated using the maximum likelihood estimator (MLE). The MLE maximizes, for each voxel separately, the likelihood function as a function of the parameter vector  $\boldsymbol{\theta}$  given a set of  $N$  PCASL difference data points. The likelihood function is closely related to the joint probability density function. Assuming independence between all  $N$  data points in a single voxel, the joint probability function is given by

$$P(\boldsymbol{\Delta M}|\boldsymbol{\theta}) = \prod_{i=1}^N p(\Delta M_i|g_i(\boldsymbol{\theta}), \sigma), \quad (4.26)$$

with  $\boldsymbol{\Delta M}$  a vector containing the  $N$  PCASL difference data points,  $\Delta M_i$  an element of  $\boldsymbol{\Delta M}$  associated with acquisition time point  $t_i$ , and  $p(\Delta M_i|g_i(\boldsymbol{\theta}), \sigma)$  the probability density function of  $\Delta M_i$ , with  $\sigma$  the standard deviation of the noise in the data. The joint probability density function is a function of the data for a given value of the parameters, while the likelihood function is a function of the parameters for a given set of observations [92]. However, as a mathematical expression, both functions are equal. Therefore, it follows from Eq.(4.26) that the

likelihood function can be written as

$$L(\boldsymbol{\theta}|\boldsymbol{\Delta M}) = \prod_{i=1}^N p(\Delta M_i|g_i(\boldsymbol{\theta}), \sigma). \quad (4.27)$$

The MLE of  $\boldsymbol{\theta}$  maximizes the likelihood function defined in Eq.(4.27):

$$\hat{\boldsymbol{\theta}} = \arg \max_{\boldsymbol{\theta}} L(\boldsymbol{\theta}|\boldsymbol{\Delta M}). \quad (4.28)$$

The MLE is known to be asymptotically efficient unbiased, which implies that it is an unbiased estimator that reaches the Cramér-Rao lower bound (i.e., a lower bound on the attainable variance of an estimator) as the number of data points increases [15]. Furthermore, the MLE is consistent; as the number of data points increases, the set of estimates of repeats of the experiment converges in probability to the underlying ground truth  $\boldsymbol{\theta}_0$  [15]. These properties are related to the fact that the distribution of the data is taken into account in the MLE. Deriving the MLE for the data distribution of typical PCASL difference data is therefore vital to be able to benefit from the properties of the MLE.

#### Arterial spin labeling data distribution

As stated before, PCASL difference data result from the voxel-wise subtraction of two magnitude images, the control and label image. Typically, the intensity of magnitude images, reconstructed from data acquired with multiple coils, follows a Rician or non-central chi-distribution, depending on the reconstruction method [93]. Deriving an analytical expression for the distribution of the difference of two Rician or non-central chi-distributed random variables is not straightforward. However, for high SNRs, both Rician and non-central chi-distributions can be adequately approximated with a Gaussian distribution [93,94]. As PCASL data is usually acquired at a low resolution [1], magnitude data in the label and control images will have a high SNR and can therefore be assumed as Gaussian distributed. In that case, the resulting difference data is also adequately described by a Gaussian distribution. Therefore, multi-variate Gaussian distributions can be used in the probability density functions in Eq.(4.27) for PCASL difference data:

$$L(\boldsymbol{\theta}|\boldsymbol{\Delta M}) = \prod_{i=1}^N \frac{1}{\sqrt{2\pi}\sigma} \exp\left(-\frac{1}{2} \left(\frac{\Delta M_i - g_i(\boldsymbol{\theta})}{\sigma}\right)^2\right). \quad (4.29)$$

### Nonlinear least squares estimator

Maximizing a likelihood function is equivalent to maximizing the natural logarithm of that likelihood function, since the logarithm is a monotonically increasing function [95]. The MLE of  $\boldsymbol{\theta}$  can be redefined as:

$$\hat{\boldsymbol{\theta}} = \arg \max_{\boldsymbol{\theta}} \ln L(\boldsymbol{\theta} | \Delta \mathbf{M}). \quad (4.30)$$

Using the likelihood function assuming independent Gaussian data points, as defined in Eq.(4.29), the MLE can be rewritten as:

$$\hat{\boldsymbol{\theta}} = \arg \max_{\boldsymbol{\theta}} \sum_{i=1}^N \ln \left[ \frac{1}{\sqrt{2\pi}\sigma} \exp \left( -\frac{1}{2} \left( \frac{\Delta M_i - g_i(\boldsymbol{\theta})}{\sigma} \right)^2 \right) \right] \quad (4.31)$$

$$= \arg \max_{\boldsymbol{\theta}} \sum_{i=1}^N \left[ \ln \frac{1}{\sqrt{2\pi}\sigma} + \ln \exp \left( -\frac{1}{2} \left( \frac{\Delta M_i - g_i(\boldsymbol{\theta})}{\sigma} \right)^2 \right) \right] \quad (4.32)$$

$$= \arg \max_{\boldsymbol{\theta}} \sum_{i=1}^N \left[ -\frac{1}{2} \left( \frac{\Delta M_i - g_i(\boldsymbol{\theta})}{\sigma} \right)^2 \right] \quad (4.33)$$

$$= \arg \min_{\boldsymbol{\theta}} \sum_{i=1}^N (\Delta M_i - g_i(\boldsymbol{\theta}))^2, \quad (4.34)$$

which makes the MLE equivalent to the least-squares estimator. Knowing that certain parameters of  $\boldsymbol{\theta}$  enter the ASL perfusion models  $g_i(\boldsymbol{\theta})$  nonlinearly, the least-squares estimator will be nonlinear in multi-time-point PCASL.

## 4.4 Performance analysis of the estimator

As the balance between accuracy and precision of parameter estimation lies at the base of each contribution in this thesis, tools are required to assess the performance of the MLE. The bias and variance of an estimator are the main statistical entities of interest. How they can be assessed depends on whether the underlying ground truth parameters  $\boldsymbol{\theta}_0$  are known. This is the case in simulations or when reference data is available from a gold standard imaging method. Yet, in most real data experiments,  $\boldsymbol{\theta}_0$  is not known.

#### 4.4.1 Accuracy analysis of the estimator

##### Known ground truth parameters

As already introduced in section 1.2, the bias of an estimator can be written as

$$\text{bias}(\hat{\boldsymbol{\theta}}) = E[\hat{\boldsymbol{\theta}}] - \boldsymbol{\theta}_0, \quad (4.35)$$

with  $E[\hat{\boldsymbol{\theta}}]$  the expectation value of the estimator. In most cases,  $E[\hat{\boldsymbol{\theta}}]$  is not known. Yet it can be estimated by repeating the experiment  $K$  times and calculating the mean of the  $K$  estimates, which leads to an estimate of the bias:

$$\widehat{\text{bias}}(\hat{\boldsymbol{\theta}}) = \langle \{\hat{\boldsymbol{\theta}}_k\}_{k=1}^K \rangle - \boldsymbol{\theta}_0. \quad (4.36)$$

The estimator of the bias of the estimator also has a finite precision, directly linked to the amount of repeats  $K$  of the experiment. Often, the reliability of an estimate of the bias of the estimator is quantified using confidence intervals. For a certain parameter  $\theta_p$  of  $\boldsymbol{\theta}$ , a  $100 \times (1 - \alpha)\%$  confidence interval for the bias is given by [96]:

$$\left[ \widehat{\text{bias}}(\hat{\theta}_p) - t_{\alpha/2, K-1} \frac{\hat{s}(\hat{\theta}_p)}{\sqrt{K}}, \widehat{\text{bias}}(\hat{\theta}_p) + t_{\alpha/2, K-1} \frac{\hat{s}(\hat{\theta}_p)}{\sqrt{K}} \right], \quad (4.37)$$

with  $t_{\alpha/2, K-1}$  the  $100 \times (1 - \alpha/2)\%$ -percentile of a  $t$ -distributed random variable with  $K - 1$  degrees of freedom and the sample standard deviation given by

$$\hat{s}(\hat{\theta}_p) = \sqrt{\frac{1}{K-1} \sum_{k=1}^K \left( \hat{\theta}_{p,k} - \langle \{\hat{\theta}_{p,k}\}_{k=1}^K \rangle \right)^2}. \quad (4.38)$$

The true value of the bias will lie within the interval defined in Eq.(4.37) with a  $100 \times (1 - \alpha)\%$  probability.

##### Unknown ground truth parameters

In most real data experiments, the true underlying parameters  $\boldsymbol{\theta}_0$  are not known. In such cases, the accuracy of an estimator can only be evaluated relative to another estimator. For example, the mean of a set of  $K$  estimates of the CBF  $f$  using a two-parameter estimator can be compared to the one of a three-parameter estimator.

#### 4.4.2 Precision analysis of the estimator

Contrary to the accuracy of an estimator, no information on the ground truth parameters  $\boldsymbol{\theta}_0$  is needed to evaluate the precision of an estimator. The precision of an estimator is closely related to the covariance of an estimator, which was already formally defined in Eq.(1.2) in section 1.2. For clarity, we define the covariance of an estimator  $\hat{\boldsymbol{\theta}}$  again:

$$\text{cov}(\hat{\boldsymbol{\theta}}) = E \left[ (\hat{\boldsymbol{\theta}} - E[\hat{\boldsymbol{\theta}}])(\hat{\boldsymbol{\theta}} - E[\hat{\boldsymbol{\theta}}])^T \right]. \quad (4.39)$$

The variance of the estimator for the individual parameters  $\theta_p$  in  $\boldsymbol{\theta}$  are equal to the respective diagonal elements of the covariance matrix. As for the bias of an estimator, the variance of an estimator of a parameter  $\theta_p$  can be estimated from the sample variance of  $K$  repeats of an experiment:

$$\widehat{\text{var}}(\hat{\theta}_p) = \frac{1}{K-1} \sum_{k=1}^K \left( \hat{\theta}_{p,k} - \langle \{\hat{\theta}_{p,k}\}_{k=1}^K \rangle \right)^2. \quad (4.40)$$

Again, an estimator of the variance of an estimator will have a certain precision of its own. A  $100 \times (1 - \alpha)\%$  confidence interval for the variance estimator is given by [96]:

$$\left[ \frac{(K-1)\widehat{\text{var}}(\hat{\theta}_p)}{\chi_{\alpha/2; K-1}^2}, \frac{(K-1)\widehat{\text{var}}(\hat{\theta}_p)}{\chi_{1-\alpha/2; K-1}^2} \right], \quad (4.41)$$

with  $\chi_{\alpha/2; K-1}^2$  the  $100 \times (1 - \alpha/2)\%$ -percentile of a  $\chi^2$ -distributed random variable with  $K-1$  degrees of freedom. The meaning of the confidence interval is the same as for the bias estimate confidence interval: the true value of the variance of the estimator will lie within this interval with a  $100 \times (1 - \alpha)\%$  probability.

The estimate of the variance of an estimator, defined in Eq.(4.40), is equivalent to the square of the sample standard deviation  $\hat{s}(\hat{\theta}_p)$ , defined in Eq.(4.38). The sample standard deviation is easier to interpret as it is in the same unit as the parameter to be estimated.

#### Known ground truth parameters

While the precision of an estimator can be evaluated without knowledge of the ground truth parameters  $\boldsymbol{\theta}_0$ , information on  $\boldsymbol{\theta}_0$  allows for an analysis of the efficiency of the estimator. The efficiency of an estimator can be defined as the ratio of the variance of an estimator and the minimally attainable variance of that

#### 4.4. Performance analysis of the estimator

---

estimator, where the same experiment is assumed in both cases (in terms of acquisition settings and the amount of data points). In other words, an estimator with maximal efficiency attains the highest precision, i.e. the lowest variance, possible given the settings of the experiment.

Statistical parameter estimation theory provides a rule for the minimally attainable (co)variance of an unbiased estimator [97], which requires knowledge of the ground truth parameter vector  $\boldsymbol{\theta}_0$ :

$$\text{cov}(\hat{\boldsymbol{\theta}}) \geq I(\boldsymbol{\theta}_0)^{-1}, \quad (4.42)$$

with  $I(\boldsymbol{\theta}_0)$  the Fisher information matrix and the symbol  $\geq$  implying that the matrix difference  $\text{cov}(\hat{\boldsymbol{\theta}}) - I(\boldsymbol{\theta}_0)^{-1}$  is a positive semidefinite matrix. In what follows,  $I(\boldsymbol{\theta}_0)^{-1}$  will be referred to as the Cramér-Rao lower bound (CRLB) matrix and its diagonal elements as the CRLBs. As a result of Eq.(4.42), the diagonal elements of  $I(\boldsymbol{\theta}_0)^{-1}$  are lower bounds on the variance of the estimator for individual parameters  $\theta_p$  of  $\boldsymbol{\theta}$ . An unbiased estimator is said to be efficient if its covariance equals the CRLB matrix [98]. The MLE reaches this lower bound asymptotically, i.e. as the amount of data points increases [95, 99].

The Fisher information matrix  $I(\boldsymbol{\theta})$ , assuming PCASL difference data  $\boldsymbol{\Delta M}$ , is defined as

$$I(\boldsymbol{\theta}) = E \left[ \left( \frac{\partial \ln P(\boldsymbol{\Delta M} | g(\boldsymbol{\theta}, \sigma))}{\partial \boldsymbol{\theta}} \right) \left( \frac{\partial \ln P(\boldsymbol{\Delta M} | g(\boldsymbol{\theta}, \sigma))}{\partial \boldsymbol{\theta}} \right)^T \right], \quad (4.43)$$

with  $P(\boldsymbol{\Delta M} | g(\boldsymbol{\theta}, \sigma))$  the joint probability density function. Assuming  $N$  independent PCASL data points, the joint probability density function is given by Eq.(4.26). In that case, the Fisher information matrix (FIM) becomes:

$$I(\boldsymbol{\theta}) = E \left[ \left( \frac{\partial \ln \prod_{i=1}^N p(\Delta M_i | g_i(\boldsymbol{\theta}), \sigma)}{\partial \boldsymbol{\theta}} \right) \left( \frac{\partial \ln \prod_{i=1}^N p(\Delta M_i | g_i(\boldsymbol{\theta}), \sigma)}{\partial \boldsymbol{\theta}} \right)^T \right] \quad (4.44)$$

$$= E \left[ \left( \sum_{i=1}^N \frac{\partial \ln p(\Delta M_i | g_i(\boldsymbol{\theta}), \sigma)}{\partial \boldsymbol{\theta}} \right) \left( \sum_{j=1}^N \frac{\partial \ln p(\Delta M_j | g_j(\boldsymbol{\theta}), \sigma)}{\partial \boldsymbol{\theta}} \right)^T \right] \quad (4.45)$$

$$= E \left[ \left( \sum_{i=1}^N \frac{\partial g_i(\boldsymbol{\theta})}{\partial \boldsymbol{\theta}} \frac{\partial \ln p(\Delta M_i | g_i(\boldsymbol{\theta}), \sigma)}{\partial g_i(\boldsymbol{\theta})} \right) \left( \sum_{j=1}^N \frac{\partial g_j(\boldsymbol{\theta})}{\partial \boldsymbol{\theta}} \frac{\partial \ln p(\Delta M_j | g_j(\boldsymbol{\theta}), \sigma)}{\partial g_j(\boldsymbol{\theta})} \right)^T \right] \quad (4.46)$$

$$= \sum_{i=1}^N \sum_{j=1}^N \frac{\partial g_i(\boldsymbol{\theta})}{\partial \boldsymbol{\theta}} \frac{\partial g_j(\boldsymbol{\theta})}{\partial \boldsymbol{\theta}^T} E \left[ \frac{\partial \ln p(\Delta M_i | g_i(\boldsymbol{\theta}), \sigma)}{\partial g_i(\boldsymbol{\theta})} \frac{\partial \ln p(\Delta M_j | g_j(\boldsymbol{\theta}), \sigma)}{\partial g_j(\boldsymbol{\theta})} \right]. \quad (4.47)$$

The expectation value in Eq.(4.47) can be written as:

$$E \left[ \frac{\partial \ln p(\Delta M_i)}{\partial g_i(\boldsymbol{\theta})} \frac{\partial \ln p(\Delta M_j)}{\partial g_j(\boldsymbol{\theta})} \right] = \int_{-\infty}^{\infty} \int_{-\infty}^{\infty} p(\Delta M_i) p(\Delta M_j) \frac{\partial \ln p(\Delta M_i)}{\partial g_i(\boldsymbol{\theta})} \frac{\partial \ln p(\Delta M_j)}{\partial g_j(\boldsymbol{\theta})} d\Delta M_i d\Delta M_j, \quad (4.48)$$

with  $p(\Delta M_i) \equiv p(\Delta M_i | g_i(\boldsymbol{\theta}), \sigma)$ . As stated in section 4.3.2, it is reasonable to assume PCASL difference data points are Gaussian distributed. Eq.(4.48) can be further simplified by using the expression for the Gaussian probability density function and considering two cases:  $i \neq j$  and  $i = j$ . When  $i \neq j$ , the integrals in Eq.(4.47) can be evaluated separately. One such an integral can be solved analytically:

$$\begin{aligned} & \int_{-\infty}^{\infty} p(\Delta M_i) \frac{\partial \ln p(\Delta M_i)}{\partial g_i(\boldsymbol{\theta})} d\Delta M_i \\ &= \int_{-\infty}^{\infty} \frac{1}{\sqrt{2\pi}\sigma} \exp \left( -\frac{1}{2} \left( \frac{\Delta M_i - g_i(\boldsymbol{\theta})}{\sigma} \right)^2 \right) \left( \frac{\Delta M_i - g_i(\boldsymbol{\theta})}{\sigma^2} \right) d\Delta M_i \quad (4.49) \\ &= 0. \quad (4.50) \end{aligned}$$

For  $i = j$ , the expectation value in Eq.(4.47) becomes

$$E \left[ \left( \frac{\partial \ln p(\Delta M_i)}{\partial g_i} \right)^2 \right] \quad (4.51)$$

$$= \int_{-\infty}^{\infty} p(\Delta M_i) \left( \frac{\partial \ln p(\Delta M_i)}{\partial g_i(\boldsymbol{\theta})} \right)^2 d\Delta M_i \quad (4.52)$$

$$= \int_{-\infty}^{\infty} \frac{1}{\sqrt{2\pi}\sigma} \exp \left( -\frac{1}{2} \left( \frac{\Delta M_i - g_i(\boldsymbol{\theta})}{\sigma} \right)^2 \right) \left( \frac{\Delta M_i - g_i(\boldsymbol{\theta})}{\sigma^2} \right)^2 d\Delta M_i \quad (4.53)$$

$$= \frac{1}{\sigma^2} \quad (4.54)$$

With these results, the FIM assuming a Gaussian probability density function can be rewritten as:

$$I(\boldsymbol{\theta}) = \frac{1}{\sigma^2} \sum_{i=1}^N \frac{\partial g_i(\boldsymbol{\theta})}{\partial \boldsymbol{\theta}} \frac{\partial g_i(\boldsymbol{\theta})}{\partial \boldsymbol{\theta}^T}. \quad (4.55)$$

The derivatives of the model function  $g_i(\boldsymbol{\theta})$  with respect to the model parameters  $\boldsymbol{\theta}$  are easily calculable if an analytical expression is available, like for the SCM as defined in Eq.(4.8). In such cases, Eq.(4.55) can be used to determine the CRLBs on the variance of any unbiased estimator. This ultimately allows for an evaluation of the efficiency of the estimator. Furthermore, CRLBs are also an interesting tool for experiment design optimization. In the contribution in Chapter 5 in Part II, the relation between CRLBs and experiment design is explained and used to optimize acquisition settings for a multi-PLD PCASL experiment.

### Unknown ground truth parameters

When no information is available on the underlying true parameter values, the efficiency of the estimator cannot be assessed. However, as stated in the first paragraph of this section, the precision of an estimator itself can be studied without knowledge of  $\boldsymbol{\theta}_0$ , contrary to evaluating the accuracy of an estimator. This is a very powerful asset when studying the performance of an estimator on real data.

Often, the estimate of the absolute variance of an estimator, as defined in Eq.(4.40), on its own is difficult to interpret. An estimate of the relative variance

of an estimator

$$\widehat{\text{var}}_{\text{rel}}(\hat{\theta}_p) = \frac{1}{K-1} \frac{\sum_{k=1}^K \left( \hat{\theta}_{p,k} - \langle \{\hat{\theta}_{p,k}\}_{k=1}^K \rangle \right)^2}{\langle \{\hat{\theta}_{p,k}\}_{k=1}^K \rangle} \quad (4.56)$$

is often more informative, as it defines the precision of an estimator as a percentage of the mean estimated value.





Part II

Contributions



## Chapter 5

# Estimating the $T_1$ of tissue alongside the perfusion parameters in multi-delay ASL

This chapter focusses on the impact of the amount of parameters to be estimated  $\theta$  on the accuracy and precision of parameter estimation in multi-PLD PCASL, as was already introduced in general in section 4.3.1. We compared two estimators that used the single-compartment model (SCM) as quantification model, yet with a different amount of parameters to be estimated. One estimator quantified the longitudinal relaxation time of tissue  $T_{1t}$  alongside the CBF and the ATT, while the other only quantified both perfusion parameters and kept  $T_{1t}$  fixed to a population average, as is conventional for quantification from multi-delay ASL data.

### 5.1 Introduction

Why is  $T_{1t}$  an interesting candidate to estimate alongside the perfusion parameters in multi-PLD PCASL? The importance of  $T_{1t}$  in the physiological process in reality is rather limited as it is known that the labeled bolus stays in the blood compartment for a significant amount of time even after it has arrived in the tissue voxel [63]. The key to its importance lies in the quantification model. The SCM, the most widely used quantification model in multi-PLD PCASL experiments, assumes that relaxation of the labeled spins is governed entirely by the longitudinal relaxation time of brain tissue  $T_{1t}$  upon arrival in the tissue voxel [52]. Therefore, regardless of the role  $T_{1t}$  plays in the real biophysical evolution of the PCASL signal,  $T_{1t}$  will always be of high importance when quantifying with the SCM. This subtle difference is crucial.

In most cases,  $T_{1t}$  is fixed to a certain population average for white matter (WM) and gray matter (GM). This can compromise the accuracy of CBF quantification for multiple reasons. Firstly, there is no consensus on average population values for  $T_{1t}$  [70]. Secondly, it has been shown that  $T_{1t}$  varies across patients, differs spatially within one tissue and changes in brain lesions with perfusion disorders, such as stroke [100], neurodegenerative diseases [101], or tumors [102,103]. Thirdly, ASL images are typically acquired at low spatial resolution, resulting in partial volume effects, which may influence the effective  $T_{1t}$ . Finally, as mentioned in the previous paragraph, the label resides in blood for a longer time than assumed in the SCM, so assigning values to  $T_{1t}$  that are closer to typical values for the longitudinal relaxation time of blood  $T_{1b}$  could result in more accurate quantification of the perfusion parameters. In short, fixing  $T_{1t}$  to a certain value is likely to cause bias in estimation of the CBF (and the ATT). In order to avoid a such an estimation bias,  $T_{1t}$  can be estimated locally alongside the CBF and the ATT. However, adding a parameter to be estimated reduces the estimation precision, which can be problematic in a low-SNR imaging modality such as ASL.

In order to maximally compensate for the expected reduced precision when estimating CBF, ATT, and  $T_{1t}$  together, the design of the multi-PLD PCASL experiment was optimized for this three-parameter estimator. ASL MRI acquisition settings have often been optimized for pulsed ASL (PASL) [104–106]. Besides the difference in the kinetic model between PASL and PCASL, experiment design of PCASL has more parameters to be optimized. Indeed, the optimization of the PASL experiment design is limited to searching optimal inversion times, while the design of the PCASL experiment can be optimized with respect to both the acquisition time points and the labeling duration, as was done in this work. Optimizing the acquisition time points and the labeling duration for a three-parameter estimator contrasts this study from recent work of Woods et al. [107], in which the PLDs of a multi-PLD PCASL experiment were optimized for two-parameter (i.e., CBF and ATT) estimation.

The effect of  $T_{1t}$  on quantification has been studied in previous work. In [108], the impact of different  $T_{1t}$  values on CBF quantification was shown for single-PLD continuous ASL. Qin et al. [37] used information criteria to conclude that estimating the CBF, the ATT and  $T_{1t}$  is feasible, yet for a very low spatial resolution (7mm isotropic). The precision of any estimator increases significantly at such a low spatial resolution, which naturally makes the feasibility of estimating  $T_{1t}$  alongside the perfusion parameters attainable. In this work, we compared fixing  $T_{1t}$  or estimating it together with the CBF and the ATT using multi-PLD PCASL data acquired at a recommended [1] spatial resolution of 4mm in-plane and 5mm through-plane.

The statistical quality assessment of the two- and three-parameter estimator was performed by means of test-retest simulation and real data experiments. Both options to solve the inverse problem at hand are at opposite sides of the accuracy-precision trade-off. It was our goal to provide insight in which option balances accuracy and precision of CBF quantification best for the recommended spatial resolution [1] in ASL.

## 5.2 Theory

This section consists of two major parts. Firstly, a two- and a three-parameter estimator for parameter quantification from multi-PLD PCASL data are defined in sections 5.2.1 and 5.2.2. Secondly, an optimal experiment design method for maximizing the precision of perfusion parameter estimation with the three-parameter estimator is proposed in section 5.2.3.

### 5.2.1 Single-compartment quantification model

The intensity and dynamic evolution of the PCASL difference signal  $\Delta M$  in a tissue voxel depend on the acquisition settings and on the global or local characteristics of the brain and its vasculatory system. When assuming that labeled water enters the tissue instantaneously upon arrival in the imaged voxel and that the concentration of labeled water is constant throughout the label bolus, as described in section 4.2.1 in more detail, PCASL difference data can be described by the SCM [52]:

$$g_i(\boldsymbol{\theta}) = \begin{cases} 0 & t_i < \Delta t \\ 2M_{0b}\alpha f T_1' \exp\left(-\frac{\Delta t}{T_{1b}}\right) \left(1 - \exp\left(-\frac{t_i - \Delta t}{T_1'}\right)\right) & \Delta t < t_i < \Delta t + \tau \\ 2M_{0b}\alpha f T_1' \exp\left(-\frac{\Delta t}{T_{1b}}\right) \exp\left(-\frac{t_i - \Delta t}{T_1'}\right) \left(\exp\left(-\frac{\tau}{T_1'}\right) - 1\right) & t_i > \Delta t + \tau, \end{cases} \quad (5.1)$$

with  $f$  the CBF,  $\Delta t$  the ATT,  $\alpha$  the labeling efficiency,  $M_{0b}$  the signal of a voxel filled with fully relaxed blood,  $T_{1b}$  the longitudinal relaxation time of blood, and  $T_{1t}' = T_{1t}\lambda/(\lambda + fT_{1t})$  the apparent longitudinal relaxation time, with  $\lambda$  the equilibrium blood/tissue partition coefficient of water [52]. The time point  $t = 0$  is defined as the beginning of labeling.

### The role of the labeling duration in data acquisition and the model

In the model described by Eq. (5.1), the labeling duration  $\tau$  is assumed to be constant. PCASL data is acquired at a certain acquisition time  $t_i = \tau + \text{PLD}_i$ . In a standard PCASL sequence, it is not possible to acquire data during labeling. Therefore, for a fixed  $\tau$ , data can only be acquired at acquisition times  $t > \tau$ . Hence, unless  $\Delta t > \tau$ , a significant part of the dynamic increase of the difference signal, described by the second regime in Eq. (5.1), is not accessible for sampling, while it might contain valuable information. A way to nevertheless acquire data at acquisition times  $t < \tau$  is to choose a shorter labeling duration  $\tau_s < \tau$  and sample the signal at  $t = \tau_s + \text{PLD}_s$ , with  $\text{PLD}_s$  a post-labeling delay that is shorter than the minimal  $\Delta t$ . This short PLD is crucial to allow sampling of the PCASL signal during the second regime. It has been shown by Buxton et al. [52] that the entire dynamic increase of the difference signal for a labeling duration  $\tau_s < \tau$  equals the initial part of this regime for a labeling duration  $\tau$  [52]. Therefore, the entire evolution of the difference signal for a constant labeling duration  $\tau$ , described by Eq. (5.1), can be sampled at each time point  $t$  by using the sampling procedure described above. Throughout this work, a multi-time-point PCASL acquisition scheme can therefore be defined by a single constant  $\tau$  and a set of acquisition time points  $\mathbf{t} = \{t_i\}_{i=1}^N$ , knowing that for each  $t_i < \tau$  the real data acquisition needs to be performed with a unique  $\tau_s < \tau$  in combination with a very short  $\text{PLD}_s$ .

#### 5.2.2 Maximum likelihood estimation

Parameter estimation in this work is performed with the maximum likelihood estimator (MLE), which takes the probability distribution of the data into account. PCASL difference data is adequately described by a Gaussian distribution, as was discussed at length in section 4.3.2 of the introductory chapters. Therefore, the joint probability density function (PDF) of PCASL difference data is well approximated by a multi-variate Gaussian distribution. For independent Gaussian distributed data, having a constant (noise induced) variance in each data point, the MLE is equivalent to the unweighted non-linear least-squares estimator (NLE) [15] (also see section section 4.3.2):

$$\hat{\boldsymbol{\theta}} = \arg \max_{\boldsymbol{\theta}} L(\boldsymbol{\theta} | \Delta \mathbf{M}) = \arg \min_{\boldsymbol{\theta}} \sum_{i=1}^N (\Delta M_i - g_i(\boldsymbol{\theta}))^2, \quad (5.2)$$

with  $\boldsymbol{\theta}$  the parameter vector,  $\hat{\boldsymbol{\theta}}$  the estimate,  $\boldsymbol{\Delta M} = \{\Delta M_i\}_{i=1}^N$  a set of PCASL difference data points acquired at acquisition times  $\mathbf{t} = \{t_i\}_{i=1}^N$  and  $L(\boldsymbol{\theta}|\boldsymbol{\Delta M})$  the likelihood function. Two options for the parameter vector,  $\boldsymbol{\theta}_1 = \{f, \Delta t\}$  and  $\boldsymbol{\theta}_2 = \{f, \Delta t, T'_{1t}\}$ , give rise to a two-parameter NLE (NLE2) and a three-parameter NLE (NLE3), respectively.

### 5.2.3 Optimization of multi-PLD PCASL acquisition settings for NLE3

#### Experiment design optimization using Cramér-Rao lower bounds

The precision of NLE3 will be lower than that of NLE2 due to the larger amount of unknown parameters to be estimated. However, the precision of NLE3 can be maximized by optimizing the experimental design. Cramér-Rao lower bound (CRLB) theory is the tool of choice to build such an optimization framework. The relation between the CRLB and the variance of any unbiased estimator  $\hat{\boldsymbol{\theta}}$  of  $\boldsymbol{\theta}$  is summarized by the Cramér-Rao inequality [97]:

$$\text{cov}(\hat{\boldsymbol{\theta}}) \geq \mathbf{I}^{-1}(\boldsymbol{\theta}), \quad (5.3)$$

with  $\text{cov}(\hat{\boldsymbol{\theta}})$  the covariance matrix of  $\hat{\boldsymbol{\theta}}$  and  $\mathbf{I}^{-1}(\boldsymbol{\theta})$  the inverse of the Fisher information matrix (FIM). The inverse of the FIM is often referred to as the CRLB matrix. The diagonal elements of the CRLB matrix are the Cramér-Rao lower bounds on the variances of unbiased estimators of the elements of  $\boldsymbol{\theta}$  [15]. In section 4.4.2, it was shown that for independent data points described by a Gaussian probability density function with constant variance  $\sigma^2$ , the FIM can be written as

$$\mathbf{I}(\boldsymbol{\theta}) = \frac{1}{\sigma^2} \sum_{i=1}^N \frac{\partial g_i(\boldsymbol{\theta})}{\partial \boldsymbol{\theta}} \frac{\partial g_i(\boldsymbol{\theta})}{\partial \boldsymbol{\theta}^T}. \quad (5.4)$$

Clearly, the FIM depends on the unknown parameter vector  $\boldsymbol{\theta}$ , captured by the parametric perfusion model  $g(\boldsymbol{\theta})$  that describes the expected values of the data points. Since this model depends on the acquisition settings of the multi-PLD PCASL experiment, so does the FIM and the CRLB matrix. This last dependency can be exploited for experiment design. The CRLBs of the parameters of interest can be minimized with respect to certain acquisition settings of the multi-PLD PCASL experiment. With an unbiased efficient estimator, it is expected that the estimator would reach its maximal precision (i.e., its lowest variance), with respect to the acquisition settings that were optimized, when presented with PCASL difference data acquired at these optimal acquisition settings.

Starting from the CRLB matrix  $I^{-1}(\boldsymbol{\theta})$ , different optimization criteria can be chosen by transforming it to a scalar function [109]:

$$q_h(\boldsymbol{\theta}) = \frac{\partial h(\boldsymbol{\theta})}{\partial \boldsymbol{\theta}^T} \mathbf{I}(\boldsymbol{\theta})^{-1} \frac{\partial h(\boldsymbol{\theta})}{\partial \boldsymbol{\theta}}, \quad (5.5)$$

with  $h(\boldsymbol{\theta})$  a scalar function and  $\partial h(\boldsymbol{\theta})/\partial \boldsymbol{\theta}^T$  a row vector. In this work, the choice was made to focus on maximizing the precision of CBF estimation as this is the main parameter of interest. The CRLB of  $f$  can be isolated by choosing  $h(\boldsymbol{\theta}) = f$  in Eq.(5.5).

### Optimization of the labeling duration and acquisition time points

For a certain choice of labeling duration  $\tau$ , the CRLB of the CBF  $f$  can be minimized with respect to the acquisition time points  $\mathbf{t}$ . Given a certain underlying parameter vector  $\boldsymbol{\theta}$ , the optimal acquisition times  $\mathbf{t}$  can be written as:

$$\hat{\mathbf{t}} = \arg \min_{\mathbf{t}} q_h(\boldsymbol{\theta}, \mathbf{t}) \Big|_{h(\boldsymbol{\theta})=f}. \quad (5.6)$$

The CRLB also depends on the underlying parameter vector  $\boldsymbol{\theta}$ , which varies spatially within the brain as well as between different subjects. Therefore, optimization of the acquisition settings should be performed for a representative prior distribution  $p(\boldsymbol{\theta})$  of  $\boldsymbol{\theta}$  in the target population. For a continuous prior distribution, the optimal acquisition times  $\mathbf{t}$ , for a given value of  $\tau$ , are found by minimizing a weighted integral:

$$\hat{\mathbf{t}} = \arg \min_{\mathbf{t}} \int_{\boldsymbol{\theta}} q_h(\boldsymbol{\theta}, \mathbf{t}) p(\boldsymbol{\theta}) d\boldsymbol{\theta} \Big|_{h(\boldsymbol{\theta})=f}. \quad (5.7)$$

Note that Eq. (5.7) represents a general framework for optimization of PCASL settings. Indeed, the scalar function  $h(\boldsymbol{\theta})$  provides flexibility with respect to which parameters are chosen for optimization of the acquisition settings. For example, the trace of  $\mathbf{I}^{-1}(\boldsymbol{\theta})$  could be minimized with  $h(\boldsymbol{\theta}) = f + \Delta t + T_{1t}'$ . The integral in Eq. (5.7) can be approximated by evaluating  $q_h(\boldsymbol{\theta}, \mathbf{t})$  at a large number  $M$  of randomly selected samples of  $p(\boldsymbol{\theta})$ . The optimization in Eq. (5.7) can therefore be

approximated by

$$\hat{\mathbf{t}} = \arg \min_{\mathbf{t}} \frac{1}{M} \sum_{j=1}^M q_h(\boldsymbol{\theta}_j, \mathbf{t}) \Big|_{h(\boldsymbol{\theta})=f}, \quad (5.8)$$

with  $\boldsymbol{\theta}_j$  a randomly selected sample from  $p(\boldsymbol{\theta})$ .

Besides  $\mathbf{t}$ , the labeling duration  $\tau$  and the number of PCASL label-control image pairs  $N$  are also optimizable. Therefore, the optimization in Eq. (5.8) can be repeated for multiple values of  $\tau$  and  $N$ :

$$\{\tilde{\mathbf{t}}, \tilde{\tau}, \tilde{N}\} = \arg \min_{\{\tau; N\}} \left\{ \min_{\mathbf{t}} \sum_{j=1}^M q_h(\boldsymbol{\theta}_j, \mathbf{t}, \tau) \Big|_{h(\boldsymbol{\theta})=f} \right\}. \quad (5.9)$$

Note that acquisition schemes are optimized for different values of  $\tau$  and  $N$  instead of optimizing them alongside  $\mathbf{t}$ , which would be impractical. Indeed, optimizing  $N$  alongside  $\mathbf{t}$  would change the dimensionality of the optimization space within the optimization, which is not possible in most optimization algorithms. Furthermore, for each labeling duration, there will be a different set of optimal acquisition time points  $\mathbf{t}$ . Therefore, optimizing  $\tau$  together with  $\mathbf{t}$  will increase the number of local minima in the optimization space, and thereby increase the risk of ending up in a local minimum. On top of that, the multi-step approach proposed in Eq. (5.9) allows to study how the minimized criterion changes as a function of  $\tau$  and  $N$ .

In order to guarantee clinically feasible results, the optimization was performed under a fixed total acquisition time constraint. The total time needed to obtain a PCASL label or control image is determined by the acquisition time  $t_i$ , the read-out time and the additional waiting period for MR specific absorption rate (SAR) limit restrictions. Only  $t_i$  is independent of the read-out approach and the subject. As it is not our goal to optimize for a specific readout strategy or a single subject, a total acquisition time constraint  $T$  was imposed only on the read-out- and subject-independent acquisition time of  $N$  PCASL label-control image pairs:

$$\{\tilde{\mathbf{t}}, \tilde{\tau}, \tilde{N}\} = \arg \min_{\{\tau; N\}} \left\{ \min_{\mathbf{t}} \sum_{j=1}^M q_h(\boldsymbol{\theta}_j, \mathbf{t}, \tau) \Big|_{h(\boldsymbol{\theta})=f, \sum_{i=1}^N 2t_i \leq T} \right\}, \quad (5.10)$$

where  $\sum_{i=1}^N 2t_i$  equals the read-out- and subject-independent total acquisition time for  $N$  multi-PLD label and control PCASL images.

## 5.3 Methods

In order to analyze the accuracy and precision of the estimators, four distinct experiments were performed. As a first indication of the identifiability of the parameters of NLE2 and NLE3, the condition number of both inverse problems is determined in section 5.3.1. In section 5.3.2, details of the optimization experiment are specified starting from the optimization framework for NLE3 introduced in section 5.2.3. The performance of NLE2 and NLE3 were compared in a simulation and a real data experiment. Details of these experiments are described in section 5.3.3 and 5.3.4, respectively. Throughout all experiments,  $\alpha = 0.85$  [31] and  $T_{1b} = 1.65$  s [34]. The equilibrium magnetization of blood  $M_{0b}$  was set to one for the optimization and in the simulation experiment. In the real data experiment, it was approximated using a proton density-weighted image  $M_{0t}$ , according to recommendations [1], and subsequently given as a fixed value to the estimator.

### 5.3.1 Parameter identifiability analysis

The identifiability of the parameters in a parameter estimation problem can be quantified by the condition number of the associated FIM. The larger this condition number, the more ill-conditioned (and hence noise sensitive) the estimation problem. The extreme case of an infinite condition number corresponds with a singular FIM, reflecting that the parameter estimation problem is ill-posed. This means that the CRLB does not exist and the model parameters are unidentifiable [15]. In a more moderate case, a high FIM condition number indicates an ill-conditioned inverse problem symptomized by a low precision, high correlations between parameters and poor identifiability [110–113]. The condition number  $\kappa$  of the FIM  $I(\boldsymbol{\theta}, \mathbf{t}, \tau)$  is calculated for NLE2 and NLE3 as [113]:

$$\kappa(I(\boldsymbol{\theta}, \mathbf{t}, \tau)) = \|I(\boldsymbol{\theta}, \mathbf{t}, \tau)^{-1}\|_2 \|I(\boldsymbol{\theta}, \mathbf{t}, \tau)\|_2 = \frac{\sigma_{\max}(I(\boldsymbol{\theta}, \mathbf{t}, \tau))}{\sigma_{\min}(I(\boldsymbol{\theta}, \mathbf{t}, \tau))}, \quad (5.11)$$

with  $\|\cdot\|_2$  the Euclidean norm, and  $\sigma_{\min}(\cdot)$  and  $\sigma_{\max}(\cdot)$  the maximal and minimal singular value of the FIM, respectively. To compare the identifiability of the parameters of the two- and three-parameter model employed by NLE2 and NLE3, respectively, the condition number of the corresponding FIMs were calculated for multiple randomly selected parameter vectors  $\boldsymbol{\theta}$  from the prior distribution  $p(\boldsymbol{\theta})$

of WM and GM, defined in section 5.3.2, and assuming an  $N = 24$  equidistant sampling scheme.

### 5.3.2 Experiment design optimization

#### Practical settings for the optimization framework

The theoretical optimization framework was, defined in section 5.2.3, given by:

$$\{\tilde{\mathbf{t}}, \tilde{\tau}, \tilde{N}\} = \arg \min_{\{\tau; N\}} \left\{ \min_{\mathbf{t}} \sum_{j=1}^M q_h(\boldsymbol{\theta}_j, \mathbf{t}, \tau) \Big|_{h(\boldsymbol{\theta})=f, \sum_{i=1}^N 2t_i \leq T} \right\}. \quad (5.12)$$

When performing the optimization for NLE3, a prior distribution  $p(\boldsymbol{\theta})$  needs to be chosen that reflects the target population. In this work, it is our goal to test the overall feasibility of NLE3, which is not specific to a certain pathology. To that end,  $p(\boldsymbol{\theta})$  was approximated by a Gaussian distribution based on reported distributions in the literature for both WM and GM in the general population [38, 64, 70, 114–116], as shown in Table 5.1. From the prior distribution of each parameter, for WM and GM, 10000 samples were randomly selected and combined to parameter vectors  $\boldsymbol{\theta}_j$ . Therefore, the resulting optimization criterion consists of a sum of  $M = 20000$  CRLBs.

As indicated by Eq. (5.12), the optimization is repeated for different values of the labeling duration  $\tau$  and the amount of PCASL data points  $N$ . The set of evaluated labeling durations  $\tau$  ranged from 0.8 to 1.8 s with increments of 0.1 s, while  $N$  ranged from 18 to 30 image pairs. As  $\tau$  is set to lower durations, the PCASL signal decreases, yet a higher amount of images  $N$  can be acquired within the time constraint  $T$ . Conversely, the PCASL signal increases with longer label durations, at a cost of a lower amount of images though. The chosen ranges for  $\tau$  and  $N$  were set wide enough to explore both extremes and find the optimum in between.

The time constraint  $T$  in Eq. (5.12) was set to 2 minutes. The resulting total acquisition time depends on the read-out approach and the SAR requirements. In this work, real data acquisition was performed using a 3D gradient-echo and spin-echo (GRASE) readout scheme [26, 43] with a readout time of 330 ms per image. For whole brain coverage, two segments would be needed, doubling the total number of images. Assuming a waiting period after each readout between 500 and 1500 ms to meet SAR requirements, the total acquisition time related to these optimized acquisition schemes was 5 to 8 minutes.

TABLE 5.1: Mean and standard deviation of Gaussian prior distributions  $p(\boldsymbol{\theta})$  representative of the distribution of the respective parameters in the general population. The prior distribution for  $T_{1t}$  is compatible with reported literature values for a 3T field strength [70].

	White matter	Gray matter
$f$ [mL/100g/min]	$23.0 \pm 5.0$ [114–116]	$53.9 \pm 11.0$ [64]
$\Delta t$ [s]	$1.15 \pm 0.30$ [38]	$0.95 \pm 0.30$ [38]
$T_{1t}$ [s]	$0.89 \pm 0.06$ [70]	$1.45 \pm 0.14$ [70]

### Optimization algorithm: pattern search

As the acquisition time points  $\mathbf{t} = \{t_i\}_{i=1}^N$  are optimized in Eq. (5.12), the objective function in Eq. (5.12) is minimized in an  $N$ -dimensional space. Knowing that the optimization needs to be performed for 18 to 30 PCASL images, the optimization space will have a high dimensionality. Because of this high dimensionality, the objective function in Eq. (5.12) is expected to have multiple local minima. Also, the objective function is too complicated to analytically calculate gradients with respect to  $\mathbf{t}$ . For these reasons, this optimization problem is well-suited for global heuristic search algorithms. With these algorithms, global solutions are searched for objective functions that contain multiple maxima or minima and where the objective function does not possess derivatives or where the derivatives are not known.

MATLAB provides a ‘Global Optimization Toolbox’ that includes global search, multistart, pattern search, genetic algorithm and simulated annealing solvers. Redundancy in the  $N$ -dimensional solution space provides guidance in choosing a solver. The order of the elements in the acquisition time point vector  $\mathbf{t}$  play no role. In other words, a permutation of the elements in  $\mathbf{t}$  will lead to the same acquisition protocol, only with a difference in the order at which the different label-control pairs are acquired. Therefore, for a certain objective function value associated with a certain acquisition time vector  $\mathbf{t}_x$  in the  $N$ -dimensional space, there exist  $N!$  permutations of  $\mathbf{t}_x$  that will lead to the exact same objective function values at  $N!$  different places in the  $N$ -dimensional space. By imposing constraints on the elements of  $\mathbf{t}$ , i.e.  $t_i < t_{i+1}$ , the optimization space is greatly reduced in size. This will speed up the calculation time significantly and reduce the risk of ending up in a local minimum. Of all the global optimization solvers, the `patternsearch` [117–119] algorithm fits best to this specific problem as it allows for constraints. If we represent the objective function of the optimization problem

### 5.3. Methods

---

by  $k(t)$ , the iterative procedure of the pattern search algorithm can be described as follows:

1. Choose a start point  $\mathbf{t}_0$  on a  $N$ -dimensional mesh grid with length  $L$  between two points on the mesh that only differ in one dimension by one unit on the mesh.
2. Calculate  $k(\mathbf{t})$  for the  $2N$  nearest points to  $\mathbf{t}_0$ , this set is defined as  $A = \{k(\mathbf{t}_j)\}_{j=1}^{2N}$ . Suppose this is iteration  $m$ .:
  - (a) If  $\min A < k(\mathbf{t}_0)$ : jump to the new minimum  $\mathbf{t}_0 = \arg \min A$ , increase the mesh grid length to  $L_{m+1} = 2L_m$  and go back to step 2.
  - (b) If  $\min A > k(\mathbf{t}_0)$ : reduce the mesh grid length to  $L_{m+1} = L_m/2$ .
    - If  $L_{m+1} > L_{\min}$ : go back to step 2.
    - If  $L_{m+1} < L_{\min}$ :  $\mathbf{t}_0 = \arg \min k(\mathbf{t})$  provides the global minimum.

An example of the iterative procedure of the pattern search solver is shown in Figure 5.1 for a two-dimensional problem.

Even with the optimization space reduced by the constraints  $t_i < t_{i+1}$ , the pattern search algorithm was still prone to ending up in local minima, dependent on the choice made for the starting points  $\mathbf{t}_0$ . Therefore, the optimization was rerun for a large number of randomly generated starting points.

#### 5.3.3 Simulation experiments

##### Data simulation

Simulation data were generated with the idea of incorporating as many aspects as possible to end up with data that would resemble reality as closely as possible. It was divided in three distinct steps.

First, a suitable model was chosen to generate PCASL data. The two-compartment model (TCM), described in section 4.2.2, was extended with a microvascular arterial compartment where no exchange between blood and tissue can occur. This leads to the following impulse response function:

$$q(t) = \begin{cases} \exp\left(-\frac{t}{T_{1b}}\right) & t \leq \tau_a \\ \beta \exp\left(-\frac{t}{T_{1t}}\right) + (1 - \beta) \exp\left(-\left(\frac{1}{\tau_{\text{trans}}} + \frac{1}{T_{1b}}\right)t\right) & \tau_a < t \leq \tau_a + \tau_c \end{cases} \quad (5.13)$$

In terms of the models described in section 4.2, this three-compartment model is a model in between the two-compartment and the multi-compartment model

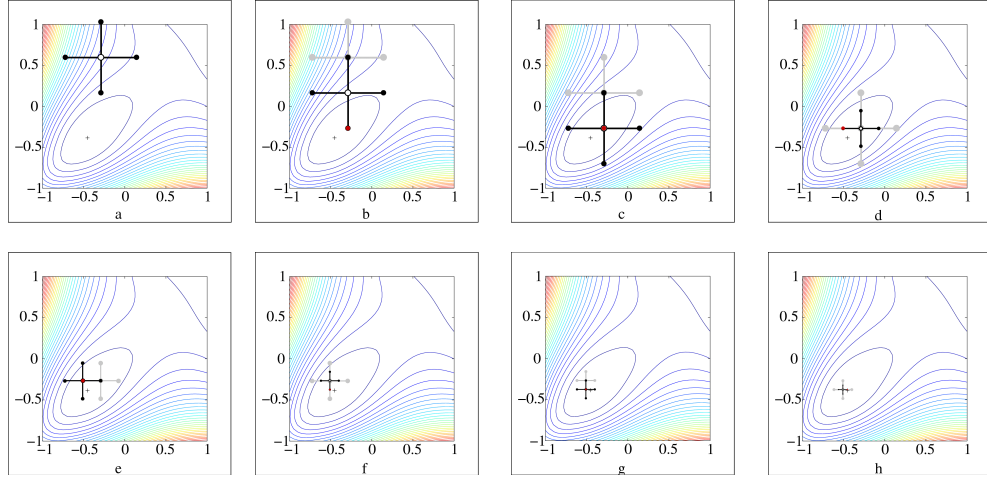


FIGURE 5.1: An example of the pattern search method applied on the Broyden function  $f(x, y) = |(3 - x)x - 2y + 1|^{\frac{7}{3}} + |(3 - y)y - x + 1|^{\frac{7}{3}}$

(MCM). It is equivalent to the five-parameter model described by Qin et al. in [37]. No dispersion effects were included in data simulation. It should be noted that the simulation model could have been made more accurate. However, we expect that incorporating the MCM and including dispersion effects (see Chapter 4) would not alter the outcome of this simulation experiment. The three-compartment model has five major local parameters: the CBF  $f$ , the ATT  $\Delta t$ ,  $T_{1t}$ , the blood-to-tissue water exchange rate  $k_w$  (equivalent to the inverse of the blood-to-tissue water transit time  $\tau_{\text{trans}}$ , as discussed in section 4.2) and the transit time through the microvascular arterial space  $\tau_a$ . For each of these parameters, ground truth high-resolution (HR) brain parameter maps were created. For  $f$ ,  $T_{1t}$ ,  $\tau_{\text{trans}}$  and  $\tau_a$ , this was achieved by assigning random values from their respective prior distributions (see Table 5.1 and 5.2) to a  $1 \times 1 \times 1 \text{ mm}^3$  HR brain tissue segmentation map derived from images of *BrainWeb* [120]. For the  $\Delta t$  map, the selection was performed pseudo-randomly to guarantee limited differences in  $\Delta t$  values between neighbouring voxels, as they are expected to be supplied by the same artery. Starting from those HR parameter maps and using the above described perfusion model, HR PCASL data was created at conventional equidistant and optimized acquisition times. The details of both acquisition schemes, which were set up to have an identical total acquisition time, are described in Table 5.3 in section 5.4.2, where the results of the optimization are presented.

### 5.3. Methods

Secondly, as PCASL data is usually acquired at a low resolution due to the low SNR, the HR data was downsampled to a resolution of  $4 \times 4 \times 5 \text{ mm}^3$  by averaging the signals of the 80 corresponding  $1 \times 1 \times 1 \text{ mm}^3$  HR voxels.

Finally, zero-mean Gaussian distributed noise with a fixed standard deviation  $\sigma$  was added voxel-wise to the LR data. Let the SNR in a voxel be defined as the difference signal intensity, averaged over the entire dynamic perfusion signal range, divided by  $\sigma$ . Then, simulation experiments were run with average SNRs of 10, 15, 20, and 25 in GM voxels. The data simulation process is summarized in a flowchart in Figure 5.2.

TABLE 5.2: Mean and standard deviation of Gaussian prior distributions of  $k_w$ , the blood-to-water exchange rate of water accounting for a finite permeability of the capillary wall, and  $\tau_a$ , the intra-voxel travel time accounting for an extended travel time through non-permeable vasculature.

	White matter	Gray matter
$k_w \text{ [s}^{-1}\text{]}$	$2.10 \pm 0.30$ [75]	$1.83 \pm 0.30$ [75]
$\tau_a \text{ [s]}$	$0.573 \pm 0.062$ [78]	$0.573 \pm 0.062$ [78]

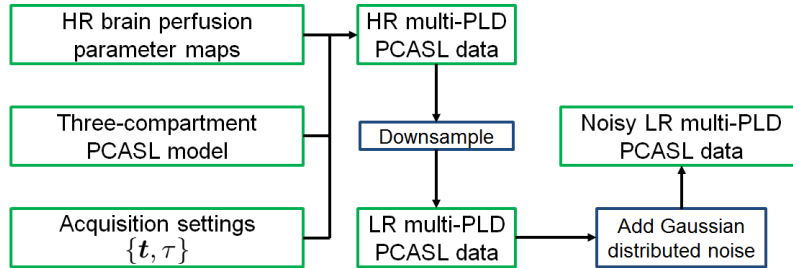


FIGURE 5.2: Flowchart of the creation of PCASL simulation data.

#### Parameter estimation

Parameter estimation was performed with maximum likelihood estimators NLE2 and NLE3, as defined in section 5.2.2. For NLE2,  $T'_{1t}$  was fixed to a tissue-specific value. Knowing that in a real data experiment the average  $T_{1t}$  in WM and GM is not accurately known, three versions of NLE2 were implemented. The  $\{T_{1,WM}, T_{1,GM}\}$ -couple was set to  $\{0.8 \text{ s}, 1.3 \text{ s}\}$ ,  $\{0.9 \text{ s}, 1.45 \text{ s}\}$  and  $\{1.0 \text{ s}, 1.6 \text{ s}\}$ , respectively. Note that the second  $\{T_{1,WM}, T_{1,GM}\}$ -couple contains the true average

simulation values. Estimation with NLE3 was studied on equidistant and optimal data. NLE2 was only evaluated using the equidistant data, as the optimization was performed specifically for NLE3.

### Statistical analysis

The process of creating noisy data and re-estimating the perfusion parameters was repeated  $K = 50$  times for each SNR. The performance of both estimators was assessed in terms of accuracy and precision. To this end, estimates of the bias and standard deviation of the estimators NLE2 and NLE3 of a given parameter of interest were obtained from the sample of  $K$  realisations by calculating the sample mean of the difference between the ground truth value of this parameter and its estimates, and the sample standard deviation of the estimates, respectively. To calculate the bias estimates, the ground truth LR parameter maps were obtained by downsampling the original ground truth HR parameter maps. Furthermore, an LR tissue segmentation map was obtained by labeling an LR voxel as a certain tissue type if more than 90% of the corresponding HR voxels were labeled as that specific tissue type. All remaining voxels were considered voxels with partial volume effects (PVE). The LR tissue segmentation map was used for two purposes. Firstly, in assigning a GM or WM  $T_{1t}$  value for quantification with NLE2. In the case of PVE voxels, the GM or WM  $T_{1t}$  value was chosen dependent on the predominant tissue type. Secondly, the tissue segmentation map allowed to analyze the simulation results per tissue type, when needed.

### 5.3.4 Real data experiments

#### Data acquisition

Whole-brain multi-PLD PCASL data were obtained from three healthy volunteers (22 year-old male, 30 year-old female, 38 year-old male) using the 3D GRASE sequence (spatial resolution =  $4 \times 4 \times 5$  mm<sup>3</sup>, readout time per shot = 330 ms, segments for whole brain coverage = 2, TE = 18ms, FOV<sub>read</sub> = 256mm, FOV<sub>phase</sub> = 192mm, FOV<sub>slice</sub> = 120mm), acquired on a Siemens 3.0T MR scanner with a 32-channel head coil. The repetition time for each label-control pair was set to the sum of the labeling duration, PLD, readout time and an additional waiting period to comply with SAR requirements, depending on the subject. The labeling plane was positioned based on a 40s angiogram, adhering to recommendations [1]. The acquired data consisted of multiple sets of  $N = 24$  label-control image pairs, obtained alternating between the equidistant and optimized acquisition scheme (see Table 5.3). The total acquisition time of each set of 24 label-control pairs

### 5.3. Methods

---

was 5 to 8 minutes, depending on individual SAR requirements. Including an HR anatomical image (sequence: MPRAGE, spatial resolution =  $1 \times 1 \times 1 \text{ mm}^3$ , TR = 2250ms, TE = 4ms, TI = 900ms, FOV<sub>read</sub> = 256mm, FOV<sub>phase</sub> = 256mm, FOV<sub>slice</sub> = 176mm) for tissue segmentation and an equilibrium magnetization image ( $M_{0t}$ ) (sequence: 3D GRASE, spatial resolution =  $4 \times 4 \times 5 \text{ mm}^3$ , segments for whole brain coverage = 2, TR = 6000ms, TE = 18ms, FOV<sub>read</sub> = 256mm, FOV<sub>phase</sub> = 192mm, FOV<sub>slice</sub> = 120mm) for absolute quantification, data acquisition was within one hour for each subject. With this acquisition time limit, the number of sets of  $N = 24$  label-control image pairs acquired at equidistant and optimal sampling schemes was  $K = 3$  for one subject and  $K = 4$  for two subjects. For each subject, the control images, label images, and  $M_{0t}$  image were scaled with a single global scaling map, kept static for the duration of data acquisition, for bias field correction. The label images, control images, and  $M_{0t}$  image per subject were mutually aligned using mutual information motion correction [121]. After registration, PCASL difference images were created by pairwise subtraction of label images from control images.

#### Parameter estimation

Perfusion parameters were estimated from the different sets of  $N = 24$  difference images with the same estimators as in the simulation experiment described in section 5.3.3. For absolute quantification,  $M_{0b}$  was approximated by  $M_{0t}/\lambda$  with  $\lambda = 0.9$  [1]. As NLE2 estimation and analysis of the results required WM and GM tissue segmentation in the LR difference images, an LR WM and GM mask was calculated in a multi-step approach. First, from the HR anatomical image, an HR WM and GM mask was obtained by means of multilevel image thresholding [122]. From the HR tissue segmentation map, an HR GM and WM mask were isolated. Second, a geometrical transformation matrix was obtained from a multi-modal intensity-based registration between the HR anatomical image and the LR  $M_{0t}$  image. Third, the geometrical transformation was applied to the HR GM and WM masks. Finally, as geometrically transforming an HR mask removes its binary character, voxels in the map resulting from the geometrical transformation of an HR mask were set to zero or one with 0.5 as a threshold to obtain an LR WM and GM mask.

#### Statistical analysis

Assuming underlying perfusion parameters remain constant within a single scan session, the repeated acquisition of the equidistant and optimized datasets allowed for a performance assessment of the different estimators. As there is no ground

truth information, the accuracy of the estimators can only be judged relative to each other by comparing their sample means for a certain parameter. The precision of the estimators for  $f$  in GM was evaluated using a voxel-wise and a slice-based metric. As a voxel-wise metric, the relative sample standard deviation  $s_{\text{rel}}(\hat{f})$  was defined as the sample standard deviation divided by the sample mean. This metric is equal to the square root of the relative variance of an estimator defined in section 4.4.2 in the introductory chapters. As a slice-based metric, the Pearson correlation coefficient (PCC) between the estimates of  $f$  of two different runs within an axial slice of the brain can be determined [123]. If there are  $K$  runs of the experiment,  $\sum_{m=1}^{K-1} m$  PCCs can be determined for a single axial slice. This procedure was performed in ten axial slices.

## 5.4 Results

The results of the identifiability analysis are presented in section 5.4.1. The optimal acquisition settings for NLE3 are presented and analyzed in section 5.4.2. The accuracy and precision of NLE2 and NLE3 are compared by examining the results of the simulation and real data experiment in section 5.4.3 and 5.4.4, respectively.

### 5.4.1 Parameter identifiability analysis

The FIM condition numbers associated with NLE2 and NLE3 are summarized in Fig.5.3. These results clearly show that the NLE3 inverse problem is more ill-conditioned. It is an indication that NLE3 will be more vulnerable to poor identifiability of parameters and low estimation precision compared to NLE2. Extracting maximal information in a certain total acquisition time by means of optimal experiment design can improve the conditionedness of the estimation problem of NLE3.

### 5.4.2 Experiment design optimization

The optimization criterion value after optimization for different  $\tau$  and  $N$  is shown in Fig. 5.4. For a fixed labeling duration, increasing the amount of images adds information up to the point where optimizing acquisition times has to be balanced with the total acquisition time constraint. The minimum of this set of values is the final result of the optimization defined in Eq. (5.10) for NLE3, which is reached for  $\tilde{N} = 24$ ,  $\tilde{\tau} = 1.1\text{s}$  and a certain set of acquisition times  $\tilde{t}$ . These optimal acquisition settings are shown in Table 5.3, alongside the equidistant sampling scheme with  $\tau = 1.8\text{s}$  used throughout this work. Note that the settings in Table

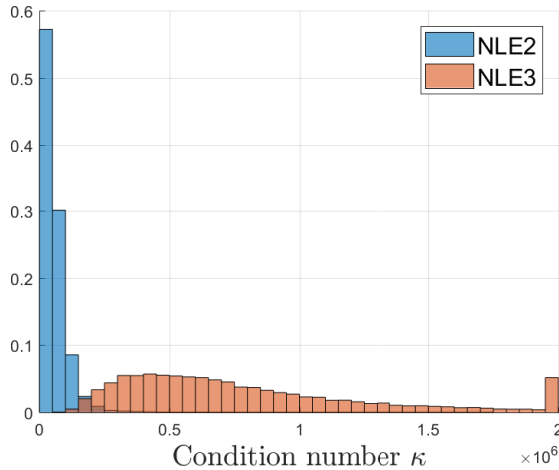


FIGURE 5.3: Distribution of the condition numbers  $\kappa(I(\boldsymbol{\theta}, \mathbf{t}, \tau))$  of NLE2 and NLE3 for multiple parameter vectors  $\boldsymbol{\theta}$  randomly selected from the prior distribution  $p(\boldsymbol{\theta})$ , defined in Table 5.1, and assuming an  $N = 24$  equidistant acquisition scheme.

5.3 are described for real data acquisition, in accordance with the explanation in the final paragraph of section 5.2.1. More specifically,  $t_i$  is shorter than  $\tau = 1.8\text{s}$  for the first 8 acquisition times in the equidistant scheme. Therefore, images were acquired with adjusted labeling durations  $\tau_s$  for these acquisition times. Furthermore, as scanner software imposed a lower limit of 100ms on the PLD in real data acquisition, the ninth acquisition time in the equidistant scheme and the first acquisition time in the optimized scheme were also acquired with a slightly shortened labeling duration (see Table 5.3). An example in a single voxel of data acquired with both acquisition schemes, accompanied by a fit of the perfusion model with the parameters estimated with NLE3, is shown in Fig. 5.5.

The distribution of the optimal acquisition times can be explained by examining the contribution of each possible acquisition time point to the Fisher information. The Fisher information for a single parameter  $\theta_j^k$  at a single time point  $t_i$ , assuming Gaussian distributed data, is closely related to the FIM and is defined as  $(\partial g(t_i; \boldsymbol{\theta}_j) / \partial \theta_j^k)^2 (1/\sigma^2)$  [15]. For  $f$ ,  $\Delta t$  and  $T'_{1t}$ , the Fisher information was calculated for each of the  $M = 20000$  parameter vectors  $\boldsymbol{\theta}_j$  at acquisition time points starting at 0s and up to 6s with increments of 1 ms. For each of the three parameter, the  $M$  Fisher information values were summed at each time point. Subsequently, for each parameter, the set of summed Fisher information values

between 0 and 6 s were normalized to the maximum value. Assuming  $\tau = 1.1$  s, the normalized summed Fisher information for  $f$ ,  $\Delta t$  and  $T'_{1t}$  at each acquisition time point is shown in Fig. 5.6. The optimal acquisition times are grouped into two distinct parts: a set distributed between 1 and 3 s and repeated measurements around 3.7 s. The distributed set coincides with the peaks of the Fisher information of the three parameters of NLE3 (Fig. 5.6). The repeated measurements around  $t = 3.7$  s can be attributed to the local maximum in the Fisher information for  $T'_{1t}$ . This shows that, despite of optimizing the acquisition settings for estimating  $f$ , the resulting optimal settings also include acquisition times that are of high importance for precisely estimating  $\Delta t$  and  $T'_{1t}$ .

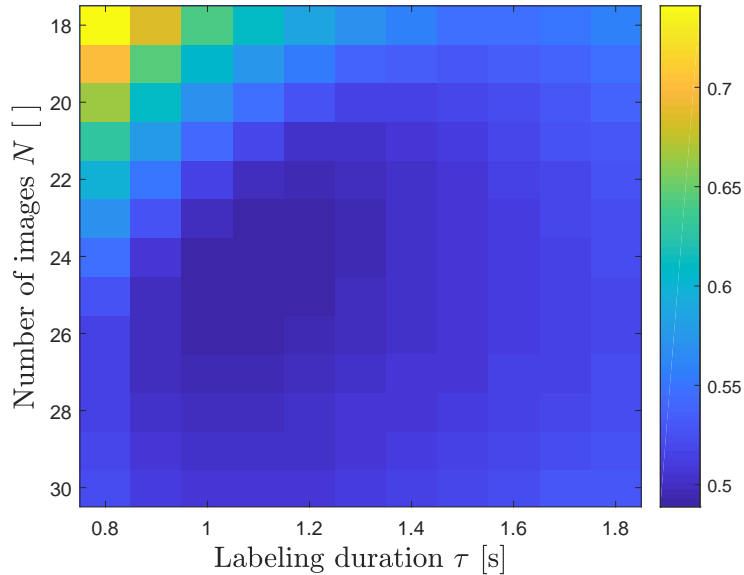


FIGURE 5.4: Minimal optimization criterion value associated with the optimal acquisition times  $\tilde{t}$ , for different combinations of  $\tau$  and  $N$ . The minimum is located at  $\tilde{N} = 24$  and  $\tilde{\tau} = 1.1$  s and corresponds with the optimal settings defined by Eq. (5.10).

## 5.4. Results

---

TABLE 5.3: (A) Equidistant and (B) optimal acquisition settings. The labeling duration  $\tau$  equals 1800ms and 1100ms for the equidistant and optimized scheme, respectively. For acquisition times  $t < \tau$ , a shorter labeling duration  $\tau_{\text{real}} < \tau$  was used for real data acquisition, as described in section 4.2.1. For  $t - \tau < 100\text{ms}$ ,  $\tau_{\text{real}}$  was also shortened to comply with a lower bound in scanner software of 100ms on the PLD. In all other cases,  $\tau_{\text{real}} = \tau$ .

$\tau_{\text{real}}$ [ms]	PLD [ms]	$t$ [ms]
400	100	500
574	100	674
748	100	848
922	100	1022
1096	100	1196
1270	100	1370
1444	100	1544
1617	100	1717
1791	100	1891
1800	265	2065
1800	439	2239
1800	613	2413
1800	787	2587
1800	961	2761
1800	1135	2935
1800	1309	3109
1800	1483	3283
1800	1657	3457
1800	1830	3630
1800	2004	3804
1800	2178	3978
1800	2352	4152
1800	2526	4326
1800	2700	4500

(A)

$\tau_{\text{real}}$ [ms]	PLD [ms]	$t$ [ms]
1033	100	1133
1100	243	1343
1100	337	1437
1100	607	1707
1100	694	1794
1100	792	1892
1100	897	1997
1100	988	2088
1100	1050	2150
1100	1100	2200
1100	1181	2281
1100	1221	2321
1100	1261	2361
1100	1314	2414
1100	1395	2495
1100	1496	2596
1100	1568	2668
1100	1665	2765
1100	2597	3697
1100	2611	3711
1100	2622	3722
1100	2624	3724
1100	2648	3748
1100	2659	3759

(B)

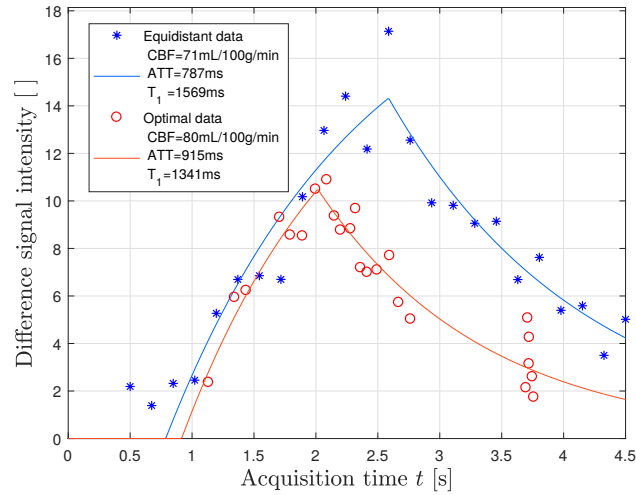


FIGURE 5.5: An example of PCASL difference data, acquired with the equidistant (blue asterisks) and optimal acquisition settings (red circles) described in Table 5.3, in a GM voxel of one of the subjects. The blue and red curve represent the NLE3 fit to both data sets.

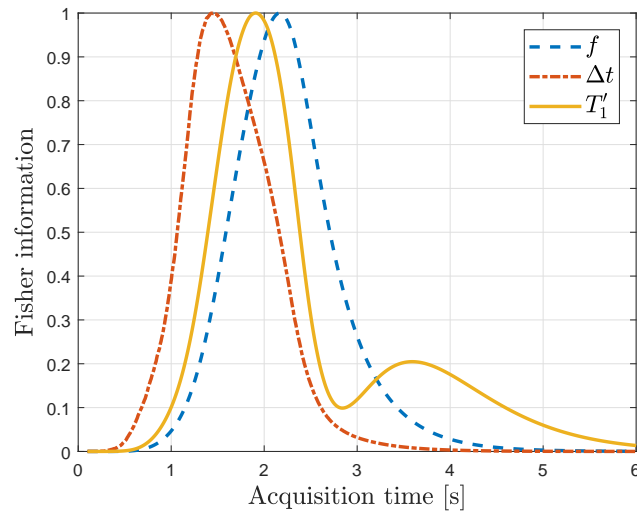


FIGURE 5.6: For each parameter of NLE3, the normalized summed Fisher information at each acquisition time point  $t_i$ , as defined in section 5.4.2, is shown. Maxima in the Fisher information correspond to acquisition times that contribute maximally to the estimation precision for that specific parameter.

### 5.4.3 Simulation experiments

The results for the simulation experiment performed with an average SNR of 10 in GM, which is to be expected in background-suppressed 3D GRASE real data [47], are summarized in Fig. 5.7. The bias and standard deviation estimates of  $f$  for NLE2 and NLE3 in a slice of the simulated brain are shown in the first two rows of Fig. 5.7.

The bias of NLE2 depends strongly on the choice of fixed  $T_{1t}$  value. In WM and GM, the spatial mean value of  $f$  increases by 15% when the  $T_{1t}$  value is reduced by approximately 10%. Regardless of the  $T_{1t}$  choice, the bias of NLE2 is highest in voxels with PVEs on the edges between WM and GM. NLE3 is showing a bias in the estimation of  $f$  that is hardly substantial, even in voxels affected by PVE. In such PVE voxels, NLE3 finds  $T'_{1t}$  values between the  $T'_{1t}$  values it would find for voxels containing only WM and only GM. While the  $T'_{1t}$  value in such voxels has no physiological meaning, it allows NLE3 to accurately estimate  $f$ . Note that among the NLE2 estimators, NLE2-3 with  $\{T'_{1,\text{WM}} = 1.0 \text{ s}, T'_{1,\text{GM}} = 1.6 \text{ s}\}$  has the lowest bias, while the underlying average values of  $T_{1t}$  are lower. This can be attributed to the creation of simulation data with a more accurate, more complex two-compartment perfusion model with a prolonged stay of the labeled bolus in the blood compartment. Compared to the SCM, relaxation towards equilibrium of the labeled spins is governed for a larger percentage by  $T_{1b}$  in the two-compartment model. Furthermore, the bias of NLE2-3 is slightly lower than the bias of NLE3, except in voxels with partial volume effects. This is remarkable, because it is not possible for NLE2 to have a better goodness of fit than NLE3, knowing that both estimators use the same model, with NLE3 having a higher degree of freedom. It can be explained by the fact that the data was simulated with a more complex model than the estimation model. This makes it possible for NLE2-3 to have a lower CBF estimation bias than NLE3, even though NLE3 provides a better model fit.

The standard deviation estimates of  $f$  show the expected superior precision of NLE2 compared to NLE3. The average gain in precision when estimating with NLE3 using optimally acquired data instead of equidistant data is 20%. Despite this improvement, the precision of NLE3 can still not compete with that of NLE2. Indeed, NLE2 and the optimized NLE3 have an average relative sample standard deviation of 9% and 19%, respectively.

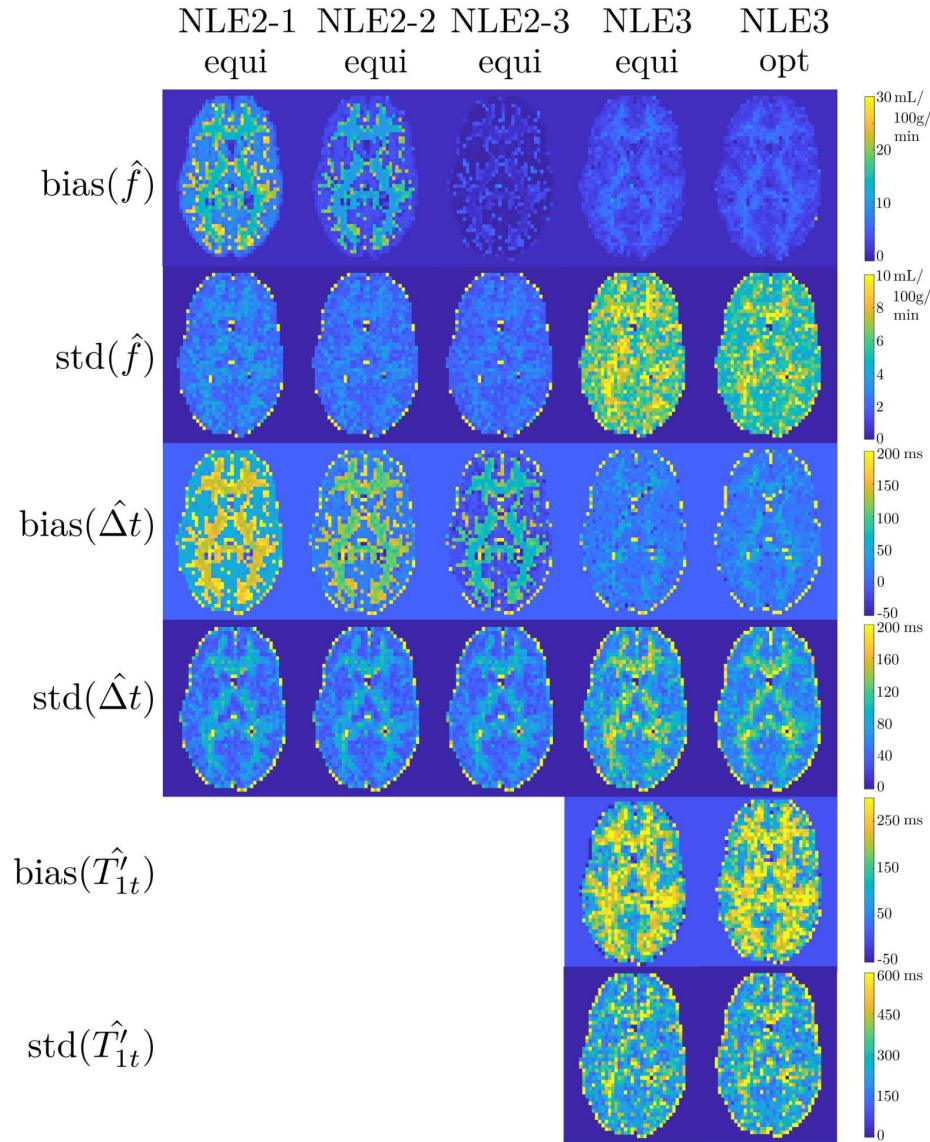


FIGURE 5.7: One slice of the estimated bias and standard deviation maps for the CBF  $f$ , the ATT  $\Delta t$  and  $T'_{1t}$ , obtained from simulation experiments for an average SNR of 10 in GM. NLE2-1, NLE2-2 and NLE2-3 refer to the different versions of NLE2 with  $T'_{1,GM}$  fixed at 1.3, 1.45 and 1.6 s, respectively. The ‘equi’ and ‘opt’ labels refer to whether equidistant or optimal datasets were used.

The results for  $\Delta t$  and  $T'_{1t}$  are shown in the remaining four rows of Fig. 5.7. Estimation of  $\Delta t$  follows the same overall trends as estimation of  $f$ , except for the fact that the average standard deviation for estimation of  $\Delta t$  with NLE3 is approximately equal when using equidistant or optimally acquired data. This is to be expected as the acquisition settings were optimized for the CBF parameter only. The bias maps for  $T'_{1t}$  show that NLE3 overestimates  $T'_{1t}$ , which is compatible with the observation that NLE2 has the lowest bias for  $T'_{1t}$  values between the underlying  $T'_{1t}$  and  $T_{1b}$ . Furthermore, compared to  $f$  and  $\Delta t$ , the standard deviation for estimation of  $T'_{1t}$ , relative to its underlying value, is significantly higher.

Besides for an SNR of 10 in GM, the simulation experiment was also repeated for an SNR of 15, 20 and 25 to assess how estimation accuracy and precision of NLE2 and NLE3 change as a function of SNR. The average relative estimation bias and average relative standard deviation for GM for the considered SNRs are shown in Fig. 5.8. In terms of estimation accuracy, there were no significant differences between the different SNRs (Fig. 5.8a). In terms of precision, an SNR of 20-25 is necessary for the NLE3 in optimized conditions to match the average standard deviation of NLE2 at an SNR of 10 (Fig. 5.8b). Assuming that doubling the total acquisition time to acquire another repetition of the data set increases the SNR of the data set with a factor  $\sqrt{2}$ , the acquisition time would need to be increased with a factor of 4 to 6.25 in order for estimation with NLE3 to be as precise as estimation with NLE2, considering their precisions are equal for an SNR of 10 and 20-25, respectively.

#### 5.4.4 Real data experiments

The estimates of  $f$  for the different runs, for one subject, are shown in Fig. 5.9. Two important features can already be observed qualitatively. Firstly, similar to the observation in the simulation experiment, estimation values of  $f$  increase as  $T_{1t}$  is fixed to a smaller value. Secondly, NLE3 produces more physiologically unrealistic results, especially in white matter. All voxels with  $f > 120$  mL/100g/min were filtered out, resulting in  $f$  maps that are more sparsely filled. The SNR in white matter is too low to estimate  $f$  with reasonable precision from 24 multi-PLD difference signals with NLE3.

For all subjects and every estimator, the spatial mean and standard deviation are shown for the different perfusion parameters in GM (Table 5.4). For each subject, an increase of 150 ms in NLE2- $T_{1,GM}$  value causes a decrease of 7% to 10% in spatial mean estimate of  $f$  (first three rows of Table 5.4a). These results confirm the dependence of NLE2 on the choice of a fixed  $T_{1t}$  value for estimation of

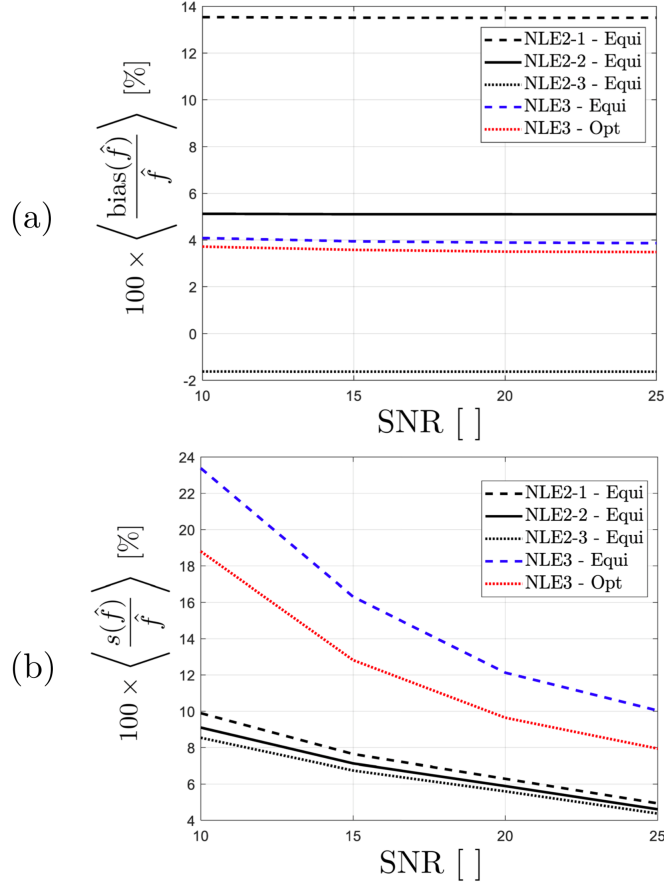


FIGURE 5.8: The average relative bias (a) and average relative standard deviation (b) for CBF estimation in GM as a function of the average SNR obtained from simulation experiments described in section 5.3.3. Results are shown for NLE2 using equidistant data, and NLE3 using equidistant and optimal data.

$f$ . A similar decrease is seen for  $\Delta t$ , however limited to 1% to 3% (first three rows of Table 5.4b). The spatial mean estimates of  $f$  and  $\Delta t$  obtained with NLE3 from equidistant and optimal data (final two rows of Table 5.4a and 5.4b) lie within the range of the results of the different versions of NLE2. Furthermore, for  $f$ , the difference in spatial mean estimate value, obtained from using NLE3 on equidistant and optimal data, respectively, is limited. However, the mean  $T'_{1,\text{GM}}$  results for NLE3 (Table 5.4c) are high compared to most literature values of  $T_{1,\text{GM}}$  [70],

#### 5.4. Results

---

knowing that the difference between  $T'_{1t}$  and  $T_{1t}$  should only be about 1% [52]. Note that this overestimation of  $T'_{1t}$  can be partly due to a prolonged stay of labeled spins in the blood compartment, which is not correctly accounted for in the SCM [37, 63]. Also, the spatial standard deviation for  $T'_{1,GM}$  is very large, indicating NLE3 is not reliable for  $T'_{1t}$  estimation. It is noteworthy that all these results are in agreement with the trends observed in the simulation experiments in section 5.4.3.

TABLE 5.4: For each subject, the spatial mean and standard deviation of the parameters in GM are shown per estimator.

	S1	S2	S3
NLE2-1-equi	$51.7 \pm 19.4$	$52.1 \pm 19.2$	$50.4 \pm 18.2$
NLE2-2-equi	$47.6 \pm 18.1$	$48.2 \pm 17.9$	$46.6 \pm 17.1$
NLE2-3-equi	$44.1 \pm 17.0$	$44.7 \pm 16.7$	$43.4 \pm 16.1$
NLE3-equi	$47.7 \pm 21.6$	$49.7 \pm 20.1$	$48.4 \pm 20.4$
NLE3-opt	$48.4 \pm 21.2$	$50.6 \pm 19.9$	$47.1 \pm 20.5$

(A)  $\hat{f}$  in GM [mL/100g/min]

	S1	S2	S3
NLE2-1-equi	$708 \pm 360$	$847 \pm 457$	$1230 \pm 575$
NLE2-2-equi	$686 \pm 358$	$827 \pm 460$	$1203 \pm 575$
NLE2-3-equi	$664 \pm 354$	$811 \pm 458$	$1181 \pm 577$
NLE3-equi	$631 \pm 266$	$830 \pm 390$	$1145 \pm 453$
NLE3-opt	$709 \pm 241$	$855 \pm 435$	$1205 \pm 387$

(B)  $\hat{\Delta}t$  in GM [ms]

	S1	S2	S3
NLE3-equi	$1687 \pm 732$	$1855 \pm 926$	$1873 \pm 914$
NLE3-opt	$1529 \pm 619$	$1901 \pm 927$	$2025 \pm 1078$

(C)  $\hat{T}'_{1t}$  in GM [ms]

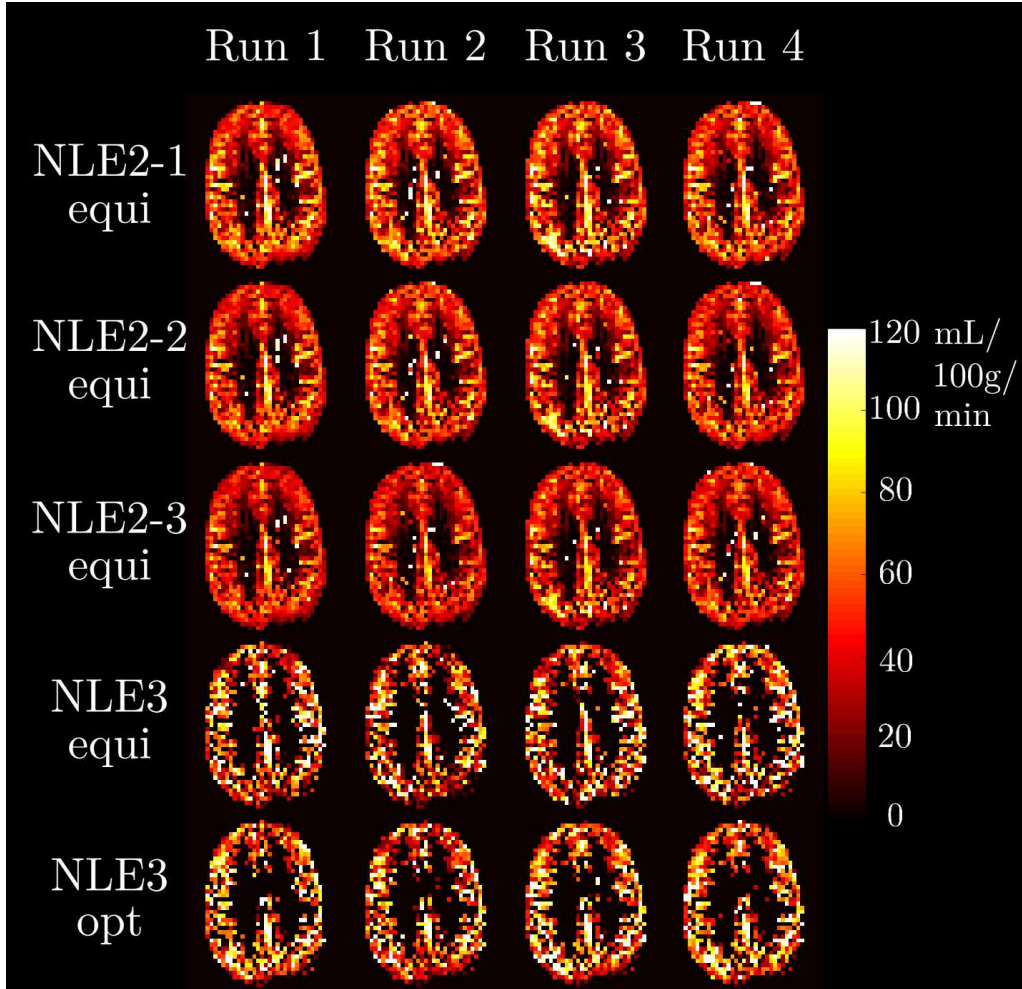


FIGURE 5.9: For one subject,  $f$  maps are shown resulting from applying NLE3 and three versions of NLE2 to the equidistant data subsets and NLE3 to the optimal data subsets. Only voxels with an  $f < 120$  mL/100g/min were retained. For NLE2, WM and GM voxels were differentiated using a segmentation map created from an acquired HR anatomical image.

The distribution of  $s(\hat{f})$  within GM for every estimator and every subject is shown in Fig. 5.10a. Similarly, for each subject and each estimator, the PCCs for  $f$  are grouped and compared in Fig. 5.10b. The relative sample standard deviation and PCC metric show compatible results. Firstly, NLE3 performs at a significantly

higher precision when applied to optimal data compared to equidistant data. Non-parametric Kruskal-Wallis (KW) tests comparing the sets of  $s(\hat{f})$  for both data types show a significantly lower median  $s(\hat{f})$  in the optimized experiment for all three subjects. Similarly, KW tests demonstrate a significantly higher correlation between test-retest results in the optimized experiment. Secondly, not surprisingly, both metrics show that NLE2 operates at a precision unattainable for NLE3, even in optimized conditions.

Note that NLE2 achieves a median relative precision between 7 and 12% for  $f$  estimation (first three boxplots for each subject in Fig. 5.10a), while for NLE3 in optimized conditions it ranges from 15 to 25% (last boxplot for each subject in Fig. 5.10a). Contrary to the slice-based metric, the relative sample standard deviation provides quantitative results on the precision of an estimator. To the best of our knowledge, no such results have been previously reported on CBF estimation in multi-PLD PCASL.

## 5.5 Discussion and conclusions

In this chapter, the accuracy and precision with which perfusion parameters can be estimated from multi-PLD PCASL data, using a single-compartment model, were studied. A two- (NLE2) and three-parameter (NLE3) estimator were compared, where the only difference between both estimators was whether  $T'_{1t}$  was fixed at a certain value or estimated alongside the perfusion parameters, respectively. As the total acquisition time for each multi-PLD PCASL imaging sequence was 5 to 8 minutes and recommendations regarding spatial resolution were respected, the reported statistical quantitative measures are representative for a clinically feasible multi-PLD PCASL experiment.

A major part of this work consisted of optimizing the acquisition settings of NLE3 in order to maximally compensate for the expected drop in precision caused by the addition of an extra parameter compared to NLE2. In PCASL, acquisition times can be optimized for a certain labeling duration or they can be optimized simultaneously. Furthermore, a choice can be made to either allow acquisition times  $t_i \leq \tau$  or conversely only allow  $t_i \geq \tau$ , which de facto becomes an optimization of the PLDs only [124]. In the present work, optimal acquisition times  $\mathbf{t}$  were searched for different labeling durations  $\tau$ , while allowing  $t_i \leq \tau$ . Compared to only optimizing the PLDs, this optimization approach pushes the boundaries of the multi-PLD PCASL experiment to higher levels of estimation precision. Simulation and real data experiments showed an increase of 10 to 20% in precision for NLE3 in optimized conditions compared to conventional equidistant

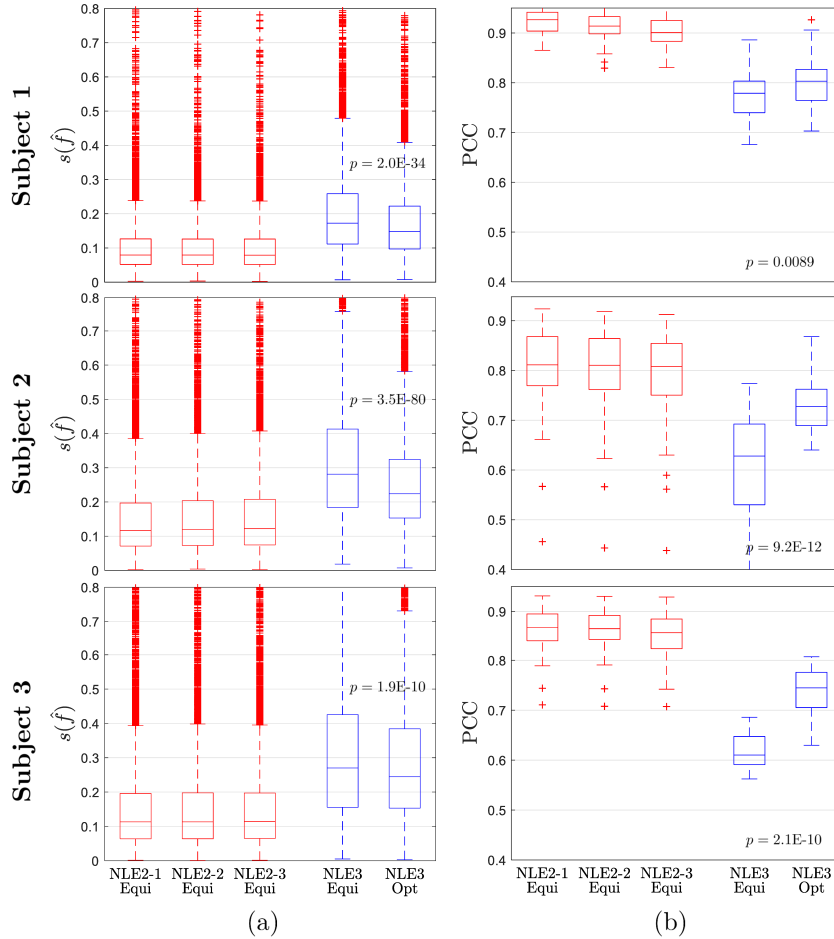


FIGURE 5.10: Boxplots of (a) the relative sample standard deviations  $s(\hat{f})$  in all GM voxels and (b) the per-slice PCCs for  $f$ . Each boxplot shows the results for a certain estimator applied to data of a certain subject. A non-parametric KW test comparing the results of NLE3 for equidistant and optimal data was performed. The p-values related to the KW test are shown between the respective boxplots.

acquisition settings. In terms of precision, however, NLE3 in combination with an optimal acquisition scheme is still no match for NLE2. More importantly, the median relative CBF precision for the optimized NLE3 was still as high as 15-25% in real data experiments. This level of reproducibility is unacceptable in a clinical

setting.

The NLE2 had a higher precision with a median sample standard deviations in the real data experiment between 7 and 12%. However, the simulation and real data experiments clearly showed a dependence of CBF estimation on the choice of fixed  $T'_{1t}$  value. A reduction of approximately 10% in  $T'_{1t}$  value for GM resulted in an average CBF value increase of 15% in the simulation experiment and 7-10% in the real data experiment. Note that these results are relative, comparing versions of NLE2 with different fixed  $T'_{1t}$  values. The simulation experiment showed that the largest inaccuracies are to be expected at the edges between two tissue types. Inaccuracies related to PVE will be present for any NLE2 estimator, independent of the fixed  $T'_{1t}$  choice. Therefore, NLE2 in combination with a fixed  $T'_{1t}$  value is inherently inaccurate. However, the simulation experiment showed that CBF estimation bias in NLE2 is lowest for a fixed  $T'_{1t}$  value in between the true underlying  $T'_{1t}$  and  $T_{1b}$  value, reflecting the prolonged stay of the labeled bolus in the blood compartment in the more accurate two-compartment model.

The optimization of PCASL acquisition settings described in sections 5.2.3 and 5.3.2 for NLE3 was also repeated for NLE2. The theoretical gain in precision compared to estimating with NLE2 using equidistant settings was found to be of the same order as for NLE3 using the optimized settings compared to the equidistant acquisition strategy, in simulations as well as in real data experiments. These results were not included in this work as they have no impact on which estimator performs better. It was shown in simulations that NLE2 and NLE3 perform approximately equally well in terms of bias when an appropriate fixed  $T_{1t}$  value is chosen for NLE2. In terms of precision, NLE3 in optimized conditions still had a significantly lower precision than NLE2 using equidistant data. As the performance balance in terms of accuracy and precision is already tipped in favor of NLE2, further increasing the precision of NLE2 by means of experiment design is not vital for the comparison between NLE2 and NLE3.

In general, a drawback of most experiment design studies, including the one in this study, is the fact that acquisition settings are optimized given a certain prior distribution of parameters that describe the underlying physiological process. Usually such a prior distribution is chosen to represent a certain population, often the general population. It can be called into question whether the optimized settings would still be beneficial in a patient setting, as lesions might be represented by outlying parameters not represented in general prior distributions. An interesting alternative is to optimize the acquisition settings in real time during scanning, based on parameter estimates obtained from data acquired moments before, as was done by Gardener and Jezzard in ASL [125].

It is important to note that, next to  $T'_{1t}$ , other parameters in the SCM (i.e.,

$T_{1b}$ ,  $M_{0b}$  and  $\alpha$ ) can also cause inaccuracies due to a difference between the fixed or determined value and the true underlying value. It should however be stressed that  $T_{1b}$ ,  $M_{0b}$  and  $\alpha$  are not good candidates to estimate voxel-wise alongside the CBF and ATT, contrary to  $T'_{1t}$ . The CBF,  $T_{1b}$ ,  $M_{0b}$  and  $\alpha$  are not independently identifiable in the SCM (see Eq.(5.1)). An alternative would be to estimate  $\alpha$  and  $T_{1b}$  from data obtained in separate MRI experiments [68, 126], similarly to how  $M_{0b}$  is estimated from a proton density image. Which one of these parameters has the highest possible impact on CBF quantification accuracy deserves further study. On top of that, the SCM is inherently biased as it is an approximation of the underlying physical perfusion process. Therefore, even with exact knowledge of all fixed parameters, CBF and ATT estimation will remain biased to a certain degree.

Replacing the SCM by a more complex (i.e., more accurate) model could be a viable option. Multiple studies have improved upon single-compartment models in terms of a more accurate representation of the evolution of the ASL signal. Accounting for a finite permeability of the capillary wall to water diffusion in a two-compartment model [63, 74], incorporating a prolonged stay of labeled water in arterial microvasculature after arriving in the imaged voxel [39, 71], allowing a change of concentration of labeled water as a function of time [74] and correcting for dispersion of the labeled bolus [86] are the most notable developments. Unfortunately, extra parameters are introduced in these models. This work has made clear that it is not a feasible option to estimate extra parameters alongside the CBF and the ATT within the boundaries of data acquisition at the recommended spatial resolution and a limited total acquisition time. Hence, extra parameters need to be fixed to certain literature values, which again introduces inaccuracies, or have to be obtained from other experiments, which prolongs the total acquisition time. The only case in which another model might improve upon the SCM in terms of estimation accuracy and precision, is if estimation of only the CBF and the ATT with this model is less susceptible to fixing certain parameters in the model. Future work will focus on finding and testing suitable candidate models. The simplified solution to the two-compartment model neglecting backflow, as proposed by Parkes et al [63], could be such a candidate.

In conclusion, it is shown that  $T_{1t}$  plays a central role in quantification of CBF from multi-PLD PCASL with the single-compartment model. Fixing  $T'_{1t}$  to a certain value may cause a significant bias when estimating the CBF and the ATT with NLE2. Estimating  $T'_{1t}$  alongside the CBF and the ATT with NLE3 is too detrimental to the precision, even with optimized acquisition settings. One may raise the question: is it at all possible to estimate the CBF with sufficient accuracy and precision while using the single-compartment model? Regarding

### 5.5. Discussion and conclusions

---

precision, the experiments presented clearly indicate that NLE2 is the only viable option within the limits of a reasonable total acquisition time and a recommended spatial resolution [1]. Despite the dependence of NLE2 CBF estimation on the  $T'_{1t}$  choice, simulation experiments suggest that fixing  $T'_{1t}$  in between the population average of  $T_{1t}$  for either WM or GM and the population average of  $T_{1b}$  minimizes the risk of a systematic bias in CBF estimation. Therefore, CBF estimation from multi-PLD PCASL data acquired at the recommended [1] spatial resolution with NLE2 using such prolonged fixed  $T'_{1t}$  values provides the optimal balance between accuracy and precision.



## Chapter 6

# The benefit of supporting measurements in ASL

In the contribution described in the previous chapter, it was shown that it is not feasible to estimate the longitudinal relaxation time of tissue  $T_{1t}$  alongside the CBF and the ATT from multi-PLD PCASL data within a scan time reasonable for a clinical setting due to too low estimation precision. A comment that was often made while presenting the work in the previous chapter is why we focussed on  $T_{1t}$ , as many researchers indicated its importance in quantification was inferior compared to other parameters in the quantification model. While we showed that  $T_{1t}$  does play an important role when quantifying with the single-compartment model, there are indeed two other parameters that are prone to variability: the labeling efficiency  $\alpha$  and the longitudinal relaxation time of blood  $T_{1b}$ . They are also usually fixed to literature values. Just like fixing the value of  $T_{1t}$ , fixing the values of  $\alpha$  and  $T_{1b}$  in the single-compartment quantification model could result in systematic errors in perfusion parameter estimation.

There are two important differences when considering  $\alpha$  and  $T_{1b}$  compared to  $T_{1t}$ . First, when considering multi-time-point ASL data and assuming quantification with the SCM, both  $\alpha$  and  $T_{1b}$  are not independently identifiable from the CBF. In other words, the labeling efficiency nor the blood relaxation time can be estimated alongside the CBF from the same set of data, contrary to the tissue relaxation time. Second, both  $\alpha$  and  $T_{1b}$  are also present in the recommended quantification model for single-PLD PCASL data, while  $T_{1t}$  is not. Essentially,  $T_{1b}$  has a much more prominent role in the single-PLD quantification model compared to in the single-compartment quantification model for multi-PLD data. In any case,  $\alpha$  and  $T_{1b}$  can only be determined from supporting (MRI) experiments. Measuring  $\alpha$  and  $T_{1b}$  and using those measured values instead of fixing both parameters to literature averages is expected to increase the accuracy of CBF estimation on a population level. However, if we assume a fixed total scan time, performing

extra experiments would diminish the scan time for acquiring the core ASL data. This is expected to reduce the precision of CBF estimation. Is it worth to sacrifice ASL scan time to perform these supporting measurements in terms of the accuracy-precision trade-off? That was the central question of this study.

## 6.1 Introduction

While the single-PLD pseudo-continuous ASL (PCASL) experiment in combination with the simplified model has proven its reliability, it is prone to several remaining sources of quantification errors [53]. The most important error sources can be divided in two categories. Firstly, certain model parameters in the consensus model are fixed to literature values, while the true underlying values may vary significantly in reality. The longitudinal relaxation time of blood  $T_{1b}$  changes with factors defining its physiological state [34, 67, 68], such as hematocrit, oxygenation fraction, and blood cell pathologies (e.g. observed in sickle cell disease [127]). The labeling efficiency  $\alpha$  depends on magnetic field inhomogeneities and blood flow velocity, and can therefore differ between individual arteries, subjects and scan sessions [31, 128]. In the consensus model,  $T_{1b}$  and  $\alpha$  are fixed to 1.65s and 0.85, respectively. The discrepancy between fixing these model parameters and the spread of their values in reality may result in significant CBF quantification bias. Secondly, the consensus model is an oversimplification of the underlying perfusion processes. It is based on two main assumptions: the entire bolus has arrived in the imaging voxel at the start of the readout and the labeled spins stay in the blood compartment during the entire experiment [1]. In order for the first assumption to be valid, the PLD has to be longer than the arterial transit time (ATT), which is the travel time of the bolus from the labeling plane to a certain imaging voxel. As the local ATT can vary within the brain and between subjects [1, 35, 38], a sufficiently long PLD of 1800ms was recommended in the consensus experiment. Unfortunately, for ATTs that are significantly shorter than the PLD, the second assumption is invalidated. In that case, labeled spins will have entered the brain tissue where they decay faster, since the longitudinal relaxation time of brain tissue ( $T_{1t}$ ) is shorter than  $T_{1b}$ . Therefore, depending on the interplay between the local ATT and the PLD, quantification with the consensus model may lead to relative over- or underestimation of CBF [53].

Both error categories described above may lead to local CBF quantification errors varying between regions of the brain, or global quantification errors varying between different subjects or scan sessions, or a combination of both. In other words, CBF can be over- or underestimated to varying degrees due to a certain

mixture of these confounders. Ultimately, in clinical contexts which depend upon quantitative values, it may impede usability of quantitative ASL scans.

CBF quantification accuracy can be increased by performing additional experiments or by using alternative versions of the ASL experiment. Such additional experiments may consist of measuring  $T_{1b}$  and  $\alpha$  with separate MRI scans [68, 126, 129, 130], instead of fixing them to literature values. Sampling the perfusion process at multiple time points by means of multi-PLD PCASL [55, 131] or time-encoded PCASL [57, 59] allows for more accurate CBF quantification along with the possibility to measure the ATT, contrary to the single-PLD PCASL consensus implementation. However, if the total acquisition time is kept constant, these suggested alterations will limit the number of label-control pairs that can be acquired during the perfusion phase. Ultimately, this will reduce the precision of CBF quantification.

Clearly, there is a trade-off between CBF quantification accuracy and precision when sacrificing ASL scan time for additional measurements or acquisition of ASL data at multiple time points, compared to the single-PLD consensus ASL experiment. Yet, accuracy and precision both impact the ability to compare absolute CBF estimates, both within a subject as well as between subjects. Therefore, the goal of the current study is to optimize the distribution of scan time for a five-minute protocol between averaging of ASL data versus performing supporting measurements.

## 6.2 Methods

In order to properly study absolute quantification accuracy, the underlying ground truth values of the parameters of interest need to be known. This requirement can be met in simulation experiments. First, the building blocks of the simulation experiment in the context of a PCASL experiment with supporting measurements are discussed. Subsequently, an overview of the entire simulation experiment is given, along with the chosen PCASL acquisition strategies. Next, the statistical analysis of the simulation results is described. Then, two slightly different versions of the main simulation experiment with potential significant implications are defined. Finally, the design of a real data experiment serving as a first validation is delineated in section 6.2.2.

### 6.2.1 Simulation experiment

#### PCASL data simulation

In this work, the noiseless PCASL difference signal  $\Delta S$  is simulated as a convolution of an arterial input function (AIF) [90, 91], described by Eq.(4.22), and an impulse residue function (IRF) [74], described by Eq.(4.17). A detailed description of this AIF and IRF can be found in Chapter 4. This AIF and IRF are considered as accurate representations of the underlying physiological process, thus resulting in highly accurate data simulation. The resulting PCASL difference signal  $\Delta S$ , acquired with a labeling duration  $\tau_j$  at a time point  $t_j = \tau_j + \text{PLD}_j$ , is then given by:

$$\Delta S(t_j, \tau_j) = nM_{0b}f[q(t) * c(t, \tau_j)]|_{t=t_j}, \quad (6.1)$$

with  $n = 2$  for single- or multi-PLD PCASL or  $n = K$  for time-encoded PCASL (te-PCASL), with  $K$  the order of the Hadamard matrix coupled to the te-PCASL acquisition scheme.

A vital part of realistic simulations is the incorporation of realistic noise. As label and control images are usually acquired at low spatial resolutions, resulting in high SNRs, it is reasonable to assume that their signal intensities are Gaussian distributed [93, 94]. The resulting difference data will also follow a Gaussian distribution. Therefore, Gaussian distributed zero-mean noise was added to the PCASL difference signals  $\Delta S$ . An appropriate standard deviation  $\sigma$  for such additive Gaussian noise was determined based on a temporal SNR (tSNR) for 3D GRASE background suppressed single-PLD PCASL data in gray matter (GM) reported in [47]. A single simulated noise disturbed PCASL difference data point  $\Delta M$  could thereby be defined as:

$$\Delta M(t_j, \tau_j) = \Delta S(t_j, \tau_j) + e_j, \quad (6.2)$$

with  $e_j \sim \mathcal{N}(0, \sigma)$  the additive noise.

### Simulation of supporting measurements

The labeling efficiency  $\alpha$  and the longitudinal relaxation time of blood  $T_{1b}$  can be estimated from MRI data acquired in separate experiments [68, 126]. In order to realistically simulate these supporting measurements, information about the estimation precision of the parameter of interest and the associated acquisition time is needed.

Chen et al. [126] proposed a sequence for measurement of the PCASL labeling efficiency  $\alpha$ . The stability of this measurement was studied by multiple repetitions of the experiment. With cardiac triggering, they found a measurement standard

deviation  $\sigma_\alpha$  of approximately 0.04. The scan time per repetition  $t_{\text{rep}}$  was approximately 7 seconds. Assuming the estimation of  $\alpha$  is unbiased and  $\alpha_i$  is the underlying ground truth labeling efficiency, the estimate  $\hat{\alpha}_i$  from data acquired during a certain scan time  $t_\alpha$  can be simulated as

$$\hat{\alpha}_i = \langle \{\hat{\alpha}_{i,p} \sim \mathcal{N}(\alpha_i, \sigma_\alpha)\}_{p=1}^P \rangle_p, \quad (6.3)$$

with  $\hat{\alpha}_{i,p}$  an estimate of  $\alpha_i$  obtained from a single repetition of the experiment,  $\langle \cdot \rangle$  the mean value of the enclosed subset, and  $P = \lfloor t_\alpha/t_{\text{rep}} \rfloor$  the number of repetitions of the experiment, with  $\lfloor \cdot \rfloor$  the floor operator.

The longitudinal relaxation time of arterial blood can be estimated in the carotid artery as proposed by Li et al. [68]. They report an intrasession coefficient of variation (CoV) of 1.1% for the estimation of arterial  $T_{1b}$  from  $T_1$ -weighted data acquired in a scan time  $t_{\text{ref}}$  of 69 seconds. For an average  $T_{1b}$  of 1.65s at 3T, the reported CoV results in an estimation standard deviation  $\sigma_{T_{1b}} = \text{CoV}_{T_{1b}} \cdot \langle T_{1b} \rangle = 0.018\text{s}$ . Assuming the estimation precision scales linearly with the total scan time, scaling the acquisition time with a factor  $R$  results in a scaling of the parameter estimation standard deviation with a factor  $1/\sqrt{R}$ . Therefore, the estimate of  $T_{1b}$  from  $T_1$ -weighted data obtained within a certain scan time  $t_{T_{1b}}$  and assumed to be unbiased can be simulated as

$$\hat{T}_{1b,i} \sim \mathcal{N} \left( T_{1b,i}, \frac{\sigma_{T_{1b}}}{\sqrt{t_{T_{1b}}/t_{\text{ref}}}} \right), \quad (6.4)$$

with  $\hat{T}_{1b,i}$  the estimate and  $T_{1b,i}$  the true blood longitudinal relaxation time.

The methods described in Eq.(6.3-6.4) were used to simulate supporting experiments for different scan durations with the appropriate associated estimation precision.

### Prior distributions of relevant parameters

As it is our goal to assess the CBF estimation over multiple perfusion states in the general population for certain five-minute protocols, the simulations should be repeated over a large number of perfusion states. The different perfusion processes representative of the general population can be approximated based upon literature by a prior distribution  $p(\boldsymbol{\theta})$  of each parameter that appears in the PCASL data simulation model as presented in section 6.2.1 (see Table 6.1). Choosing either a normal or a uniform distribution for a certain parameter was based on the spread of the reported GM values in the considered publications. In terms of this simulation experiment, a perfusion process is defined by a random draw  $\boldsymbol{\theta}_i$  from

the prior distribution  $p(\boldsymbol{\theta})$  defined in Table 6.1. The ground truth CBF was kept constant at  $f = 50\text{mL}/100\text{g}/\text{min}$  for all perfusion states to allow easy interpretation of the results. This has a negligible impact on the generality of the results, as the relative quantification accuracy and precision are approximately independent of the considered CBF value, due to the approximately linear relation between the CBF and the PCASL signal in the single-compartment quantification model [52]. The equilibrium blood magnetization  $M_{0b}$  was kept constant at unity.

	Parameter	Parameter distribution
	labeling efficiency $\alpha$ [ ]	$\mathcal{N}(0.80, 0.06)$ [65, 66]
	blood longitudinal relaxation time $T_{1b}$ [s]	$\mathcal{N}(1.65, 0.12)$ [67–69]
<b>IRF</b>	tissue longitudinal relaxation time $T_{1t}$ [s]	$\mathcal{N}(1.45, 0.14)$ [70]
	blood-to-tissue water transit time $\tau_{\text{trans}}$ [s]	$\mathcal{U}(0.30, 3.60)$ [75–77]
	arterial microvascular transit time $\tau_a$ [s]	$\mathcal{U}(0.30, 1.00)$ [78–80]
	tracer capillary distribution volume $V_c$ [mL/100g]	$\mathcal{U}(2.0, 4.0)$ [63, 81]
	tracer venous distribution volume $V_v$ [mL/100g]	$\mathcal{U}(1.0, 3.0)$ [82, 83]
<b>AIF</b>	arterial transit time $\Delta t$ [s]	$\mathcal{N}(0.82, 0.15)$ [35, 38]
	center-of-vessel travel time $t_0$ [s]	$\mathcal{N}(0.10, 0.01)$ [90, 91]

TABLE 6.1: The prior distribution  $p(\boldsymbol{\theta})$  of the model parameters  $\boldsymbol{\theta} = \{\alpha, T_{1b}, T_{1t}, \tau_{\text{trans}}, \tau_a, V_c, V_v, \Delta t, t_0\}$  in GM in the general population. A normal distribution is described as  $\mathcal{N}(\mu, \sigma)$  with  $\mu$  the mean and  $\sigma$  the standard deviation; a uniform distribution is described as  $\mathcal{U}(l, u)$  with  $l$  and  $u$  the lower and upper bound, respectively.

### Quantification model

After simulating PCASL data and supporting measurements for a certain sequence setting and perfusion state, quantification of CBF is the final step in the simulation experiment. For single-PLD PCASL experiments, the CBF  $f$  was calculated as

$$f = \frac{\Delta M \exp(\text{PLD}/T_{1b})}{2\alpha T_{1b} M_{0b} (1 - \exp(-\tau/T_{1b}))}, \quad (6.5)$$

with  $\Delta M$  the mean of the single-PLD PCASL difference data. For multi-PLD PCASL or te-PCASL experiments, the CBF  $f$  and ATT  $\Delta t$  were quantified with a

nonlinear least-squares estimator by fitting the Buxton single-compartment model [52]

$$g(t) = \begin{cases} 0 & 0 < t < \Delta t \\ n\alpha M_{0b} f T_{1t} \exp(-\Delta t/T_{1b}) \left(1 - \exp(-\frac{t-\Delta t}{T_{1t}})\right) & \Delta t < t < \tau + \Delta t \\ n\alpha M_{0b} f T_{1t} \exp(-\Delta t/T_{1b}) \exp(-\frac{t-\tau-\Delta t}{T_{1t}}) (1 - \exp(-\tau/T_{1t})) & t > \tau + \Delta t \end{cases} \quad (6.6)$$

to the multi-time-point PCASL data. The unit of each estimated CBF value was converted from mL/g/s to mL/100g/min by multiplication with a factor of 6000.

If scan time was assigned to the additional experiments,  $\alpha$  and  $T_{1b}$  in Eq.(6.5) and Eq.(6.6) were set to the estimated values as defined in Eq.(6.3) and Eq.(6.4), respectively, otherwise standard literature values were assumed ( $\alpha = 0.8$  and  $T_{1b} = 1.65\text{s}$ ). Measurement of  $M_{0b}$  was simulated in each quantification by randomly selecting a value from a normal distribution  $\mathcal{N}(1.00, 0.09)$ , which represents the variability in different measurement methods for  $M_{0b}$  [132]. For multi-time-point PCASL data, the tissue longitudinal relaxation time  $T_{1t}$  was fixed at 1.45s [70], compatible with a 3T scanner.

### Overview of the entire simulation experiment

The building blocks of the simulation experiment, discussed in section 6.2.1, are summarized in a flowchart in Figure 6.1. The framework starts with the selection of a ground truth perfusion process, simulates the relevant data and measurements, and ends with the quantification of the CBF. The entire simulation experiment was formed by repeating the steps in this framework on three distinct levels.

Firstly, multiple five-minute protocols were examined. On the one hand, distribution of the five-minute scan time  $T_{\text{tot}}$  between acquisition of PCASL data and supporting scans was varied. The percentages of scan time assigned to measurement of  $\alpha$  and  $T_{1b}$  were increased from 0 up to 40% of  $T_{\text{tot}}$  in increments of 2%, including all possible combinations. On the other hand, three acquisition strategies were considered for PCASL: single-PLD, equidistant sequential multi-PLD and a free-lunch version of te-PCASL (te-FL PCASL). Details of the PCASL acquisition settings are summarized in Table 6.2. Each of these PCASL sampling protocols were repeated maximally within the scan time  $T_{\text{tot}} - t_{\alpha} - t_{T_{1b}}$  to obtain multiple averages. This process is straightforward for single-PLD and te-FL PCASL: fit as many repeats of label-control pairs or the Hadamard acquisition scheme within the available scan time. For multi-PLD, after repeating the entire

imaging sequence maximally, the remaining scan time was used to acquire data points at a randomized subset of the PLDs.

Secondly, for each of these five-minute protocols, the simulation framework was run for 1000 ground truth perfusion states  $\theta_i$  randomly drawn from the prior distribution  $p(\theta)$  as defined in Table 6.1.

Thirdly, for each five-minute experiment and for each ground truth perfusion state, 100 repeats of data simulation and quantification were performed with different noise realizations. In this setting, different noise realizations are equivalent to repeated simulation of PCASL data  $\{\Delta M(t_j, \tau_j)\}_{j=1}^N$  and estimates  $\hat{\alpha}_i$  and  $\hat{T}_{1b,i}$ .

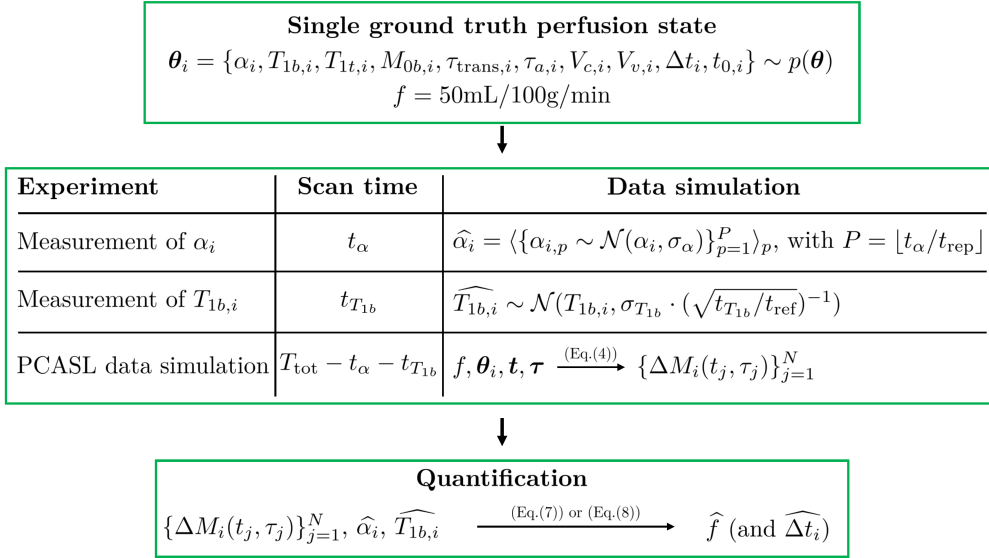


FIGURE 6.1: Flowchart of one run of the simulation experiment for a certain five-minute protocol and a certain ground truth perfusion state. The amount of PCASL difference data points  $N$  depends on the available scan time  $T_{\text{tot}} - t_\alpha - t_{T_{1b}}$  and the acquisition strategy (single-PLD, multi-PLD or time-encoded).

## 6.2. Methods

Acquisition strategy	Labeling duration [s]	PLD [s]
single-PLD	1.8	1.8
equidistant multi-PLD	1.8	0.2, 0.4, 0.6, 0.8, 1.0, 1.2, 1.4, 1.6, 1.8, 2.0
free-lunch time-encoded	1.8, 0.175, 0.175, 0.175, 0.175, 0.175, 0.175, 0.175, 0.175	1.8, 1.625, 1.45, 1.275, 1.1, 0.925, 0.75, 0.575, 0.4, 0.225, 0.05

TABLE 6.2: Details of the PCASL acquisition strategies used in the simulation experiment.

### Statistical analysis

The goal of the current study is to find the five-minute protocol that attains the lowest level of CBF estimation variability across all considered confounding sources of variation, namely differences in the underlying perfusion states and random noise in the data. For a certain five-minute protocol, multiple runs of data simulation, as described in Figure 6.1, will result in data sets from different perfusion states  $\theta_i$  and with varying random noise, yet with the same underlying CBF value. A five-minute protocol is then considered to have a low CBF estimation variability if the spread in the entire pool of obtained CBF estimates is low. A suitable metric to describe this estimation variability is the standard deviation  $s$  of the set of CBF estimates quantified from the  $Q = 100$  repetitions of noisy data sets from each of the  $P = 1000$  considered perfusion processes, i.e. the standard deviation over 100.000 CBF estimations:

$$s = \sqrt{\frac{1}{P + Q - 1} \sum_{i=1}^P \sum_{k=1}^Q (\hat{f}_{i,k} - \bar{f})^2}, \quad (6.7)$$

with  $\bar{f}$  the sample mean.

It is important to stress that the standard deviation of such a set of CBF estimates, described by Eq.(6.7), captures CBF estimation variability of a certain protocol on a population level. Statistical measures describing such a set of estimates, like its standard deviation and mean, need to be differentiated from statistical concepts that describe the estimator used for CBF quantification, namely the accuracy (or bias) and precision. Indeed, when referring to the bias or precision of an estimator of CBF, a single underlying perfusion state (i.e., fixed  $\alpha$ ,  $T_{1b}$ ,  $T_{1t}$  and  $\Delta t$ ) is assumed. This difference in terminology is followed rigorously in what follows.

### Simulation sub-studies

In the main simulation experiment, a more realistic, more complicated model is used for data simulation than for quantification. While this option was chosen in order to match a real data experiment as closely as possible, it adds a potential source of bias to the quantification. Therefore, the entire simulation experiment described in section 6.2.1 was repeated by using the single-compartment model (Eq.(6.6)) for data simulation as well as quantification. The resulting CBF estimate distributions were compared to the ones from the main simulation experiment in order to separate the contribution of supporting measurements to a reduced CBF estimation variability from potential bias caused by an oversimplified quantification.

Simulation of the supporting measurements, as described in subsection 6.2.1, assumes estimation of the respective parameters is unbiased. As in reality such supporting measurements could be biased, the entire simulation experiment was also repeated assuming a consistent relative overestimating bias of 5% in both supporting measurements. With this sub-experiment, it was examined whether such a bias has a detrimental effect on potential benefits of the supporting measurements by comparing the CBF estimate distributions linked to the unbiased and biased versions of the supporting measurements. The choice for overestimation instead of underestimation was arbitrary, as there is no reason to expect either option is more likely than the other.

### 6.2.2 Real data validation experiment

As a first validation of the simulation results, a real data study was designed that allowed for a comparison between CBF quantification using either the population average  $T_{1b}$  value or individually estimated  $T_{1b}$  values. From a population study with healthy volunteers in which single-PLD PCASL data (scanner: Siemens 3.0 T, readout: 3D GRASE, spatial resolution =  $4 \times 4 \times 5$  mm<sup>3</sup>, number of segments for whole-brain coverage = 2, labeling duration = 1.8 s, PLD = 1.8 s, number of averages = 4, TR = 5 s, total acquisition time = 80 s) and blood samples prior to scanning were acquired, five subjects with a low hematocrit (Hct= $0.345 \pm 0.011$ ) and five subjects with a high hematocrit (Hct= $0.464 \pm 0.015$ ) were selected. From each hematocrit measurement, the  $T_1$  of blood was estimated [67]. Furthermore, for each subject, an equilibrium magnetization image ( $M_{0t}$ ) (sequence: 3D GRASE, spatial resolution =  $4 \times 4 \times 5$  mm<sup>3</sup>, number of segments for whole brain coverage = 2, TR = 5 s, TE = 18 ms), for absolute quantification of the CBF, and a high-resolution anatomical image (sequence: MPRAGE, spatial resolution =  $1 \times 1 \times 1$

## 6.2. Methods

---

mm<sup>3</sup>, TR = 2250 ms, TE = 4 ms, TI = 900 ms), for tissue segmentation, were acquired.

The data for each subject was analyzed as follows. First, all relevant MRI data (label images, control images, and the proton density ‘ $M_{0t}$ ’ image) were mutually registered. Second, an averaged perfusion-weighted image was obtained by pairwise subtraction of label-control pairs and subsequent averaging of the resulting difference images. Third, CBF quantification was performed twice, once using the population average  $T_{1b}$  value, and once using the individually estimated  $T_{1b}$  value. Finally, CBF values from gray matter voxels were isolated by downsampling and coregistering a GM mask to the CBF maps, following the procedure described in [133]. The GM mask was obtained from a high-resolution anatomical image by means of multilevel image thresholding [122]. Potential differences in CBF estimation variability between using the recommended population average  $T_{1b}$  value and using individually estimated  $T_{1b}$  values were assessed by comparing the standard deviations of the set of GM CBF estimates, pooled over all subjects, for both quantification methods.

As this real data experiment is a simplified version of the main simulation setup, a modified version of the simulation experiment mimicking the real data protocol was also run. For this purpose, the framework of the simulation experiment, described in section 6.2.1, was slightly adapted: instead of generating 1000 perfusion states with randomized  $T_{1b}$  values and a fixed CBF, 1000 perfusion states were generated with randomized CBF values for each of the 10 individually estimated  $T_{1b}$  values from the real data experiment; random CBF values were drawn from a normal distribution of gray matter CBF values (i.e.,  $\mathcal{N}(54, 11)$  mL/100g/min) reflecting reported literature ranges [64]; the set of 1000 perfusion states per  $T_{1b}$  value simulates the underlying perfusion variations over different parts of the brain of an individual. Single-PLD PCASL data was simulated according to the real data acquisition protocol. Subsequently, CBF was quantified from the simulation data twice for each perfusion state: once using the fixed  $T_{1b}$  value of 1.65 s, which is the recommended population average for  $T_{1b}$ , and once using the appropriate individual  $T_{1b}$  value. The distributions of the CBF estimates resulting from the real data experiment and those of the modified simulation experiment were compared in terms of the overall CBF estimation variability, allowing for an assessment of the validity of the simulation experiment.

## 6.3 Results

### 6.3.1 Simulation experiment

Figure 6.2 shows the standard deviation  $s$  of the CBF estimates as defined in section 6.2.1 for all considered five-minute protocols. The value in the top left of Figure 2a, highlighted in black, depicts the CBF estimation variability in the recommended single-PLD PCASL implementation when separate estimates for  $\alpha$  and  $T_{1b}$  are not made. It serves as a starting point reflecting how differences in perfusion states and noise within and between subjects affect CBF estimation. If the standard deviation  $s$ , defined in section 2.3, is a measure for the absolute variability of CBF estimation, the relative variability can be defined as the ratio between  $s$  and the underlying ground truth CBF value. For single-PLD PCASL without supporting measurements, a relative variability of 12.2% was found. While there is no literature study that matches one-to-one with this simulation experiment, the between-subject standard deviation reported in the QUASAR reproducibility study [35] is closely related to the CBF estimation variability reported in this simulation study. The ratio of the reported average between-subject standard deviation and average mean gray matter CBF value in [35] is equal to 11.6%, which shows that the relative variability reported above reflects reality. The standard deviations shown in the top left corners of Figure 2b and 2c represent the CBF estimation variability for the te-FL and multi-PLD PCASL protocol without supporting measurements, respectively. The relative variabilities of these protocols (12.6% and 12.2%, respectively) are comparable to the one of their single-PLD counterpart.

For each ASL acquisition strategy, the standard deviation  $s$  reduced when allocating scan time for supporting measurements. The protocols with the lowest standard deviation are highlighted in red in Figure 6.2 for each ASL acquisition type. For these protocols, a relative variability of 8.6%, 8.0% and 7.2% was found for single-PLD, te-FL and multi-PLD PCASL, respectively. Compared to the result of the single-PLD protocol without supporting measurements shown above, this implies a reduction in relative variability of 26%, 33% and 42% for single-PLD, te-FL and multi-PLD PCASL, respectively. Note that the standard deviation landscapes shown in Figure 6.2 are relatively flat. In other words, for all three ASL acquisition strategies, there is a rather wide range of scan time distributions that result in a similar CBF estimation variability as for the protocols highlighted in red.

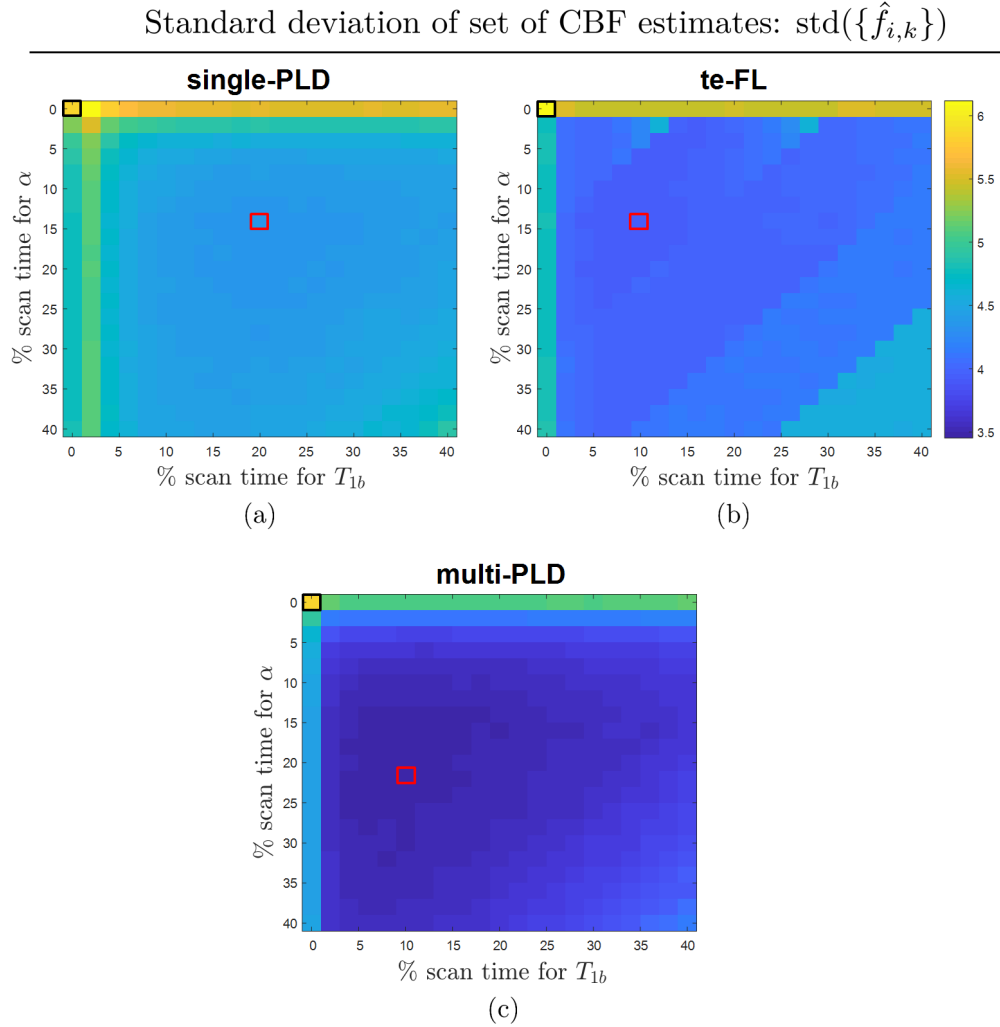


FIGURE 6.2: The standard deviation of the set of CBF estimates  $\{\hat{f}_{i,k}\}_{i=1, k=1}^{1000,100}$  for five-minute combinations of a (a) single-PLD (b) free-lunch time-encoded (te-FL) and (c) equidistant multi-PLD PCASL experiment with supporting experiments to estimate  $\alpha$  and  $T_{1b}$ . The standard deviations linked to the single-PLD, te-FL and multi-PLD protocols without supporting measurements are highlighted with black boxes, while the protocols with the lowest standard deviation in each ASL modality are highlighted with a red box.

While the results in Figure 6.2 describe the main statistical entity of interest, i.e. the CBF estimation variability, it provides no information about the overall mean of the set of CBF estimates of each protocol. Therefore, the distribution of the set of CBF estimates is showcased in Figure 6.3 for the six protocols highlighted in Figure 6.2.

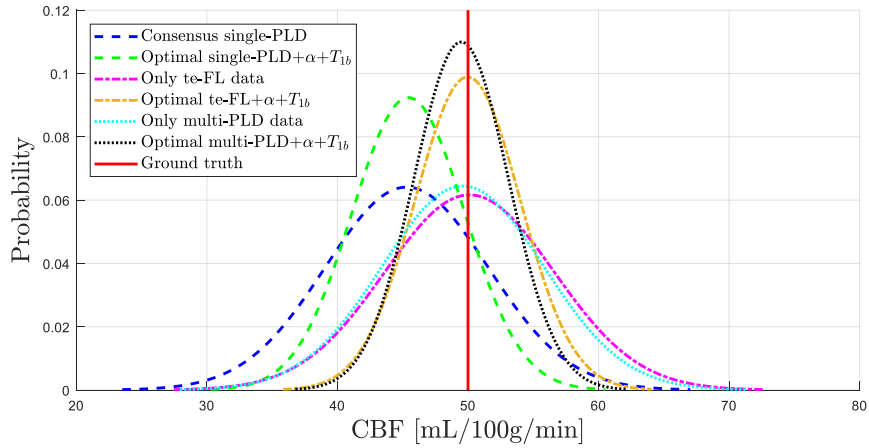


FIGURE 6.3: The normalized distribution of CBF estimates from the six protocols highlighted in Figure 6.2: the protocol with only single-PLD PCASL data, only te-FL PCASL data, and only multi-PLD PCASL data, as well as the optimal protocol for each considered ASL modality.

Each standard deviation of the set of CBF estimates for each protocol shown in Figure 6.2 is the combined result of bias from different perfusion states and noise in the data. Each protocol suffers from both effects to a different degree, which is shown in more detail in Figure 6.4. Figure 6.4a visualizes the contrast between only acquiring ASL data and combining it with the measurement of  $\alpha$  and  $T_{1b}$  by demonstrating the CBF estimation bias and precision for different underlying physiological perfusion states. It shows the trade-off when sacrificing ASL scan time; a reduced spread in estimation bias comes at a cost of lower individual estimation precision. When the decision is made to perform supporting measurements, there is again a trade-off between improving the estimation of  $\alpha$  and  $T_{1b}$  and maintaining a sufficient SNR of the PCASL data (Figure 3b). On the one hand, when a very small percentage of time is used for supporting measurements, estimation of  $\alpha$  and  $T_{1b}$  is very imprecise. On the other hand, when supporting measurements take up most of the scan time, the SNR of the ASL data is very

### 6.3. Results

low. Both extremes lead to lower CBF estimation precision, which is ultimately reflected in a higher variability. The optimal distribution of scan time lies in between these extreme cases.

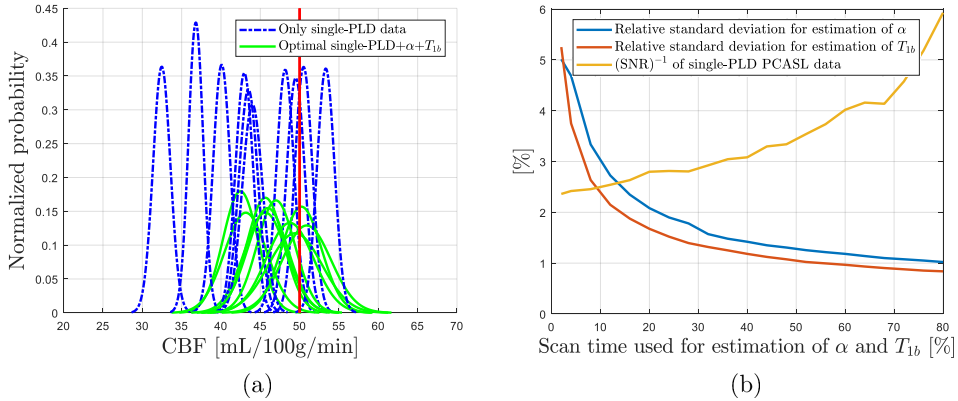


FIGURE 6.4: (a) A visualization of the trade-off between the estimation precision on a voxel level and the spread in estimation bias on a population level. Each normalized distribution represents the fit to the histogram of CBF estimates originating from 100 data simulation repeats for a specific ground truth perfusion state  $\theta_i$ . These fits were performed for estimates from 10 of the 1000 considered ground truth perfusion states, for the case of only single-PLD data and the combination of single-PLD data acquisition with supporting measurements with the lowest variability of CBF estimation in Figure 6.2a. (b) The average relative standard deviation for estimating  $\alpha$  and  $T_{1b}$  is contrasted with the average inverse of the single-PLD PCASL data SNR for the protocols represented on the diagonal in Figure 6.2a. For these protocols, the scan times for both supporting measurements are equal. The scan time shown on the  $x$ -axis in (b) is the sum of both scan times. The SNR of single-PLD PCASL data is defined as the ratio of the mean and standard deviation of the set of difference data repeats, where the number of repeats depends on the allocated ASL scan time.

The results of the simulation sub-studies, defined in section 6.2.1, are summarized in Figure 6.5. In Figure 6.5a, CBF estimate distributions are shown when using the same model for data simulation as for quantification in a comparison to

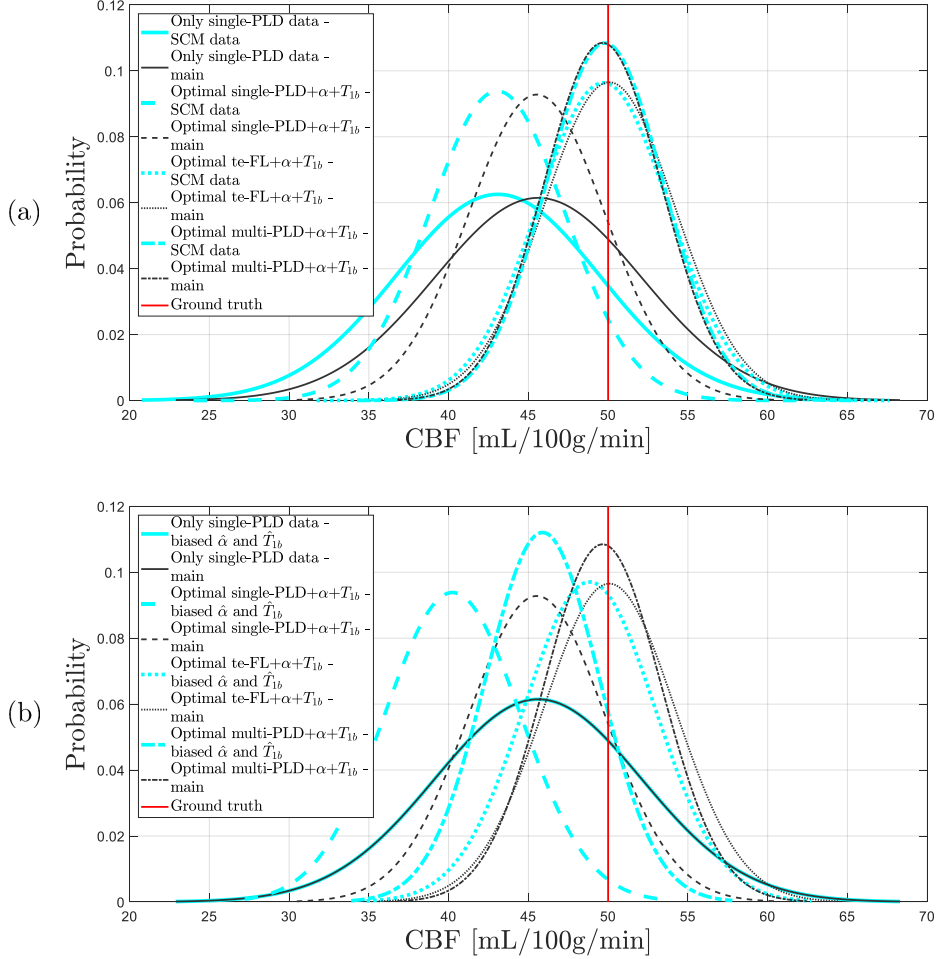


FIGURE 6.5: The black curves in subfigures (a) and (b) represent the normalized distributions of CBF estimates obtained from the main implementation of the simulation experiment with the realistic data simulation model. The cyan curves in subfigure (a) represent CBF estimate distributions for the same protocols, yet for data simulation using the SCM as defined in Eq.(6.6). In subfigure (b), the cyan curves represent CBF estimate distributions for the same protocols with an offset bias of 5% overestimation of both  $\alpha$  and  $T_{1b}$ .

the distributions obtained from the main implementation of the simulation experiment. In terms of CBF estimation variability, a difference in the complexity of

data simulation clearly has no significant effect. In terms of a bias offset, there is only a significant difference between both implementations of the simulation experiment for single-PLD protocols. The results of the second sub-experiment are summarized in Figure 6.5b. Having an offset bias in the estimation of  $\alpha$  and  $T_{1b}$  from the supporting experiments has no effect on the CBF estimation variability compared to having unbiased supporting measurements. It only causes a fixed global bias in CBF estimation, consistent with the relation between  $\alpha$  and  $T_{1b}$  on the one hand and CBF on the other hand in the quantification model, independent of the underlying perfusion state or noise in the data.

#### 6.3.2 Real data validation experiment

The distribution of the set of estimated CBF values, pooled over the considered population, for both quantification strategies is shown in Figure 6.6a. On a population level, there is a lower CBF estimation variability when using individual  $T_{1b}$  estimates, indicated by the standard deviation of the set of CBF estimates dropping from 21.0 mL/100g/min when using a fixed  $T_{1b}$  value to 17.6 mL/100g/min when using individually measured  $T_{1b}$  values. Note that, in contrast to the main simulation experiment, there are no ground truth CBF values to compare the estimated CBF values to and that those underlying ground truth CBF values differ in each considered voxel (i.e., not fixed to 50mL/100g/min). Despite that, the standard deviation of the set of CBF estimates is still indicative of CBF estimation variability.

In Figure 6.6b, the CBF estimates are shown resulting from the modified simulation experiment, which mimics the real data experiment. There is a similar relative reduction in estimation variability. The absolute estimation variability is higher in the real data experiment, which is likely caused by partial volume effects, resulting in very low CBF estimates, and data outliers or remaining macrovascular signal, resulting in CBF overestimation. Such effects are not present in the simulation experiment. Both in real data and in simulations, there is a difference in the mean CBF value for both quantification methods. This can be attributed to the difference between the recommended quantification value for  $T_{1b}$  (i.e., 1.65 s) and the mean of the estimated  $T_{1b}$  values in this specific population (i.e., 1.75 s). Overall, the real data and simulation results, shown in Figure 6.6, clearly align.

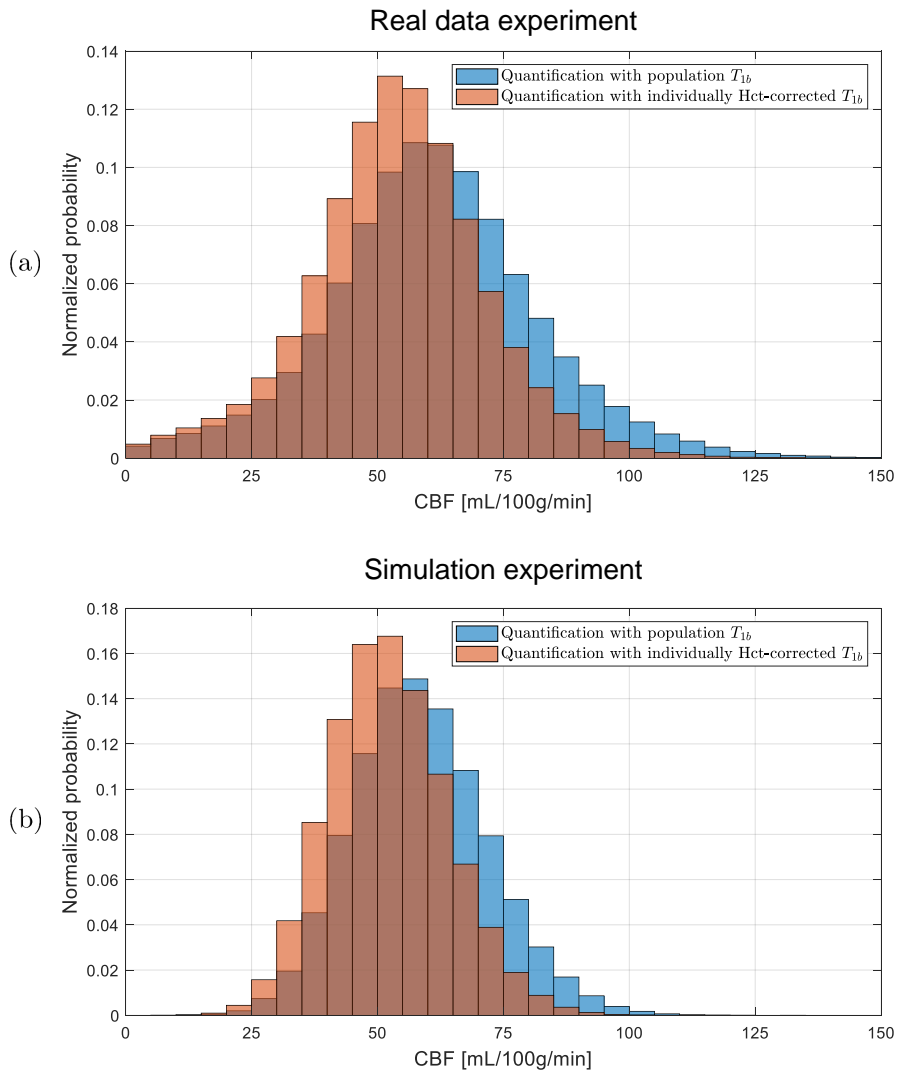


FIGURE 6.6: (a) Normalized distribution of the set of estimated GM CBF values, pooled over the considered population of 10 healthy volunteers, for quantification with a single population average for blood  $T_1$  (blue) and with individual blood  $T_1$  values (orange), estimated from a hematocrit measurement. (b) Normalized distribution of the set of estimated GM CBF values for the simulation experiment that closely mimicked the real data experiment.

## 6.4 Discussion and Conclusions

In this work, a range of five-minute MRI protocols was examined with respect to the CBF estimation variability for a multitude of physiological situations, as would be expected to be found in the general population. It was shown that there is a clear benefit in sacrificing some averages of PCASL for supporting measurements of the labeling efficiency  $\alpha$  and the longitudinal relaxation time of blood  $T_{1b}$ . Combining these additional experiments with multi-delay PCASL modalities instead of a single-PLD PCASL scheme further reduced the estimation variability. The results presented above and discussed in this section are for a total scan time of five minutes. The simulation experiment was repeated for a total scan time of two and ten minutes (results not shown), which resulted in the same general trends as described above regarding optimal scan time distribution and relative differences in CBF estimation variability between the three considered PCASL acquisition strategies.

The variability measures visualized in Figure 6.2 show that, compared to only acquiring PCASL data, it is beneficial to sacrifice part of the PCASL scan time for the measurement of  $\alpha$  and  $T_{1b}$ . While optimal protocols were highlighted for each ASL acquisition strategy, many other protocols with different scan time distributions show comparable variabilities of CBF estimation. It is only when a supporting measurement is not performed or when very few ASL data is acquired that the CBF estimation variability significantly increases. The standard deviation landscape for the te-FL PCASL acquisition strategy does however show some different behavior in the form of discrete jumps. This is mainly related to the temporal footprint of data acquisition of time-encoded ASL, which is bound to repetitions of the entire set of Hadamard-encoded images, while single- and multi-PLD PCASL allow for more fine steps in allocating ASL scan time.

Comparing the results for the protocols without supporting measurements to the ones with supporting measurements for all three considered PCASL sampling strategies in Figure 6.3 allows to clearly isolate the benefit of using a percentage of the total scan time for estimation of  $\alpha$  and  $T_{1b}$ . It is vital to emphasize that this benefit occurs on a population level. Estimating  $\alpha$  and  $T_{1b}$ , compared to fixing it to a population average, reduces CBF estimation bias. On a population level, where  $\alpha$  and  $T_{1b}$  can vary considerably, this leads to a reduced spread in CBF estimation bias (see Figure 6.4a). As a result, the CBF estimation variability on a population level decreases (see Figure 6.3). In short, reducing bias by performing the supporting measurements reduces the standard deviation of the total set of CBF estimates obtained from a large population, which might have seemed paradoxical at first. The priorities are different when considering a single individual.

In a single diagnostic perfusion scan,  $T_{1b}$  is constant and  $\alpha$  should not vary too much between different feeding arteries; estimating  $\alpha$  and  $T_{1b}$  will only result in a global scaling of the CBF map, which for many diagnostic scans is not worth the accompanying loss in CBF estimation precision.

The optimal combinations of both multi-delay PCASL modalities with supporting measurements outperform the optimal single-PLD experiment in terms of CBF estimation variability (Fig.6.3). In fact, this is the case for most five-minute protocols (Fig.6.2). There are two main reasons. First, estimating the ATT alongside the CBF eliminates a source of bias, as not accounting for the ATT is known to lead to under- or overestimation. Second, for the considered prior distribution of the ATTs (see Table 6.1), both multi-delay PCASL acquisition strategies sample the perfusion signal more optimally in terms of precise parameter estimation compared to the single-PLD PCASL scheme. This statement is trivial for the te-FL PCASL acquisition strategy, as the waiting period of the single-PLD sequence is used to obtain extra data without affecting the temporal SNR of the data linked to the long labeling, i.e. the perfusion block [59]. For the equidistant multi-PLD sequence, the spread in PLDs guarantees sampling of the PCASL signal around its peak for most of the ATTs in the prior distribution. On the other hand, the PLD of the recommended single-PLD experiment is chosen to be longer than most ATTs that can be expected in the general population. Therefore, this PLD is much longer than the majority of ATTs from the considered distribution (see Table 6.1), resulting in an unnecessary large signal loss due to  $T_1$  decay. Note that these statements are specifically in reference to CBF estimation variability. The qualitative perfusion map for a single subject obtained from the single-PLD or from the first block of the te-FL PCASL experiment will still have a higher SNR than the averaged difference maps obtained only from the longest PLDs of the multi-PLD PCASL experiment, due to the difference in the number of repetitions.

Apart from a lower CBF estimation variability, quantification in multi-delay PCASL methods clearly results in more accurate estimation of CBF on average compared to single-delay PCASL protocols (Fig.6.3). This is caused by the difference in quantification model (Eq.(6.5-6.6)). In multi-delay methods, the ATT is taken into account and part of the longitudinal relaxation is assumed to be governed by the  $T_1$  of tissue. Of course, this increased accuracy is a result of the way the simulation data was generated, which resembled the multi-delay quantification model more than the single-delay model (see also the study limitations). Furthermore, it is noteworthy that the mean of the set of CBF estimates for the optimal multi-delay protocols almost coincides with the true underlying CBF value (Fig.6.3). This is not trivial, as PCASL data was simulated with a complex multi-compartment perfusion model that includes dispersion effects, while CBF

was quantified with a single-compartment model. It is a clear indication of the value of the single-compartment model (Eq.(6.6)) as a valid approximation of more complex models with multiple compartments and dispersion effects.

Two sub-studies of the main implementation of the simulation experiment were performed. First, PCASL data were simulated with the same model as used for quantification. As using this model for data simulation only results in a bias offset in quantification for the single-PLD experiment (Figure 6.5a), reported differences in the CBF estimation variability between different protocols obtained from the main implementation of the simulation experiment can be attributed with confidence to the supporting measurements. In terms of bias offset, it is not surprising that there is no significant difference between both implementations of the simulation experiment for the multi-PLD and te-FL protocol, as the main implementation of the experiment with a mismatch between simulation model and quantification model already hardly showed a bias offset compared to the underlying ground truth CBF value. Remarkably, the single-PLD quantification model (Eq.(6.5)) estimates CBF more accurately when data was simulated with the more complicated model, compared to the single-compartment model. Second, when an offset bias is introduced in the simulated supporting measurements, it results in an offset bias in the set of CBF estimates (Figure 6.5b). As there is no impact on the CBF estimation variability compared to unbiased supporting measurements, incorporating slightly biased supporting measurements would still be beneficial compared to only acquiring ASL data in terms of how comparable CBF estimates are between different subjects and/or different scan sessions.

The real data validation experiment showed a first indication of the potential benefit of supporting measurements in terms of decreasing the CBF estimation variability. However, it has multiple limitations compared to the main simulation experiments of this work. First, only the effect of  $T_{1b}$  measurements was studied, while simulation results indicate that measuring both  $T_{1b}$  and  $\alpha$  will reduce CBF estimation variability more drastically (see Figure 6.2a). Second, only single-PLD data was considered, while combining multi-time-point PCASL data with supporting measurements is expected to be more beneficial (see Figure 6.3). Third,  $T_{1b}$  was only estimated once in each subject. Repeated estimation of the  $T_1$  of blood and the labeling efficiency from additional scans and repeated PCASL data acquisition would allow one to study the interplay of sacrificing ASL scan time and measurement variability within a fixed total acquisition time, as was studied in the main simulation experiments. Nonetheless, the close agreement between the results of the real data experiment and those of the simulation sub-experiment, mimicking the real data experiment, supports the validity of the simulation experiments performed in this work.

It is interesting to note that, in the quantification model, the equilibrium magnetization of blood  $M_{0b}$  plays a similar role as the labeling efficiency  $\alpha$ , as they both appear as a multiplicative factor. Contrary to  $\alpha$ ,  $M_{0b}$  is always estimated from supporting experiments in conventional ASL experiments. There are many options to estimate  $M_{0b}$ , as is discussed in a recent comparative study of Pinto et al. [134]. Regardless of which option is chosen to approximate  $M_{0b}$ , it can be expected that potential inaccuracies and limited precision of  $M_{0b}$  estimation will affect the accuracy and precision of CBF estimation in a similar way as estimating  $\alpha$  would.

There are several limitations to the simulation experiment performed in this study. First, the prior distributions of the respective parameters in the perfusion model used for data simulation play a central role. Each prior distribution represents the variability of a certain parameter in the considered population. Therefore, the importance of estimating  $\alpha$ ,  $T_{1b}$  and  $\Delta t$  is directly related to their underlying prior distribution. In this study, emphasis was put on carefully selecting prior distributions that match reported literature values in the general population, in order to maximize the confidence to extrapolate these results from simulation to real data. Optimal scan time distributions will be different when the underlying prior distributions of relevant parameters would be different, for example when more robust tagging techniques become mainstream or when dealing with specific patient populations. Note that in such cases, this simulation experiment should be rerun with adjusted parameter prior distributions to indicate the potential use of supporting measurements. However, it can still be expected that the general conclusion that some time should be attributed to support measurements will remain valid. Second, any data simulation model, regardless of its complexity, is an imperfect approximation of the underlying biophysical PCASL perfusion process. Nevertheless, in this study, a simulation model was used with the aspiration to match the biophysical reality as closely as possible. Ideally, these results need in vivo validation. Note that this would require a large subject group to sufficiently capture population variability. Furthermore, the analysis of the results would be challenging due to a lack of knowledge about the underlying ground truth parameter values. Third, the presented results are dependent on the parameter estimation method. In this study, parameter estimation from multi-delay PCASL data was performed with a nonlinear least squares estimator. An alternative to this strategy is Bayesian inference [135–137], which would also allow for the estimation of extra parameters with limited prior uncertainty alongside the CBF and ATT. However, it should be stressed that  $T_{1b}$  and  $\alpha$  are not good candidates for estimation alongside the perfusion parameters. The  $T_1$  of arterial blood can be considered as a global constant parameter throughout the brain. Estimating it

separately in every voxel will result in local differences in  $T_{1b}$  that have no clear physical meaning. Regarding the labeling efficiency, it is impossible to estimate it alongside the CBF as they are not independently identifiable in the quantification model. Finally, the three ASL acquisition strategies selected in this study were selected pragmatically. The recommended single-PLD implementation served as an evident benchmark. The time-encoded free-lunch PCASL protocol is a simple extension of the single-PLD experiment and an equidistant version of the multi-PLD PCASL experiment is the conventional implementation in most multi-delay ASL studies. Estimation precision could be further increased for each of these three ASL modalities by means of experiment design optimization using Cramér-Rao lower bound theory [107]. Nonetheless, the fact that it proves to be beneficial to sacrifice part of the ASL scan time for supporting measurements in three entirely different ASL sampling strategies (see Figure 6.3) strongly suggests that the merit of these supporting measurements is independent of the chosen sampling strategy. Indeed, it was shown that reducing estimation bias by means of supporting measurements is the driving force behind reducing the CBF estimation variability on a population level (see Figure 6.4a).

In conclusion, we demonstrated the benefit of sacrificing part of the ASL scan time for supporting measurements to estimate the labeling efficiency and the blood longitudinal relaxation time in terms of CBF estimation variability by means of a simulation experiment. When absolute quantification of CBF from PCASL data is required, such supporting experiments turn out to be indispensable. Furthermore, for the considered population statistics, multi-time-point PCASL methods seem to further improve CBF estimation reliability compared to the recommended single-PLD PCASL acquisition strategy.



## Chapter 7

# Super-resolution reconstruction strategies for ASL

The previous two contributions revolved around the quantification model and which parameters should be estimated in the light of their known variability. It was shown that those decisions impact the accuracy and precision of CBF estimation. Apart from that, it was also explored through experiment design how the PCASL acquisition settings impact the precision of perfusion parameter estimation in the first contribution (Chapter 5). In this contribution, the effects of the acquisition strategy on perfusion parameter estimation are further explored. More specifically, the potential of combining super-resolution reconstruction techniques with ASL is studied.

### 7.1 Introduction

In the clinical recommendations for ASL, segmented 3D readout schemes are preferred over single-shot 2D multi-slice variants [1]. There are two main reasons. Firstly, the SNR of the ASL signal is expected to be higher in 3D readout. In any case, 3D readout has an intrinsically higher SNR than 2D readout as the whole volume is excited with a single excitation [24]. Furthermore, specifically in ASL, 3D readout allows for uniform background suppression, which increases the SNR of the ASL signal by diminishing the physiological noise component originating from the background signal present in both the label and the control image [41, 44, 45, 47]. Indeed, as there is only one excitation pulse in 3D readout, inversion pulses can be timed so that optimal background suppression is attained for the entire segment. In 2D multi-slice readout, there is an excitation pulse for every slice. Therefore, background suppression can only be maximal in one slice. Secondly, the total readout time for whole-brain coverage, assuming the same field-of-view (FOV) and the same voxel size, is significantly shorter for 3D readout compared to 2D

multi-slice readout [47]. Apart from scan time considerations, a long total readout time has an additional downside in 2D readout: the effective PLD increases for subsequent slices. Assuming a sufficiently long base PLD as recommended, this implies that the ASL signal decreases in subsequent slices due to longitudinal relaxation. Therefore, ultimately, this will come at a cost of SNR in later acquired slices.

Despite the advantages of 3D readout, 2D multi-slice readout still has some significant advantages. The acquisition of a typical segment in 3D gradient-and-spin-echo (GRASE) readout, at the recommended resolution for PCASL imaging, takes 300-400 ms, while a single slice in 2D echo-planar-imaging (EPI) has a readout around 50 ms [43, 47]. The faster acquisition per excitation makes 2D multi-slice readout less susceptible for artifacts caused by motion during readout [1] and it allows the use of ASL for fMRI experiments (when the labeling duration and delay are not too long) [138–140]. 3D readout is also susceptible to  $T_2$ -related signal changes over subsequent echoes which results in through-plane blurring [1]. It can therefore be argued that 2D acquisition still has its place in ASL. Are there ways to suppress some of the disadvantages listed in the previous paragraph? In other words, are there ways to perform whole-brain PCASL imaging with 2D multi-slice readout methods, while circumventing the typical low-SNR problems due to increasing effective PLDs and fading background suppression in later-acquired slices? Performing super-resolution reconstruction (SRR) on low-resolution ASL images is an interesting candidate.

The goal of super-resolution reconstruction (SRR) is to restore a high-resolution (HR) image from a set of 2D multi-slice images with a low through-plane resolution and with varying slice encoding directions [141–143]. Images directly acquired at a high resolution or parameter maps estimated from images directly acquired at a high resolution are bound to a conventional trade-off between SNR, spatial resolution and scan time. In structural MRI, relaxometry and diffusion MRI, it has been shown that super-resolution (SR) reconstructed HR images or HR parameter maps can improve on this trade-off [144–147]. For example, for a fixed spatial resolution and scan time, an SR reconstructed HR image would have a higher SNR than an image directly acquired at that same high resolution (with the same readout method). A substantial part of the success of SRR in the aforementioned MRI modalities is due to the fact that lowering the spatial resolution in readout significantly reduces the scan time per acquired 3D image, allowing to acquire much more images within a certain unit of scan time compared to the acquisition of HR images. That effect will be limited in ASL, as the labeling duration and the PLD take up most of the time of the sequence.

Fortunately, there are two other inherent advantages to the SRR acquisition

process when considering its application in ASL. First, images are obtained with a lower through-plane resolution. Lowering the spatial resolution by default increases the SNR of the signal on a voxel level. Furthermore, as fewer slices need to be acquired to cover the same FOV compared to a higher through-plane resolution, the average effective PLD will be shorter and the average level of background suppression will be significantly higher (see Figure 7.1). This will ultimately result in an extra boost of the SNR of the ASL signal throughout the entire volume. Second, it is paramount for SRR to acquire multiple LR images. This provides a natural fit with ASL, as multiple label-control pairs are usually acquired by default for averaging to attain a sufficient SNR of the ASL signal. Apart from that, each of those LR images needs to be acquired in a unique way in order to allow for SRR. An efficient way to acquire LR images suitable for SRR is by rotating the slice-encoding direction around the phase-encoding direction. In that way, each LR image would have a unique slice-encoding direction. The reasoning behind these acquisition demands is extensively explained in section 7.2. Apart from the technical requirement for SRR, different slice-encoding directions also have a distinct benefit in ASL. Indeed, by ensuring a different slice-encoding direction for each label-control pair, the effects of longer effective PLDs and fading background suppression will affect different regions of the brain in each label-control pair. When an HR perfusion-weighted image is reconstructed from such LR label-control pairs, negative effects of the PLD and background suppression on the SNR of the ASL signal are expected to be limited throughout the brain, as low-SNR slices in the LR images are not tied to one specific region of the brain. Conversely, in a conventional ASL experiment, all label-control pairs are acquired in an identical way. In that case, assuming an ascending slice order as recommended [1], the ASL signal will have a decreasing SNR towards the upper parts of the brain.

In this work, we explored the feasibility of combining super-resolution reconstruction methods with single-PLD PCASL and its potential when whole-brain coverage and 2D multi-slice readout are both required. Furthermore, it was compared to a conventional single-PLD PCASL experiment with 2D multi-slice readout to determine whether SRR could also improve on the balance between SNR, resolution and scan time to which the conventional experiment is limited.

## 7.2 Theory

### 7.2.1 Super-resolution reconstruction in MRI: concept

As stated in the introduction, in SRR, an HR image or HR parameter map is restored from a set of 2D multi-slice images, with a low through-plane resolution

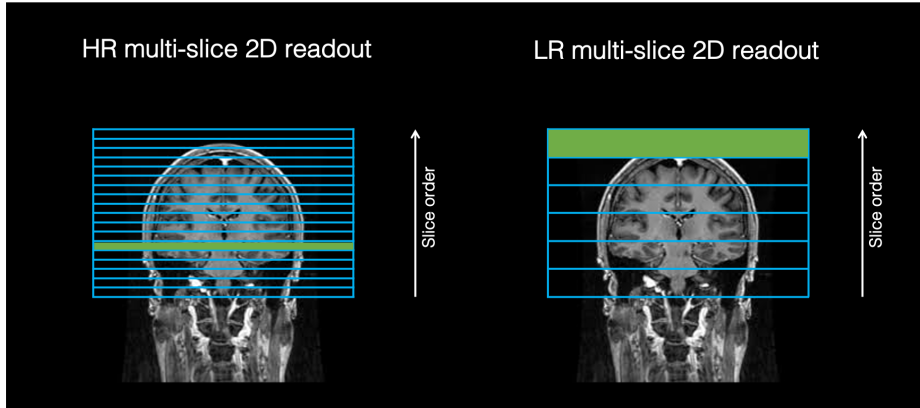


FIGURE 7.1: A schematic representation of a multi-slice readout with a high (left) and a low (right) through-plane resolution, both with an ascending acquisition order, as recommended for ASL [1]. Assuming the acquisition of an HR and an LR slice take up the same amount of scan time, the highlighted slices in green in both readout schemes will have the exact same effective PLD and level of background suppression. Regardless of the difference in SNR due to the difference in spatial resolution, the overall shorter effective PLD and the overall higher level of background suppression in the LR readout scheme will result in a higher SNR of the ASL signal on average throughout the brain.

and with varying slice encoding directions. The basis for SRR is formed by spatial aliasing that occurs in the through-plane direction of a multi-slice image [148–150]. Aliasing is high-spatial frequency information that is being disguised as low frequency information in the 2D readout sampling process. A more detailed description of the theory behind sampling and aliasing in the slice-encoding direction can be found in [151] and [152]. In-plane in a slice of an image acquired with 2D readout or in 3D readout, aliasing does not occur. Therefore, when defining SRR as the recovery of high-frequency components corrupted by aliasing [142], SRR is not possible in-plane in 2D readout, nor in 3D readout [144, 153, 154].

In general, SRR consists of two important parts: acquisition of images appropriate for SRR and a reconstruction method.

### 7.2.2 Super-resolution reconstruction in MRI: acquisition

In general, given the fact that spatial resolution can only be improved in the through-plane direction, the in-plane resolution is usually chosen higher than the

through-plane resolution. The spatial resolution of the LR images for SRR is therefore anisotropic. The anisotropy factor can be defined as the ratio of the through-plane resolution and the in-plane resolution.

Regarding the sampling strategy, there are different options that allow SRR. Three options stand out. First, the LR acquisition matrix can be shifted by sub-pixel distances along the slice-encoding direction for subsequent images [155, 156] (see Figure 7.2). This method is not recommended as the highest frequency regions of k-space are not sampled in all dimensions [154]. Second, LR images can be acquired with the slice-encoding direction chosen along three orthogonal directions (Figure 7.3) [157, 158]. This method is an improvement compared to the sub-pixel shift method in terms of coverage of high-frequencies in three-dimensional k-space. However, for large anisotropy factors, some high-frequency regions are still not uniformly sampled. Third, LR images can be acquired with rotational increments of the slice-encoding direction around the phase- or frequency-encoding direction [149], which guarantees a more uniform sampling of higher k-space frequencies [154], as illustrated in Figure 7.4. It is argued in [154] and [149] that the rotational approach is most efficient when acquiring data for SRR, because of its superior k-space coverage.

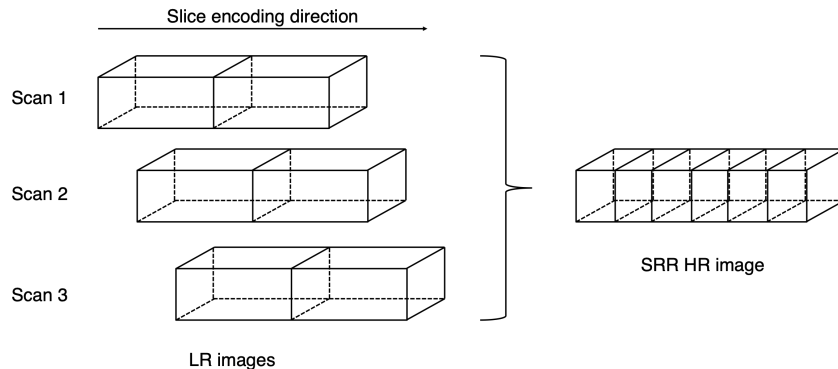


FIGURE 7.2: Schematic representation of the sub-pixel shift acquisition method for SRR.

### 7.2.3 Super-resolution reconstruction in MRI: reconstruction

Once anisotropic LR images are acquired in one of the ways described in the previous subsection, the actual reconstruction part of SRR can be performed. The goal is to recover an HR image with an isotropic resolution from the set of LR images. In general, reconstruction methods can be divided in two categories: the

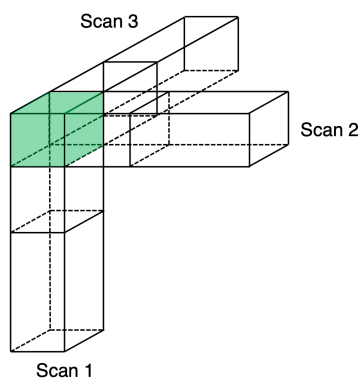


FIGURE 7.3: Schematic representation of the three orthogonal LR image scans for SRR. The area in green represents the isotropic resolution of the to be reconstructed HR image.

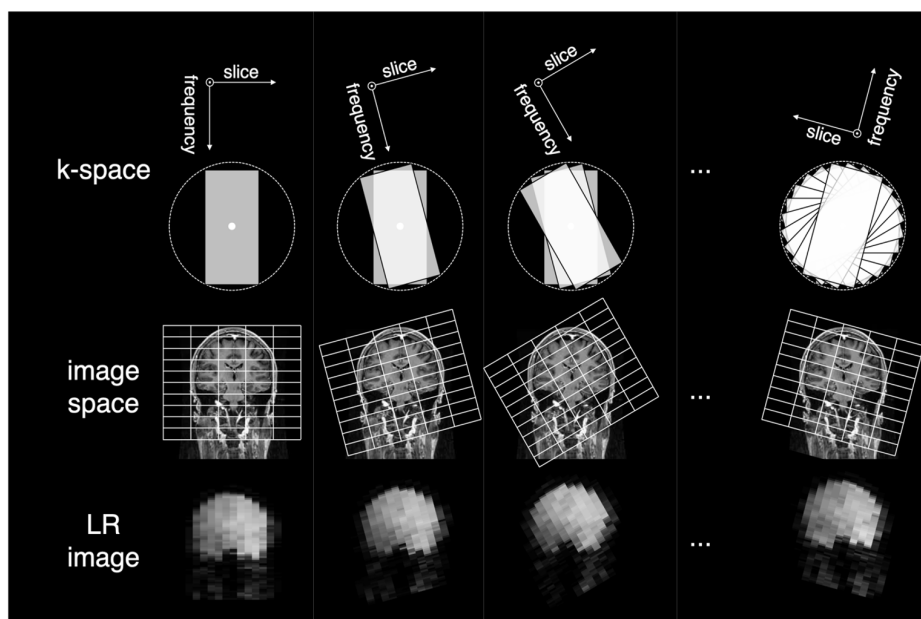


FIGURE 7.4: Schematic representation of the rotational acquisition approach for SRR. Note that the more LR images are acquired, the smaller the rotational increments can be chosen, the better the k-space will be covered.

frequency (i.e., k-space) domain and the spatial domain approach. In this work, the spatial domain approach is used as a framework for SRR. Detailed information about the frequency domain approach can be found in [141, 159, 160].

In the spatial domain, the observation model can be represented as:

$$\mathbf{y} = \mathbf{H}\mathbf{x} + \mathbf{e}, \quad (7.1)$$

with  $\mathbf{y} \in \mathbb{R}^{M \times 1}$  the anisotropic LR images lexicographically ordered,  $\mathbf{x} \in \mathbb{R}^{N \times 1}$  the unknown, isotropic HR image,  $\mathbf{H} \in \mathbb{R}^{M \times N}$  the forward model capturing all operations that allow to describe the LR images starting from the HR image, and  $\mathbf{e} \in \mathbb{R}^{M \times 1}$  the additive noise in the LR images. In the introductory chapters, the maximum likelihood estimator (MLE) was introduced as the go-to estimator when the distribution of the data is to be taken into account (see section 4.3.2). Assuming zero mean, Gaussian distributed noise, which is a reasonable assumption for PCASL data (see section 4.3.2), the MLE of  $\mathbf{x}$  is given by [161]:

$$\hat{\mathbf{x}} = \arg \max_{\mathbf{x}} L(\mathbf{x}|\mathbf{y}) = \arg \min_{\mathbf{x}} (\mathbf{y} - \mathbf{H}\mathbf{x})^T \mathbf{R}_{ee}^{-1} (\mathbf{y} - \mathbf{H}\mathbf{x}), \quad (7.2)$$

with  $L(\mathbf{x}|\mathbf{y})$  the likelihood function of  $\mathbf{x}$  given the data  $\mathbf{y}$  and  $\mathbf{R}_{ee} \in \mathbb{R}^{M \times M}$  the autocorrelation matrix of the Gaussian noise. If all data points in  $\mathbf{y}$  are considered independent and the noise variance  $\sigma^2$  is spatially invariant,  $\mathbf{R}_{ee} = \sigma^2 \mathbf{I}$  with  $\mathbf{I}$  the identity matrix. In that case, Eq. (7.2) simplifies to the unweighted least-squares solution:

$$\hat{\mathbf{x}} = \arg \min_{\mathbf{x}} (\mathbf{y} - \mathbf{H}\mathbf{x})^T (\mathbf{y} - \mathbf{H}\mathbf{x}). \quad (7.3)$$

As this solution satisfies the normal equation, the MLE can be written as a closed-form expression:

$$\hat{\mathbf{x}} = (\mathbf{H}^T \mathbf{H})^{-1} \mathbf{H}^T \mathbf{y}. \quad (7.4)$$

Unfortunately, for typical MR image dimensions, the matrix  $\mathbf{H}$  will be too large to perform the matrix operations in Eq. (7.4) and even too large to be stored as a sparse matrix. The former problem can be solved by using iterative reconstruction methods to approximate Eq. (7.3). Different iterative reconstruction methods for SRR have been studied [154], yet no particular method outperformed the others. The conjugate gradient method is a widely used option that generally reaches convergence quickly [145–147]. That leaves the problem of storing  $\mathbf{H}$ , considering its size. The matrix  $\mathbf{H}$  projects the HR image onto each of the LR images (see Figure 7.5). It captures the downsampling, geometric transformations, blurring

and potential motion [162, 163]. By considering these operations separately,  $\mathbf{H}$  can be described by a combination of affine transformations and a filter operation. A fast way to carry out affine transformations is by describing them as a series of shear operations [144].

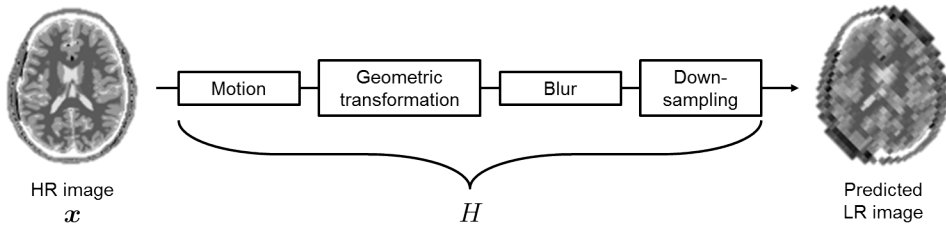


FIGURE 7.5: The SRR acquisition forward model.

### Regularized SRR

While using iterative reconstruction methods and using efficient ways to implement the forward model  $H$  make SRR feasible from a computational point-of-view, Eq. (7.3) remains a badly conditioned or even under-determined problem due to the high resolution at which the image is set to be reconstructed. Certain high spatial frequencies in the HR grid will not be present in any of the LR images, which is the reason for Eq. (7.3) being potentially ill-conditioned. In order to remedy this, a regularization term can be added to Eq. (7.3), which reduces the variance of the solution:

$$\hat{\mathbf{x}} = \arg \min_{\mathbf{x}} (\mathbf{y} - \mathbf{H}\mathbf{x})^T (\mathbf{y} - \mathbf{H}\mathbf{x}) + \mathbf{x}^T \mathbf{K}^T \mathbf{K} \mathbf{x}, \quad (7.5)$$

with  $\mathbf{K} \in \mathbb{R}^{N \times N}$  specifying the regularization term. As some high spatial frequencies will not be present in the acquired images, a suitable regularization is one that constrains these high frequencies. This can be achieved with the squared Laplacian of  $\mathbf{x}$ :

$$\hat{\mathbf{x}} = \arg \min_{\mathbf{x}} \|\mathbf{y} - \mathbf{H}\mathbf{x}\|_2^2 + \lambda \|\Delta \mathbf{x}\|_2^2, \quad (7.6)$$

with  $\Delta$  the Laplace operator, and  $\lambda$  a parameter that determines the weight of the regularization. The net effect of this type of regularization is a spatial smoothing of the reconstructed image. For a more detailed description of this regularization process, see [164].

**Model-based SRR**

Up to this point, the assumption was made that the only real difference between the LR images and the to be reconstructed HR image is spatial resolution and grid orientation. However, SRR can also be combined with a certain parametric model to directly quantify HR parameter maps from a set of LR images. Its potential has already been shown in quantification of relaxometry and diffusion parameters [146, 147]. From a conceptual point of view, this can be seen as an extra operation added to the acquisition forward model  $\mathbf{H}$  as described in Figure 7.5. However, often such parameter models are nonlinear, so they cannot be described by a matrix operation. Therefore, the MLE for the SR reconstructed HR parameter maps is given by:

$$\hat{\boldsymbol{\theta}} = \arg \min_{\boldsymbol{\theta}} (\mathbf{y} - \tilde{\mathbf{H}}\tilde{\mathbf{x}}(\boldsymbol{\theta}))^T (\mathbf{y} - \tilde{\mathbf{H}}\tilde{\mathbf{x}}(\boldsymbol{\theta})), \quad (7.7)$$

with  $\boldsymbol{\theta} \in \mathbb{R}^{N_{\text{par}}N \times 1}$  the  $N_{\text{par}}$  HR parameter maps lexicographically ordered,  $N_{\text{par}}$  the number of different parameters in the model function,  $\tilde{\mathbf{x}}(\boldsymbol{\theta}) \in \mathbb{R}^{N_{\text{LR}}N \times 1}$  the  $N_{\text{LR}}$  predicted HR images obtained from letting the model function operate on the parameters  $\boldsymbol{\theta}$  describing the different physiological conditions for each of the  $N_{\text{LR}}$  acquired LR images, and  $\tilde{\mathbf{H}} \in \mathbb{R}^{M \times N_{\text{LR}}N}$  a matrix projecting the predicted HR images on the predicted LR images.

The same type of regularization as described above can be implemented in model-based SRR:

$$\hat{\boldsymbol{\theta}} = \arg \min_{\boldsymbol{\theta}} (\mathbf{y} - \tilde{\mathbf{H}}\tilde{\mathbf{x}}(\boldsymbol{\theta}))^T (\mathbf{y} - \tilde{\mathbf{H}}\tilde{\mathbf{x}}(\boldsymbol{\theta})) + \boldsymbol{\theta}^T \tilde{\mathbf{K}}^T \tilde{\mathbf{K}} \boldsymbol{\theta}, \quad (7.8)$$

with  $\tilde{\mathbf{K}} \in \mathbb{R}^{N_{\text{par}}N \times N_{\text{par}}N}$  the regularization matrix, which is applied to the lexicographically ordered parameter maps  $\boldsymbol{\theta}$  in model-based SRR. In this case, a separate regularization term for each parameter map is needed to reduce the variance of the solution:

$$\hat{\boldsymbol{\theta}} = \arg \min_{\boldsymbol{\theta}} \|\mathbf{y} - \tilde{\mathbf{H}}\tilde{\mathbf{x}}(\boldsymbol{\theta})\|_2^2 + \sum_{i=1}^{N_{\text{par}}} \lambda_i \|\Delta \boldsymbol{\theta}_i\|_2^2, \quad (7.9)$$

where  $\boldsymbol{\theta}_i \in \mathbb{R}^{N \times 1}$  is an HR parameter map, lexicographically ordered, for one of the  $N_{\text{par}}$  parameters in the model function.

## 7.3 Methods

The comparison of single-PLD PCASL with a conventional 2D multi-slice readout strategy, on the one hand, and the combination of single-PLD PCASL with SRR, on the other hand, was studied in a simulation and real data experiment.

### 7.3.1 Data simulation and acquisition

#### Simulation experiment

As explained in section 7.1, potential benefits of SRR single-PLD PCASL are tied to remedying negative effects of elongating effective PLDs and fading background suppression in 2D multi-slice readout. Therefore, in order to compare the conventional 2D multi-slice readout strategy with the SRR strategy in a meaningful way with simulation experiments, it is vital to correctly incorporate the effects of effective PLDs and background suppression in data simulation.

#### SRR single-PLD PCASL data simulation

SRR Single-PLD PCASL was simulated assuming the rotational acquisition option as depicted in Figure 7.4. In order to sample k-space as uniformly as possible, a unique slice-encoding direction is preferred for each label-control pair. Therefore, it is useful to know the number of label-control pairs  $N_{lc}$  that can be acquired in advance. The relation between the total available scan time  $T$  and  $N_{lc}$  is given by:

$$N_{lc} = \frac{T}{2(\tau + \text{PLD}_{\text{base}} + N_{\text{slice}}t_{\text{read}})}, \quad (7.10)$$

with  $\tau$  the labeling duration,  $\text{PLD}_{\text{base}}$  the time between the end of labeling and the start of readout of the first slice,  $N_{\text{slice}}$  the number of slices in the 2D readout, and  $t_{\text{read}}$  the readout time per slice. Assuming  $T = 210$  s,  $\tau = 1.8$  s,  $\text{PLD}_{\text{base}} = 1.8$  s,  $t_{\text{read}} = 50$  ms (in-plane resolution of 3 mm isotropic), and  $N_{\text{slice}} = 16$  slices with a thickness of 12 mm, it would be possible to acquire  $N_{lc} = 24$  whole-brain label-control image pairs. Therefore, 24 different slice-encoding directions were generated by rotating the slice-encoding direction around the phase-encoding direction, positioned in the anterior-posterior direction, over 24 unique angles equiangularly spaced between 0 and 180 degrees.

For each slice-encoding direction, a  $3 \times 3 \times 12$  mm<sup>3</sup> LR label and control image was simulated. The SRR data simulation forward model is summarized in a flowchart in Figure 7.6. Data was simulated as follows:

1. Ground-truth  $3 \times 3 \times 3 \text{ mm}^3$  HR parameter maps for the CBF, the proton density (PD), and the relaxation time of tissue  $T_{1t}$  were generated starting from an HR tissue segmentation map. Both in gray matter (GM) and in white matter (WM), fixed average values were chosen for each parameter and assigned to the respective voxels (see Table 7.1).
2. HR PCASL difference images and HR PCASL control images were simulated. An HR difference image was obtained from the ground-truth CBF map, the ground-truth PD map, and an appropriate effective PLD map using the recommended quantification equation (see Eq.(3.4)). The effective PLD map is unique for each of the 24 label-control pairs, reflecting the increase in PLD from LR slice to LR slice along the unique slice-encoding direction. Equivalently, fading of the background suppression from LR slice to LR slice was taken into account in simulation of an HR control image. The background suppression was simulated to be perfect in the first slice, i.e. the control signal intensity equal to zero. In subsequent slices, the background signal was simulated to increase towards its PD value with relaxation time  $T_{1t}$ . An example of the HR difference and control signal intensities for different slice-encoding directions is shown in Figure 7.7.
3. HR PCASL label images were created by subtracting each HR difference image from its respective HR control image.
4. Each HR label-control image pair is geometrically rotated around the phase-encoding axis, consistent with the assumed rotation of the slice-encoding direction around the phase-encoding axis.
5. All rotated HR label-control image pairs were downsampled along the slice-encoding direction to obtain the  $3 \times 3 \times 12 \text{ mm}^3$  LR label-control image pairs. Downsampling was performed by summing the signal of four voxels along the slice-encoding axis into one voxel. An example of the geometric rotation (step 4) and downsampling (step 5) step in data simulation is shown in Figure 7.8.
6. In order to account for fading background suppression, the effects of physiological noise, which scales with the background signal [41], need to be incorporated. Therefore, additive zero-mean Gaussian distributed noise was added to the data with the following standard deviation:

$$\sigma = \sqrt{\sigma_0^2 + \sigma_P^2}, \quad (7.11)$$

with  $\sigma_0$  the typical raw noise,  $\sigma_P = cS$  the physiological noise, with  $S$  the signal intensity in the considered voxel and  $c$  a scaling factor. Values for  $\sigma_0$  and  $c$  were chosen to result in a tSNR ranging from approximately 3, in regions with almost no background suppression, to 10, in regions with perfect background suppression, respectively, for the recommended spatial resolution [47]. For more details on background suppression and physiological noise, we refer to section 3.1.3.

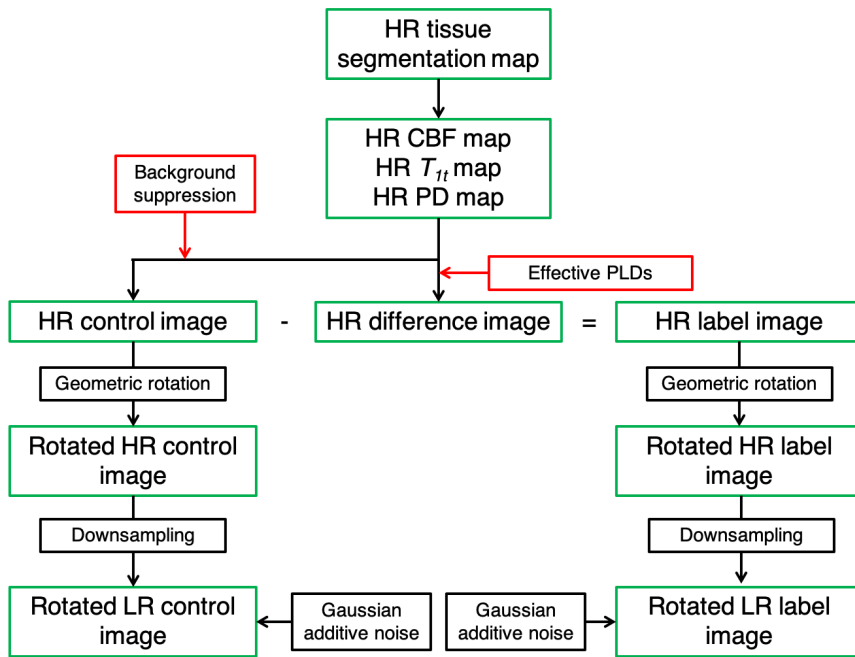


FIGURE 7.6: A flowchart of the data simulation process.

TABLE 7.1: Fixed average values used for the HR CBF,  $T_{1t}$  and the PD ground truth parameter maps.

	White matter	Gray matter
CBF [mL/100g/min]	23.0 [114–116]	53.9 [64]
$T_{1t}$ [s]	0.89 [70]	1.45 [70]
PD [ ]	0.65 [165]	0.80 [165]

### 7.3. Methods

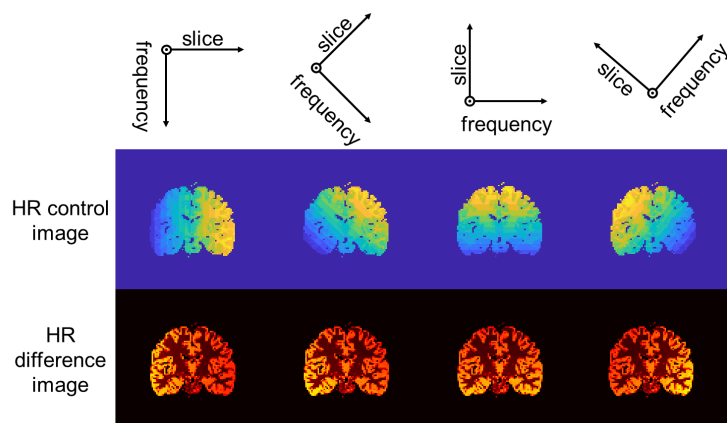


FIGURE 7.7: Coronal slices of the HR difference and HR control image for four slice-encoding directions. Signal intensities are all shown in arbitrary units.

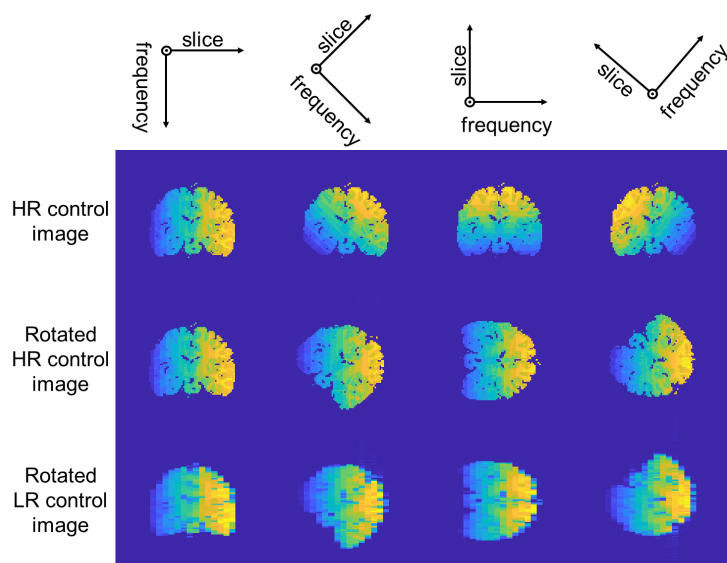


FIGURE 7.8: Coronal slices of the evolution of a control image to an LR control image according to the fourth and fifth step of the data simulation process. Signal intensities are all shown in arbitrary units.

Data simulation for single-PLD PCASL using conventional 2D multi-slice readout

---

In the conventional multi-slice approach data is acquired directly at the target spatial resolution. For a slice thickness of 3 mm, it takes about 40 slices for whole-brain coverage. Note that this is a smaller field-of-view (FOV) than for SRR single-PLD PCASL data, where 16 12-mm-thick slices were used. The larger FOV in SRR is needed because of the rotations of the slice-encoding direction. For each angle, the entire brain has to be within the FOV, which would not be possible with a 12 cm FOV. Assuming  $N_{\text{slice}} = 40$  slices with a thickness of 3 mm, while  $T$ ,  $\tau$ ,  $\text{PLD}_{\text{base}}$ , and  $t_{\text{read}}$  remain unchanged compared to the SRR simulation,  $N_{\text{lc}} = 22$  label-control image pairs can be acquired (see Eq. (7.10)). Note that, even though the readout time is significantly longer when acquiring 40 slices instead of 16, this results in only 2 label-control image pairs less than in the SRR acquisition strategy. This is a direct consequence of the fact that the labeling duration and the PLD take up most of the scan time, as explained in the introduction. Contrary to the rotational acquisition in SRR, in conventional multi-slice readout for single-PLD PCASL, these 22 label-control image pairs are simulated all in the same way. An ascending slice order was implemented, following recommendations [1]. When using an ascending slice order, one has the highest chance to sample the ASL signal at a similar point in its dynamic evolution in each slice, knowing that arterial transit times will on average increase towards the top of the brain.

In terms of the data simulation forward model, there are two main differences compared to the one for the SRR acquisition strategy. First, the fourth and fifth step regarding geometrical rotations and downsampling are skipped. Second, the spatial variation in the effective PLD and the level of background suppression is the same in each repetition of the label-control image pair simulation.

### Real data experiment

The comparison between the SRR version and the conventional multi-slice readout version of single-PLD PCASL was also studied using real data from one subject, as a proof-of-concept. For the acquisition of multi-slice single-PLD PCASL data, the recommended single-shot 2D echo-planar imaging (EPI) readout method was used. As for the simulation experiment, both data for SRR and conventional multi-slice data directly acquired at a high resolution were obtained. Most of the acquisition settings used in the simulation experiment were kept the same for the real data experiment. The relevant settings are listed in Table 7.2. The only exception is the use of simultaneous multi-slice (SMS, also referred to as multiband) in the conventional acquisition strategy. When acquiring 40 slices without multiband,

### 7.3. Methods

---

the effective PLD will have become so long that in most voxels the ASL signal will have vanished almost completely. Therefore, a multiband factor 2 was used, meaning that, for  $n = 1, 2, \dots, 20$ , slice  $n$  and slice  $n + 20$  are acquired at the same time, with the same effective PLD. In addition to the PCASL data, an equilibrium magnetization image was also acquired at isotropic high resolution for absolute CBF quantification.

	<b>LR data for SRR</b>	<b>Conventional HR data</b>
Labeling duration [ms]	1800	1800
PLD [ms]	1800	1800
In-plane spatial resolution [mm <sup>2</sup> ]	$3 \times 3$	$3 \times 3$
Slice thickness [mm]	12	3
Number of slices	16	40
TR [ms]	4400	4800
Number of label-control pairs	24	22
Total scan duration [min:sec]	3:30	3:30
Number of slice encoding directions	24	1
Slice orientation angles [°]	0, 7.5, 15, 22.5, 30, 37.5, 45, 52.5, 60, 67.5, 75, 82.5, 90, 97.5, 105, 112.5, 120, 127.5, 135, 142.5, 150, 157.5, 165, 172.5	90

TABLE 7.2: Acquisition settings for SRR data and conventionally acquired data using multi-slice readout. A slice orientation angle of  $0^\circ$  is compatible with the slice-encoding axis directed from left to right, with the phase-encoding axis perpendicular directed from anterior to posterior. Each angle listed above is a rotation of the slice-encoding axis around the phase-encoding direction counter-clockwise. Therefore, a  $90^\circ$  angle is consistent with an ascending slice order. These rotations are consistent with the rotations visualized in Figure 7.4.

#### 7.3.2 Reconstruction and quantification

After image acquisition, an HR perfusion-weighted image is reconstructed and a CBF map is quantified. In this section, the SR reconstruction options for PCASL

data are presented. The difference with the conventional reconstruction process and the quantification step are also shortly discussed.

### SRR ASL pipelines

Compared to other MRI modalities where SRR has been studied, like relaxometry and diffusion MRI [144–147], combining SRR with ASL provides an extra degree of freedom due to the acquisition of label and control images. In this work, we studied three options.

- SRR ASL 1: First, the LR label-control image pairs are pair-wise subtracted to obtain a set of LR PCASL difference images, each with its unique slice order. In a second step, SRR is performed on these LR difference images (see Figure 7.9a).
- SRR ASL 2: The order of the operations in the SRR ASL 1 pipeline can be reversed. First, an HR label image and an HR control image are reconstructed from the separate sets of LR label and LR control images. Then, the HR difference image is obtained by subtracting the HR label image from the control image (see Figure 7.9b).
- SRR ASL 3: Instead of a two-step process, all operations can also be combined in a model-based version of SRR. In this pipeline, an HR PCASL difference image is directly reconstructed from the LR label and control images (see Figure 7.9c).

The SR reconstructions in SRR ASL 1 and 2 were performed with the regularized scalar version of SRR, described by Eq. (7.6). The forward model  $\mathbf{H}$ , projecting the HR image  $\mathbf{x}$  onto the predicted LR images, typically consists of motion modelling, geometric transformation, blurring and downsampling, as discussed in section 7.2.3. In this study, motion correction on the acquired LR images was performed prior to the SRR step. Therefore, it was assumed the motion modelling step could be omitted from the forward model. In that case, the forward model can be described as

$$\mathbf{H} = \bar{\mathbf{D}}\mathbf{G}, \quad (7.12)$$

with  $\mathbf{G} \in \mathbb{R}^{N_{\text{LR}}N \times N}$  describing all geometric rotations and  $\bar{\mathbf{D}} \in \mathbb{R}^{M \times N_{\text{LR}}N}$  describing downsampling by averaging, which includes blurring, along the slice-encoding direction [166, 167]. Details about the computationally efficient implementation of  $\bar{\mathbf{D}}$  and  $\mathbf{G}$  that was used in these experiments can be found in [166].

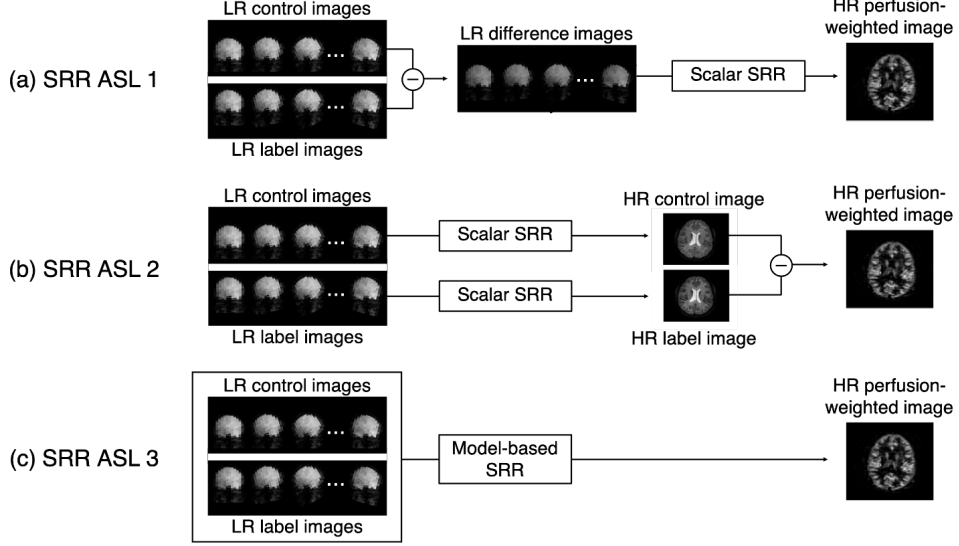


FIGURE 7.9: Considered pipelines for performing SRR on single-PLD PCASL data.

For SRR ASL 3, the model-based version of SRR was required, described by Eq. (7.9). In most applications of model-based SRR, the model is related to the underlying physiological process that has been sampled at different time points [146, 147, 166]. In this case, it is the pair-wise subtraction of label and control images that needs to be modelled. This can be achieved by defining a parameter vector  $\boldsymbol{\theta} = \{\boldsymbol{\theta}_{\text{diff}}, \boldsymbol{\theta}_c\} \in \mathbb{R}^{2N \times 1}$  that contains the signal intensities of the HR PCASL difference image  $\boldsymbol{\theta}_{\text{diff}} \in \mathbb{R}^{N \times 1}$  and HR PCASL control image  $\boldsymbol{\theta}_c \in \mathbb{R}^{N \times 1}$ , lexographically ordered. From these two images,  $N_{\text{LR}}/2^1$  HR label and  $N_{\text{LR}}/2$  HR control images can be deduced using a vector  $\boldsymbol{t} = \{t_i\}_{i=1}^{N_{\text{LR}}}$ :

$$\boldsymbol{x}_i(\boldsymbol{\theta}) = \boldsymbol{\theta}_c + \boldsymbol{\theta}_{\text{diff}} t_i, \quad (7.13)$$

with  $t_i = 0$  if  $i$  is an odd number and  $t_i = -1$  if  $i$  is an even number. In the latter case,  $\boldsymbol{x}_i(\boldsymbol{\theta}) \in \mathbb{R}^{N \times 1}$  is an HR control image, while it is an HR label image in the former case, both lexographically ordered. Let  $\tilde{\boldsymbol{x}}(\boldsymbol{\theta})$  in Eq. (7.9) be

<sup>1</sup>Note that the acquired data  $\boldsymbol{y}$  consists of both the LR control and LR label images in case of SRR ASL 3, while in the case of SRR ASL 1 and 2 the SRR step is performed on the LR difference images or on the LR label and control images separately, respectively. Considering the acquisition settings discussed in section 7.3.1,  $N_{\text{LR}} = 24$  for SRR ASL 1 and 2, while  $N_{\text{LR}} = 48$  for SRR ASL 3.

defined as:  $\tilde{\mathbf{x}}(\boldsymbol{\theta}) = \{\mathbf{x}_i(\boldsymbol{\theta})\}_{i=1}^{N_{LR}} \in \mathbb{R}^{N_{LR}N \times 1}$ . The forward model  $\tilde{H} \in \mathbb{R}^{M \times N_{LR}N}$ , a concatenated version of repetitions of the forward model defined in Eq. (7.12), contains the matrix operations related to the geometric transformations, blurring and downsampling to project the  $N_{LR}/2$  HR label and  $N_{LR}/2$  HR control images onto the  $N_{LR}/2$  LR label and  $N_{LR}/2$  LR control images.

### Reconstruction for conventionally acquired data

For the single-PLD PCASL data acquired with a conventional ascending multi-slice readout method, conventional post-processing consists of registration of the images, pair-wise subtraction of the label images from the control images, and subsequent averaging of the difference images (see Figure 7.10). In what follows, all results related to the multi-slice data conventionally acquired, directly at a high resolution, will be referred to as HR ASL.

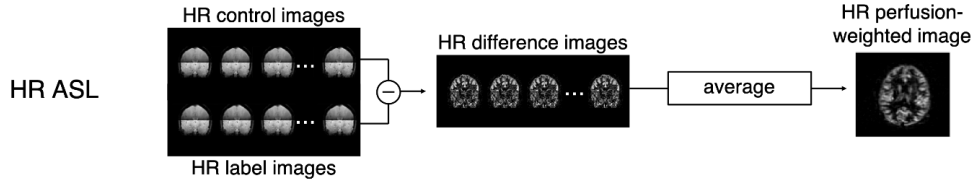


FIGURE 7.10: Post-processing pipeline for conventionally acquired single-PLD PCASL data.

### Quantification

CBF estimation is performed using the recommended quantification formula for single-PLD PCASL data [1]. The labeling efficiency  $\alpha$ , the brain-blood partition coefficient  $\lambda$ , and the longitudinal relaxation time of blood  $T_{1b}$  were fixed at their recommended population averages. For the HR ASL experiment, the effective PLD is exactly known in each slice, which was taken into account in quantification. In the SRR experiments, a unit of tissue in a certain part of the brain will be located in different slices for the different acquired LR images. Because of this, there is no single exact effective PLD that can be assigned to each HR voxel of an SR reconstructed HR perfusion-weighted image. Therefore, the average effective PLD, for a base PLD of 1.8 s and the acquisition of 16 slices with a readout time of 50 ms per slice, of 2.2 s was assigned globally.

### 7.3.3 Performance analysis

#### Simulation experiment

The process of simulating data, performing the reconstruction and quantifying the CBF was repeated  $K = 100$  times for the model-based SRR ASL 3 and the HR ASL pipeline. This allowed for a voxel-wise analysis of the bias and precision of both CBF estimation methods, by means of Eq. (4.36) and Eq. (4.40), respectively, as described in detail in sections 4.4.1 and 4.4.2 in the introductory chapters.

#### Real data experiment

An HR perfusion-weighted image was reconstructed with all three SRR ASL pipelines. Regularization weighting factors were chosen ensuring the ratio between the data fidelity term and the regularization term, or sum of regularization terms in case of SRR ASL 3, was the same for each SRR pipeline. Furthermore, CBF maps were quantified from the SR reconstructed HR perfusion-weighted images. These results were then qualitatively compared to the results obtained from the conventional HR ASL data.

## 7.4 Results

### 7.4.1 Simulation experiment

The estimate of the bias of CBF estimation in each voxel of a coronal slice of the simulated brain for the HR ASL and the SRR ASL 3 pipeline is shown in Figure 7.11. For the HR ASL experiment, estimation is close to unbiased in most voxels, which was expected due to the one-to-one similarity between the simulation and quantification model (Figure 7.11a). In the upper part of the brain, however, there is a significant bias in some voxels in white matter. This can be attributed to the SNR of the ASL signal becoming extremely low in these slices, which had the longest effective PLDs and the lowest degree of background suppression. On average, the bias is much more significant for the SRR ASL 3 experiment (Figure 7.11b). This is caused by the globally averaged PLD that is used in quantification for the SRR pipelines, as there is no single effective PLD that can be attributed to each voxel due to the different slice-encoding directions in image acquisition. In the lower parts of the brain, this averaged PLD used in quantification will be slightly longer than the actual average of the effective PLDs linked to the acquisition settings of the set of LR images, resulting in CBF overestimation. In

the upper parts of the brain, the CBF is underestimated as the averaged PLD will be shorter than the actual average effective PLD in these voxels.

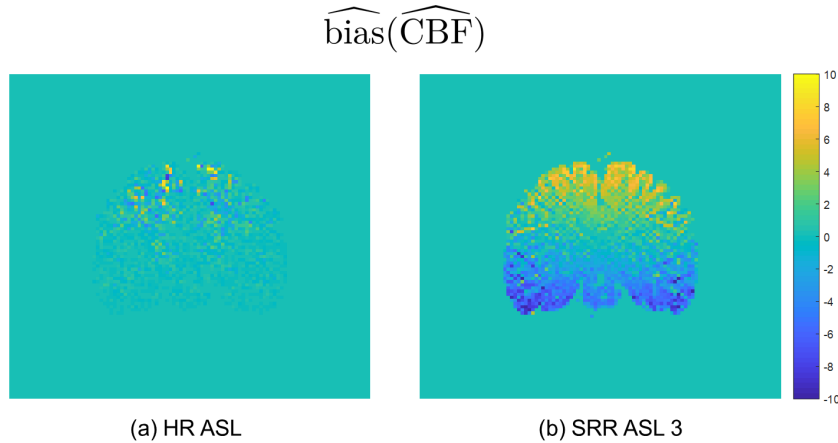


FIGURE 7.11: Bias estimates of CBF estimation, consistent with Eq.(4.35), for (a) the conventional HR multi-slice and (b) the model-based SRR single-PLD PCASL experiment. Values are shown in standard ‘mL/100g/min’ units.

The estimates of the standard deviation of CBF estimation, a measure for estimation precision, are shown in Figure 7.12. The increase in standard deviation for the conventional HR ASL experiment is exponential with the slice number; therefore differences between the HR and SRR version of the experiment are better evaluated on the natural logarithm scale, as shown in Figure 7.13. Four aspects stand out. First, the standard deviation for the conventional HR multi-slice read-out increases from the lower parts of the brain towards the top parts of the brain (Figure 7.13a). This is consistent with the ascending slice order in this acquisition strategy. The effective PLD becomes longer and the background suppression becomes less effective as subsequent slices are acquired, as discussed in the introduction. Both effects lower the SNR of the ASL signal, which results in a lower CBF estimation precision. Second, the precision of CBF estimation is much more uniform, per tissue type, throughout the brain when using the SRR strategy (Figure 7.13b). This can be attributed to the overall higher SNR of the ASL signal due to the benefits of lowering the spatial resolution in terms of background suppression efficiency and effective PLD durations, as well as to the changing high-SNR regions in the LR images when using the rotational SRR acquisition strategy. Both effects were extensively discussed in the third paragraph of the introduction of this chapter. Third, when comparing HR ASL with SRR ASL in Figure 7.13,

it is clear that CBF estimation precision is higher for the conventional HR multi-slice single-PLD PCASL experiment in approximately the lowest one-fourth part of the coronal slice of the brain. It is caused by the fact that in the conventional approach, the high-SNR slices are located in that part of the brain for each acquisition of a label-control pair, while those high-SNR regions are different for each acquired image in the rotational SRR acquisition strategy. However, as the fourth and final point, in the upper three quarters of the brain, the precision of CBF estimation is higher in the SRR ASL experiment. As was the case for the second point, this is linked to the overall higher SNR of the ASL signal in these regions in the set of LR images with their individual unique slice orders.

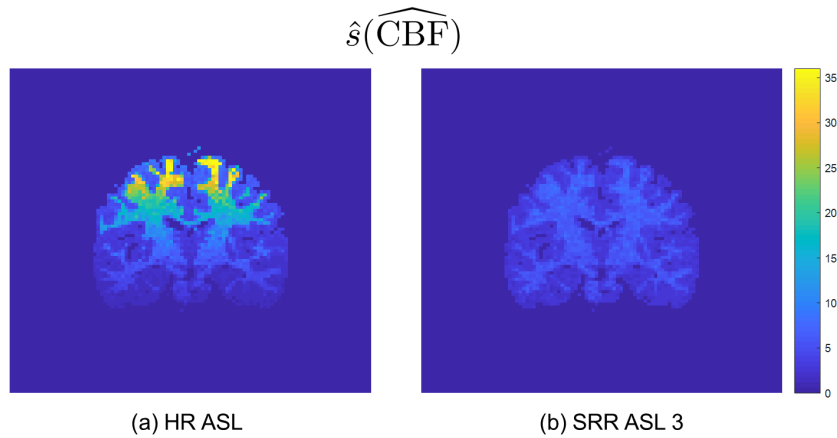


FIGURE 7.12: Estimates of the standard deviation of CBF estimation, consistent with Eq. (4.38), for (a) the conventional HR multi-slice and (b) the model-based SRR single-PLD PCASL experiment. Values are shown in standard ‘mL/100g/min’ units.

In section 7.3.1, it was indicated that a multiband factor of 2 was used for real data acquisition of the conventional HR multi-slice data, because acquiring 40 HR slices consecutively was expected to result in extremely low SNRs of the ASL signal in slices acquired latest. This is reflected by the high estimated standard deviations in the upper parts of the brain shown in Figure 7.12a. In order to compare the simulation experiment one-to-one with the real data experiment, the HR ASL simulation experiment was repeated multiple times simulating the use of a multiband factor 2. The resulting estimates of the standard deviation of CBF estimation are again compared to those of the SRR ASL 3 experiment in Figure 7.14. With the multiband factor of 2 applied for the conventional HR multi-slice acquisition, the overall precision of CBF estimation increases when compared

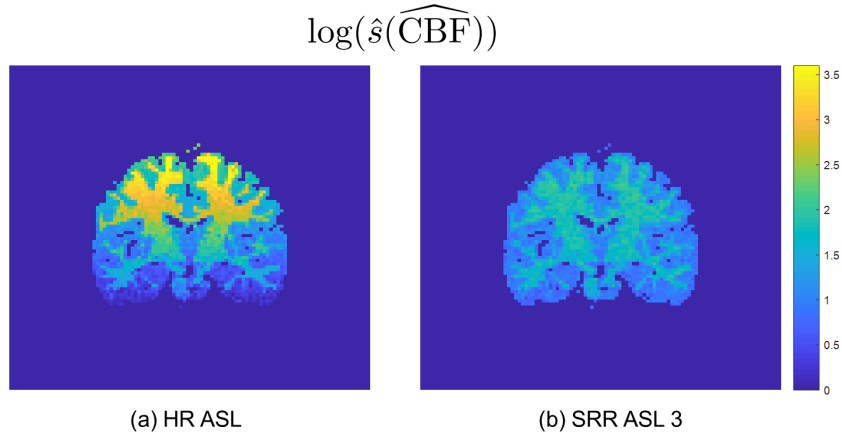


FIGURE 7.13: The natural logarithm of the estimates of the standard deviation of CBF estimation shown in Figure 7.12.

with the results shown in Figure 7.12a. Only in the last few acquired slices in both multiband segments, the precision is expected to be lower in HR ASL compared to the SRR experiment.

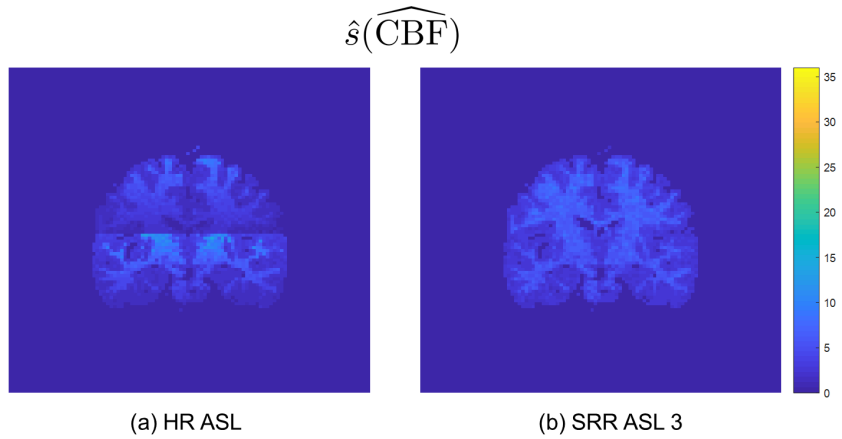


FIGURE 7.14: Estimates of the standard deviation of CBF estimation, consistent with Eq. (4.38), for (a) the conventional HR multi-slice with a multiband factor of 2 and (b) the model-based SRR single-PLD PCASL experiment. Values are shown in standard ‘mL/100g/min’ units.

### 7.4.2 Real data experiment

The results of the reconstructed HR perfusion-weighted difference image are shown in Figure 7.15. When comparing the different SRR ASL approaches, the model-based SRR-ASL-3 pipeline qualitatively outperforms the other two SRR pipelines. In SRR ASL 1, SRR is performed on overall low-SNR difference images, explaining the higher noise-level in the reconstructed HR perfusion-weighted images. For SRR-ASL-2, SRR is performed on the LR label and control images separately. These images have a much higher SNR, which is expected to benefit the reconstruction. However, the subtraction step is not taken into account in the two separate reconstructions, making this pipeline more vulnerable to registration errors. Moreover, regularization is performed on the unsubtracted images, which show less high-contrast details than perfusion-weighted images. The super-resolution post-processing step and the pairwise subtraction of label-control pairs are modelled in one single optimization framework in SRR ASL 3, making it less susceptible to error propagation. At the same time, robustness is maintained because regularization is performed directly on the final HR perfusion-weighted outcome image.

When comparing SRR ASL 3 to the conventional HR ASL experiment, two aspects stand out. First, the SR reconstructed HR perfusion-weighted images are comparable in terms of visualized anatomical structures to the averaged perfusion-weighted images obtained from the conventional multi-slice data, directly acquired at HR. This is particularly clear when comparing the last three slices for both methods in Figure 7.15. To our knowledge, this is the first real-data proof-of-concept demonstrating the feasibility of combining SRR with single-PLD PCASL. Second, in certain slices (i.e., the first two slices in Figure 7.15), the SRR strategy appears to even outperform the conventional HR ASL experiment in terms of reconstruction of the underlying anatomy. It is a direct consequence of the benefit of acquiring LR data for SRR ASL in terms of SNR. The reconstructed slices shown in Figure 7.15 for the SRR ASL pipelines all have comparable signal intensities. This reflects the relative uniformity in average SNR throughout all regions in the brain related to the SNR benefits of acquiring LR images and the rotational acquisition strategy. For the averaged perfusion-weighted image obtained from the conventional HR multi-slice data, the first two slices shown in Figure 7.15 clearly suffer from low SNR due to long effective PLDs and limited background suppression. In Figure 7.16, the location of the transverse slices shown for HR ASL in Figure 7.15 are highlighted on a coronal view of the averaged HR ASL difference image. It clearly shows that the first two slices are acquired late in the first multiband segment, explaining the low SNR, while the other three are acquired relatively early in the second multiband segment.

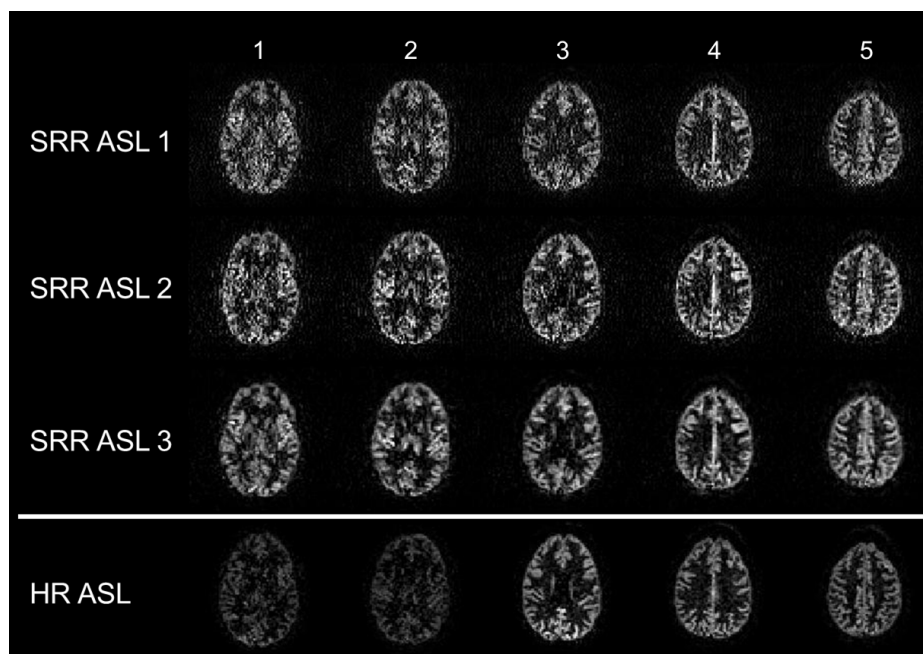


FIGURE 7.15: HR ( $3 \times 3 \times 3 \text{ mm}^3$ ) perfusion-weighted transverse slices at locations ‘1’ to ‘5’, as highlighted in Figure 7.16. The top three rows represent the reconstructions obtained from the three SRR pipelines described in Figure 7.9, respectively. The bottom row shows the averaged HR difference image obtained from the conventional HR multi-slice PCASL data. In this bottom row, note that the jump in signal intensity from the second to the third slice is caused by the multiband acquisition; data acquisition for the second slice was performed with a much longer effective PLD and a much worse background suppression compared to the third slice.

The results of CBF quantification are shown in Figure 7.17 for the same transverse slices as in Figure 7.15. In terms of quality of reconstructed anatomy, the same superiority of SRR ASL 3 compared to HR ASL as in the HR perfusion-weighted images is visible for the first two slices. In terms of absolute values, the CBF estimates resulting from the SRR-ASL pipelines are in the same range as those obtained from the HR ASL experiment. However, there are some clear regional differences between SRR ASL 3 and HR ASL. This could be caused by accumulation of information from different effective PLDs in each voxel stemming from the different slice orientations of the LR images, whereas each slice has a

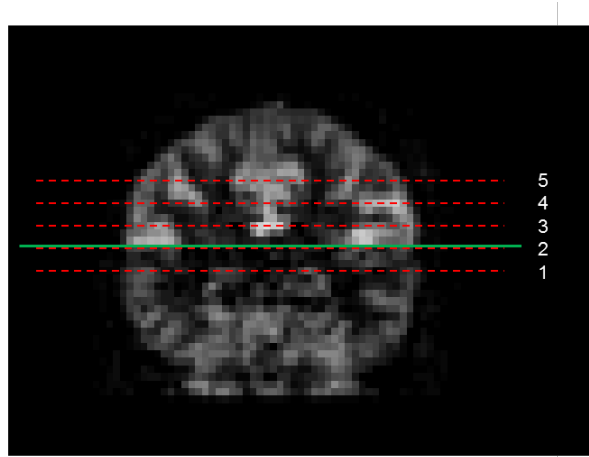


FIGURE 7.16: A coronal slice of the averaged perfusion-weighted image obtained from the conventional HR multi-slice experiment. The red dotted lines represent the locations of the transverse slices shown in Figure 7.15.

single exact effective PLD in HR ASL. In other words, the SRR ASL pipelines are expected to be slightly biased, as was already shown in simulations (Figure 7.11b).

As stated above, a version of the simulation experiment was run, mimicking the same multiband factor of 2 in the HR ASL experiment. Note that the stability of the signal intensities across slices in SRR (see Figure 7.15) is consistent with the uniform precision of CBF estimation from SR reconstructed data shown in the simulation experiment (see Figure 7.14b). Both effects trace back to the aforementioned SNR benefits related to acquiring images at a lower resolution and the rotational acquisition strategy.

Furthermore, the higher quality of the CBF map obtained from the SRR ASL 3 experiment compared to that of the HR ASL experiment in regions of the brain that were imaged latest within the multiband segment (see the first two slices shown in Figure 7.17) matches with the difference in precision of CBF estimation between both methods in those same regions as predicted in the simulation experiment (see Figure 7.14). While it is difficult to compare a qualitative assessment (real data) with a quantitative measurement of precision (simulation data), it is reasonable to assume both effects are correlated. It serves as an indication of the validity of the simulation experiment.

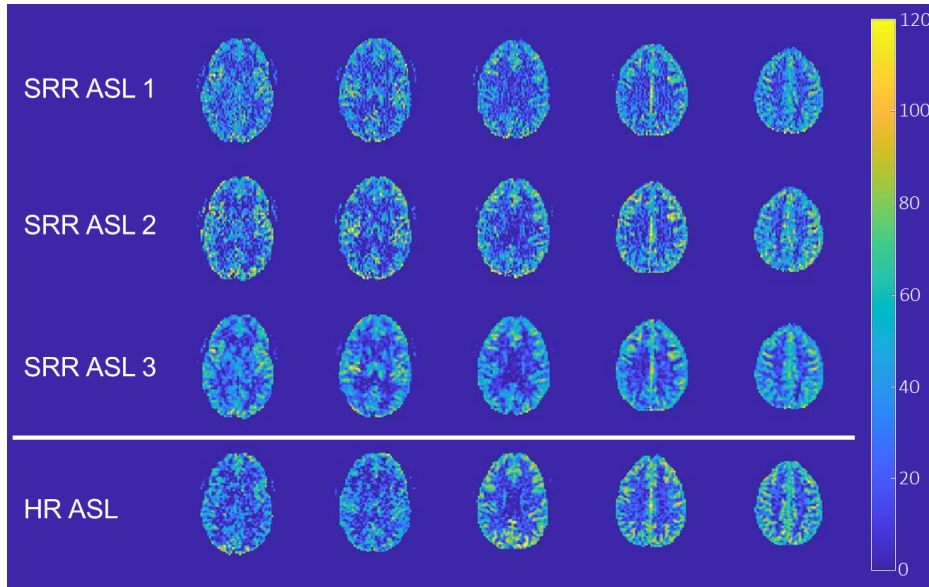


FIGURE 7.17: Transverse slices at different locations in the brain of the HR ( $3 \times 3 \times 3 \text{mm}^3$ ) CBF maps, quantified from the HR perfusion-weighted image slices shown in Figure 7.15.

## 7.5 Discussion and conclusions

When using a multi-slice readout strategy for PCASL, the SNR of the PCASL signal reduces in subsequently acquired slices due to longer effective PLDs and fading background suppression. This limits the amount of slices that can be acquired with a sufficient SNR. It makes whole-brain coverage using a conventional sequential multi-slice readout strategy, without multiband, infeasible when isotropic high-resolution single-PLD PCASL data (i.e.,  $3 \times 3 \times 3 \text{mm}^3$ ) is required. In this work, it was shown that SRR offers a path towards whole-brain coverage and an isotropic high resolution for single-PLD PCASL when 2D multi-slice acquisition is the readout method of choice.

While the potential of SRR single-PLD PCASL was demonstrated, there are a number of limitations in the current format of this contribution. First, the SRR ASL pipelines presented above are inherently biased, as was shown in the simulation experiment (see Figure 7.11). As discussed in section 7.4.1, this is due to not being able to take variations in effective PLDs throughout the different LR images correctly into account when reconstructing the HR perfusion-weighted image. In future work, this will be remedied by directly estimating the HR CBF map from

the set of differently acquired LR label-control pairs using an extended version of the model-based SRR ASL 3 framework. That will allow to correctly take the variation in effective PLDs into account. Second, the comparison between the three considered SRR ASL pipelines is dependent on the chosen regularization weights. In order to compare the performance of different pipelines in a reliable manner, ideally, the level of regularization should be the same in all reconstructions. However, as the images to be reconstructed differed in each pipeline, regularization weights could not simply be chosen equal in all pipelines. Instead, as mentioned in section 7.3.3, it was opted to keep the ratio between the data fidelity term and the regularization term the same in all pipelines. This approach is debatable, yet, to our knowledge, there is no standard practice for this type of comparison. Third, a more fair comparison between SRR ASL and HR ASL would be achieved when multiband is (not) used in both experiments. One could argue that the current real data comparison was skewed in favour of the conventional HR ASL experiment, because multiband was only used for HR ASL data acquisition. However, this choice was made for two reasons. On the one hand, a multiband factor of 2 was used in the HR ASL experiment, as there would have been practically no ASL signal remaining in most of the upper part of the brain if it would not have been implemented. As this was a proof-of-concept study, being able to verify whether the SR reconstructed perfusion-weighted images showed anatomical details comparable to those of HR ASL was more important than a true one-to-one comparison of the HR ASL and SRR ASL experiment. On the other hand, multiband was not used in the SRR ASL experiment, because multiband acquisition required a prescan to be performed before acquisition of each LR image. This would have taken up too much of the available total scan time. In future work, we intend to study whether the SRR acquisition strategy can be combined with multiband more efficiently, to allow for a more fair comparison between both strategies. Finally, the SRR ASL experiment needs to be validated on more subjects in order to demonstrate its robustness. Furthermore, ideally, data should be acquired repeatedly in individual subjects, in order to be able to determine sample standard deviations for CBF map estimates, similarly to the analysis done in simulations. This allows to quantify the performance of SRR ASL and HR ASL, complementary to the qualitative analysis on real data performed above.



## Chapter 8

# Conclusions

Improving on the state-of-the-art balance between the accuracy and precision of perfusion parameter estimation in pseudo-continuous arterial spin labeling was at the core of each of the three main contributions of this dissertation. In Chapter 3 and 4, it was shown that this balance can be influenced by many aspects of both the imaging and the quantification part of the PCASL experiment. This work reflects this versatility as each contribution focussed on a different point of entry for potential improvements.

In Chapter 5, the limit on the number of parameters to be estimated from multi-PLD PCASL data was studied as a function of the accuracy and precision. Estimating perfusion parameters from multi-PLD PCASL data is commonly tackled by fitting the single-compartment model, with CBF and ATT as free parameters. The longitudinal relaxation time of tissue  $T_{1t}$  is an important parameter in this model, as it governs the decay of the perfusion signal entirely upon entry in the imaging voxel. Conventionally,  $T_{1t}$  is fixed to a population average. This approach can cause CBF quantification errors, as  $T_{1t}$  can vary significantly inter- and intra-subject. Therefore, the impact of either fixing  $T_{1t}$ , the conventional approach, or estimating it alongside CBF and ATT was studied. It was shown that the conventional approach can cause a significant bias in CBF. Indeed, simulation experiments reveal that if  $T_{1t}$  is fixed to a value that is 10% off its true value, this may already result in a bias of 15% in CBF. On the other hand, as was shown by both simulation and real data experiments, estimating  $T_{1t}$  along with CBF and ATT results in a loss of CBF estimation precision of the same order, even after optimizing the experiment design using Cramér-Rao lower bound theory. Simulation experiments suggested that an optimal balance between accuracy and precision of CBF estimation from multi-PLD PCASL data can be expected when choosing a fixed  $T_{1t}$  value between population averages of  $T_{1t}$  and the longitudinal relaxation time of blood  $T_{1b}$ .

While we demonstrated that  $T_{1t}$  does play an important role when quantifying with the single-compartment model, there are two other parameters that are prone to variability: the labeling efficiency  $\alpha$  and the longitudinal relaxation time of blood  $T_{1b}$ . They are also usually fixed to literature values, again potentially resulting in estimation inaccuracies. Contrary to  $T_{1t}$ ,  $\alpha$  and  $T_{1b}$  cannot be estimated together with the perfusion parameters from the same set of data. They can only be determined from supporting (MRI) experiments. In Chapter 6, it was studied in simulations whether sacrificing ASL scan time for such supporting experiments in a five-minute total scan time was beneficial in the general population. Compared to single-PLD PCASL without support measurements as recommended in the consensus statement, a 26%, 33% and 42% reduction in relative CBF estimation variability was found for optimal combinations of supporting measurements with single-PLD, free-lunch time-encoded, and multi-PLD PCASL data acquisition, respectively. The benefit of taking the individual variation of blood  $T_1$  into account was also demonstrated in a real data experiment. Spending time to measure the labeling efficiency and the blood  $T_1$  instead of acquiring more averages of the PCASL data was shown to be advisable for robust CBF quantification in the general population.

The quantification model and which parameters should be estimated in the light of their known variability were the focal points of the previous two contributions. Furthermore, in Chapter 5, the impact of the PCASL acquisition settings on perfusion parameter estimation precision was studied. In Chapter 7, the effects of the acquisition strategy on perfusion parameter estimation were further explored. More specifically, the potential of combining super-resolution reconstruction techniques with single-PLD PCASL was demonstrated, when whole-brain coverage is required and 2D multi-slice readout is preferred. In simulations, it was shown that overall CBF estimation precision drastically improved when using SR reconstructed PCASL HR images compared to the precision related to a conventional sequential multi-slice HR readout strategy. The results of a real data validation experiment aligned with these simulation results. Indeed, the quality of the SR reconstructed PCASL HR perfusion-weighted image was high in the entire brain, while a diminishing image quality was observed along the slice-encoding direction in the averaged HR perfusion-weighted image resulting from the conventional multi-slice readout. In short, it was shown that SRR offers a path towards whole-brain coverage and an isotropic high resolution (i.e.,  $3 \times 3 \times 3 \text{ mm}^3$ ) for single-PLD PCASL when 2D multi-slice acquisition is the readout method of choice.





# Epilogue

I would like to finish this dissertation with a final outlook on the field based on my trajectory through the academic world of ASL research. Starting in a research group with a vast expertise in statistical parameter estimation in MRI, yet with no prior projects in ASL, gave me the opportunity to explore the state-of-the-art ASL research and potential research opportunities with an open mind. The evolution of the parameter estimation aspect in ASL is truly fascinating. The work of Alsop and Detre [39] stands out, as it showed how to reduce the sensitivity of CBF quantification to the locally varying transit times in the brain. It is arguably the most important work that led to the clinical recommendation of quantifying the CBF from ASL data acquired at a single time point [1]. The (relative) simplicity of the recommended single-PLD PCASL experiment, both in terms of data acquisition and in quantification, is undoubtedly at the base of the booming clinical adoption of ASL and expanding research efforts in ASL. In terms of parameter estimation, the recommended experiment results in very high estimation precision. Yet, from the start of my project, I was drawn to the many potential sources of bias when quantifying the CBF using the recommended implementation. Multi-time-point ASL, where perfusion parameters are quantified by fitting a certain model to the data, allows for much more flexibility in terms of estimation accuracy and precision.<sup>1</sup> In certain settings, such as large population studies or longitudinal prognostic studies, accuracy is at least as important as precision to make trustworthy comparisons between CBF maps. For such studies, I am confident that the current clinical recommendations are not the best option. Yet, it is my belief that a large part of the ASL community underestimates the relatively low accuracy of the consensus experiment because of its high reproducibility related to the high CBF estimation precision. Therefore, I encourage the ASL research community to remain critical for the current clinical recommendations, without detracting anything from its immense value so far. Large population studies where different ASL

---

<sup>1</sup>On a small tangent, a perfect starting point for ASL model selection is the work of Buxton et al. [52]. It deepened my understanding of ASL as a whole and was at the base of most research trajectories I explored throughout the past years. I recommend it strongly to anyone interested in parameter estimation in ASL.

experiments are compared to a gold standard experiment for CBF quantification would be my choice when asked what might advance the field as a whole.





# Bibliography

- [1] Alsop DC, Detre JA, Golay X, Günther M, Hendrikse J, Hernandez-Garcia L, Lu H, MacIntosh BJ, Parkes LM, Smits M, van Osch MJP, Wang DJJ, Wong EC, Zaharchuk G. Recommended implementation of arterial spin-labeled perfusion MRI for clinical applications: A consensus of the ISMRM perfusion study group and the European consortium for ASL in dementia. *Magnetic Resonance in Medicine* 2015;73:102–116.
- [2] Detre J, Rao H, Wang D, Chen Y, Wang Z. Applications of arterial spin labeled MRI in the brain. *Journal of Magnetic Resonance Imaging* 2012; 35:1026–1037.
- [3] Hendrikse J, Petersen E, Golay X. Vascular disorders: Insights from arterial spin labeling. *Neuroimaging Clinics of North America* 2012;22:259–269.
- [4] Jezzard P, Chappell MA, Okell TW. Arterial spin labeling for the measurement of cerebral perfusion and angiography. *Journal of Cerebral Blood Flow & Metabolism* 2018;38:603–626.
- [5] Detre J, Leigh J, Williams D, Koretsky A. Perfusion imaging. *Magnetic Resonance in Medicine* 1992;23:37–45.
- [6] Singer JR. Blood flow rates by nuclear magnetic resonance measurements. *Science* 1959;130:1652–1653.
- [7] Herscovitch P, Markham J, Raichle M. Brain blood flow measured with intravenous H<sub>2</sub>(15)O. I. Theory and error analysis. *Journal of Nuclear Medicine* 1983;24:782–789.
- [8] Raichle ME, Martin W, Herscovitch P, Mintun M, Markham J. Brain blood flow measured with intravenous H<sub>2</sub>15O. II. Implementation and validation. *Journal of Nuclear Medicine* 1983;24:790–798.
- [9] Gur D, Good W, Wolfson S, Yonas H, Shabason L. In vivo mapping of local cerebral blood flow by xenon-enhanced computed tomography. *Science* 1982; 215:1267–1268.

- [10] Villringer A, Rosen BR, Belliveau JW, Ackerman JL, Lauffer RB, Buxton RB, Chao YS, Wedeen VJ, Brady TJ. Dynamic imaging with lanthanide chelates in normal brain: contrast due to magnetic susceptibility effects. *Magnetic Resonance in Medicine* 1988;6:164–174.
- [11] Rosen BR, Belliveau JW, Vevea JM, Brady TJ. Perfusion imaging with NMR contrast agents. *Magnetic Resonance in Medicine* 1990;14:249–265.
- [12] Calamante F, Gadian D, Connelly A. Quantification of perfusion using bolus tracking magnetic resonance imaging in stroke: assumptions, limitations, and potential implications for clinical use. *Stroke* 2002;33:1146–1151.
- [13] Le Bihan D, Breton E, Lallemand D, Grenier P, Cabanis E, Laval-Jeantet M. MR imaging of intravoxel incoherent motions: application to diffusion and perfusion in neurologic disorders. *Radiology* 1986;161:401–407.
- [14] Pekar J, Ligeti L, Ruttner Z, Lyon R, Sinnwell T, van Gerderen P, Fiat D, Moonen C, McLaughlin A. In vivo measurement of cerebral oxygen consumption and blood flow using  $^{17}\text{O}$  magnetic resonance imaging. *Magnetic Resonance in Medicine* 1991;21:313–319.
- [15] van den Bos A. *Parameter Estimation for Scientists and Engineers*. Wiley, New York, 2007.
- [16] Liang ZP, Lauterbur PC. *Principles of magnetic resonance imaging: a signal processing perspective*. SPIE Optical Engineering Press, 2000.
- [17] Hanson LG. Is quantum mechanics necessary for understanding magnetic resonance? *Concepts in Magnetic Resonance Part A* 2008;32:329–340.
- [18] Bohr N. *Collected works. volume 3: The correspondence principle (1918–1923)*, 1976.
- [19] Bloch F. Nuclear induction. *Physical Review* 1946;70:460.
- [20] Bloembergen N. Proton relaxation times in paramagnetic solutions. *Journal of Chemical Physics* 1957;27:572–573.
- [21] Korb J, Bryant R. Magnetic field dependence of proton spin-lattice relaxation times. *Magnetic Resonance in Medicine* 2002;48:21–26.
- [22] Lauterbur PC. Image formation by induced local interactions: examples employing nuclear magnetic resonance. *Nature* 1973;242:190–191.

## BIBLIOGRAPHY

---

- [23] Kumar A, Welte D, Ernst RR. NMR fourier zeugmatography. *Journal of Magnetic Resonance* 1975;18:69–83.
- [24] Bernstein M, King K, Zhou X. *Handbook of MRI Pulse Sequences*. Academic Press, 2004.
- [25] Gregori J. *Dynamic Arterial Spin Labeling Measurements of Physiological Parameters-Permeability and Oxygenation*. Ph.D. thesis, 2009.
- [26] Günther M, Oshio K, Feinberg DA. Single-shot 3D imaging techniques improve arterial spin labeling perfusion measurements. *Magnetic Resonance in Medicine* 2005;54:491–498.
- [27] Kwong KK, Chesler DA, Weisskoff RM, Donahue KM, Davis TL, Ostergaard L, Campbell TA, Rosen BR. MR perfusion studies with T1-weighted echo planar imaging. *Magnetic Resonance in Medicine* 1995;34:878–887.
- [28] Wong EC, Buxton RB, Frank LR. A theoretical and experimental comparison of continuous and pulsed arterial spin labeling techniques for quantitative perfusion imaging. *Magnetic Resonance in Medicine* 1998;40:348–355.
- [29] Kim SG. Quantification of relative cerebral blood flow change by flow-sensitive alternating inversion recovery (FAIR) technique: application to functional mapping. *Magnetic Resonance in Medicine* 1995;34:293–301.
- [30] Williams D, Detre J, Leigh J, Koretsky A. Magnetic resonance imaging of perfusion using spin inversion of arterial water. *Proceedings of the National Academy of Sciences of the USA* 1992;89:212–216.
- [31] Dai W, Garvia D, de Bazelaire C, Alsop D. Continuous flow-driven inversion for arterial spin labeling using pulsed radio frequency and gradient fields. *Magnetic Resonance in Medicine* 2008;60:1488–1497.
- [32] Wong EC, Cronin M, Wu WC, Inglis B, Frank LR, Liu TT. Velocity-selective arterial spin labeling. *Magnetic Resonance in Medicine* 2006;55:1334–1341.
- [33] Schmid S, Heijtel DF, Mutsaerts HJ, Boellaard R, Lammertsma AA, Nederveen AJ, Van Osch MJ. Comparison of velocity- and acceleration-selective arterial spin labeling with [15O] H<sub>2</sub>O positron emission tomography. *Journal of Cerebral Blood Flow & Metabolism* 2015;35:1296–1303.
- [34] Lu H, Clingman C, Golay X, van Zijl PCM. Determining the longitudinal relaxation time (T<sub>1</sub>) of blood at 3.0 Tesla. *Magnetic Resonance in Medicine* 2004;52:679–682.

- [35] Petersen ET, Mouridsen K, Golay X. The QUASAR reproducibility study, part II: Results from a multi-center arterial spin labeling test-retest study. *NeuroImage* 2010;49:104 – 113.
- [36] Bokkers R, Van Der Worp H, Mali W, Hendrikse J. Noninvasive MR imaging of cerebral perfusion in patients with a carotid artery stenosis. *Neurology* 2009;73:869–875.
- [37] Qin Q, Huang AJ, Hua J, Desmond JE, Stevens RD, van Zijl PCM. 3D whole-brain perfusion quantification using pseudo-continuous arterial spin labeling MRI at multiple post-labeling delays: Accounting for both arterial transit time and impulse response function. *NMR in Biomedicine* 2014; 27:116–128.
- [38] Qiu M, Paul Maguire R, Arora J, Planeta-Wilson B, Weinzimmer D, Wang J, Wang Y, Kim H, Rajeevan N, Huang Y, Carson RE, Constable RT. Arterial transit time effects in pulsed arterial spin labeling CBF mapping: Insight from a PET and MR study in normal human subjects. *Magnetic Resonance in Medicine* 2010;63:374–384.
- [39] Alsop DC, Detre JA. Reduced transit-time sensitivity in noninvasive magnetic resonance imaging of human cerebral blood flow. *Journal of Cerebral Blood Flow & Metabolism* 1996;16:1236–1249.
- [40] Edelstein W, Glover G, Hardy C, Redington R. The intrinsic signal-to-noise ratio in NMR imaging. *Magnetic Resonance in Medicine* 1986;3:604–618.
- [41] Krüger G, Glover GH. Physiological noise in oxygenation-sensitive magnetic resonance imaging. *Magnetic Resonance in Medicine* 2001;46:631–637.
- [42] Bodurka J, Ye F, Petridou N, Murphy K, Bandettini PA. Mapping the MRI voxel volume in which thermal noise matches physiological noise-implications for fMRI. *NeuroImage* 2007;34:542–549.
- [43] Vidorreta M, Balteau E, Wang Z, De Vita E, Pastor MA, Thomas DL, Detre JA, Fernández-Seara MA. Evaluation of segmented 3D acquisition schemes for whole-brain high-resolution arterial spin labeling at 3T. *NMR in Biomedicine* 2014;27:1387–1396.
- [44] Maleki N, Dai W, Alsop DC. Optimization of background suppression for arterial spin labeling perfusion imaging. *Magnetic Resonance Materials in Physics, Biology and Medicine* 2012;25:127–133.

## BIBLIOGRAPHY

---

- [45] Garcia DM, Duhamel G, Alsop DC. Efficiency of inversion pulses for background suppressed arterial spin labeling. *Magnetic Resonance in Medicine* 2005;54:366–372.
- [46] Fernández-Seara MA, Wang Z, Wang J, Rao HY, Guenther M, Feinberg DA, Detre JA. Continuous arterial spin labeling perfusion measurements using single shot 3D GRASE at 3 T. *Magnetic Resonance in Medicine* 2005; 54:1241–1247.
- [47] Vidorreta M, Wang Z, Rodríguez I, Pastor MA, Detre JA, Fernández-Seara MA. Comparison of 2D and 3D single-shot ASL perfusion fMRI sequences. *NeuroImage* 2013;66:662–671.
- [48] Asllani I, Borogovac A, Brown TR. Regression algorithm correcting for partial volume effects in arterial spin labeling MRI. *Magnetic Resonance in Medicine* 2008;60:1362–1371.
- [49] Chappell MA, Groves AR, MacIntosh BJ, Donahue MJ, Jezzard P, Woolrich MW. Partial volume correction of multiple inversion time arterial spin labeling MRI data. *Magnetic Resonance in Medicine* 2011;65:1173–1183.
- [50] Liang X, Connelly A, Calamante F. Improved partial volume correction for single inversion time arterial spin labeling data. *Magnetic Resonance in Medicine* 2013;69:531–537.
- [51] Pimentel M, Vilela P, Sousa I, Figueiredo P. Correction of partial volume effects in PASL perfusion measurements. In: *Proceedings of the ISMRM*. volume 18, 2010; 4062.
- [52] Buxton RB, Frank LR, Wong EC, Siewert B, Warach S, Edelman RR. A general kinetic model for quantitative perfusion imaging with arterial spin labeling. *Magnetic Resonance in Medicine* 1998;40:383–396.
- [53] van Osch MJP, Teeuwisse WM, Chen Z, Suzuki Y, Helle M, Schmid S. Advances in arterial spin labelling MRI methods for measuring perfusion and collateral flow. *Journal of Cerebral Blood Flow & Metabolism* 2018; 38:1461–1480.
- [54] van der Thiel M, Rodriguez C, Giannakopoulos P, Burke M, Lebel RM, Gninenko N, Van De Ville D, Haller S. Brain perfusion measurements using multidelay arterial spin-labeling are systematically biased by the number of delays. *American Journal of Neuroradiology* 2018;39:1432–1438.

- [55] Gonzalez-At JB, Alsop DC, Detre JA. Cerebral perfusion and arterial transit time changes during task activation determined with continuous arterial spin labeling. *Magnetic Resonance in Medicine* 2000;43:739–746.
- [56] Wang D, Alger J, Qiao J, Gunther M, Pope W, Saver J, Salamon N, Liebeskind D. Multi-delay multi-parameteric arterial spin-labeled perfusion MRI in acute ischemic stroke - Comparison with dynamic susceptibility contrast enhanced perfusion imaging. *Neuroimage Clinical* 2013;3:1–7.
- [57] Gunther M. Encoded continuous arterial spin labeling. In: ISMRM workshop on cerebral perfusion and brain function: novel techniques and applications, Salvador da Bahia, Brazil. 2007; abstract number 3.
- [58] Sylvester JJ. LX. Thoughts on inverse orthogonal matrices, simultaneous signsuccessions, and tessellated pavements in two or more colours, with applications to Newton’s rule, ornamental tile-work, and the theory of numbers. *The London, Edinburgh, and Dublin Philosophical Magazine and Journal of Science* 1867;34:461–475.
- [59] Teeuwisse WM, Schmid S, Ghariq E, Veer IM, van Osch MJP. Time-encoded pseudocontinuous arterial spin labeling: Basic properties and timing strategies for human applications. *Magnetic Resonance in Medicine* 2014;72:1712–1722.
- [60] Woods J, Chappell M, Okell T. Comparison of optimized single-PLD, sequential multi-PLD and time-encoded PCASL for cerebral blood flow measurements. In: *Proceedings of the 27th Annual Meeting of ISMRM, Paris, France*. 2018; 26:2162.
- [61] Dai W, Shankaranarayanan A, Alsop DC. Volumetric measurement of perfusion and arterial transit delay using hadamard encoded continuous arterial spin labeling. *Magnetic Resonance in Medicine* 2013;69:1014–1022.
- [62] Guo J, Holdsworth SJ, Fan AP, Lebel MR, Zun Z, Shankaranarayanan A, Zaharchuk G. Comparing accuracy and reproducibility of sequential and hadamard-encoded multidelay pseudocontinuous arterial spin labeling for measuring cerebral blood flow and arterial transit time in healthy subjects: a simulation and in vivo study. *Journal of Magnetic Resonance Imaging* 2018;47:1119–1132.
- [63] Parkes LM, Tofts PS. Improved accuracy of human cerebral blood perfusion measurements using arterial spin labeling: Accounting for capillary water permeability. *Magnetic Resonance in Medicine* 2002;48:27–41.

## BIBLIOGRAPHY

---

- [64] Fan AP, Jahanian H, Holdsworth SJ, Zaharchuk G. Comparison of cerebral blood flow measurement with [15O]-water positron emission tomography and arterial spin labeling magnetic resonance imaging: A systematic review. *Journal of Cerebral Blood Flow & Metabolism* 2016;36:842–861.
- [65] Jung Y, Wong EC, Liu TT. Multiphase pseudocontinuous arterial spin labeling (MP-PCASL) for robust quantification of cerebral blood flow. *Magnetic Resonance in Medicine* 2010;64:799–810.
- [66] Zhao L, Vidorreta M, Soman S, Detre JA, Alsop DC. Improving the robustness of pseudo-continuous arterial spin labeling to off-resonance and pulsatile flow velocity. *Magnetic Resonance in Medicine* 2017;78:1342–1351.
- [67] Hales PW, Kirkham FJ, Clark CA. A general model to calculate the spin-lattice (T1) relaxation time of blood, accounting for haematocrit, oxygen saturation and magnetic field strength. *Journal of Cerebral Blood Flow & Metabolism* 2016;36:370–374.
- [68] Li W, Liu P, Lu H, Strouse JJ, Zijl PCM, Qin Q. Fast measurement of blood T1 in the human carotid artery at 3T: Accuracy, precision, and reproducibility. *Magnetic Resonance in Medicine* 2016;77:2296–2302.
- [69] Li W, Grgac K, Huang A, Yadav N, Qin Q, van Zijl PCM. Quantitative theory for the longitudinal relaxation time of blood water. *Magnetic Resonance in Medicine* 2016;76:270–281.
- [70] Bojorquez JZ, Bricq S, Acqutter C, Brunotte F, Walker PM, Lalande A. What are normal relaxation times of tissues at 3 T? *Magnetic Resonance Imaging* 2017;35:69–80.
- [71] Wang J, Alsop DC, Li L, Listerud J, Gonzalez-At JB, Schnall MD, Detre JA. Comparison of quantitative perfusion imaging using arterial spin labeling at 1.5 and 4.0 Tesla. *Magnetic Resonance in Medicine* 2002;48:242–254.
- [72] Liu P, Uh J, Lu H. Determination of spin compartment in arterial spin labeling MRI. *Magnetic Resonance in Medicine* 2011;65:120–127.
- [73] Zhou J, Wilson DA, Ulatowski JA, Traystman RJ, van Zijl PCM. Two-compartment exchange model for perfusion quantification using arterial spin tagging. *Journal of Cerebral Blood Flow & Metabolism* 2001;21:440–455.

- [74] St Lawrence K, Frank J, McLaughlin A. Effect of restricted water exchange on cerebral blood flow values calculated with arterial spin tagging: A theoretical investigation. *Magnetic Resonance in Medicine* 2000;44:440–449.
- [75] St Lawrence KS, Owen D, Wang DJJ. A two-stage approach for measuring vascular water exchange and arterial transit time by diffusion-weighted perfusion MRI. *Magnetic Resonance in Medicine* 2012;67:1275–1284.
- [76] Herscovitch P, Raichle ME, Kilbourn MR, Welch MJ. Positron emission tomographic measurement of cerebral blood flow and permeability-surface area product of water using [15O]water and [11C]butanol. *Journal of Cerebral Blood Flow & Metabolism* 1987;7:527–542.
- [77] Gregori J, Schuff N, Kern R, Günther M. T2-based arterial spin labeling measurements of blood to tissue water transfer in human brain. *Journal of Magnetic Resonance Imaging* 2013;37:332–342.
- [78] Francis ST, Bowtell R, Gowland PA. Modeling and optimization of look-locker spin labeling for measuring perfusion and transit time changes in activation studies taking into account arterial blood volume. *Magnetic Resonance in Medicine* 2008;59:316–325.
- [79] Hua J, Qin Q, Pekar JJ, van Zijl PCM. Measurement of absolute arterial cerebral blood volume in human brain without using a contrast agent. *NMR in Biomedicine* 2011;24:1313–1325.
- [80] Li K, Zhu X, Hylton N, Jahng GH, Weiner MW, Schuff N. Four-phase single-capillary stepwise model for kinetics in arterial spin labeling MRI. *Magnetic Resonance in Medicine* 2005;53:511–518.
- [81] Pawlik G, Rackl A, Bing RJ. Quantitative capillary topography and blood flow in the cerebral cortex of cats: an in vivo microscopic study. *Brain Research* 1981;208:35 – 58.
- [82] Ma Y, Koo A, Kwan H, Cheng K. On-line measurement of the dynamic velocity of erythrocytes in the cerebral microvessels in the rat. *Microvascular Research* 1974;8:1 – 13.
- [83] Fenton BM, Zweifach BW. Microcirculatory model relating geometrical variation to changes in pressure and flow rate. *Annals of Biomedical Engineering* 1981;9:303–321.

## BIBLIOGRAPHY

---

- [84] Gallichan D, Jezzard P. Modeling the effects of dispersion and pulsatility of blood flow in pulsed arterial spin labeling. *Magnetic Resonance in Medicine* 2008;60:53–63.
- [85] Petersen ET, Lim T, Golay X. Model-free arterial spin labeling quantification approach for perfusion MRI. *Magnetic Resonance in Medicine* 2006; 55:219–232.
- [86] Chappell MA, Woolrich MW, Kazan S, Jezzard P, Payne SJ, MacIntosh BJ. Modeling dispersion in arterial spin labeling: Validation using dynamic angiographic measurements. *Magnetic Resonance in Medicine* 2013;69:563–570.
- [87] Hrabe J, Lewis D. Two analytical solutions for a model of pulsed arterial spin labeling with randomized blood arrival times. *Journal of Magnetic Resonance* 2004;167:49–55.
- [88] Ozyurt O, Dincer A, Ozturk C. A modified version of Hrabe-Lewis model to account dispersion of labeled bolus in arterial spin labeling. In: *Proceedings of the 18th Annual Meeting of ISMRM, Stockholm, Sweden*. 2010; 18:4065.
- [89] Kazan SM, Chappell MA, Payne SJ. Modeling the effects of flow dispersion in arterial spin labeling. *IEEE Transactions on Biomedical Engineering* 2009; 56:1635–1643.
- [90] Gall P, Guether M, Kiselev V. Model of blood transport couples delay and dispersion and predicts ASL bolus measurements. In: *Proceedings of the 18th Annual Meeting of ISMRM, Stockholm, Sweden*. 2010; 18:1736.
- [91] Kellner E, Gall P, Günther M, Reisert M, Mader I, Fleysher R, Kiselev VG. Blood tracer kinetics in the arterial tree. *PLoS One* 2014;9:1–11.
- [92] den Dekker AJ, Van Aert S, van den Bos A, Van Dyck D. Maximum likelihood estimation of structure parameters from high resolution electron microscopy images. Part I: A theoretical framework. *Ultramicroscopy* 2005; 104:83–106.
- [93] Aja-Fernández S, Pieciak T, Vegas-Sánchez-Ferrero G. Spatially variant noise estimation in MRI: A homomorphic approach. *Medical Image Analysis* 2015;20:184–197.

- [94] Bouhrara M, Spencer RG. Fisher information and Cramér-Rao lower bound for experimental design in parallel imaging. *Magnetic Resonance in Medicine* 2018;79:3249–3255.
- [95] Sijbers J, den Dekker AJ, Raman E, Van Dyck D. Parameter estimation from magnitude MR images. *International Journal of Imaging Systems and Technology* 1999;10:109–114.
- [96] Chatfield C. *Statistics for Technology: A Course in Applied Statistics*, Third Edition. Chapman and Hall, London, 1983.
- [97] Papoulis A, Pillai S. *Probability, Random Variables and Stochastic Processes with Errata* Sheer, McGraw-Hill Education, New York, NY. 2002; .
- [98] Norton J. *An Introduction to Identification*. Academic Press, London, 1986.
- [99] van den Bos A. *Handbook of Measurement Science*, volume 1. Edited by P. H. Sydenham, Wiley, Chichester, England, 1982.
- [100] Grillon E, Provent P, Montigon O, Segebarth C, Rémy C, Barbier EL. Blood–brain barrier permeability to manganese and to Gd-DOTA in a rat model of transient cerebral ischaemia. *NMR in Biomedicine* 2008;21:427–436.
- [101] Vymazal J, Righini A, Brooks RA, Canesi M, Mariani C, Leonardi M, Pezzoli G. T1 and T2 in the brain of healthy subjects, patients with Parkinson disease, and patients with multiple system atrophy: Relation to iron content. *Radiology* 1999;211:489–495.
- [102] Kettunen MI, Sierra A, Närväinen MJ, Valonen PK, Ylä-Herttua S, Kauppinen RA, Gröhn OHJ. Low spin-lock field T1 relaxation in the rotating frame as a sensitive MR imaging marker for gene therapy treatment response in rat glioma. *Radiology* 2007;243:796–803.
- [103] Bastin ME, Sinha S, Whittle IR, Wardlaw JM. Measurements of water diffusion and T1 values in peritumoural oedematous brain. *Neuroreport* 2002;13:1335–1340.
- [104] Xie J, Gallichan D, Gunn RN, Jezzard P. Optimal design of pulsed arterial spin labeling MRI experiments. *Magnetic Resonance in Medicine* 2008; 59:826–834.

## BIBLIOGRAPHY

---

- [105] Sanches J, Sousa I, Figueiredo P. Bayesian Fisher information criterion for sampling optimization in ASL-MRI. In: 2010 IEEE International Symposium on Biomedical Imaging: From Nano to Macro. 2010; 880–883.
- [106] Owen D, Melbourne A, Thomas D, De Vita E, Rohrer J, Ourselin S. Optimisation of arterial spin labelling using Bayesian experimental design. In: Proceedings of MICCAI 2016. Lecture Notes in Computer Science. Springer, volume 9902, 2016; 511–518.
- [107] Woods JG, Chappell MA, Okell TW. A general framework for optimizing arterial spin labeling MRI experiments. *Magnetic Resonance in Medicine* 2019;81:2474–2488.
- [108] Debacker CS, Daoust A, Köhler S, Voiron J, Warnking J, Barbier EL. Impact of tissue T1 on perfusion measurement with arterial spin labeling. *Magnetic Resonance in Medicine* 2017;77:1656–1664.
- [109] Poot DHJ, den Dekker AJ, Achten E, Verhoye M, Sijbers J. Optimal experimental design for diffusion kurtosis imaging. *IEEE Trans Med Imag* 2010; 29:819–829.
- [110] Seber GAF, Wild CJ. *Nonlinear Regression*. Wiley, New Jersey, 2005.
- [111] Rodriguez-Fernandez M, Mendes P, Banga J. A hybrid approach for efficient and robust estimation in biochemical pathways. *BioSystems* 2006;83:248–65.
- [112] Lankford CL, Does MD. On the inherent precision of mcDESPOT. *Magnetic Resonance in Medicine* 2012;69:127–136.
- [113] Collier Q, Veraart J, Jeurissen B, Vanhevel F, Pullens P, Parizel PM, den Dekker AJ, Sijbers J. Diffusion kurtosis imaging with free water elimination: A bayesian estimation approach. *Magnetic Resonance in Medicine* 2018; 80:802–813.
- [114] Henriksen OM, Larsson HB, Hansen AE, Grüner JM, Law I, Rostrup E. Estimation of intersubject variability of cerebral blood flow measurements using MRI and positron emission tomography. *Journal of Magnetic Resonance Imaging* 2012;35:1290–1299.
- [115] Zhang K, Herzog H, Mauler J, Filss C, Okell TW, Kops ER, Tellmann L, Fischer T, Brocke B, Sturm W, Coenen HH, Shah NJ. Comparison of cerebral blood flow acquired by simultaneous [15O]water positron emission

- tomography and arterial spin labeling magnetic resonance imaging. *Journal of Cerebral Blood Flow & Metabolism* 2014;34:1373–1380.
- [116] van Golen LW, Kuijter JP, Huisman MC, IJzerman RG, Barkhof F, Diamant M, Lammertsma AA. Quantification of cerebral blood flow in healthy volunteers and type 1 diabetic patients: Comparison of MRI arterial spin labeling and [15O]H<sub>2</sub>O positron emission tomography (PET). *Journal of Magnetic Resonance Imaging* 2014;40:1300–1309.
- [117] MATLAB. version 9.2.0 (R2017a). The MathWorks Inc., Natick, Massachusetts, 2017.
- [118] Audet C, Dennis, Jr JE. Analysis of generalized pattern searches. *SIAM Journal on Optimization* 2002;13:889–903.
- [119] Hooke R, Jeeves T. Direct search solution of numerical and statistical problems. *Journal of the Association for Computing Machinery* 1961;8:212–229.
- [120] Collins DL, Zijdenbos AP, Kollokian V, Sled JG, Kabani NJ, Holmes CJ, Evans AC. Design and construction of a realistic digital brain phantom. *IEEE Transactions on Medical Imaging* 1998;17:463–468.
- [121] Maes F, Collignon A, Vandermeulen D, Marchal G, Suetens P. Multimodality image registration by maximization of mutual information. *IEEE Transactions on Medical Imaging* 1997;16:187–198.
- [122] Otsu N. A threshold selection method from gray-level histograms. *IEEE Transactions on Systems, Man, and Cybernetics* 1979;9:62–66.
- [123] Weir JP. Quantifying test-retest reliability using the intraclass correlation coefficient and the SEM. *Journal on Strength & Conditioning Research* 2005; 19:231–240.
- [124] Zhao L, Meyer CH. Optimal PLD design and maximum likelihood CBF estimation for dynamic PCASL with Rician noise. In: *Proceedings of the ISMRM*. 2013; 2164.
- [125] Gardener AG, Jezzard P. Investigating white matter perfusion using optimal sampling strategy arterial spin labeling at 7 Tesla. *Magnetic Resonance in Medicine* 2015;73:2243–2248.
- [126] Chen Z, Zhang X, Yuan C, Zhao X, van Osch MJP. Measuring the labeling efficiency of pseudocontinuous arterial spin labeling. *Magnetic Resonance in Medicine* 2017;77:1841–1852.

## BIBLIOGRAPHY

---

- [127] Lindstrom TR, Koenig SH. Magnetic-field-dependent water proton spin-lattice relaxation rates of hemoglobin solutions and whole blood. *Journal of Magnetic Resonance* 1974;15:344–353.
- [128] Wu WC, Fernández-Seara M, Detre JA, Wehrli FW, Wang J. A theoretical and experimental investigation of the tagging efficiency of pseudocontinuous arterial spin labeling. *Magnetic Resonance in Medicine* 2007;58:1020–1027.
- [129] Aslan S, Xu F, Wang PL, Uh J, Yezhuvath US, van Osch M, Lu H. Estimation of labeling efficiency in pseudocontinuous arterial spin labeling. *Magnetic Resonance in Medicine* 2010;63:765–771.
- [130] Günther M, Valsala PI. A novel technique to improve the reliability of pseudo continuous arterial spin labeling. In: *University of Michigan International Workshop on Arterial Spin Labeling MRI: Technical Updates and Clinical Experience*, Ann Arbor, Michigan, USA. 2019; abstract number: 9.
- [131] Kramme J, Gregori J, Diehl V, Madai VI, von Samson-Himmelstjerna FC, Lentschig M, Sobesky J, Günther M. Improving perfusion quantification in arterial spin labeling for delayed arrival times by using optimized acquisition schemes. *Zeitschrift für Medizinische Physik* 2015;25:221–229.
- [132] Chen Y, Wang Z, Detre J. Impact of equilibrium magnetization of blood on ASL quantification. In: *Proceedings of the 19th Annual Meeting of ISMRM*, Montréal, Canada. 2011; 19:300.
- [133] Bladt P, den Dekker AJ, Clement P, Achten E, Sijbers J. The costs and benefits of estimating T1 of tissue alongside cerebral blood flow and arterial transit time in pseudo-continuous arterial spin labeling. *NMR in Biomedicine* ;e4182.
- [134] Pinto J, Chappell MA, Okell TW, Mezue M, Segerdahl AR, Tracey I, Vilela P, Figueiredo P. Calibration of arterial spin labeling data - potential pitfalls in post-processing. *Magnetic Resonance in Medicine* 2020;83:1222–1234.
- [135] Woolrich MW, Chiarelli P, Gallichan D, Perthen J, Liu TT. Bayesian inference of hemodynamic changes in functional arterial spin labeling data. *Magnetic Resonance in Medicine* 2006;56:891–906.
- [136] Chappell MA, Groves AR, Whitcher B, Woolrich MW. Variational bayesian inference for a nonlinear forward model. *IEEE Transactions on Signal Processing* 2009;57:223–236.

- [137] Santos N, Sanches J, Figueiredo P. Bayesian optimization of perfusion and transit time estimation in PASL-MRI. In: 2010 Annual International Conference of the IEEE Engineering in Medicine and Biology. 2010; 4284–4287.
- [138] Silva AC, Kim SG. Pseudo-continuous arterial spin labeling technique for measuring CBF dynamics with high temporal resolution. *Magnetic Resonance in Medicine* 1999;42:425–429.
- [139] Ivanov D, Poser BA, Huber L, Pfeuffer J, Uludağ K. Optimization of simultaneous multislice EPI for concurrent functional perfusion and BOLD signal measurements at 7T. *Magnetic Resonance in Medicine* 2017;78:121–129.
- [140] Suzuki Y, Okell TW, Chappell MA, van Osch MJ. A framework for motion correction of background suppressed arterial spin labeling perfusion images acquired with simultaneous multi-slice EPI. *Magnetic Resonance in Medicine* 2019;81:1553–1565.
- [141] Park SC, Park MK, Kang MG. Super-resolution image reconstruction: a technical overview. *IEEE Signal Processing Magazine* 2003;20:21–36.
- [142] Kang MG, Chaudhuri S. Super-resolution image reconstruction. *IEEE Signal Processing Magazine* 2003;20:19–20.
- [143] Tian J, Ma KK. A survey on super-resolution imaging. *Signal, Image and Video Processing* 2011;5:329–342.
- [144] Poot DHJ, Van Meir V, Sijbers J. General and efficient super-resolution method for multi-slice MRI. In: *International Conference on Medical Image Computing and Computer-Assisted Intervention*. Springer, 2010; 615–622.
- [145] Poot DHJ, Jeurissen B, Bastiaensen Y, Veraart J, Van Hecke W, Parizel PM, Sijbers J. Super-resolution for multislice diffusion tensor imaging. *Magnetic Resonance in Medicine* 2013;69:103–113.
- [146] Van Steenkiste G, Jeurissen B, Veraart J, den Dekker AJ, Parizel PM, Poot DHJ, Sijbers J. Super-resolution reconstruction of diffusion parameters from diffusion-weighted images with different slice orientations. *Magnetic Resonance in Medicine* 2016;75:181–195.
- [147] Van Steenkiste G, Poot DHJ, Jeurissen B, den Dekker AJ, Vanhevel F, Parizel PM, Sijbers J. Super-resolution T1 estimation: Quantitative high resolution T1 mapping from a set of low resolution T1-weighted images with

## BIBLIOGRAPHY

---

- different slice orientations. *Magnetic Resonance in Medicine* 2017;77:1818–1830.
- [148] Greenspan H. Super-resolution in medical imaging. *The Computer Journal* 2009;52:43–63.
- [149] Shilling RZ, Robbie TQ, Bailloeul T, Mewes K, Mersereau RM, Brummer ME. A super-resolution framework for 3-D high-resolution and high-contrast imaging using 2-D multislice MRI. *IEEE Transactions on Medical Imaging* 2008;28:633–644.
- [150] Hefnawy AA. An efficient super-resolution approach for obtaining isotropic 3-D imaging using 2-D multi-slice MRI. *Egyptian Informatics Journal* 2013; 14:117–123.
- [151] Noll DC, Boada FE, Eddy WF. A spectral approach to analyzing slice selection in planar imaging: optimization for through-plane interpolation. *Magnetic Resonance in Medicine* 1997;38:151–160.
- [152] Pipe JG. Asymmetric sampling along  $k_{\text{slice-select}}$  in two-dimensional multi-slice MRI. *Magnetic Resonance in Medicine* 1998;39:625–634.
- [153] Scheffler K. Superresolution in MRI? *Magnetic Resonance in Medicine: An Official Journal of the International Society for Magnetic Resonance in Medicine* 2002;48:408–408.
- [154] Plenge E, Poot DHJ, Bernsen M, Kotek G, Houston G, Wielopolski P, van der Weerd L, Niessen WJ, Meijering E. Super-resolution methods in MRI: can they improve the trade-off between resolution, signal-to-noise ratio, and acquisition time? *Magnetic Resonance in Medicine* 2012;68:1983–1993.
- [155] Ben-Ezra A, Greenspan H, Rubner Y. Regularized super-resolution of brain MRI. In: 2009 IEEE International Symposium on Biomedical Imaging: From Nano to Macro. 2009; 254–257.
- [156] Greenspan H, Oz G, Kiryati N, Peled S. MRI inter-slice reconstruction using super-resolution. *Magnetic Resonance Imaging* 2002;20:437–446.
- [157] Souza A, Senn R. Model-based super-resolution for MRI. In: 2008 30th Annual International Conference of the IEEE Engineering in Medicine and Biology Society. 2008; 430–434.

- [158] Gholipour A, Estroff JA, Warfield SK. Robust super-resolution volume reconstruction from slice acquisitions: application to fetal brain MRI. *IEEE Transactions on Medical Imaging* 2010;29:1739–1758.
- [159] Kim S, Bose NK, Valenzuela HM. Recursive reconstruction of high resolution image from noisy undersampled multiframe. *IEEE Transactions on Acoustics, Speech, and Signal Processing* 1990;38:1013–1027.
- [160] Kim SP, Su WY. Recursive high-resolution reconstruction of blurred multi-frame images. *IEEE Transactions on Image Processing* 1993;2:534–539.
- [161] Elad M, Feuer A. Restoration of a single superresolution image from several blurred, noisy, and undersampled measured images. *IEEE Transactions on Image Processing* 1997;6:1646–1658.
- [162] Van Reeth E, Tham IW, Tan CH, Poh CL. Super-resolution in magnetic resonance imaging: a review. *Concepts in Magnetic Resonance Part A* 2012;40:306–325.
- [163] Tourbier S, Bresson X, Hagmann P, Thiran JP, Meuli R, Cuadra MB. An efficient total variation algorithm for super-resolution in fetal brain MRI with adaptive regularization. *NeuroImage* 2015;118:584–597.
- [164] Poot DHJ. Advances in the reconstruction and statistical processing of Magnetic Resonance images. Ph.D. thesis, University of Antwerp, 2010.
- [165] Cocosco C, Kollokian V, Kwan R, Evans A. Brainweb: Online interface to a 3D MRI simulated brain database. *NeuroImage* 1997;5:S425.
- [166] Beirinckx Q, Ramos-Llordén G, Jeurissen B, Poot DHJ, Parizel PM, Verhoye M, Sijbers J, den Dekker AJ. Joint maximum likelihood estimation of motion and T1 parameters from magnetic resonance images in a super-resolution framework: a simulation study. *Fundamenta Informaticae* 2020;172:105–128.
- [167] Li Y, Matej S, Metzler SD. Image reconstructions from super-sampled data sets with resolution modeling in PET imaging. *Medical physics* 2014;41:121912.





# List of Abbreviations

AIF	arterial input function
ASL	arterial spin labeling
ATT	arterial transit time
CASL	continuous arterial spin labeling
CBF	cerebral blood flow
CoV	coefficient of variation
CRLB	Cramér-Rao lower bounds
CT	computed tomography
DSC	dynamic susceptibility contrast
EPI	echo-planar imaging
FIM	Fisher information matrix
FOV	field of view
GM	gray matter
GRASE	gradient and spin echo
HR	high-resolution
IRF	impulse response (or residue) function
ISMRM	International Society of Magnetic Resonance in Medicine
IVIM	intravoxel incoherent motion
LR	low-resolution
MCM	multi-compartment model
MLE	maximum likelihood estimator
MRI	magnetic resonance imaging
NLE	non-linear least-squares estimator
PASL	pulsed arterial spin labeling
PCASL	pseudo-continuous arterial spin labeling
PCC	Pearson correlation coefficient
PD	proton density
PDF	probability density function
PET	positron emission tomography
PLD	post-labeling delay

---

PVE	partial volume effect
RF	radiofrequency
SAR	specific absorption rate
SCM	single-compartment model
SNR	signal-to-noise ratio
SRR	super-resolution reconstruction
TCM	two-compartment model
TE	echo time
te-PCASL	time-encoded pseudo-continuous arterial spin labeling
te-FL	time-encoded free lunch
TR	repetition time
WM	white matter

# List of Symbols

Throughout this dissertation, lower case Roman and Greek symbols that are written in bold represent a vector. Upper case Roman letters in bold represent a matrix. Transposition of a vector or matrix is denoted by a superscript  $T$ . Non-bold symbols are scalars.

In what follows, the first column contains the symbol, the second column contains the explanation, and the third column the unit (if applicable). Symbols that are used only once in the text are not shown here.

$\boldsymbol{\theta}$	parameter vector	
$\hat{\boldsymbol{\theta}}$	estimator	
$E[\cdot]$	expectation operator	
$\boldsymbol{J}$	intrinsic angular momentum of an atomic nucleus	
$\hat{\boldsymbol{J}}$	angular momentum operator	
$\boldsymbol{I}$	intrinsic spin of an atomic nucleus	
$\hat{\boldsymbol{I}}$	spin operator	
$\boldsymbol{\mu}$	magnetic dipole moment of an atomic nucleus	
$\gamma$	gyromagnetic ratio of an atomic nucleus	
$\boldsymbol{B}$	magnetic field	[T]
$\omega_L$	Larmor frequency	
$\boldsymbol{M}$	macroscopic magnetization in a unit sample	
$T_1$	longitudinal relaxation time	[s]
$T_2$	transversal relaxation time	[s]
$G_z$	slice encoding magnetic gradient	[T]
$G_x$	frequency encoding magnetic gradient	[T]
$G_y$	phase encoding magnetic gradient	[T]
$k$	wave number	[m <sup>-1</sup> ]
$S$	signal intensity	
$\sigma_0$	standard deviation of signal-independent noise in MR	
$\sigma_P$	standard deviation of signal-dependent physiological noise in MR	
$\lambda$	blood/brain partition coefficient	[mL/g]

---

$\Delta M$	difference magnetization between an ASL label and control signal	
$\Delta S$	difference signal between an ASL label and control signal	
$T_{1b}$	longitudinal relaxation time of blood	[s]
$T_{1t}$	longitudinal relaxation time of tissue	[s]
$S_{PD}$	proton density signal	
$\alpha$	labeling efficiency	
$\tau$	labeling duration	[s]
$M_{0b}$	equilibrium magnetization of arterial blood in a unit voxel	
$f$	cerebral blood flow	[mL/100g/min]
$\Delta t$	arterial transit time	[s]
$t$	acquisition time point with $t = 0$ at the start of labeling	[s]
$c(t)$	arterial input function in convolution approach for ASL modeling	
$r(t)$	residue function in convolution approach for ASL modeling	
$m(t)$	magnetization relaxation function in convolution approach for ASL modeling	
$q(t)$	impulse residue function; equal to $r(t)m(t)$ in convolution approach for ASL modeling	
$\tau_{trans}$	blood-to-tissue water transit time at blood-brain barrier	[s]
$V_c$	distribution volume of labeled molecules in capillary space	[mL/100g]
$PS$	capillary permeability-surface area product	[mL/100g/s]
$\tau_a$	microvascular arterial transit time	[s]
$\tau_c$	microvascular capillary transit time	[s]
$\tau_v$	microvascular venous transit time	[s]
$V_v$	distribution volume of labeled molecules in venous space	[mL/100g]
$g_i(\boldsymbol{\theta})$	perfusion model function at time point $t_i$ with $\boldsymbol{\theta}$ the parameter vector to be estimated	
$L(\mathbf{a} \mathbf{b})$	likelihood function of parameters $\mathbf{a}$ given a set of observations $\mathbf{b}$	
$p(\mathbf{b} \mathbf{a})$	probability density function of observations $\mathbf{b}$ given a set of parameters $\mathbf{a}$	
$I(\boldsymbol{\theta})$	Fisher information matrix	





# Academic overview

## Journal papers

- Pullens P, **Bladt P**, Sijbers J, Maas AIR, Parizel PM. Technical note: A safe, cheap and easy-to-use isotropic diffusion phantom for clinical and multicenter studies. *Medical Physics* 2017;44(3):1063-1070.
- **Bladt P**, den Dekker AJ, Clement P, Achten E, Sijbers J. The costs and benefits of estimating T1 of tissue alongside cerebral blood flow and arterial transit time in pseudo-continuous arterial spin labeling. *NMR in Biomedicine* 2019; in press (e4182).
- Byl E, **Bladt P**, Lebeer S, Kiekens F. Importance of pressure plasticity during compression of probiotic tablet formulations. *European Journal of Pharmaceutics and Biopharmaceutics* 2019;145:7-11.
- **Bladt P**, van Osch MJP, Clement P, Achten E, Sijbers J, den Dekker AJ. Supporting measurements or more averages? How to quantify cerebral blood flow most reliably in 5 minutes by arterial spin labeling. *Magnetic Resonance in Medicine* 2020;00:1-17.

## Conference papers

- **Bladt P**, Van Steenkiste G, Ramos-Llordén G, den Dekker AJ, Sijbers J. Multi-voxel algorithm for quantitative bi-exponential MRI T1 estimation. In *Proceedings of SPIE 9784, Medical Imaging* 2016: Image Processing, 978402.

## Conference abstracts

- **Bladt P**, Ramos-Llordén G, Van Steenkiste G, den Dekker AJ, Sijbers J. Quantitative T1 estimation from T1-weighted images affected by partial volume effects. In *Proceedings of the second Belgian Neuroinformatics Congress*, Leuven, Belgium, 2015.

- 
- Pullens P, **Bladt P**, Parizel PM. A highly standardized, easy to produce and cost-effective isotropic PVP diffusion phantom for quality assessment and multi-center studies. In *Proceedings of the International Society for Magnetic Resonance in Medicine*, volume 23, page 2760, Toronto, Canada, 2015.
  - **Bladt P**, den Dekker AJ, Sijbers J. Challenges in state-of-the-art arterial spin labeling perfusion MRI. In *Proceedings of the International Society for Magnetic Resonance in Medicine Benelux*, volume 8, Eindhoven, The Netherlands, 2016.
  - **Bladt P**, den Dekker AJ, Clement P, Achten E, Sijbers J. Optimal sampling strategy for pseudo-continuous arterial spin labeling MRI. In *Proceedings of the International Society for Magnetic Resonance in Medicine Benelux*, volume 9, Tilburg, The Netherlands, 2017.
  - **Bladt P**, Beirinckx Q, Van Steenkiste G, Jeurissen B, Achten E, den Dekker AJ, Sijbers J. Super-resolution multi-PLD PCASL: a simulation study. In *Proceedings of the European Society for Magnetic Resonance in Medicine & Biology*, volume 23, Barcelona, Spain, 2017.
  - **Bladt P**, den Dekker AJ, Clement P, Achten E, Sijbers J. Maximizing precision in PCASL MRI using an optimized sampling strategy. In *Proceedings of the European Society for Magnetic Resonance in Medicine & Biology*, volume 23, Barcelona, Spain, 2017.
  - Ramos-Llordén G, den Dekker AJ, **Bladt P**, Cuyt A, Sijbers J. Statistically optimal separation of multi-component MR signals with a Majorize-Minimize approach: application to MWF estimation. In *Proceedings of the European Society for Magnetic Resonance in Medicine & Biology*, volume 23, Barcelona, Spain, 2017.
  - **Bladt P**, den Dekker AJ, Clement P, Achten E, Sijbers J. Absolute CBF quantification in multi-time point ASL: the T1 issue. In *Proceedings of the International Society for Magnetic Resonance in Medicine Benelux*, volume 10, Antwerp, Belgium, 2018.
  - **Bladt P**, van Osch MJP, Achten E, den Dekker AJ, Sijbers J. Beyond the consensus: should measurement of T1 of blood and labeling efficiency be included and should a single- or multi-PLD protocol be used in a five-minute protocol for PCASL? In *Proceedings of the International Society for Magnetic Resonance in Medicine Benelux*, volume 11, Leiden, The Netherlands, 2019.

- 
- **Bladt P**, van Osch MJP, Achten E, den Dekker AJ, Sijbers J. Beyond the consensus: is sacrificing part of the PCASL scan time for measurement of labeling efficiency and T1 of blood beneficial? In *Proceedings of University of Michigan international workshop on arterial spin labeling MRI: technical updates and clinical experience*, Ann Arbor, Michigan, USA, 2019.
  - **Bladt P**, van Osch MJP, Achten E, den Dekker AJ, Sijbers J. Beyond the consensus: what to include when 5 minutes are available for perfusion imaging by PCASL? In *Proceedings of the International Society for Magnetic Resonance in Medicine*, volume 27, number 4953, Montréal, Canada, 2019.
  - Beirinckx Q, **Bladt P**, van der Plas MCE, Schmid S, Teeuwisse WM, Jeurissen B, den Dekker AJ, Sijbers J, van Osch MJP. Super-resolution strategies for single-PLD pseudo-continuous ASL. In *Proceedings of the International Society for Magnetic Resonance in Medicine Benelux*, volume 12, Arnhem, The Netherlands, 2020.
  - **Bladt P**, Beirinckx Q, van der Plas MCE, Schmid S, Teeuwisse WM, Jeurissen B, den Dekker AJ, Sijbers J, van Osch MJP. Super-resolution reconstruction of single-PLD pseudo-continuous ASL images. Accepted for presentation at the *28th Annual Meeting of the International Society for Magnetic Resonance in Medicine*, Paris, France, 2020.

## Awards

- *Strategic basic research FWO PhD fellowship* - Jan 2016 - Dec 2019
- *Oral Presentation Award* - Optimal Sampling Strategy for Pseudo-Continuous Arterial Spin Labeling MRI. The 9th Annual Meeting of ISMRM Benelux, 20th January 2017, Tilburg, The Netherlands.
- *Educational Stipend Award* for the submitted work, entitled: Beyond the consensus: what to include when 5 minutes are available for perfusion imaging by PCASL? at the 27th Annual Meeting of the International Society of Magnetic Resonance in Medicine, Montréal, Canada, 2019.

## Research stays

- C.J. Gorter Center for High Field MRI, Leiden University Medical Center, Leiden, The Netherlands. From September 9th 2019 to November 6th 2019, supervised by Prof. Dr. M.J.P. van Osch.

---

## Invited talks

- *Multi-voxel algorithm for quantitative bi-exponential MRI T1 estimation*, Annual meeting of the Interuniversity Attraction Poles (IUAP) VII/11, Leuven, Belgium, 2016.
- *Accuracy and precision of parameter estimation in arterial spin labeling perfusion MRI*, Annual meeting of the FWO Scientific Research Network (WOG) "Turning images into value through statistical parameter estimation", Leuven, Belgium, 2018.

## Courses and workshops

- Annual meeting of the FWO Scientific Research Network (WOG) "Turning images into value through statistical parameter estimation": Kick-off meeting, Antwerp, Belgium, September 25, 2017.
- ESMRMB Workshop on Measurement of Perfusion and Capillary Exchange, Bremen, Germany, June 21-23, 2017.
- Annual meeting of the FWO Scientific Research Network (WOG) "Turning images into value through statistical parameter estimation": Bayesian inference, Hasselt, Belgium, September 25, 2017.
- Annual meeting of the FWO Scientific Research Network (WOG) "Turning images into value through statistical parameter estimation": Model selection, Leuven, Belgium, June 11, 2018.
- University of Michigan international workshop on arterial spin labeling MRI: technical updates and clinical experience, Ann Arbor, Michigan, USA, March 9-10, 2019.

## Teaching and supervision

- 2015-2016: Co-supervisor of Roel Daneels' Bachelor thesis in Physics: *Optimaal experiment ontwerp ASL-MRI*, University of Antwerp.
- 2017-2018: Co-supervisor of Roel Daneels' Master thesis in Physics: *Vergelijkende studie van conventionele en Hadamard geëncodeerde arterial spin labeling*, University of Antwerp.

- 
- 2017-2019: Ombudsperson for the Bachelor of Physics, University of Antwerp.
  - 2015-2019: Tutor exercises 'Fysica m.i.v. wiskunde' (1st year B. Sc. Pharmacy and 1st year B. Sc. Biomedical Sciences), supervising lecturer: Prof. Dr. Jan Sijbers.
  - 2016-2019: Tutor exercises 'Fysica voor biomedisch onderzoek' (1st year B. Sc. Biomedical Sciences), supervising lecturer: Prof. Dr. Jan Sijbers.